

Photocatalytic and Electrocatalytic Reduction of Carbon Dioxide in Pressurized Systems

THÈSE N° 6985 (2016)

PRÉSENTÉE LE 6 AVRIL 2016

À LA FACULTÉ DES SCIENCES DE BASE

LABORATOIRE D'ÉLECTROCHIMIE PHYSIQUE ET ANALYTIQUE

PROGRAMME DOCTORAL EN CHIMIE ET GÉNIE CHIMIQUE

ÉCOLE POLYTECHNIQUE FÉDÉRALE DE LAUSANNE

POUR L'OBTENTION DU GRADE DE DOCTEUR ÈS SCIENCES

PAR

Patrick VOYAME

acceptée sur proposition du jury:

Prof. A.-C. Corminboeuf, présidente du jury

Prof. H. Girault, directeur de thèse

Prof. A. Deronzier, rapporteur

Dr L. Plasseraud, rapporteur

Prof. G. Laurenczy, rapporteur



ÉCOLE POLYTECHNIQUE
FÉDÉRALE DE LAUSANNE

Suisse
2016

Acknowledgments

This thesis work could not have happened without the help of the many protagonists that have crossed my life during the past five years.

First of all, I would to say a sincere thank you to Professor Hubert Girault, who has welcomed me in his research group and motivated me to work on the challenging topic of carbon dioxide reduction. Thank you for your support and for always bringing new ideas to develop the project.

I would also like to acknowledge the work of the Jury members, Professor Anne-Clémence Corminboeuf, Professor Gabor Laurenczy, Professor Alain Deronzier and Doctor Laurent Plasseraud for taking the time to read the present thesis and providing an interesting discussion and valuable comments.

Thank you also to the colleagues that I have been working with on this project: Dr Kathryn Toghil, Dr Manuel Méndez. Thank you very much for your guidance, advice and for your friendship. Thank you also to Dr Heron Vrubel, who has been a valuable help in the field of catalyst synthesis. Thank you to Dr Astrid Olaya and Dr Véronique Amstutz, the persons who have read my thesis and provided suggestions and comments.

I would also say a big thank you to Madame Patricia Byron for her permanent kindness and continuous help in any kind of administrative works during these years. Thank you also to Madame Anne Lene Odegaard for her help in the administrative aspects related to the doctoral school.

Throughout the thesis different custom built reactors have been designed and made by the team of the mechanical workshop. So, I would like to thank them sincerely and especially Roger Mottier for his help and disponibility. Thank you also to the team of the magasin CH and the electronic workshop for their help. Thank you also to Madame Valérie Devaud and Dr Fernando Cortez for their help concerning security and the ordering of new material.

I would like to thank every member of the LEPA group that I have known during these years. The office mates in Lausanne and Sion: Veronique, Sunny, Haiqiang, Manuel, Géraldine, Justine, Alexandra, Yindi, Désiré, Joana, Andres, Fang, Ruslan, Igor and Alina. I have been passing very good time sharing an office and having nice and interesting discussions. Also a big thank you to all the people in the lab, that are: Lucie, Micheal, Jonnathan, Peiyu, Liang, Dmitry, Imren Eugene, Andreas, Pekka, Alberto, Christopher, Natalia, Millica, Elena T., Elena

V., Grégoire, Mickael, Anne-Laure, Reza, Hongyan, Tzu-en Xiaqin, Shiwei, Pingping, Lei, Xiajun and Hualan. It has been very enriching for me to meet you all.

Finally, I would like to thank my friends and my family for their support and all the cheerful time we have been sharing together during and before my PhD project.

Abstract

The depletion of carbon-based fossil fuels and the rise in atmospheric carbon dioxide concentration will force an inevitable change in the future global energy landscape. CO₂ reduction presents the advantages of decreasing its atmospheric concentration and storing energy in chemical form in CO₂ reduction products. With a predicted conversion to renewable energy such as solar or wind energy, energy storage will become a key process in the near future for buffering the fluctuating energy production.

The objective of the present work was to study the efficiency towards CO₂ reduction of different molecular catalysts. In particular, conducting experiments in high-pressure and supercritical conditions and observing the effect of CO₂ pressure or concentration on the efficiency and selectivity of the reaction. As supercritical CO₂ (scCO₂) has poor solubilisation capabilities, experiments were conducted in biphasic systems or with addition of an organic co-solvent.

To drive the reduction reaction of CO₂, a catalyst is needed to overcome the kinetic limitations of the reaction, but an energy input is also necessary. Three different forms for this energy input were used in this work. In a first time a sacrificial product, decamethylferrocene (DMFc), was used to transfer electrons to CO₂ in biphasic water/scCO₂ systems. Complete oxidation of the DMFc was observed in presence of anion capable of transporting protons from water to the DMFc present in the supercritical phase.

A photosensitization cycle was used to supply a water soluble catalyst, NI(II)cyclam, in electron at the required potential to drive the reduction of CO₂ into carbon monoxide in water/scCO₂ system. The creation of the interface in the system appeared highly favourable to the efficiency of the catalyst.

A second catalyst, a ruthenium polypyridyl carbonyl complex, was used for the photocatalytic reduction of CO₂. Pressure had an important impact on the production of one of

the two reduction product, carbon monoxide, while the production of formate was unaffected by CO₂ pressure.

As limitations in productivity in photocatalytic experiments were coming principally from the photosensitizer cycle or the sacrificial electron donor, photosensitizer was replaced by an electrode to provide the catalyst in electrons. Voltammetry in CO₂-expanded liquids was described and determination of important parameters such as catalyst concentration and diffusion coefficient as a function of pressure was performed.

Electrocatalytic reduction of CO₂ by ruthenium and rhenium polypyridyl carbonyl complexes was studied in CO₂-expanded liquids. The catalytic mechanisms were observed to be highly influenced by CO₂ concentration.

Keywords : Carbon dioxide, molecular catalyst, high-pressure, supercritical CO₂, expanded liquid, photosensitization, voltammetry

Résumé

L'épuisement des réserves en combustibles fossiles basé sur le carbone et l'augmentation de la concentration atmosphérique de dioxyde carbone va conduire à un inévitable changement dans le paysage énergétique mondial. La réduction du CO₂ présente les avantages de diminuer sa concentration atmosphérique tout en permettant le stockage d'énergie sous forme chimique dans les produits de réduction. Dû au développement attendu des énergies renouvelables telles que l'énergie solaire et éolienne, le stockage d'énergie deviendra un procédé essentiel dans les années à venir pour absorber les fluctuations de production d'énergie.

L'objectif de ce travail était d'étudier l'efficacité de différents catalyseurs moléculaires pour la réduction du CO₂. En particulier, conduire des expériences à haute pression et en conditions supercritiques afin d'observer les effets de la pression de CO₂ sur l'efficacité et la sélectivité de la réaction. Comme le CO₂ supercritique (scCO₂) a de faibles capacités de solubilisation, les expériences étaient conduites dans des systèmes biphasiques ou en présence d'un co-solvant organique.

Pour permettre la réaction de réduction du CO₂, un catalyseur est nécessaire pour surmonter les limitations cinétiques de la réaction, mais un apport d'énergie est également nécessaire. Trois formes différentes pour cet apport d'énergie ont été utilisées dans ce travail. Dans un premier temps un produit sacrificiel, le decaméthylferrocène (DMFc), était utilisé pour transférer des électrons au CO₂ dans un système biphasique eau/scCO₂. L'oxydation complète du DMFc était observée en présence d'anions capables de transporter des protons de la phase aqueuse au DMFc présent dans la phase supercritique.

Un cycle de photosensibilisation était utilisé pour fournir des électrons au potentiel requis à un catalyseur soluble dans l'eau pour conduire la réaction de réduction du CO₂ en monoxyde de carbone dans un système eau/scCO₂. La création de l'interface dans le système est apparue comme étant très favorable à l'efficacité du catalyseur.

Un second catalyseur, un complexe de ruthénium comprenant des ligands polypyridyle et carbonyle, a été utilisé pour la réduction du CO₂ photocatalysée. La pression avait un impact important sur la production d'un des deux produits de réduction, le monoxyde de carbone, alors que la production de formate n'était pas affectée par la pression de CO₂.

Comme les limitations de productivité dans les expériences de photocatalyse venaient principalement du cycle de photosensibilisation ou du donneur sacrificiel d'électrons, le photosensibilisateur a été remplacé par une électrode fournissant les électrons au catalyseur. La voltammétrie dans des liquides expansés au CO₂ a été décrite et la détermination de paramètres importants comme la concentration du catalyseur ou son coefficient de diffusion a été effectuée.

La réduction électrocatalysée du CO₂ par des complexes de ruthénium et de rhénium contenant des ligands polypyridyle et carbonyle a été étudiée dans des liquides expansés au CO₂. Les mécanismes catalytiques ont été observés comme étant hautement influencés par la concentration de CO₂.

Mots-clés : Dioxyde de carbone, catalyseur moléculaire, haute pression, CO₂ supercritique, liquide expansé, photosensibilisation, voltammétrie

Table of contents

1 Introduction	1
1.1 Global energy landscape.....	1
1.1.1 Global energy overview	1
1.1.2 CO ₂ and climate change.....	2
1.1.3 Natural photosynthesis	4
1.1.4 Artificial photosynthesis and solar fuel	7
1.2 CO ₂ reduction	8
1.2.1 Thermodynamics of CO ₂ reduction	8
1.2.2 Photocatalytic reduction	11
1.2.3 Electrocatalytic reduction	16
1.2.4 Catalysts for CO ₂ reduction	19
1.3 Supercritical CO ₂	28
1.4 Scope of the present work.....	34
1.5 Bibliography	36
2 Experimental and instrumentation	43
2.1 Introduction	43
2.2 Material.....	44
2.2.1 Pump system	44
2.2.2 Reactors	45
2.2.3 Light sources	48
2.2.4 Catalysts synthesis	49
2.3 Procedures	50
2.3.1 Product analysis	50

2.3.2 reduction by DMFc in biphasic systems	53
2.3.3 High pressure spectroscopy	53
2.3.4 High pressure NMR	54
2.3.5 Photocatalytic reduction	55
2.3.6 Three-electrode voltammetry	56
2.3.7 Wilhelmy plate surface tension measurements.....	56
2.3.8 Pendant drop surface tension measurements	58
2.3.9 Phase behavior of expanded liquids.....	58
2.3.10 High pressure electrochemistry.....	59
2.4 Bibliography	61
3 Reduction by decamethylferrocene in biphasic systems	63
3.1 Introduction	63
3.2 DMFc as electron donor for hydrogen evolution	64
3.3 CO ₂ reduction in water-scCO ₂ systems.....	67
3.3.1 Choice of anion	69
3.3.2 Production yield of reduction products.....	70
3.4 NMR analysis	74
3.5 Conclusions	80
3.6 Bibliography.....	81
4 Photocatalytic reduction by nickel cyclam in biphasic systems	83
4.1 Introduction	83
4.2 Voltammetry of catalyst and photosensitizer	84
4.3 Photocatalytic reduction of CO ₂	85
4.4 pH effect on the reactivity	87
4.5 Interfacial tension measurement.....	90

4.6	Conclusions	96
4.7	Bibliography	97
5	Photocatalytic reduction by [Ru(bpy)₂(CO)L]ⁿ⁺	99
5.1	Introduction	99
5.2	Optimal solvent conditions	102
5.3	Effect of pressure	104
5.4	Turnover number and frequency	107
5.5	Limiting factors	108
5.5.1	Catalyst and photosensitizer concentration	109
5.5.2	Electron donor	112
5.5.3	Interferences	114
5.6	Mathematic model	117
5.7	Conclusions	124
5.8	Bibliography	126
6	Electrochemistry in expanded liquid and supercritical fluids	129
6.1	Introduction	129
6.2	Electrochemistry in expanded liquids	130
6.2.1	Phase composition	131
6.2.2	Diffusion coefficient as function of pressure	133
6.3	Electrochemistry in scCO ₂	137
6.3.1	Conductivity in scCO ₂	139
6.3.2	Scan rate dependence of DMFc in CH ₃ CN and scCO ₂ /CH ₃ CN	142
6.3.3	Diffusion in the scCO ₂ /CH ₃ CN single phase	144
6.4	Conclusions	146
6.5	Bibliography	148

7	Electrocatalytic reduction by ruthenium and rhenium catalysts	151
7.1	Introduction	151
7.2	Ruthenium catalyst	154
7.2.1	Voltammetric behaviour	154
7.2.2	Variation on protons and CO ₂ concentrations	156
7.2.3	Pressure effect on glassy carbon electrode	162
7.3	Rhenium catalyst	163
7.3.1	Voltammetric behaviour	163
7.3.2	Proton donor concentration.....	165
7.3.3	Pressure effect.....	166
7.3.4	Proton donor concentration at high-pressure	170
7.4	Conclusions	172
7.5	Bibliography.....	174
8	General conclusions and perspectives	175
9	Curriculum vitae	179

CHAPTER 1

Introduction

1.1. Global energy landscape

1.1.1. Global energy overview

Among the main challenges humanity will have to face in the coming decades, energy supply is one of the most important. With the rising of standard of living in the developing world, and the world population predicted to reach up to 13 billion by 2100 [1], the global energy consumption is predicted to keep increasing in the coming decades. Predictions forecast a 41% increase from 2012 to 2035 [2] and up to 56% by 2040 [3].

Currently, the global energy landscape relies at 86.7% on the burning of fossil fuels, in the form of coal (30.1%), oil (32.9%) and natural gas (23.7%). Only a small fraction is supplied through hydroelectricity (4.4%) or other renewable energy sources (2.2%) [4]. The depletion of carbon containing natural resources will make it inevitable to find an alternative

source of energy and simultaneously an alternative source of carbon to exploit as chemical feedstock.

1.1.2. CO₂ and climate change

Another major concern for the imminent future is the global impact of carbon dioxide accumulated in the atmosphere since industrial revolution. Carbon dioxide is part of the dynamic cycle of photosynthesis that maintains a level of CO₂ in the atmosphere and sustains life on earth. Of the anthropogenic emissions of CO₂, 91% is generated by the burning of fossil fuel and cement production. Of this amount of CO₂ generated by human activities, 50 % remains in the atmosphere while 26% and 24% are absorbed by land and ocean respectively [5, 6].

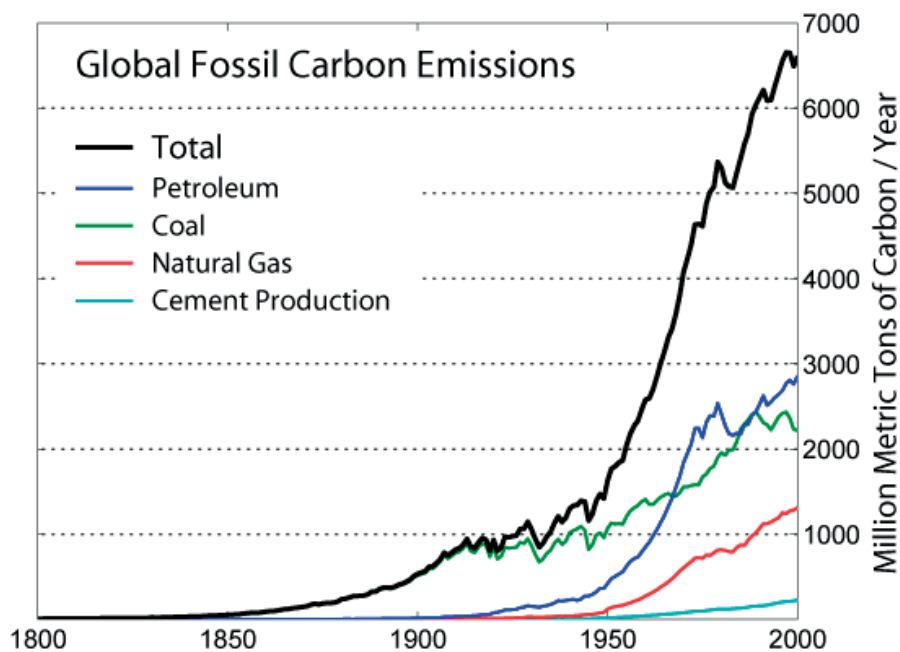


Figure 1.1. Global fossil carbon emissions for 1800–2007 [5].

The continuous increase in CO₂ emissions over the past two hundred years and the limited amount oceans and lands can absorb inevitably leads to an increase of CO₂ atmospheric concentration over years. In the past two hundred years the concentration has increased by more than 100 ppm in atmosphere, exceeding 400 ppm at the present time as shown in Figure 1.2. A level higher than it has ever been in the past 800,000 years.

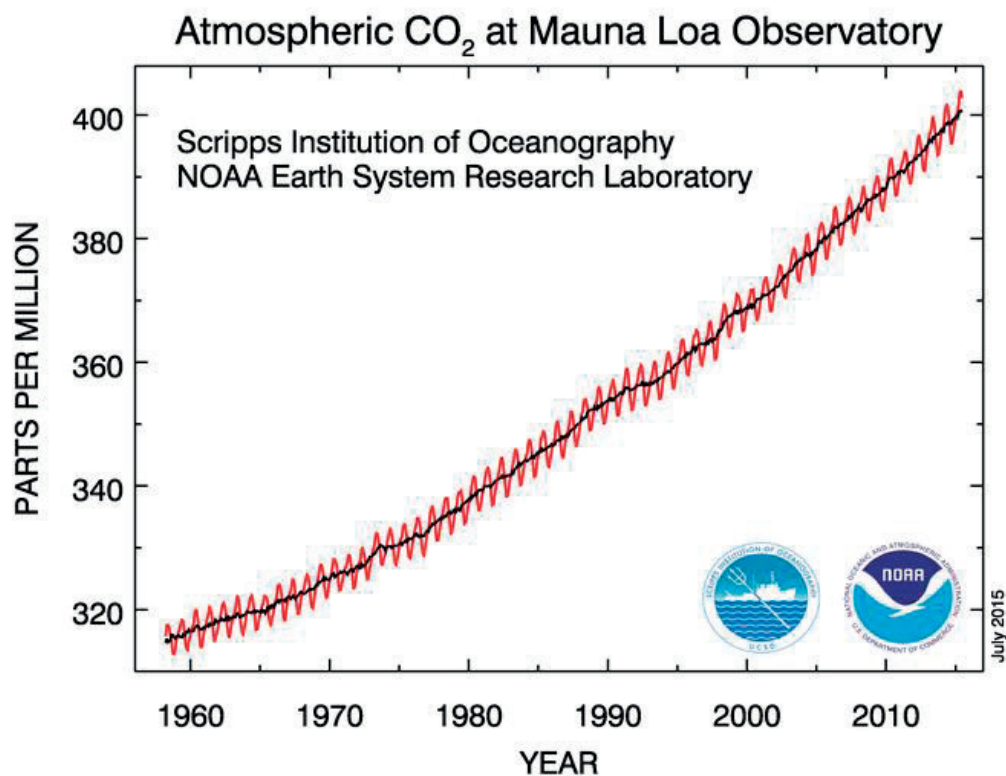


Figure 1.2. Atmospheric carbon dioxide concentration increase over the last decades [7].

It is now well admitted by the scientific community that global earth temperature and atmospheric CO₂ concentration are correlated to each other through the greenhouse effect [5, 8]. With the predicted increase in energy demands in the coming decades, decrease in CO₂ emission is not likely to occur. Even with the development of green and renewable energy sources, the amount of CO₂ accumulated in the atmosphere has already reached a worrying level. It will take many more years before the CO₂ level in the atmosphere will naturally decrease to its concentration of two centuries ago. This delay is of concerns, as before CO₂ levels decrease many environmental disasters are likely to occur, such as climate change [9],

higher global temperatures which in turn would lead to loss of water reserves and sea level rising [10] and, thus causing significant ecological ramifications. Consequently, there is an urgent need for solutions to reduce this atmospheric concentration of carbon dioxide.

Strategies for reducing emissions or capturing and burying large amounts of CO₂ are already in use. Burying CO₂ is still a highly debatable means of addressing this issue, as the long-term consequences are not really known. An alternative direction is to use this cheap and inexhaustible source of carbon as a starting material to produce chemicals or fuels by its chemical reduction, as achieved in photosynthetic systems. Carbon-based fuels have been intensively used due to their high gravimetric and volumetric energy density. Converting CO₂ into fuels combine multiple advantages in terms of energy density of the products and low cost of the starting material. As CO₂ reduction is an endergonic process, the transformation of CO₂ into fuels requires a supply of energy to drive the reaction. Among the different renewable energy sources, solar energy is by far the largest exploitable resource. The total sunlight energy hitting the earth in one hour provides more energy than the total amount consumed in one year by the entire human population [11]. Due to the intermittency of insolation and the disparity of intensity over the globe surface, solar energy need to be stored to become a major primary energy source. Converting solar energy into carbon based fuels through atmospheric CO₂ reduction appears as an appealing solution for the future of energy demands.

1.1.3. Natural photosynthesis

Solar energy storage and conversion of CO₂ into carbohydrate occur in plants through the mechanism of natural photosynthesis. The overall mechanism can be separated into a light-dependant chain of reaction that stores the light energy in the reduced molecules of nicotinamide adenine dinucleotide phosphate (NADPH) and adenosine triphosphate (ATP), and a light-independent mechanism that uses the reducing potential of NADPH and ATP to convert CO₂ to sugar through the Calvin cycle.

In the light-dependent process, represented schematically in Figure 1.3., photons are absorbed by a molecular photosensitizer located within photosystem II (PSII). The absorption of photon creates an electron-hole pair, which is stabilized by spatially separating the reducing and oxidizing species in different protein structures. Four oxidizing equivalents are accumulated on a catalytic site of the PSII in order to oxidise two water molecules into oxygen and protons. Electrons are transferred to a second photosystem (PSI) through an electron transport chain, which leads to the reduction of NADP to NADPH with the energy input of another photon. The overall result of the light-dependent mechanism is the accumulation of electrons in the form of the reducing agent NADPH on one side of the membrane, together with the oxidation of water and accumulation of protons on the other side of the membrane. The proton gradient and therefore the transmembrane electrochemical potential generated thereby is used as an energy source to power ATP synthesis[12].

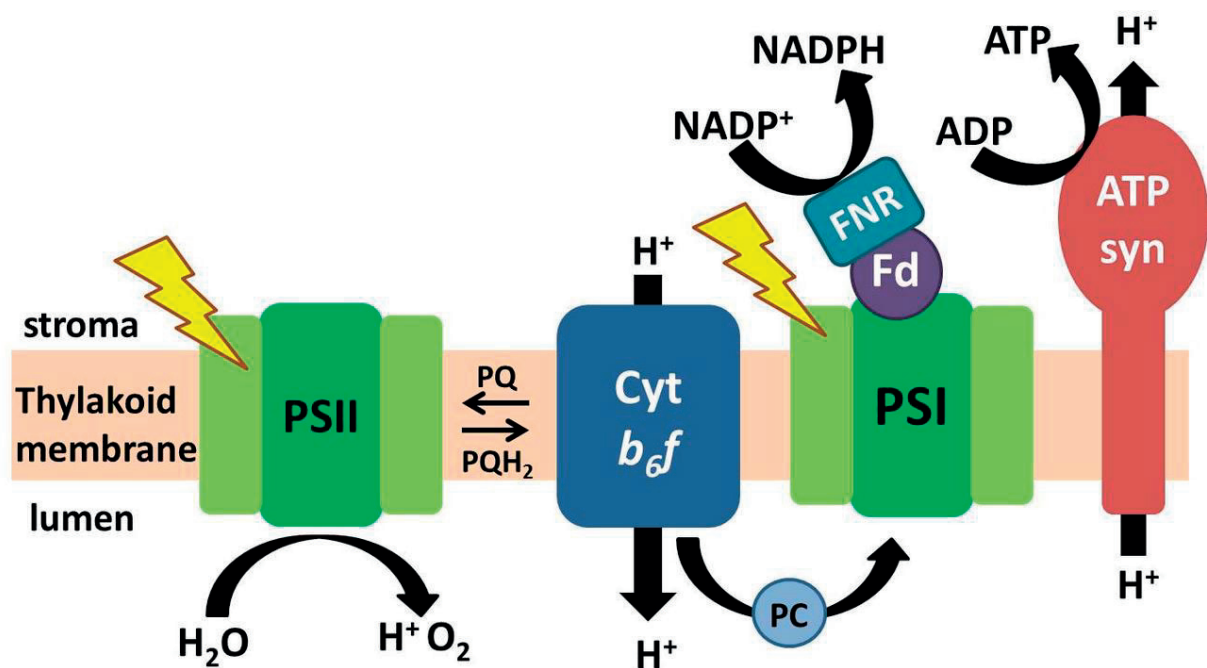


Figure 1.3. Simplified representation of the light-dependent photosynthetic reactions [12].

In the light-independent mechanism, summarized in Figure 1.4., the enzyme RuBisCO captures CO_2 and releases carbon sugar, through a process called Calvin cycle. This process requires the reducing potential of the previously formed NADPH and the chemical energy contained in ATP. In this cycle, CO_2 is initially absorbed by the RuBisCO enzyme and further

reacts with a 5-carbon molecule, ribulose-1,5-bisphosphate, which leads to the formation of two molecules of glyceralate 3-phosphate through hydrolysis. In the following steps, ATP is consumed to transform glyceralate 3-phosphate into 1,3-bisphosphoglycerate, which is then further reduced by NADPH into sucrose and starch. The energy stored in the molecule of NADPH and ATP during the light-dependent process is used in the Calvin cycle to produce sugar, and no additional energy is stored from the overall process.

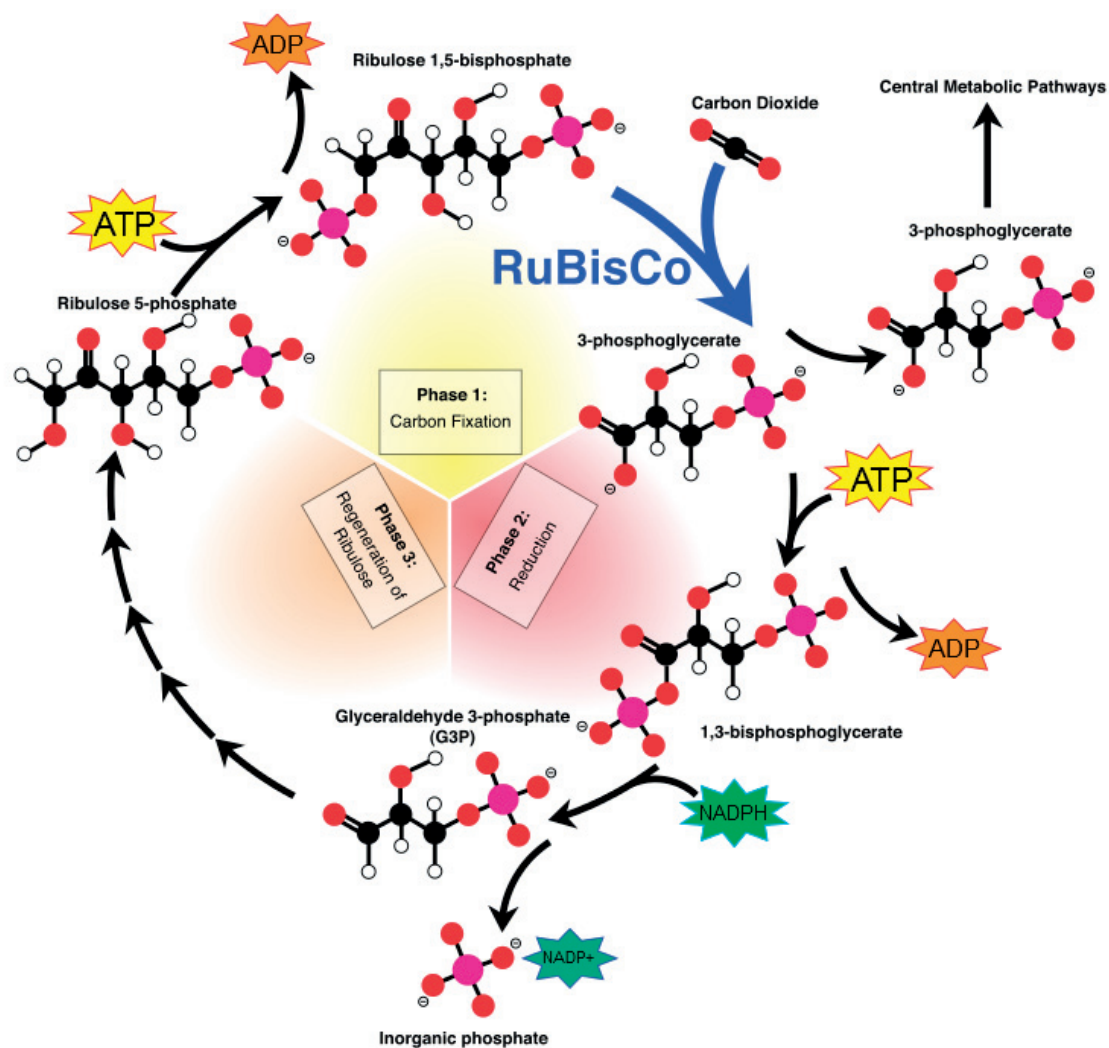


Figure 1.4. Overview of the Calvin cycle [13].

1.1.4. Artificial photosynthesis and solar fuel

During the last few decades much interest has been focused on artificial photosynthetic systems to harvest solar energy and convert it into a chemical form, from systems based on a copy of the natural machinery to purely artificial systems. The system developed in the late 90s by Moore *et al.* is a good example of the success achieved in the mimicking of the natural machinery [14, 15]. It consisted in generating a pH gradient through the membrane of an artificial vesicle under illumination in a manner similar to the natural photosynthesis. The pH gradient generated is subsequently used to power an ATPase immobilized in the membrane of the vesicle. The simplicity and the ability of this artificial system to convert sunlight into ATP is impressive when compared to the natural photosynthetic system. But the coupling of this system to a second one that could make use of the generated ATP is very difficult. Therefore, the energy conversion step aiming at creating a useful product was not achieved.

Several groups have focused their attention on the second step of photosynthesis, storing a flow of electrons into chemical bonds. Conversion of CO₂ into CO using a NiFe₄ CO-dehydrogenase from *Carboxydotherrnus hydrogenoformans* adsorbed on graphite electrode was demonstrated by Armstrong *et al.* in 2007 [16]. Similarly in 2008, Hirst *et al.* [17] demonstrated an efficient conversion of CO₂ into formate using a W-based formate dehydrogenase from the anaerobic bacteria *Syntrophobacter fumaroxidans* immobilised on a graphite electrode. Both systems are able to convert CO₂ efficiently at moderate potentials. However, the fragility, complexity and high production cost of these systems limit seriously their use as base component in artificial photosynthetic systems. Reduction of the production costs and improvement of the stability of the system could be achieved by focusing on the active site of the enzymes. Despite very close mimics of the primary coordination sphere of the natural active site have been synthesized, none have shown any noteworthy activity towards CO₂ reduction so far.

As it appears in these different examples, mimicking the natural photosynthesis process is not the ideal solution. But inspiration from biological principles is a base to build

fully synthetic system. Additionally, synthetic systems are not limited by the specific parameters required by a cell to maintain its existence, neither by the very narrow range of elements at disposal.

1.2. CO₂ reduction

1.2.1. Thermodynamics of CO₂ reduction

Thermodynamic requirements need to be considered, as CO₂ reduction is a very challenging reaction. Being the final combustion product of every carbon-based fuel, and the most oxidized form of carbon, CO₂ has an exceptional thermodynamic stability. On inert electrodes, as shown in Figure 1.5., the direct one-electron reduction to the radical CO₂^{•-} is the initial step of all product formation [18], but is a very energy intensive and unfavourable process [19]. Other pathways are much more favourable, as summarized in Table 1.1. They are all proton coupled electron transfer reactions, as observed in natural photosynthetic systems, and required much less energy, as indicated by less negative potentials [20, 21].

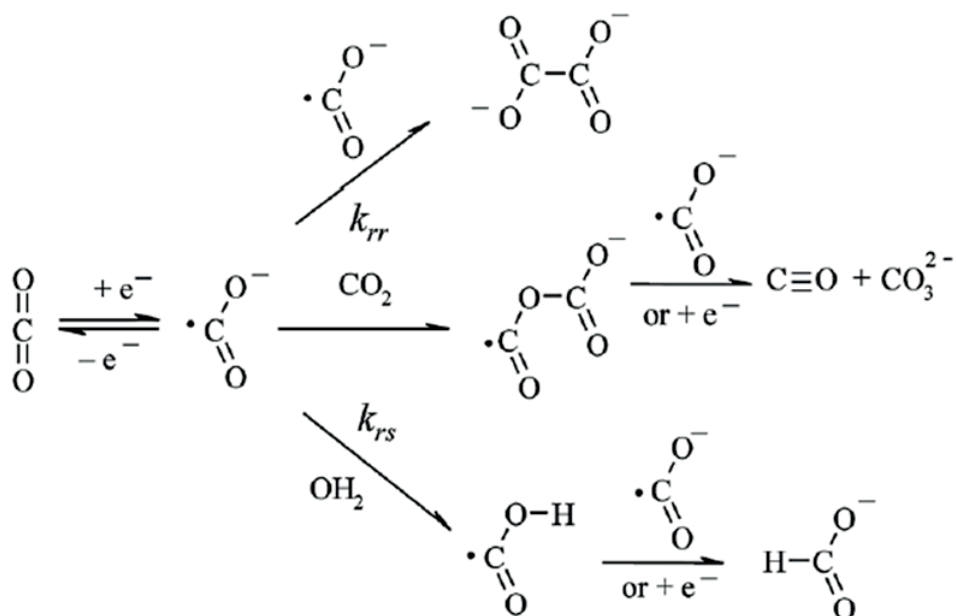


Figure 1.5. Reaction pathways of CO₂ reduction in oxalate, carbon monoxide and formate on inert electrodes [18].

Table 1.1 CO₂ Reduction Potentials for various CO₂ reduction reactions [22].

Reactions	E° (V) vs. SHE (at pH 7)
$\text{CO}_2 + e^- \rightarrow \text{CO}_2^{\bullet -}$	-1.89
$\text{CO}_2 + 2e^- + 2\text{H}^+ \rightarrow \text{HCOOH}$	-0.6
$\text{CO}_2 + 2e^- + 2\text{H}^+ \rightarrow \text{CO} + \text{H}_2\text{O}$	-0.52
$\text{CO}_2 + 4e^- + 4\text{H}^+ \rightarrow \text{C} + \text{H}_2\text{O}$	-0.19
$\text{CO}_2 + 4e^- + 4\text{H}^+ \rightarrow \text{HCHO} + \text{H}_2\text{O}$	-0.45
$\text{CO}_2 + 6e^- + 6\text{H}^+ \rightarrow \text{CH}_3\text{OH} + \text{H}_2\text{O}$	-0.35
$\text{CO}_2 + 8e^- + 8\text{H}^+ \rightarrow \text{CH}_4 + 2\text{H}_2\text{O}$	-0.23

Compared to the one-electron reduction of CO₂, the proton coupled multi-electron transfer reductions require less energy therefore they are much more favourable. A trend can

be observed: the potential become less negative when an increasing number of electrons are involve in the reaction, as presented in Figure 1.6. Two compounds are off the trend line, ascorbic acid requires a much more negative potential probably due to the formation of the carbon-carbon bond, and carbon monoxide, which is below the trend line.

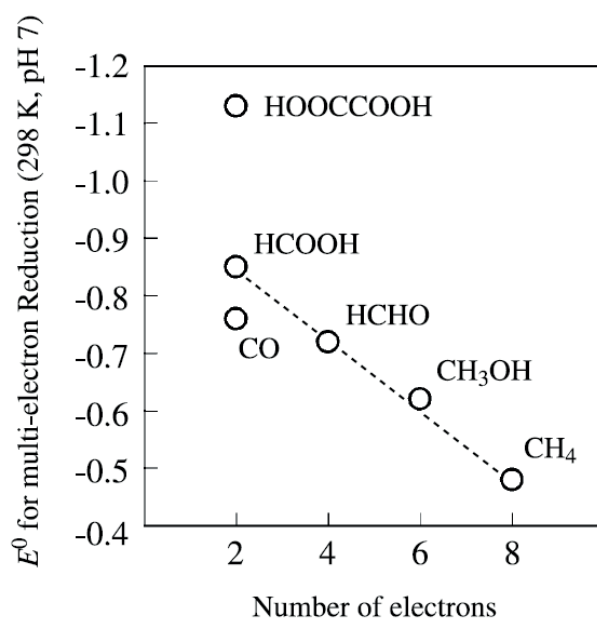


Figure 1.6. Reduction potential versus saturated calomel electrode and trend [23].

Although thermodynamically more favourable, proton coupled electron transfer reduction still requires energy, but more importantly it also requires a catalyst. Catalysts are needed to overcome kinetic limitations, and energy drives electrons at the required reaction potential. Different methods can be used to supplement energy to the system: (i) a sacrificial compound can be consumed to directly reduce CO_2 if the oxidation potential of the compound is negative enough to react with CO_2 , (ii) similarly to nature inspired system, light can be used to pump energy into the catalytic system, or (iii) an electrode can be used either as catalytic surface or to transfer electrons at the desired potential to the catalytic specie.

1.2.2. Photocatalytic reduction

Considering the potentials required for driving the multi electron-multi proton reduction of carbon dioxide, supplementing energy to the system is essential to promote electrons at negative potentials. As an example, the change of oxidative and reductive properties of the excited state of a common photosensitizer, ruthenium tris-bipyridine $[\text{Ru}(\text{bpy})_3]^{2+}$ is presented in Figure 1.7. In their electronic excited states, molecular photosensitizers have strong reductive and oxidative properties due to the promotion of one electron to a higher energy level and to the hole left on a lower orbital respectively.

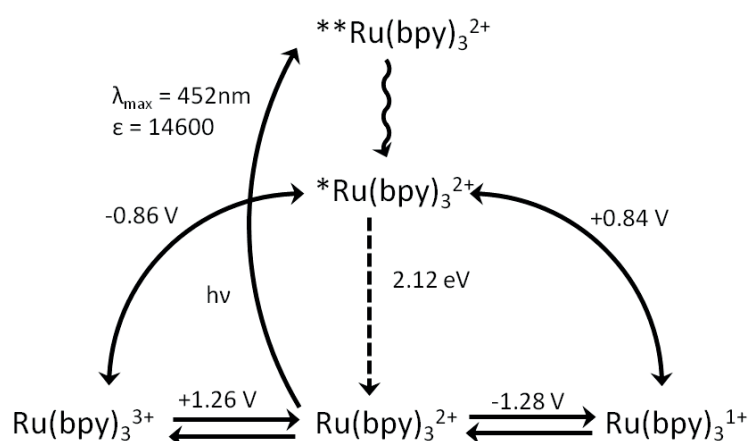
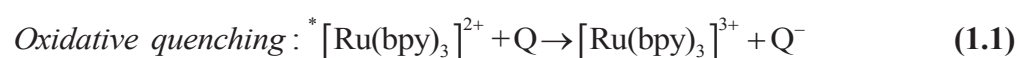
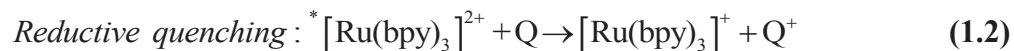


Figure 1.7. Molecular quantities of $[\text{Ru}(\text{bpy})_3]^{2+}$ relevant for energy and electron transfer processes, with potential vs. SHE [24].

Lifetime of the excited state is rather small, 600 nanoseconds in water [25], therefore the probability that the sensitizer in the excited state encounters the catalyst in solution is very low when the concentration of the two species is in the millimolar range. Efficiency of the sensitizer is improved using a quencher that can be used in higher concentrations, in the molar range. The collision probability is therefore a thousand-fold higher. The two possible quenching reactions are shown in reactions (1.1) and (1.2):





Using a quencher presents also the advantage of recycling the photosensitizer, therefore only the quencher is used as a sacrificial reactant. For $[\text{Ru}(\text{bpy})_3]^{2+}$, the oxidation potential after the reductive quenching is enough to drive all the multi electron-multi proton reduction processes presented in Table 1.1. While every redox-active species appears to be usable as quencher, in practice the irreversibility of its oxidation or reduction is of primary importance to avoid a back electron transfer. The different quenchers that have been widely used in reductive quenching processes are ascorbic acid (H_2A), triethanolamine (TEOA) and 1-benzyl-1,4-dihydronicotinamide (BNAH).

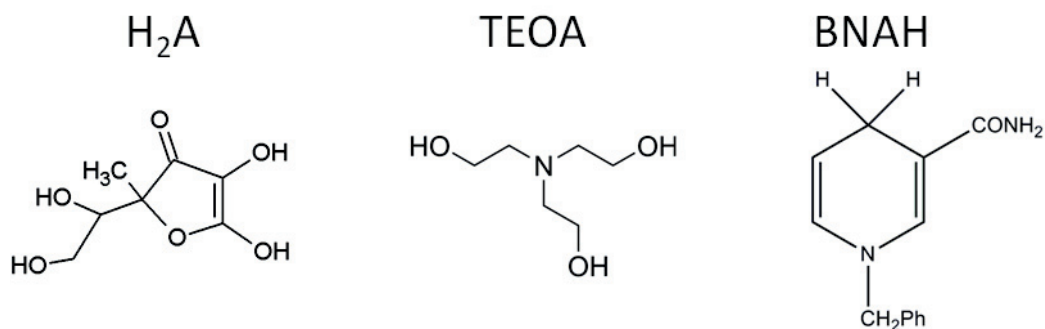


Figure 1.8. Structure of the quencher ascorbic acid, triethanolamine, and 1-benzyl-1,4-dihydronicotinamide

These three compounds have similarities in their reactivity. The first oxidation of these organic molecules generates an unstable radical, which is a very strong proton donor. In presence of a proton acceptor, generally the solvent, the loss of proton occurs immediately after the oxidation of the molecule, as shown in Figure 1.9. The reactions following the oxidation render the back electron transfer from photosensitizer to the electron donor impossible. These chain reactions have also the advantage of providing a source of protons, for each electron transfer to the photosensitizer a proton is generated in the solution. As all CO_2 reduction reaction required the same amount of proton and electron, the concentration of protons in the reaction media remains constant. Therefore the quencher acts also as a sacrificial proton donor.

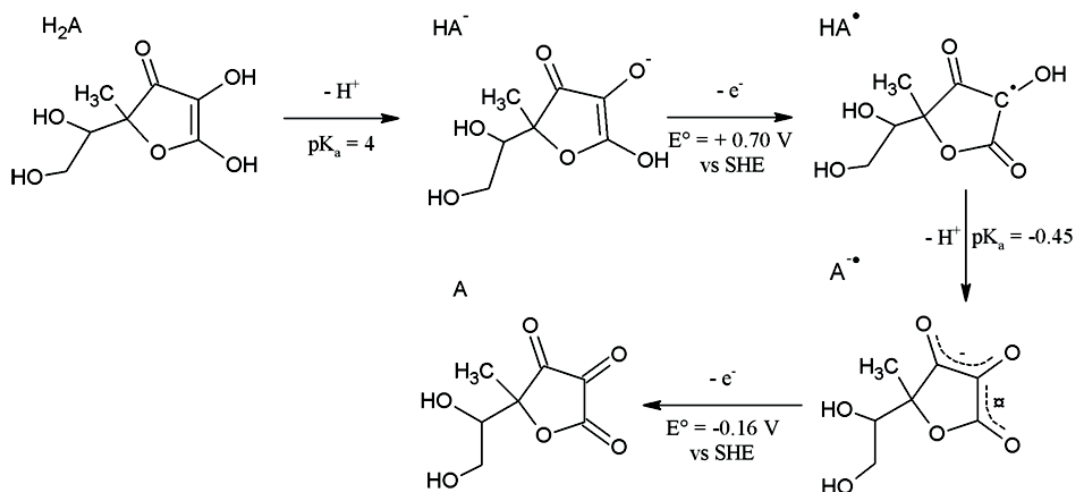


Figure 1.9. Chain reaction of the oxidation of ascorbic acid [26].

Electron transfer to the catalyst happens in three successive steps. In the first step, light is absorbed by the photosensitizer. The hole left in the HOMO of the photosensitizer is then filled by oxidation of the reductive quencher. The electron promoted in the LUMO by light absorption has now a potential negative enough to be transferred to the molecular catalyst in solution and activate the CO_2 reduction mechanism.

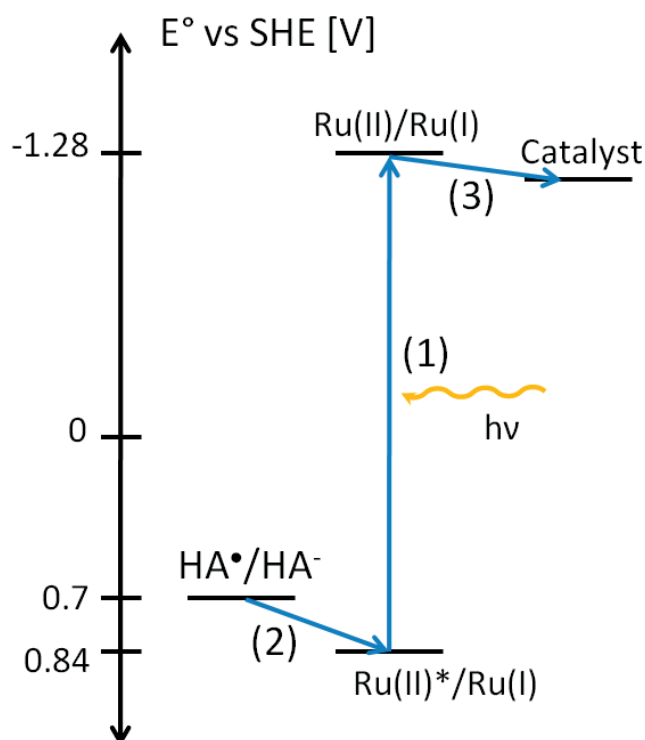


Figure 1.10. Diagram representing the steps required for the activation of the catalyst.

Four terms are commonly used to characterize a photocatalytic CO₂ reduction process: catalytic selectivity (*CS*), catalyst turnover number (*TON*) and frequency (*TOF*) and the quantum yield of the photocatalytic system.

CS is defined as the molar ratio of the CO₂ reduction product to the amount of hydrogen generated as side product:

$$CS = \frac{[\text{CO}_2 \text{ reduction product}]}{[\text{H}_2]} \quad (1.3)$$

TON is the number of reduction cycle that occurs per catalyst over the catalyst lifetime, calculated as the molar ratio of CO₂ reduction products to the amount of catalyst initially present:

$$TON = \frac{[\text{CO}_2 \text{ reduction product}]}{[\text{catalyst}]} \quad (1.4)$$

For photocatalytic systems, the catalytic activity can stop without degradation of the catalyst. Indeed, degradation of the photosensitizer or the presence of inhibiting products in the reaction media can hinder the catalysis without degradation of the catalyst. The turnover number is therefore more commonly reported as the number of reduction cycle per catalyst over the time interval until catalysis ceases.

In addition to the turnover number, the *TOF* is commonly reported. It is defined as the number of catalytic cycle per catalyst molecule and per unit of time:

$$TOF = \frac{[\text{CO}_2 \text{ reduction product}]}{[\text{catalyst}][\text{time}]} = \frac{TON}{[\text{time}]} \quad (1.5)$$

Turnover frequency generally decreases quickly due to partial deactivation of the catalyst, the photosensitizer or depletion of the quencher. To have a good measure of the catalytic activity in absence of deactivation, the initial turnover frequency is commonly reported, which is measured over a short time span in the initial conditions.

The photochemical quantum yield (Φ) is a measure of the efficiency of conversion of light into reduction product. It is defined as the fraction of incident photons that results in CO₂ reduction products:

$$\Phi = \frac{[\text{CO}_2 \text{ reduction product}] \cdot n}{\#(\text{incident photons})/N_A} \quad (1.6)$$

where n is the number of electrons involved in the reduction of CO₂ and N_A the Avogadro constant. In the case of the use of a non-monochromatic light source, the number of incident photon can be difficult to estimate. But with a monochromatic light of wavelength λ , the number of incident photon is calculated by:

$$\#(\text{incident photons}) = \frac{\text{Light power} \cdot \text{time}}{hc/\lambda} \quad (1.7)$$

where h is Planck constant and c the speed of light. These four characterisation terms associated to the efficiency of the photocatalytic process are not describing the activity of the

catalyst alone but are influenced by all the component of the systems, from the nature of the electron donor to the light intensity. Comparison of the efficiency of different catalysts is therefore difficult if the experiments are not done in the exact similar conditions.

1.2.3. Electrocatalytic reduction

Instead of using light to directly convert CO₂ into fuels, a second option consists of a preliminary conversion of light into electricity followed by the electrochemical reduction of CO₂. Electrocatalytic reduction can be divided into two different categories according to the nature of the catalyst: heterogeneous and homogeneous catalysis. In heterogeneous catalysis, the electrode is the locus of the reduction of carbon dioxide. Hori *et al.* [27] reported an overview of the catalytic activity of many metallic electrodes. The metals can be classified into three classes depending on the major reduction product in aqueous conditions. With Cd, Sn, Pb and In the major product is formate, while with Cu, Ag and Au it is carbon monoxide. Other metals, such as Ni and Fe are shown to be highly inefficient for CO₂ reduction as their major product in aqueous conditions is hydrogen. Recently, particular interest has been given to copper electrode with the work of Kanan *et al.* [28], where copper electrodes covered with a layer of Cu₂O proved to be very efficient in term of rates, overpotentials and selectivity for the reduction of carbon dioxide into carbon monoxide.

In the present work, the attention will be focused on the second type of electrocatalytic reduction, the homogeneous reduction. In this system, the electrode serves the exact same purpose as the photosensitizer in photocatalytic reduction, that is to transfer the electron to a molecular catalyst in solution.

In chapter 7, the homogeneous electrocatalytic reduction will be studied by the standard method of macroscale cyclic voltammetry. This technique allows an easy and fast differentiation between totally reversible electrochemical reduction, electrochemical reduction coupled to a chemical reaction, and electrochemical reduction coupled to a catalytic reaction.

For the following simple reversible reaction:



cyclic voltammetry shows a reversible reduction wave, with the peak current, i_p , following Randles-Sevcik equation :

$$i_p = 0.4463nFAC \left(\frac{nFvD}{RT} \right)^{1/2} \quad (1.9)$$

where F is the Faraday constant, A the electrode surface, C the concentration of the redox species considered, v the scan rate (in V/s) and D the diffusion coefficient of the redox species.

In the presence of a chemical reaction coupled to a reversible electrochemical reduction, the two reactions involved are the following:



In the case of fast electron transfer reactions, the following chemical reaction is the only rate-limiting factor other than diffusion. The electrochemical response is function of two parameters: the first order equilibrium constant of the chemical reaction K , and a dimensionless kinetic parameter λ , that measures the competition between chemical reaction and diffusion. In cyclic voltammetry:

$$\lambda = \frac{k_+ + k_-}{v} \frac{RT}{nF} \quad (1.11)$$

A large equilibrium constant is required to observe a significant influence of the chemical reaction on the voltammetric behaviour. Similarly for a small λ value, the voltammetry will obey a reversible unperturbed Nernstian behaviour. Conversely, for a large λ value, the system will appear as completely irreversible in the voltammetric time scale. No reverse wave is observed as the compound R reacts in solution immediately after its generation and before

being able to reach back the electrode to be re-oxidized to the compound O. Moreover, the reduction wave is slightly sharper and higher compared to reversible systems. In such cases the peak current is defined by a modified Randles-Sevcik equation:

$$i_p = 0.496nFAC \left(\frac{nFvD}{RT} \right)^{1/2} \quad (1.12)$$

In presence of a catalytic reaction following the reversible electrochemical reduction, the reactions considered are the following:



This system appears highly simplified compared to the possible mechanism for CO₂ reduction, as all required electrons are transferred in one single step, and all chemical steps for the catalysis are grouped together, with k_{cat} being the rate constant of the rate determining step. However, this simplified system is sufficient to understand the voltammetry of a catalytic system. The dimensionless kinetic parameter λ becomes:

$$\lambda = \frac{k_{cat} C_{CO_2}^*}{v} \frac{RT}{nF} \quad (1.14)$$

With $C_{CO_2}^*$ being the bulk concentration of carbon dioxide. In presence of a catalyst, the redox active specie is recycled in the diffusion layer, and, as a result, the current measured will then be increased. But this catalytic response is observed only if the dimensionless kinetic parameter is large enough (large rate constant or low scan rate). For a large concentration of substrate (here CO₂) compared to the concentration of catalyst, the current is purely limited by the kinetics, with the current independent on the scan rate. In these conditions, the voltammogram appears as a S-shaped wave, and the rate constant can be derived straightforwardly from the measurement of the plateau current:

$$i_{plateau} = nFAC_O^* \sqrt{D_O k_{cat} C_{CO_2}^*} \quad (1.15)$$

This limiting current arises when the rate of removal of O by reduction at the electrode is exactly compensated by the rate of production of O by the chemical reaction. So that the concentration of O at the electrode attains a value independent on scan rate. In this pure kinetic conditions, the equation for the wave on the voltammogram is:

$$i = \frac{nFAC_O^* \sqrt{D_O k_{cat} C_{CO_2}^*}}{1 + \exp\left[\frac{nF}{RT}(E - E_{O/R}^\circ)\right]} \quad (1.16)$$

1.2.4. Catalysts for CO₂ reduction

Since the 1970s, several molecular compounds have been tested as catalyst for the CO₂ reduction reaction. Two classes of molecular catalysts will be discussed in the present thesis: tetraaza-macrocyclic complexes of nickel and carbonyl polypyridine complexes of rhenium and ruthenium.

Transition-metal tetraaza-macrocyclic compounds were initially investigated by Tinnemans in photocatalytic CO₂ reduction [29]. The mechanism of the catalytic cycle of this compound was pioneered electrochemically by Sauvage [30] and photochemically by Calvin [31]. The catalytic unit, shown in Figure 1.11., is a 16 electrons, low spin, square planar complex with symmetry group D_{4h}. This configuration leaves two free coordination positions for CO₂ to bind to the complex and undergo reduction.

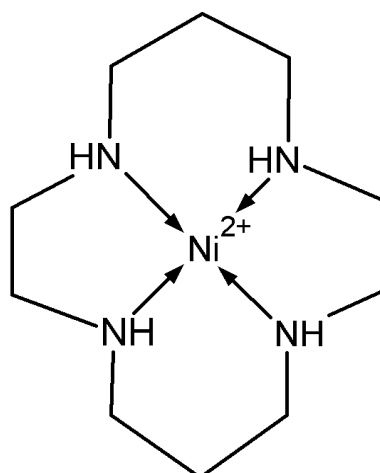


Figure 1.11. Structure of Nickel(II) 1,4,8,11-tetraazacyclotetradecane (Ni(II)cyclam).

For this class of catalysts, different mechanisms have been proposed over the past 30 years to explain the formation of the main reduction products: formate and carbon monoxide. Recently, Fujita has proposed a complete overview of the different pathways for the production of the two latter products and hydrogen [22].

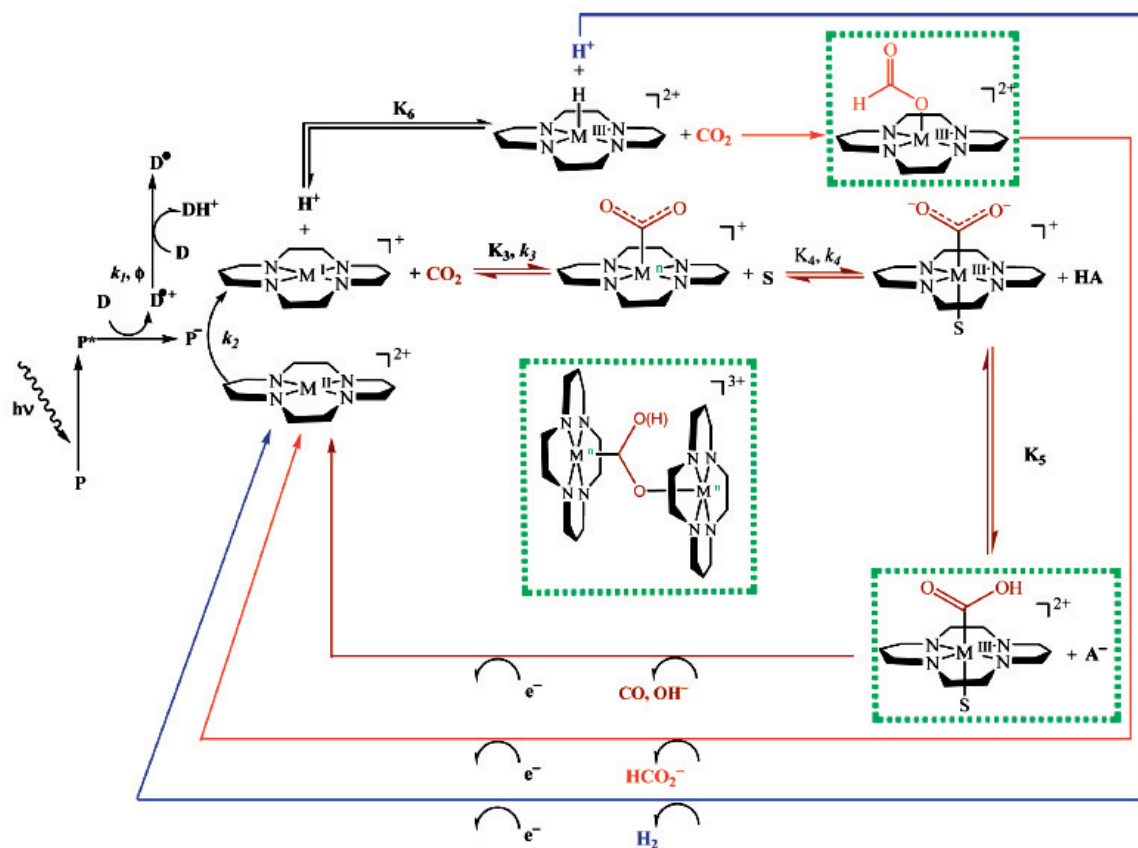


Figure 1.12. Recently mechanisms proposed by Fujita *et al.* for CO₂ reduction by metal tetraaza-macrocyclic complex, in blue: H₂ evolution, in red: formate production, in brown: CO production, putative intermediate shown in green. M = Co or Ni, D is an electron donor such as triethanolamine (TEOA) or ascorbate and P the photosensitizer [22].

It is well admitted that the reduction of CO₂ into the two different products, formate and carbon monoxide occurs through two different catalytic cycles. The product generated will depend on the species that will bind to the complex once it is reduced, photochemically or electrochemically. In this case it can be either a proton or CO₂. The oxidative addition of protons leads to formate in case of a successive reaction with CO₂ or hydrogen if a second proton interacts with the hydride. For the evolution of carbon monoxide, CO₂ must first bind to the reduced complex. It is followed by proton addition on CO₂ and subsequent hydroxide elimination. In the three different catalytic pathways a second reduction of the complex is necessary to release the product.

The second classes of complexes that will be investigated for the catalytic reduction of CO₂ in this thesis are the polypyridyl complexes of ruthenium and rhenium. Polypyridyl

ligands are redox active and can therefore assist multi-electron reactions, as electrons can be stored in the ligands of metallic complexes. Other metallic centres have been reported to also catalyze effectively the reduction of CO₂. Most of the metallic centres are from the 4*d* and 5*d* transition metals such as osmium [32-35], rhodium [36-38], iridium [36, 39], molybdenum [40] and tungsten [40]. But some successful results were also achieved with less expensive materials from the 3*d* transition metals. Manganese [41-43], iron [44, 45], cobalt [46], nickel [47] and copper [48] polypyridyl complexes shows noticeable activity toward CO₂ reduction. Despite the large range of possible catalysts, this thesis will focus exclusively on the ruthenium and rhenium catalyst, as they are the most referenced catalysts of this large class of compounds.

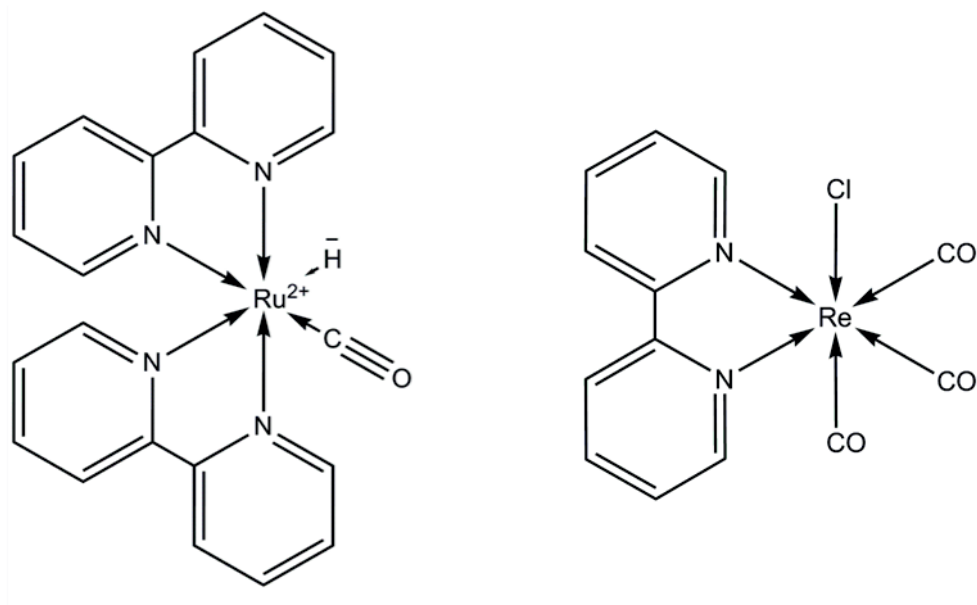


Figure 1.13. Structure of common polypyridyl catalysts of ruthenium and rhenium

The ruthenium polypyridyl class of catalysts has been used with considerable success towards CO₂ reduction, the most referenced of this family of catalyst is [Ru(bpy)₂(CO)L]ⁿ⁺ where bpy is 2, 2' bipyridine, L is a hydride or carbonyl ligand (*i.e.* H, CO₂, C(O)OH, CO) and *n* = 0, 1 or 2. These catalysts, introduced by Tanaka [49-53] but also developed by others such as Meyer [35, 54, 55] and Lehn [56, 57], are electrochemically active, and readily react with carbon dioxide to form formic acid and carbon monoxide. Over the past 30 years, several groups have studied the mechanism of formation of carbon monoxide, formate and hydrogen

by this kind of complexes. As for the Ni(II)cyclam catalyst, formate and carbon monoxide production follow two different pathways. Formate is produced through CO₂ insertion in a hydride bond, as reported by Meyer [58], and carbon monoxide is produced through oxidative addition of CO₂ on the reduced catalyst, as reported by Tanaka [49].

In the case of the catalytic cycle releasing carbon monoxide, proposed by Tanaka *et al.* [59], the initial step is the localised reduction of [Ru(bpy)₂(CO)₂]²⁺ (intermediate (8) in Figure 1.14.) at the bpy ligand, occurring at -1.20 V vs. saturated calomel electrode (SCE) in aqueous solution. These surplus electrons in the π^* orbital of the bipyridyl redistributed across the metal centre and the σ^* orbital of the Ru-CO bond, thus cleaving the CO molecule from the complex. In the presence of CO₂, the now neutral penta-coordinated complex (1) is sensitive to an electrophilic attack, resulting in a CO₂ ligand. In aqueous acidic solutions, this complex dehydrates to the starting complex, [Ru(bpy)₂(CO)₂]²⁺, completing the catalytic cycle. In the absence of water, an organic proton carrier, such as triethanolamine, might be able to protonate the bound CO₂ and induce the release of water. Another possibility is through the formation of bicarbonate from the abstraction of hydroxide by CO₂ (between 7 and 8). Tanaka and co-workers claim that the formation of formate occurs in the equilibration of the three interchangeable species (6-8), but without specific proton attack of the carbon atom, this is debatable. Yet, pH dependence studies by these researchers demonstrated that an alkaline pH favours formate production.

Meyer [58] proposed an alternative mechanism for the formation of formic acid, based on an earlier work by Hawecker [60] regarding formate formation using only [Ru(bpy)₃]²⁺ and TEOA in DMF. This second proposed cycle has a common species with the carbon monoxide cycle: [Ru(bpy)₂(CO)]⁰ (1). This common intermediate is produced upon reductive elimination of either formate (cycle right) or CO (cycle left) Figure 1.14. The resultant coordinatively unsaturated neutral complex, contains an available coordination site for a new ligand. The nature of this ligand would seem to dictate the product to be ultimately formed. Hence, CO will be preferentially produced *via* direct CO₂ coordination, whereas formate predominates when a hydride intermediate is formed instead, followed by CO₂ insertion into the metal-hydride bond.

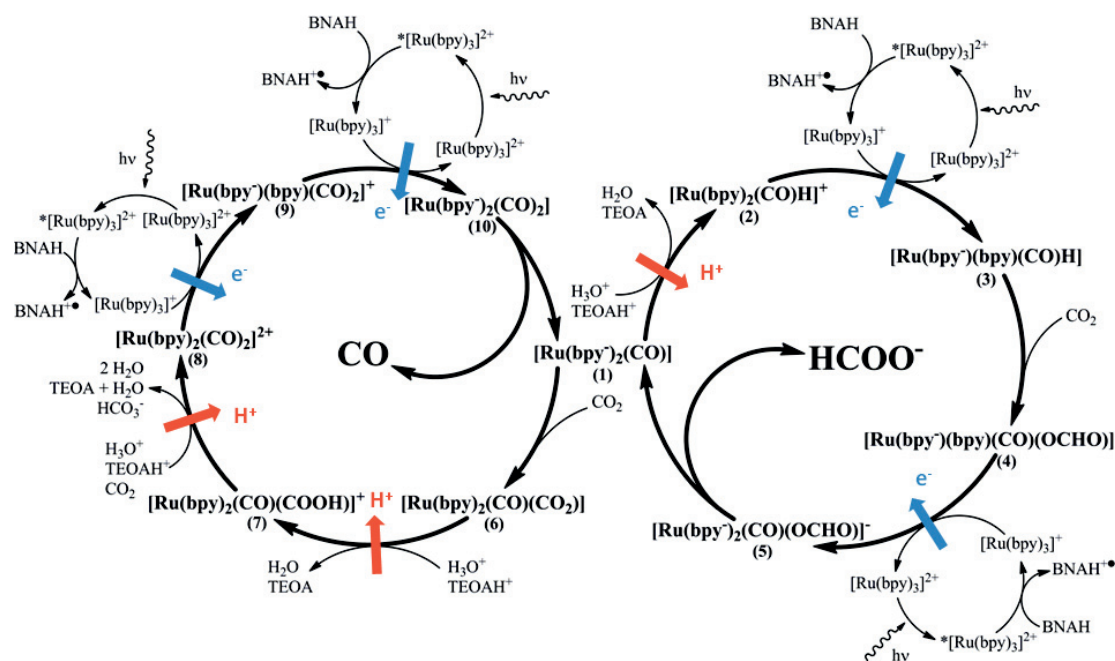


Figure 1.14. The combination of two catalytic cycles for the $[\text{Ru}(\text{bpy})_2(\text{CO})\text{L}]^{n+}$ in the photocatalytic reduction of CO_2 to formate or carbon monoxide [61]

For ruthenium complexes, the catalysts are not limited to a single metallic centre. Deronzier *et al.* [62] reported that $\text{cis}(\text{Cl})\text{-}[\text{Ru}(\text{bpy})(\text{CO})_2\text{Cl}_2]$ catalyzes the reduction of CO_2 . They stated that the loss of a chloride could lead to the formation of Ru-Ru dimers, acting as the catalytic species. Furthermore in electrolysis, they reported the formation of a polymeric film of $[\text{Ru}(\text{bpy})(\text{CO})_2]_n$ on the electrode catalyzing the reduction of CO_2 . Recently, Ishida [63] showed that the ratio of formation of carbon monoxide and formate was influenced by the catalyst concentration. The selectivity towards formate is favoured at higher concentrations of catalyst, as the formation of a Ru-Ru bond is a key step in the catalytic cycle of formate evolution.

The rhenium polypyridyl class of catalyst can act both as photo- and electrocatalyst. The most studied catalysts of this class are based on the $[\text{Re}(\text{bpy})(\text{CO})_3\text{X}]$ type of compounds, which study was pioneered by Lehn, Ziessel and Hawecker [64-66] reporting selective evolution of carbon monoxide. Meyer [67] studied the electrochemical reduction of CO_2 by $[\text{Re}(\text{bpy})(\text{CO})_3\text{Cl}]$ and proposed the first mechanism for this catalyst. By voltammetry they observed two one-electron reduction, the first one is attributed to the reduction of the bpy

ligand, and the second reduction, attributed to the reduction of the Re(I) metal centre, is irreversible. Two catalytic pathways were proposed, operating through either a one- or a two-electron initial reduction of the complex. In the one-electron reduction pathway (on the left of Figure 1.15.), a slow intramolecular electron transfer is required to reduce the metallic centre to trigger the slow loss of the chloride ligand. Cyclic voltammetry displays no current enhancement at the first reduction of the complex due to a very slow process. In the catalytic cycle, CO₂ disproportionates to CO and CO₃²⁻. In contrast, the two-electron pathway displays in a fast kinetics, but requires a higher potential to first reduce the metallic centre, immediately followed by the rapid loss of the chloride ligand. In the catalytic cycle, CO₂ is reduced to CO through a one-electron process, but in the presence of an oxide acceptor.

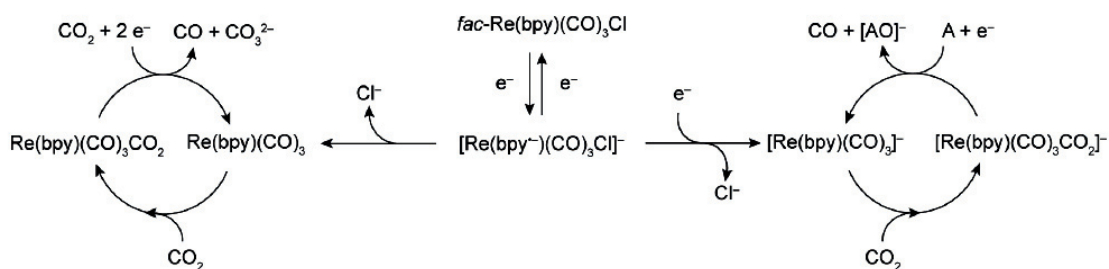


Figure 1.15. One- and two electron pathway mechanisms proposed by Meyer. Compound A is an oxide acceptor [67].

Following the initial research from Meyer, the mechanism of the catalytic cycle was intensively studied. The one- and two-electron pathways for activation of the catalyst were confirmed by IR spectroelectrochemistry by Johnson [68]. They showed that the one-electron activation of the catalyst is only possible in a weakly coordinating solvent such as THF, which renders solvent exchange with chloride possible. Deep insight into the catalytic mechanism for CO₂ reduction was obtained recently by Kubiak *at al.* [69] by density functional theory computation. Activation of the catalyst requires two successive reductions, and the catalytic mechanism for reducing CO₂ into CO is highly similar to mechanism of CO evolution presented in Figure 1.12. and Figure 1.14. CO₂ binds to the reduced complex, water is then eliminated *via* two successive protonations. Two one-electron reductions are necessary to release the product. Two possible cycles are proposed in the mechanism depending on the order in which the protons and the electrons are transferred to the catalyst. But in terms of

energy barrier and reduction potential these two catalytic cycles are very similar. The high selectivity of this catalyst for CO evolution compared to hydrogen evolution is explained by the barrier-less interaction with CO₂, compared to a 21.6 kcal/mol activation energy with protons. However, the DFT analysis could not explain all the possible catalytic pathways as the one-electron activation is not described. Additionally, it is experimentally observed that the reduction of CO₂ by this catalyst leads to the formation of CO and CO₃²⁻.

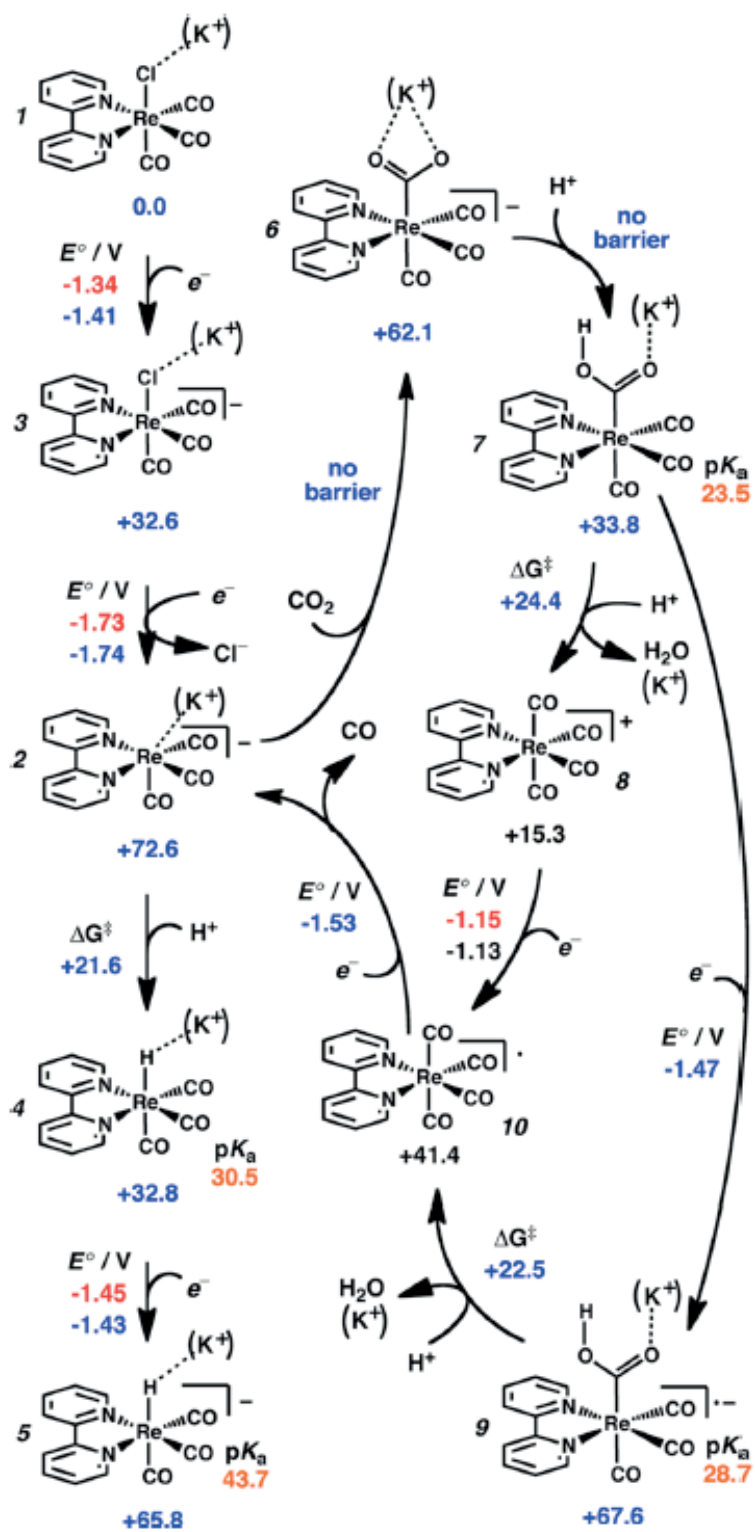


Figure 1.16. Complete mechanism of CO₂ reduction by [Re(bpy)(CO)₃Cl] proposed by Kubiak [69]

Ruthenium and rhenium complexes remain among the most effective homogeneous catalysts for CO₂ reduction, and are still the focus of recent studies as the mechanisms of catalysis is still not fully understood. With this type of complexes, fine-tuning of the ligand leads to modification of the reduction potential of the complex. As well as attachment of bulky groups on the bipyridyl group avoids formation of dimers. Ishitani *et al.* [70] have also greatly improved the photocatalytic reduction of CO₂ by rhenium complexes by synthesizing a supramolecular Ru-Re complex that combines a catalyst and a photosensitizer in a single molecule.

1.3. Supercritical CO₂

Efficiency of CO₂ reduction in standard conditions, even with appropriate catalysts remains generally quite low, and is additionally in competition with hydrogen evolution in protic media. The approach used in this thesis is to vastly increase the reactant concentration, converting CO₂ when it is in a liquid or supercritical state, highly pressurised and highly concentrated to maximize efficiency and selectivity.

By definition, a supercritical fluid is a substance at a temperature and pressure above its critical temperature and pressure. In supercritical conditions, fluids have properties of both liquid and gas simultaneously. Supercritical fluids are characterised by a density similar to that of liquids, while having mass transfer properties close to those of gases. These properties are highly interesting as supercritical fluids can dissolve materials and have a viscosity generally one order of magnitude smaller than liquids. The low viscosity of the solvent has clear implications upon the diffusion of species and hence on the overall kinetics of chemical processes. For CO₂ the critical point is at 31.1°C and 73.8 bars as shown in Figure 1.17, which are moderate conditions compared to most of the supercritical fluids commonly used.

Supercritical CO₂ (scCO₂) is already commonly employed as solvent in chemical synthesis [71], particularly in the food and pharmaceutical industries. This is due to its physical and chemical properties rendering it a rather “green” solvent that is completely

removed on decompression to “harmless” gaseous CO₂. A well-known application in the food industry is caffeine extraction [72].

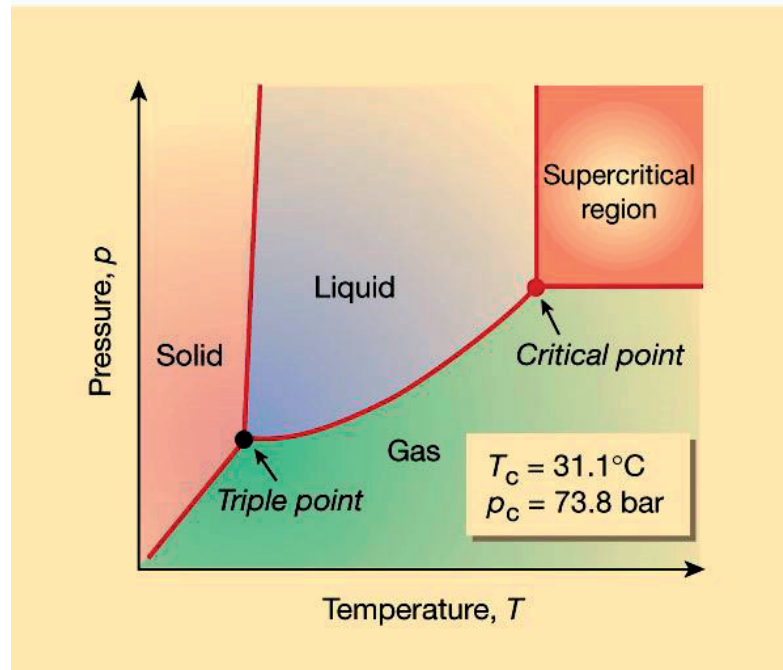


Figure 1.17. CO₂ phase diagram [71].

An interesting property of scCO₂ is the tunability of its properties, such as viscosity and density. In the supercritical region, these two properties are easily tuneable by slightly changing temperature or pressure as seen in Figure 1.18., with density ranging from 200 to 800 g/L.

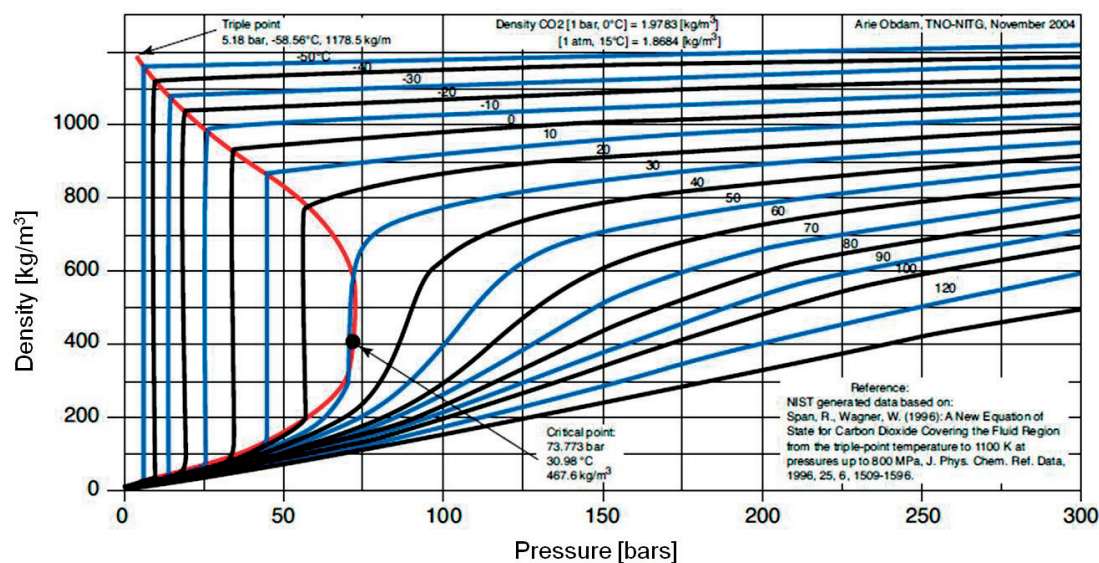


Figure 1.18. CO₂ density diagram from 0 to 300 bars and -50° to 140°C [73].

The major drawback of scCO₂ is its extremely low capacity of dissolving charged species, because of its low dielectric constant ($\epsilon < 1.8$). This is highly detrimental for electrochemical studies. The main approach used since the early electrochemical studies in scCO₂ is the introduction of a co-solvent to increase the solubility of ionic species.

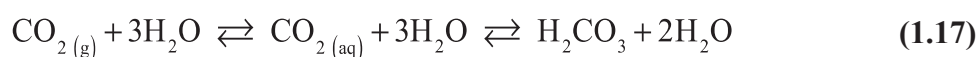
In the late 1980s, Wightman *et al.* [74-76] used water as a co-solvent, but water is not miscible with scCO₂ and its solubility is poor, therefore the amount of ionic species that can be dissolved in such mixture is limited. They needed an arrangement of microelectrodes to be able to observe a defined redox wave of ferrocene. Increasing the amount of water in the supercritical phase can lead to a higher increase in the conductivity with the proper stirring of the phase to generate a water-in-scCO₂ microemulsion. These types of microemulsions were used by Odhe *et al.* to obtain well defined voltammograms on microelectrodes [77]. Water-in-CO₂ microemulsions were further applied to the field of electrochemical deposition for the formation of ZnO mesocrystals [78] and electroplating of copper [79] and nickel [80]. The formation of an emulsion with water is due to the immiscibility of water and scCO₂, but in contact with organic co-solvents scCO₂ forms a single phase with scCO₂ and hence increases the solubility of ionic species in a homogeneous phase. To date methanol [81, 82], dimethylformamide [83] and acetonitrile [84, 85] have been employed. This mixed solvent

phase has been largely documented in the field of electrodeposition [81, 86, 87], with Bartlett *et al.* recently reviving interest in supercritical fluid as electroplating media.

In this thesis, three different solvents systems will be considered for the reduction of CO₂ :

- A biphasic system constituted of water and scCO₂, with interfacial reduction of CO₂.
- Addition of a co-solvent to the CO₂ supercritical phase to increase solubility of ionic species.
- CO₂ expanded liquid, as organic solvents can dissolve an abundant amount of CO₂ as the pressure is increased.

Placing scCO₂ in contact with water has three major consequences, allowing for a more efficient reduction of CO₂. First of all, the concentration of CO₂ in water can be increased up to 50-fold compared to a non-pressurized system. At standard temperature and pressure, the solubility of CO₂ in pure water is very small, and reaches only 0.0286 mol/kg water at atmospheric pressure and 30°C. In supercritical conditions, this solubility can be increased to 1.361 mol/kg water at 100 bars and 30°C[88]. The second major consequence is the formation of a very particular interface when an aprotic solvent is in contact with a very protic solvent [89]. If a compound catalysing CO₂ reduction adsorbs at this interface, it will be simultaneously in contact with a huge concentration of CO₂ and protons, potentially increasing the production rate of reduction products. The last effect, linked to the increase in concentration of CO₂ in water. The aqueous solvation of CO₂ accompanied by hydration, results in carbonic acid, and subsequent acid-base chemistry leading to bicarbonate and carbonate, as shown in the two following reactions.[90]



The net result of those two reactions will be an important decrease in the pH of the water. The pH of the solution can have important effects on the efficiency of the catalyst and its selectivity for CO₂ reduction versus proton reduction. However, the pH of the solution can be readily controlled by the introduction of a buffer into the aqueous phase.

Supercritical CO₂ is immiscible with water, with only a small portion of the CO₂ in the molar range, dissolving into the water. Organic solvents such as dimethylformamide (DMF) and acetonitrile (AcN) are totally miscible with scCO₂ and can be used as co-solvents in the supercritical CO₂. For these systems a single phase will be maintained regardless of the molar ratio of the two solvents. These solvents are however not ideal for the catalytic reduction of CO₂ due to their non-protic character. Addition of a proton source is therefore requested. These proton sources are either water or other organic solvent, such as trifluoromethanol or triethanolamine. Addition of organic solvents has no effect on the phase equilibrium due to their miscibility with scCO₂. But mixture of water, organic solvent and scCO₂ are rather complex in term of phase equilibrium, depending on the ratio of the three solvents, the system is either biphasic or single phase. The nature of the organic solvent is also of importance, Figure 1.19. presents ternary phase diagrams of three different organic solvents : isopropanol, methanol and acetone. Apices of the triangles represent the single pure component, the top apex is liquid carbon dioxide, the bottom-left apex the water and the bottom-right the organic solvent. The sides of the triangle, directly opposite the apex, represent 0% of that apex component. The compositions of regions indicated inside the triangle are a mixture of the three components. The curves inside the triangles are the limit between the one-phase and two-phase region, with the two-phase region inside the curve. Intersection between the tie lines and the curve give the composition of the two phases when the mixture composition is “inside” the two-phase region. In general, to obtain a single phase an important fraction of organic solvent is necessary. In the case of formation of two phases, for isopropanol and methanol, one phase is almost pure CO₂ while the other phase contains water and organic solvent. For acetone, one phase is mainly composed of water, while the second is a mixture of CO₂ and acetone.

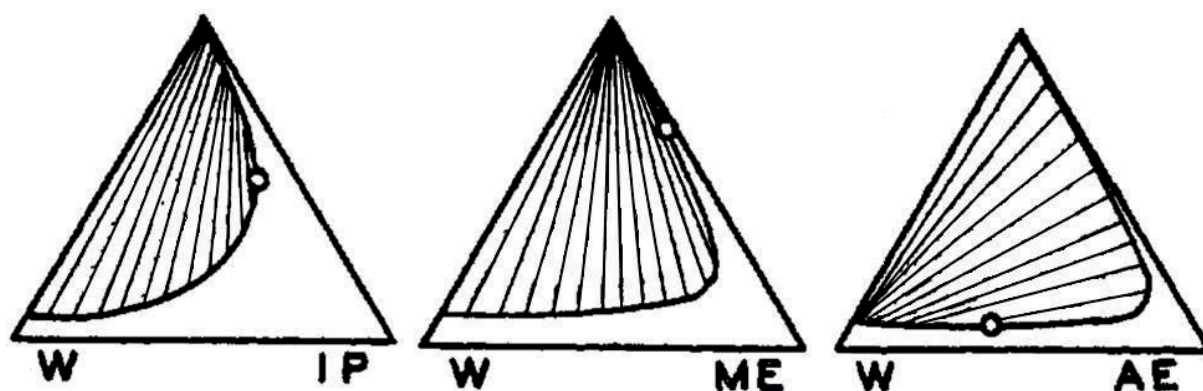


Figure 1.19. Ternary phase diagrams of three liqCO₂-water-organic solvent systems, IP stand for isopropanol, ME for methanol and AE for acetone[91]

The third solvent system that will be used in this work is a gas expanded liquid, which is a mixed solvent composed of a compressible gas dissolved in an organic solvent under pressure. Even in mild pressure conditions, the amount of gas dissolved in the organic solvent represents a concentration large enough to noticeably increase the volume of the liquid phase. The conditions of pressure and temperature are therefore below supercritical values. CO₂-expanded liquids are the most commonly used gas expanded liquid [92]. These liquid media represent a range from neat organic solvents to liquid or supercritical CO₂. These solvents have been exploited in a variety of applications, such as separation [93], precipitation of fine particles [94] and as reaction media for catalytic reactions [95].

Physical properties, such as density, of pure CO₂ are well understood[96] and tabulated [97], but for mixtures with other solvents, phase density or concentration of CO₂ are influenced by a lot of different factors. Among them, pressure and temperature, but also it differs from an organic solvent to another. Solubilisation of a large amount of ionic species will also tend to decrease the concentration of CO₂ in the phase. Phase density and CO₂ concentration are therefore impossible to predict and will have to be determined experimentally.

1.4. Scope of the present work

This work is devoted to fundamental research on carbon dioxide reduction catalyzed by molecular catalysts. Principally focusing on the understanding of the mechanism of the reaction and on the effect of the CO₂ concentration or pressure on the efficiency and selectivity of CO₂ reduction.

Chapter 2 is devoted to the description of the material, the experimental procedures and the synthesis of the different catalysts. For the following chapters, this work is separated according to the type of catalyst and the method used to input the energy required for the reaction to take place. As seen in section 1.2.1, CO₂ reduction is a highly endergonic reaction, and three different methods can be used to input energy in the catalytic system.

Chapter 3 is dedicated to the use of Decamethylferrocene (DMFc) as catalyst and sacrificial electron donor to drive the reduction of carbon dioxide in a biphasic system composed of water and scCO₂.

In a similar solvent system, chapter 4 is dedicated to the study of the photocatalytic reduction of CO₂ by the aqueous catalyst nickel(II)cyclam. As part of the photosensitizing cycle ruthenium(II) tris bipyridine and ascorbic acid are used as photosensitizer and sacrificial electron donor respectively.

With the objective to improve the photocatalytic reduction of carbon dioxide, in chapter 5, polypyridyl carbonyl complex of ruthenium are used as catalyst with ruthenium(II) tris bipyridine as photosensitizer and 1-benzyl-1,4-dihydronicotinamide as sacrificial electron donor. Due to poor solubility of these compounds in aqueous solution, the main solvent is dimethylformamide.

Chapter 6 is dedicated to the understanding of the voltammetry in expanded liquid and supercritical CO₂. With determination of phase behaviour, concentration of CO₂ and diffusion coefficient of species in these specific solvent systems.

In chapter 7, the voltammetry in expanded liquid and in supercritical conditions is adapted to the study of the electrocatalytic reduction of carbon dioxide by two different

catalysts : polypyridyl carbonyl complexes of ruthenium and $[\text{Re}(\text{bpy})(\text{CO})_3\text{X}]$. Objectives of this chapter are to understand the different catalytic mechanisms of these complexes and to determine the effect of pressure on the catalytic rate.

1.5. Bibliography

1. Gerland, P., et al., *World population stabilization unlikely this century*. Science, 2014. **346**(6206): p. 234-237.
2. *BP Energy Outlook*, 2015.
3. *EIA projects world energy consumption will increase 56% by 2040*, 2013.
4. *BP Statistical Review of World Energy June 2014*.
5. Canadell, J.G., et al., *Contributions to accelerating atmospheric CO₂ growth from economic activity, carbon intensity, and efficiency of natural sinks*. Proceedings of the National Academy of Sciences, 2007. **104**(47): p. 18866-18870.
6. Le Quere, C., et al., *Trends in the sources and sinks of carbon dioxide*. Nature Geosci, 2009. **2**(12): p. 831-836.
7. Tans, D.P. NOAA/ESRL (www.esrl.noaa.gov/gmd/ccgg/trends/) and Dr. Ralph Keeling, Scripps Institution of Oceanography (scrippsco2.ucsd.edu/).
8. Halmann, M.M. and M. Steinberg, *Greenhouse gas carbon dioxide mitigation: Science and technology*, in *Other Information: PBD: 19991999*. p. Medium: X; Size: 1284 p.
9. Houghton, J.T., *Climate Change 1995: The Science of Climate Change*, ed. C.U. Press 1996, Cambridge.
10. Wigley, T.M.L., *Global-mean temperature and sea level consequences of greenhouse gas concentration stabilization*. Geophysical Research Letters, 1995. **22**(1): p. 45.
11. *United Nations Development Program, 2003, World Energy Assessment Report: Energy and the Challenge of Sustainability*.
12. Berg JM, T.J., Stryer L., *Biochemistry*. 5th edition, 2002: New York.
13. Boundless, *Boundless Microbiology*. Regulation of the Calvin Cycle 2015.
14. Steinberg-Yfrach, G., et al., *Conversion of light energy to proton potential in liposomes by artificial photosynthetic reaction centres*. Nature, 1997. **385**(6613): p. 239-241.
15. Steinberg-Yfrach, G., et al., *Light-driven production of ATP catalysed by F₀F₁-ATP synthase in an artificial photosynthetic membrane*. Nature, 1998. **392**(6675): p. 479-482.
16. Parkin, A., et al., *Rapid and Efficient Electrocatalytic CO₂/CO Interconversions by Carboxydotherrmus hydrogenoformans CO Dehydrogenase I on an Electrode*. Journal of the American Chemical Society, 2007. **129**(34): p. 10328-10329.
17. Reda, T., et al., *Reversible interconversion of carbon dioxide and formate by an electroactive enzyme*. Proceedings of the National Academy of Sciences, 2008. **105**(31): p. 10654-10658.
18. Costentin, C., M. Robert, and J.-M. Savéant, *Catalysis of the electrochemical reduction of carbon dioxide*. Chemical Society Reviews, 2013. **42**(6): p. 2423-2436.
19. Schwarz, H.A. and R.W. Dodson, *Reduction potentials of CO₂- and the alcohol radicals*. The Journal of Physical Chemistry, 1989. **93**(1): p. 409-414.
20. Willner, I., et al., *Photosensitized reduction of carbon dioxide to methane and hydrogen evolution in the presence of ruthenium and osmium colloids: strategies to design selectivity of products distribution*. Journal of the American Chemical Society, 1987. **109**(20): p. 6080-6086.

21. Barton Cole, E., et al., *Using a One-Electron Shuttle for the Multielectron Reduction of CO₂ to Methanol: Kinetic, Mechanistic, and Structural Insights*. Journal of the American Chemical Society, 2010. **132**(33): p. 11539-11551.
22. Morris, A.J., G.J. Meyer, and E. Fujita, *Molecular Approaches to the Photocatalytic Reduction of Carbon Dioxide for Solar Fuels*. Accounts of Chemical Research, 2009. **42**(12): p. 1983-1994.
23. Tanaka, K. and D. Ooyama, *Multi-electron reduction of CO₂ via Ru-CO₂, -C(O)OH, -CO, -CHO, and -CH₂OH species*. Coordination Chemistry Reviews, 2002. **226**(1-2): p. 211-218.
24. Juris A., B.V., Barigelletti F., Campagna S., Belser P., Von Zelewsky A., *Ru(II) polypyridine complexes: photophysics, photochemistry, electrochemistry, and chemiluminescenc*. Coordination Chemistry Reviews, 1988. **84**: p. 192.
25. Creutz, C., et al., *Lifetimes, spectra, and quenching of the excited states of polypyridine complexes of iron(II), ruthenium(II), and osmium(II)*. Journal of the American Chemical Society, 1980. **102**(4): p. 1309-1319.
26. Creutz, C., *Complexities of ascorbate as a reducing agent*. Inorganic Chemistry, 1981. **20**(12): p. 4449-4452.
27. Hori, Y., K. Kikuchi, and S. Suzuki, *PRODUCTION OF CO AND CH₄ IN ELECTROCHEMICAL REDUCTION OF CO₂ AT METAL ELECTRODES IN AQUEOUS HYDROGENCARBONATE SOLUTION*. Chemistry Letters, 1985. **14**(11): p. 1695-1698.
28. Li, C.W. and M.W. Kanan, *CO₂ Reduction at Low Overpotential on Cu Electrodes Resulting from the Reduction of Thick Cu₂O Films*. Journal of the American Chemical Society, 2012. **134**(17): p. 7231-7234.
29. Tinnemans, A.H.A., et al., *Tetraaza-macrocyclic cobalt(II) and nickel(II) complexes as electron-transfer agents in the photo(electro)chemical and electrochemical reduction of carbon dioxide*. Recueil des Travaux Chimiques des Pays-Bas, 1984. **103**(10): p. 288-295.
30. Beley, M., et al., *Nickel(II)-cyclam: an extremely selective electrocatalyst for reduction of CO₂ in water*. Journal of the Chemical Society, Chemical Communications, 1984(19): p. 1315-1316.
31. Grant, J.L., et al., *Photochemical reduction of carbon dioxide to carbon monoxide in water using a nickel(II) tetra-azamacrocyclic complex as catalyst*. Journal of the Chemical Society, Dalton Transactions, 1987(9): p. 2105-2109.
32. Bruce, M.R.M., et al., *Electrocatalytic reduction of carbon dioxide based on 2,2'-bipyridyl complexes of osmium*. Inorganic Chemistry, 1992. **31**(23): p. 4864-4873.
33. Chardon-Noblat, S., et al., *A Novel Organometallic Polymer of Osmium(0), [Os(2,2'-bipyridine)(CO)₂]_n: Its Electrosynthesis and Electrocatalytic Properties Towards CO₂ Reduction*. European Journal of Inorganic Chemistry, 2001. **2001**(3): p. 613-617.
34. Chauvin, J., et al., *Towards New Molecular Photocatalysts for CO₂ Reduction: Photo-Induced Electron Transfer versus CO Dissociation within [Os(NN)(CO)₂Cl₂] Complexes*. Chemistry – A European Journal, 2011. **17**(15): p. 4313-4322.
35. Sullivan, B.P., et al., *Hydrido carbonyl complexes of osmium(II) and ruthenium(II) containing polypyridyl ligands*. Organometallics, 1984. **3**(8): p. 1241-1251.
36. Bolinger, C.M., et al., *Electrocatalytic reduction of carbon dioxide by 2,2'-bipyridine complexes of rhodium and iridium*. Inorganic Chemistry, 1988. **27**(25): p. 4582-4587.

37. Caix, C., S. Chardon-Noblat, and A. Deronzier, *Electrocatalytic reduction of CO₂ into formate with $[(\eta^5\text{-Me}_5\text{C}_5)\text{M}(\text{L})\text{Cl}]^+$ complexes (L = 2,2'-bipyridine ligands; M = Rh(III) and Ir(III))*. Journal of Electroanalytical Chemistry, 1997. **434**(1–2): p. 163-170.
38. Paul, P., et al., *Synthesis and Characterization of Rhodium Complexes Containing 2,4,6-Tris(2-pyridyl)-1,3,5-triazine and Its Metal-Promoted Hydrolytic Products: Potential Uses of the New Complexes in Electrocatalytic Reduction of Carbon Dioxide*. Inorganic Chemistry, 1998. **37**(22): p. 5733-5742.
39. Reithmeier, R.O., et al., *Mono- and bimetallic Ir(III) based catalysts for the homogeneous photocatalytic reduction of CO₂ under visible light irradiation. New insights into catalyst deactivation*. Dalton Transactions, 2014. **43**(35): p. 13259-13269.
40. Clark, M.L., et al., *Electrocatalytic CO₂ reduction by $\text{M}(\text{bpy-R})(\text{CO})_4$ (M = Mo, W; R = H, tBu) complexes. Electrochemical, spectroscopic, and computational studies and comparison with group 7 catalysts*. Chemical Science, 2014. **5**(5): p. 1894-1900.
41. Bourrez, M., et al., *Pulsed-EPR Evidence of a Manganese(II) Hydroxycarbonyl Intermediate in the Electrocatalytic Reduction of Carbon Dioxide by a Manganese Bipyridyl Derivative*. Angewandte Chemie International Edition, 2014. **53**(1): p. 240-243.
42. Sampson, M.D., et al., *Manganese Catalysts with Bulky Bipyridine Ligands for the Electrocatalytic Reduction of Carbon Dioxide: Eliminating Dimerization and Altering Catalysis*. Journal of the American Chemical Society, 2014. **136**(14): p. 5460-5471.
43. Smieja, J.M., et al., *Manganese as a Substitute for Rhenium in CO₂ Reduction Catalysts: The Importance of Acids*. Inorganic Chemistry, 2013. **52**(5): p. 2484-2491.
44. Chen, J., et al., *Iron(II) and Ruthenium(II) Complexes Containing P, N, and H Ligands: Structure, Spectroscopy, Electrochemistry, and Reactivity*. Inorganic Chemistry, 2010. **49**(20): p. 9380-9391.
45. Pun, S.-N., et al., *Iron(II) complexes of 2,9-bis(2-hydroxyphenyl)-1,10-phenanthroline (H₂dophen) as electrocatalysts for carbon dioxide reduction. X-Ray crystal structures of $[\text{Fe}(\text{dophen})\text{Cl}]_2[\text{middle dot}]_2\text{HCON}(\text{CH}_3)_2$ and $[\text{Fe}(\text{dophen})(\text{N-MeIm})_2]\text{ClO}_4$ (N-MeIm = 1-methylimidazole)*. Journal of the Chemical Society, Dalton Transactions, 2002(4): p. 575-583.
46. Richard Keene, F., C. Creutz, and N. Sutin, *Reduction of carbon dioxide by tris(2,2'-bipyridine)cobalt(I)*. Coordination Chemistry Reviews, 1985. **64**: p. 247-260.
47. Garnier, L., Y. Rollin, and J. Périchon, *Electrosynthesis of symmetrical ketones from organic halides and carbon dioxide catalysed by 2,2'-bipyridine-nickel complexes*. Journal of Organometallic Chemistry, 1989. **367**(3): p. 347-358.
48. Haines, R.J., R.E. Wittrig, and C.P. Kubiak, *Electrocatalytic Reduction of Carbon Dioxide by the Binuclear Copper Complex $[\text{Cu}_2(6\text{-}(\text{diphenylphosphino-2,2}'\text{-bipyridyl})_2(\text{MeCN})_2][\text{PF}_6]_2$* . Inorganic Chemistry, 1994. **33**(21): p. 4723-4728.
49. Ishida, H., K. Tanaka, and T. Tanaka, *Electrochemical CO₂ reduction catalyzed by ruthenium complexes $[\text{Ru}(\text{bpy})_2(\text{CO})_2]^{2+}$ and $[\text{Ru}(\text{bpy})_2(\text{CO})\text{Cl}]^+$. Effect of pH on the formation of CO and HCOO*. Organometallics, 1987. **6**(1): p. 181-186.
50. Ishida, H., K. Tanaka, and T. Tanaka, *Photoreduction of carbon dioxide in the $[\text{Ru}(\text{bpy})_2(\text{CO})_2]^{2+}$ (bpy = 2,2'-bipyridine)/ $[\text{Ru}(\text{bpy})_3]^{2+}$ or $[\text{Ru}(\text{phen})_3]^{2+}$ (phen = phenanthroline)/triethanolamine/N,N-dimethylformamide system*. Chem. Lett., 1987(6): p. 1035-8.

51. Ishida, H., et al., *Selective formation of formate in the electrochemical carbon dioxide reduction catalyzed by $[Ru(bpy)_2(CO)_2]^{2+}$ ($bpy = 2,2'$ -bipyridine).* J. Chem. Soc., Chem. Commun., 1987(2): p. 131-2.
52. Tanaka, K., M. Morimoto, and T. Tanaka, *The water gas shift reaction catalyzed by ruthenium carbonyl complexes.* Chem. Lett., 1983(6): p. 901-4.
53. Ishida, H., et al., *Selective formation of $HCOO^-$ in the electrochemical CO_2 reduction catalysed by $[Ru(bpy)_2(CO)_2]^{2+}$ ($bpy = 2,2'$ [prime or minute]-bipyridine).* Journal of the Chemical Society, Chemical Communications, 1987(2): p. 131-132.
54. Pugh, J.R., et al., *Formation of a metal-hydride bond and the insertion of carbon dioxide. Key steps in the electrocatalytic reduction of carbon dioxide to formate anion.* Inorg. Chem., 1991. **30**(1): p. 86-91.
55. Sullivan, B.P. and T.J. Meyer, *Photoinduced irreversible insertion of carbon dioxide into a metal-hydride bond.* J. Chem. Soc., Chem. Commun., 1984(18): p. 1244-5.
56. Hawecker, J., J.M. Lehn, and R. Ziessel, *Photochemical and electrochemical reduction of carbon dioxide to carbon monoxide mediated by (2,2'-bipyridine)tricarbonylchlororhenium(I) and related complexes as homogeneous catalysts.* Helv. Chim. Acta, 1986. **69**(8): p. 1990-2012.
57. Lehn, J.M. and R. Ziessel, *Photochemical reduction of carbon dioxide to formate catalyzed by 2,2'-bipyridine- or 1,10-phenanthroline-ruthenium(II) complexes.* J. Organomet. Chem., 1990. **382**(1-2): p. 157-173.
58. Pugh, J.R., et al., *Formation of a metal-hydride bond and the insertion of carbon dioxide. Key steps in the electrocatalytic reduction of carbon dioxide to formate anion.* Inorganic Chemistry, 1991. **30**(1): p. 86-91.
59. Tanaka, K., *Metal-catalyzed reversible conversion between chemical and electrical energy designed towards a sustainable society.* The Chemical Record, 2009. **9**(3): p. 169-186.
60. Hawecker, J., J.-M. Lehn, and R. Ziessel, *Photochemical reduction of carbon dioxide to formate mediated by ruthenium bipyridine complexes as homogeneous catalysts.* J. Chem. Soc., Chem. Commun., 1985(2): p. 56-58.
61. Voyame, P., et al., *Photoreduction of CO_2 Using $[Ru(bpy)_2(CO)L]^{n+}$ Catalysts in Biphasic Solution/Supercritical CO_2 Systems.* Inorganic Chemistry, 2013. **52**(19): p. 10949-10957.
62. Chardon-Noblat, S., et al., *Formation of Polymeric $[Ru^0(bpy)(CO)_2]_n$ Films by Electrochemical Reduction of $[Ru(bpy)_2(CO)_2](PF_6)_2$: Its Implication in CO_2 Electrocatalytic Reduction.* Inorganic Chemistry, 1994. **33**(19): p. 4410-4412.
63. Kuramochi, Y., et al., *Unexpected effect of catalyst concentration on photochemical CO_2 reduction by trans (Cl)- $Ru(bpy)(CO)_2Cl_2$: new mechanistic insight into the $CO/HCOO^-$ selectivity.* Chemical Science, 2015. **6**(5): p. 3063-3074.
64. Hawecker, J., J.-M. Lehn, and R. Ziessel, *Efficient photochemical reduction of CO_2 to CO by visible light irradiation of systems containing $Re(bipy)(CO)_3X$ or $Ru(bipy)_3^{2+}-Co^{2+}$ combinations as homogeneous catalysts.* Journal of the Chemical Society, Chemical Communications, 1983(9): p. 536-538.
65. Hawecker, J., J.-M. Lehn, and R. Ziessel, *Electrocatalytic reduction of carbon dioxide mediated by $Re(bipy)(CO)_3Cl$ ($bipy = 2,2'$ [prime or minute]-bipyridine).* Journal of the Chemical Society, Chemical Communications, 1984(6): p. 328-330.

66. Hawecker, J., J.-M. Lehn, and R. Ziessel, *Photochemical and Electrochemical Reduction of Carbon Dioxide to Carbon Monoxide Mediated by (2,2'-Bipyridine)tricarbonylchlororhenium(I) and Related Complexes as Homogeneous Catalysts*. Helvetica Chimica Acta, 1986. **69**(8): p. 1990-2012.
67. Sullivan, B.P., et al., *One- and two-electron pathways in the electrocatalytic reduction of CO₂ by fac-Re(bpy)(CO)₃Cl (bpy = 2,2[prime or minute]-bipyridine)*. Journal of the Chemical Society, Chemical Communications, 1985(20): p. 1414-1416.
68. Johnson, F.P.A., et al., *Electrocatalytic Reduction of CO₂ Using the Complexes [Re(bpy)(CO)₃L]_n (n = +1, L = P(OEt)₃, CH₃CN; n = 0, L = Cl⁻, Otf⁻; bpy = 2,2'-Bipyridine; Otf⁻ = CF₃SO₃) as Catalyst Precursors: Infrared Spectroelectrochemical Investigation*. Organometallics, 1996. **15**(15): p. 3374-3387.
69. Keith, J.A., et al., *Elucidation of the Selectivity of Proton-Dependent Electrocatalytic CO₂ Reduction by fac-Re(bpy)(CO)₃Cl*. Journal of the American Chemical Society, 2013. **135**(42): p. 15823-15829.
70. Nakada, A., et al., *Highly efficient visible-light-driven CO₂ reduction to CO using a Ru(ii)-Re(i) supramolecular photocatalyst in an aqueous solution*. Green Chemistry, 2015.
71. Leitner, W., *Green chemistry: Designed to dissolve*. Nature, 2000. **405**(6783): p. 129-130.
72. Peker, H., et al., *Caffeine extraction rates from coffee beans with supercritical carbon dioxide*. AIChE Journal, 1992. **38**(5): p. 761-770.
73. Roland Span, W.W., *A New Equation of State for Carbon Dioxide Covering the Fluid region from the Triple-Point Temperature to 1100 K at Pressure up to 800 MPa*. Journal of Physical & Chemical Reference Data, 1996. **25**(6): p. 87.
74. Michael, A.C. and R.M. Wightman, *Microelectrodes coated with ionically conducting polymer membranes for voltammetric detection in flowing supercritical carbon dioxide*. Analytical Chemistry, 1989. **61**(3): p. 270-272.
75. Niehaus, D., et al., *Voltammetry of ferrocene in supercritical carbon dioxide containing water and tetrahexylammonium hexafluorophosphate*. The Journal of Physical Chemistry, 1989. **93**(16): p. 6232-6236.
76. Philips, M.E., et al., *Effect of added water on voltammetry in near-critical carbon dioxide*. The Journal of Physical Chemistry, 1987. **91**(15): p. 3934-3936.
77. Ohde, H., et al., *Voltammetric measurement in supercritical CO₂ utilizing a water-in-CO₂ microemulsion*. Analytical Chemistry, 2000. **72**(19): p. 4738-4741.
78. Lin, W.H., et al., *Supercritical CO₂-assisted electrochemical deposition of ZnO mesocrystals for practical photoelectrochemical applications*. Journal of Physical Chemistry C, 2013. **117**(48): p. 25596-25603.
79. Chang, T.-F.M., et al., *Effects of pressure on electroplating of copper using supercritical carbon dioxide emulsified electrolyte*. Thin Solid Films, 2013. **529**(0): p. 25-28.
80. Chang, T.-F.M. and M. Sone, *Function and mechanism of supercritical carbon dioxide emulsified electrolyte in nickel electroplating reaction*. Surface and Coatings Technology, 2011. **205**(13-14): p. 3890-3899.
81. Bartlett, P.N., et al., *Phase behaviour and conductivity study on multi-component mixtures for electrodeposition in supercritical fluids*. Physical Chemistry Chemical Physics, 2010. **12**(2): p. 492-501.

-
82. Jun, J. and P.S. Fedkiw, *Ionic conductivity of alkali-metal salts in sub- and supercritical carbon dioxide+methanol mixtures*. Journal of Electroanalytical Chemistry, 2001. **515**(1–2): p. 113-122.
 83. Chanfreau, S., et al., *Electrochemical determination of ferrocene diffusion coefficient in liquid media under high CO₂ pressure: Application to DMF–CO₂ mixtures*. Journal of Electroanalytical Chemistry, 2007. **604**(1): p. 33-40.
 84. Cook, D., et al., *The electrodeposition of copper from supercritical CO₂/acetonitrile mixtures and from supercritical trifluoromethane*. Physical Chemistry Chemical Physics, 2010. **12**(37): p. 11744-11752.
 85. Toghiani, K.E., et al., *Steady-state macroscale voltammetry in a supercritical carbon dioxide medium*. Physical Chemistry Chemical Physics, 2013. **15**(3): p. 972-978.
 86. Bartlett, P.N., et al., *Electrodeposition from supercritical fluids*. Physical Chemistry Chemical Physics, 2014.
 87. Ke, J., et al., *Electrodeposition of metals from supercritical fluids*. Proceedings of the National Academy of Sciences of the United States of America, 2009. **106**(35): p. 14768-14772.
 88. Duan, Z. and R. Sun, *An improved model calculating CO₂ solubility in pure water and aqueous NaCl solutions from 273 to 533 K and from 0 to 2000 bar*. Chemical Geology, 2003. **193**(3–4): p. 257-271.
 89. da Rocha, S.R.P., et al., *Molecular Structure of the Water–Supercritical CO₂ Interface*. The Journal of Physical Chemistry B, 2001. **105**(48): p. 12092-12104.
 90. Adamczyk, K., et al., *Real-Time Observation of Carbonic Acid Formation in Aqueous Solution*. Science, 2009. **326**(5960): p. 1690-1694.
 91. Francis, A.W., *Ternary Systems of Liquid Carbon Dioxide*. The Journal of Physical Chemistry, 1954. **58**(12): p. 1099-1114.
 92. Jessop, P.G. and B. Subramaniam, *Gas-Expanded Liquids*. Chemical Reviews, 2007. **107**(6): p. 2666-2694.
 93. Scurto, A.M., S.N.V.K. Aki, and J.F. Brennecke, *CO₂ as a Separation Switch for Ionic Liquid/Organic Mixtures*. Journal of the American Chemical Society, 2002. **124**(35): p. 10276-10277.
 94. Anand, M., L.A. Odom, and C.B. Roberts, *Finely Controlled Size-Selective Precipitation and Separation of CdSe/ZnS Semiconductor Nanocrystals Using CO₂-Gas-Expanded Liquids*. Langmuir, 2007. **23**(13): p. 7338-7343.
 95. Wei, M., et al., *CO₂-Expanded Solvents: Unique and Versatile Media for Performing Homogeneous Catalytic Oxidations*. Journal of the American Chemical Society, 2002. **124**(11): p. 2513-2517.
 96. Huang, F.-H., et al., *AN ACCURATE EQUATION OF STATE FOR CARBON DIOXIDE*. Journal of Chemical Engineering of Japan, 1985. **18**(6): p. 490-496.
 97. NIST. *CO₂ DATA*. Available from:
<http://webbook.nist.gov/cgi/cbook.cgi?Name=carbon+dioxide&Units=SI/>.

CHAPTER 2

Experimental and Instrumentation

2.1. Introduction

In this chapter, detailed descriptions of the material and the different experimental procedures and techniques employed are provided. First of all, the material and instrumentation used in this thesis are described. The supercritical equipment used throughout this thesis has been designed and manufactured in-house. This includes the high-pressure setup, the different reactors used for the various experiments. In the second part, the different procedures used in this thesis are described in details starting with the procedures for CO₂ reduction product analysis, as these procedures are common to all chapters. Following, the different specific procedures in the order of appearance in the following chapters are presented

2.2. Material

2.2.1. Pump system

The experimental setup used in standard CO₂ reduction experiments is presented in Figure 2.1. and Figure 2.2. The system is composed of two piston pumps (Teledyne, Isco Model100 DX, USA), with one dedicated to CO₂ and one to water, therefore the volume of the two phases can be controlled and the reactor can be compressed by addition of water or CO₂. For experiments with organic solvents, only the pump dedicated to CO₂ was used. Between the CO₂ pump and the reactor, a piezoelectric pressure sensor (Swagelok, UK) monitors the pressure in the line and the reactor. The temperature is monitored by a thermocouple plugged into the reactor. For decompression of the reactor, a series of two autoclaves are used, one to trap the water or solvent escaping the reactor during decompression and one to recover a gas sample for analysis.



Figure 2.1. Experimental setup used for supercritical conditions.

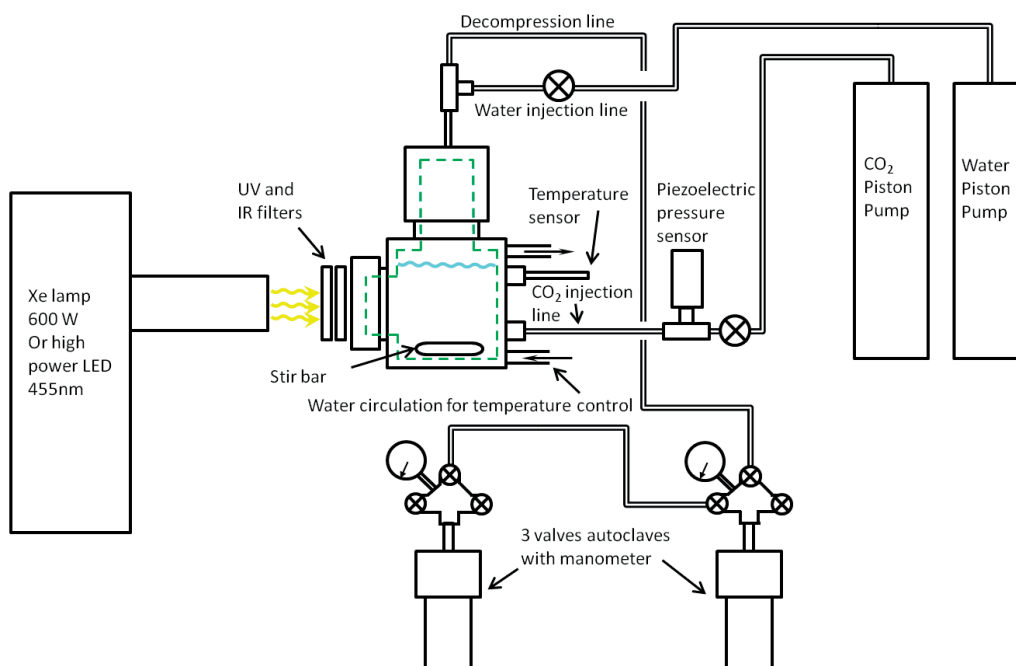


Figure 2.2. Schematic illustration of the double pump system for photocatalytic experiment.

2.2.2. Reactors

For the different experiments, four types of reactors have been used. The simplest reactor is a three-valve autoclave, as shown in Figure 2.3. This reactor is used for reactions that take place in the dark, but also for taking gas sample during decompression of the reactor. Two of these reactors are connected in series to act as a liquid trap and gas collector for sample analysis. This stainless steel reactor, with an inner volume of 37 mL, is equipped with three valves and an integrated manometer. For temperature control, it can be fitted into a water circulation chamber connected to a thermostated bath.



Figure 2.3. Three-valve autoclave.

For UV-visible spectrophotometric measurements and pendant drop experiments, a three sapphire window (Rayotek, USA) reactor, of inner volume 50 mL, was used. Two windows are aligned and the third one is perpendicular to the others. In this reactor, water circulation is integrated into the walls of the reactor for temperature control. It has two gas or liquid inlets and one inlet to connect a thermocouple for accurate temperature monitoring.

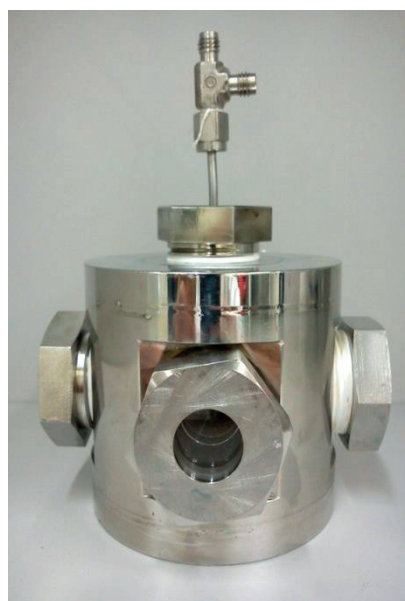


Figure 2.4. Three-window view cell.

The reactor used in most of the photocatalytic experiments is a single window reactor, shown in Figure 2.5. Compared to the previous reactor, this reactor has the advantage of a smaller inner volume (31 mL), a larger bottom area, which allows a more efficient stirring, and is more convenient to use due to a cap manually screwed in and out. This reactor is also less prone to gas-leaks. This reactor has also been adapted for electrochemistry in scCO_2 by building an additional cap equipped with three electrodes. The electrodes are sealed in PEEK and Teflon and includes a silver wire quasi reference electrode, platinum wire counter electrode and an interchangeable working electrode. Three different working electrodes have been built; gold disk (geometric area 0.0173cm^2), copper disk (4mm diameter) and glassy carbon disk (2mm diameter). But for the glassy carbon electrode, a good connection between the glassy carbon rod and the copper connection was never achieved and the electrode appeared resistive to current flow. To integrate a glassy carbon electrode into the reactor, commercial glassy carbon electrode (BASi, USA) of the appropriate diameter ($1/4''$ inch) has been equipped with a high-pressure ferule to connect to high-pressure connector of the reactor (Swagelok, UK). The temperature in the reactor is controlled by water circulation integrated into the walls of the reactor.



Figure 2.5. Reactor used for photoreduction experiments, the three-electrode cap and glassy carbon electrode equipped with high-pressure connection.

The last reactor used in this thesis, is a high-pressure sapphire tube, with an inner volume of 7 ml. The reactor is used for the NMR experiments carried at high pressures and also for expansion measurements of gas expanded liquids.



Figure 2.7. High-pressure NMR tube.

2.2.3. Light sources

Two different light sources have been used for photocatalytic experiments and spectroscopic analysis:

- A white light source 600W Xenon lamp (ORIEL Model 66021, USA), UV and IR radiation can be removed with optical filters (UV cut-off filter $<420\text{nm}$ and IR cut-off filter $>650\text{nm}$).

- A 455nm monochromatic high power LED (ThorLabs M455L2, USA) mounted on a lens tube equipped with three lenses to collimate the light beam to a diameter of about 1 cm.

Due to easier quantification of the quantum yield of photocatalytic experiments with monochromatic light, the high power LED was preferred in photocatalytic experiments.

Spectroscopic measurements were performed using the Xenon lamp as light source and a UV/VIS spectrometer (Ocean Optics, model USB2000, USA). Grey filters with optical density from 0.8 to 3 were used to decrease the light brightness.

2.2.4. Catalysts synthesis

Decamethylferrocene (DMFc) (ABCR) was purified by sublimation to produce a highly crystalline solid.

Synthesis of the complex dichloro-(1,2,8,11-tetraazacyclotetradecane) Nickel(II), also named Ni(II)cyclam, was carried out following a reported procedure[1]. Nickel(II) chloride hexahydrate (Sigma) was dissolved in ethanol and was added to a solution of the ligand (1.1 equivalent) in ethanol. The resulting light brown solution was heated to 40°C for 10 minutes. Then, diethyl ether was added to obtain a light mauve precipitate, which was then filtered and rinsed with diethyl ether. Recrystallization was done by adding ether to a saturated solution of product dissolved in methanol. The final product was dried overnight in vacuum.

$[\text{Ru}(\text{bpy})_2\text{Cl}_2]$, $[\text{Ru}(\text{bpy})_2\text{CO}_3]$, $[\text{Ru}(\text{bpy})_2(\text{CO})(\text{OCHO})](\text{PF}_6)$ and $[\text{Ru}(\text{bpy})_2(\text{CO})(\text{H})](\text{PF}_6)$ were synthesized stepwise following methods reported by Meyer and Ishitani [2-5]. Synthesis was conducted under a nitrogen atmosphere on a Schlenk line. $[\text{Ru}(\text{bpy})_2\text{Cl}_2]$ was synthesized from $\text{RuCl}_3 \times 3\text{H}_2\text{O}$ (Sigma, CH) with 2.1 equivalent of bipyridine and 0.1 equivalent of LiCl heated at reflux for 8 hours in dimethylformamide. After cooling down to room temperature, acetone was added and the resultant solution was cooled down to 0°C overnight. Filtering yields a dark green microcrystalline product. The solid was washed with water and diethyl ether.

For the synthesis of $[\text{Ru}(\text{bpy})_2\text{CO}_3]$, the previously obtained product, $[\text{Ru}(\text{bpy})_2\text{Cl}_2]$, was suspended in deaerated water and heated at reflux for 15 minutes. 10 equivalent of sodium carbonate was added and the solution was heated at reflux for 2 hours. After cooling at room temperature the solution was filtered, yielding dark purple crystals, which were then washed with water.

Synthesis of $[\text{Ru}(\text{bpy})_2(\text{CO})(\text{OCHO})](\text{PF}_6)$ was obtained by dissolving $[\text{Ru}(\text{bpy})_2\text{CO}_3]$ in formic acid 90%. The mixture was heated at reflux for 1 hour. The formic was removed after cooling of the solution to room temperature on a rotary evaporator. The resultant sticky solid was dissolved in water. The product is precipitated by addition of saturated solution of NH_4PF_6 . The bright yellow solid was subsequently filtered and washed with water and diethyl ether.

For synthesis of $[\text{Ru}(\text{bpy})_2(\text{CO})(\text{H})](\text{PF}_6)$, the previously obtained $[\text{Ru}(\text{bpy})_2(\text{CO})(\text{OCHO})](\text{PF}_6)$ was dissolved in 2-methoxyethanol and heated at reflux for 5 hours. The solution was then cooled to room temperature and saturated solution of NH_4PF_6 and water were added. The yellow-orange flocculent product was filtered then washed with water and diethyl ether.

Synthesis of $[\text{ReCl}(\text{bpy})(\text{CO})_3]$ was carried out following reported methods [6]. $\text{Re}(\text{CO})_5\text{Cl}$ (Sigma) and one equivalent of bipyridine were dissolved in a mixture of toluene and heptanes (50:50) and heated at reflux for 2 hours. The product precipitates upon cooling down to room temperature. The resulting yellow-brown crystal were filtered and washed with toluene.

2.3. Procedures

2.3.1. Product analysis

Ionic chromatography was used for the detection and quantification of formate in aqueous and organic samples recovered from the reactor after decompression. The presence of other

anions, such as acetate, fluoride, chloride, oxalate, etc. can also be determined using this technique. A Metrohm 883 Basic IC plus ion chromatograph (Metrohm, CH) equipped with an injection loop of 20 μ L, a polymethacrylate-based column (75 x 4.6mm, Metrosep Dual 2, Metrohm, CH) and a chemical suppressor was employed. The eluent for these measurements was a solution of 1.3 mM Na₂CO₃ and 2mM NaHCO₃. The procedure differs slightly for aqueous and organic samples; as organic solvents are inevitably containing traces of formic acid. For water samples analysis, a 100 μ L sample was taken from the reactor and diluted 10 folds with pure water to match the sample concentration with the calibration curve (1 to 20 mg/L formate). For organic samples (dimethylformamide or acetonitrile), the amount of formic acid generated was determined from the difference in concentration between the sample recovered after decompression and a sample taken from the reactor before sealing it. This second sample was kept aside during the reaction time. Both samples were diluted 10 folds with pure water. The dilution step is performed right before the injection to avoid further degradation of the organic solvent into formic acid. Indeed DMF/H₂O mixtures are known to spontaneously decompose to formate, especially for mixture of high water content, this production is favoured in presence of organic bases such as TEOA [7]. Control reactions without catalysts or without light were conducted to confirm that the formate detected is solely produced by CO₂ reduction and not by the degradation of solvent during reaction. A typical chromatogram obtain after reaction is shown in Figure 2.8., with identification of the different peaks. The carbonate peak is a systematic peak as the eluent is a carbonate/bicarbonate buffer solution. Quantification of this peak is impossible due to its important concentration in the eluent solution. The calibration curve used for quantification in DMF/water is also shown. All measurements for this calibration were performed in the same DMF/water mixtures, the amount of formate originally present in the solvent mixture was subtracted for every measurement.

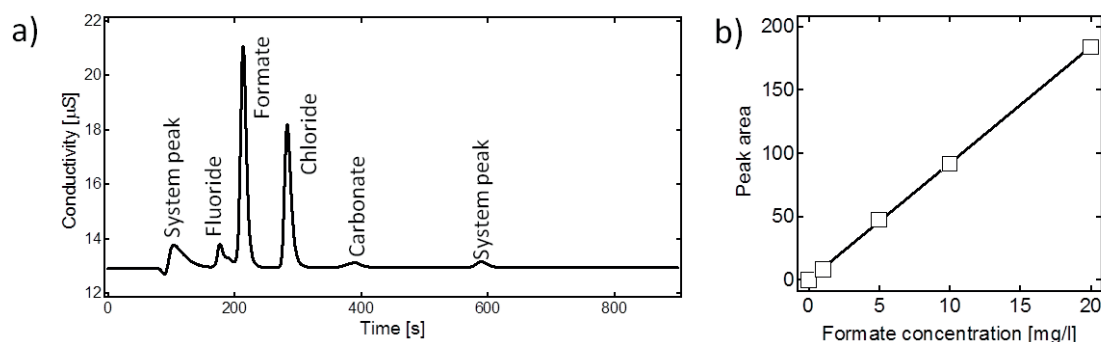


Figure 2.8. a) Chromatogram obtained for a standard reaction diluted 10x in pure water b) Calibration curve for formate measured in water-DMF mixture.

Gas chromatography was used for analysis of the gas collected upon decompression of the reactor. For hydrogen determination, the autoclave is connected to a silicon tube and the gas is bubbled in a beaker containing water for 1 minute. Then, a gas sample of 1 mL is collected with a gas-tight syringe followed by on-column injection of a GC-TCD (Perkin Elmer, Clarus 500, USA). Argon was chosen as the carrier gas according to the significant difference in thermal conductivity with hydrogen. CO and CH₄ quantification was performed on a GC-FID (Perkin Elmer Clarus 500, USA) equipped with a methanizer operating at 400 °C. The reactor was decompressed into an autoclave, which was then connected to the injection six-way valve of the gas chromatograph, and the gas was gently flowing through the injection loop for 1 minute before injection into the column. Calibration was performed by injection of certified gas mixtures in nitrogen at a concentration of 500 ppm (Carbagas, CH). As CO₂ is present in large amounts in the sample, the methanizer valve was switched before the peak of CO₂ appears to protect the methanizer. Exact determination of the total amount of CO₂ in the reactor was necessary for the quantification of the amount of CO produced. For biphasic water-scCO₂ systems, the amount of CO₂ was calculated from density and phase volume, as the amount of CO₂ dissolved in water is negligible. With organic solvents, determination of the amount of CO₂ in the reactor in given conditions of pressure, temperature and volume of the different component was calculated by injecting a known amount of CH₄ and determining its concentration in the reactor after compression at 150 bar by gas chromatography and calculating the dilution factor.

For the determination of methanol and other volatile organic molecules, analysis of headspace of water sample was performed on another gas chromatograph (Perkin Elmer, Autosystem Gas Chromatograph, USA), equipped with a polar column (PermaBond CW 20m x 0.25 μ m, CH) and a FID. Samples of 1 mL in 5 mL vials equipped with a rubber septum were heated at 80°C and 0.5 mL of the headspace was injected on column.

2.3.2. Reduction by DMFc in biphasic systems

Experiments with DMFc were performed in a three-valve autoclave reactor connected to both the CO₂ and the water pump. Presence of oxygen in the reactor was avoided by setting a small gas flow through the reactor for 20 minutes before compression. As DMFc is soluble in scCO₂ but not in water, it was introduced initially in the reactor and CO₂ was injected up to a pressure of 80 bars, with the temperature maintained at 40 °C. The reactor was stirred for 20 minutes to solubilise the DMFc in the supercritical phase. Then, an aqueous solution of an hydrophobic anion, generally lithium tetrakis(pentafluorophenyl)borate (LiTB) was added to the reactor using the second pump up the desired pressure of 150 bars. This solution was also deoxygenated before injection into the pump. The reactor was decompressed after a reaction time of 2 hours with analysis of the gas phase for CO and H₂ determination. The aqueous solution was analyzed by ionic chromatography for formate quantification. Solid DMFc and DMFcTB was recovered on the wall of reactor as it precipitate in the supercritical phase, this solid was then analyzed by UV/VIS spectrometry and mass spectrometry.

2.3.3. High-pressure spectroscopy

To monitor the progress of the reaction with DMFc, spectrophotometric measurements were carried out in scCO₂ using the three-window viewcell. A white light source was set on a side with a UV/VIS spectrometer on the other. Spectra were recorded through the supercritical

phase, to determine the variation of concentration of DMFc and DMFc⁺ over time. DMFc⁺TB⁻ is insoluble in scCO₂, and its precipitation on the windows was hindering spectrophotometric measurements. Acetonitrile was therefore added as co-solvent in the reaction medium to limit precipitation of DMFc⁺TB⁻ and improve light transmission through the supercritical phase.

In chapter 4, a similar setup was used for the determination of the pH of water in contact with scCO₂. Absorption spectra of the two selected pH indicators, bromophenol blue and bromocresol purple, were recorded in pH controlled solutions prior to measurements in the reactor to obtain calibration curves. *In situ* spectra of water in contact with CO₂ were done in the three-window viewcell. The reactor was firstly loaded with 25 mL of water, the blank spectra was recorded then the pH indicator was injected, the solution saturated with CO₂ at atmospheric pressure and the reactor sealed. Spectra were recorded as the inner pressure was increased from 1 to 150 bars.

2.3.4. High-pressure NMR

High-pressure NMR was used in chapter 3 for the investigation of the reduction of CO₂ by decamethylferrocene with HTB as the proton source. Two sets of experiments were performed in CD₂Cl₂, one under nitrogen at atmospheric pressure and one under 50 bars of CO₂. For the measurement without CO₂, DMFc and HTB were mixed together in the tube shown in Figure 2.7. under nitrogen atmosphere. NMR spectra were recorded every five minutes for 2 hours. For measurements with CO₂, the time between the introduction of DMFc and HTB in solution and the beginning of the recording of the spectra is quite long due to the additional preparative step needed to compress with CO₂. To start the NMR recording at the beginning of the reaction a capillary tube containing a solution of HTB in CD₂Cl₂ was inserted in the NMR tube containing the solution of DMFc in CD₂Cl₂. Therefore, the two solutions could not mix before the compression with CO₂. Before insertion into the NMR, the tube was shaken to mix the solutions of DMFc and HTB together to initiate the reaction. NMR spectra were also recorded every 5 minutes for 2 hours.

2.3.5. Photocatalytic reduction

For photocatalytic reduction of CO₂ catalyzed by Ni(II)cyclam, suitable volumes of separated aqueous solutions of the catalyst, the photosensitizer and the sacrificial electron donor were loaded into the reactor. CO₂ was gently flowing through the reactor and the autoclaves used for decompression, to saturate the entire system with CO₂. The reactor was then sealed, the temperature raised to 313 K and CO₂ was finally compressed into the reactor by the piston pump up to the desired pressure. The light source used was the 600 W Xenon lamp, with a cutoff filter ($\lambda < 400$ nm). After the desired reaction time the reactor was decompressed in two autoclaves connected in series, with the first one acting a solvent trap and the second as gas sample vessel for H₂ and CO quantification by gas chromatography. Quantification of formate by ionic chromatography was impossible due to the overlapping of the peak on the ionic chromatography of formate and ascorbate used as sacrificial electron donor.

For photocatalytic reductions with a ruthenium catalyst, the reactor was filled in a similar manner, with introduction of the solution of catalyst, photosensitizer and electron donor in DMF/water solutions. Before sealing of the reactor, a 100 μ L sample was taken for initial formate concentration determination. The reactor was then purged with CO₂ and the pressure was increased by compression with the CO₂ pump. For this catalyst, the light source has been changed to the 455 nm monochromatic LED. Decompression of the reactor was also performed with the two autoclaves connected in series with H₂ and CO quantification by gas chromatography. After total decompression a liquid sample was taken from the reactor for formate quantification.

2.3.6. Three-electrode voltammetry

Conventional three-electrode electrochemical analyzes were conducted using an Autolab potentiostat 30 (Metrohm, CH) or a Palmsens portable potentiostat (Ivium Technologies, NL). The working electrode was a glassy carbon electrode, platinum grid as counter electrode, and for reference electrode a Ag/AgCl in KCl 3 M reference electrode (Sarstedt, DEU) was used for experiments in water, and a silver wire quasi reference electrode with calibration with ferrocene or decamethylferrocene was used in organic solvents. As electrolytes, 0.1 M KCl or LiClO₄ was used in water and tetrabutylammonium hexafluorophosphate (TBAPF₆) in organic solvents. The cell was sealed during measurements and the solution was saturated with argon or CO₂ between measurements.

2.3.7. Wilhemy plate surface tension measurements

The Wilhelmy plate method was used for the determination of the interfacial tension and surface concentration of catalyst in chapter 4. In this method, a paper strip immersed in a solution is attached to a pressure sensor. Pressure-area isotherms were initially measured for pure water with a computerized Langmuir trough (NIMA Model 611, Nima technology Ltd., Coventry, UK) to confirm the absence of surface-active molecules.

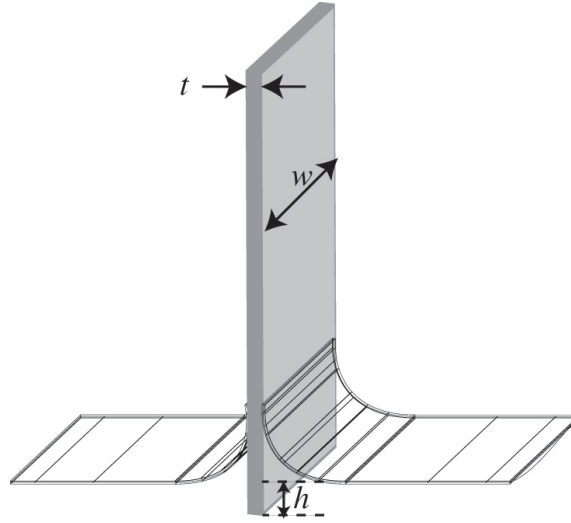


Figure 2.9. Wilhelmy strip probe for interfacial tension measurements. w = strip width, t = thickness and h = distance between the surface and the immersed extremity of the strip.

Then, measurements of the surface tension of water were performed with an increasing concentration of nickel(II)cyclam catalyst ranging from 0 to 100 mM. Experiments were carried at 25 °C with a 1cm-wide filter paper. Assuming a contact angle between the strip and the liquid of 0° , the net force acting on the plate is:

$$F_{net} = \gamma(2w + 2t) - \rho g h t w \quad (2.1)$$

where ρ is the liquid density and g the gravity. Given that these experiments are generally carried out with very thin probes and with the probe about to detach from the surface of the liquid. Equation 2.1. can then be simplified as the right hand side of the equation vanished ($h \rightarrow 0$) and the contribution of the strip thickness is extremely small compared to its width:

$$\gamma \approx \frac{F_{net}}{2w} \quad (2.2)$$

2.3.8. Pendant drop surface tension measurements

As the method of the Wilhelmy plate is invasive, it was only suitable for surface tension measurements of the air-water interface. To estimate the tension of the water-supercritical CO₂ interface a custom-built pendant drop system was used. The three-window viewcell was equipped with a syringe needle (inner diameter = 0.5 mm) on the roof on the inside of the reactor. The shape of aqueous pendant droplets of 15 μL formed at the tip of the needle was recorded with a high resolution handheld microscope (ProscopeHR, Bodelyn Technologies, USA) mounted on one side window of the viewcell opposite to a light source. Potentially destabilizing pressure gradient were successfully avoided by operating the CO₂ pump at a constant pressure of 140 bar, while the pump dedicated to the injection of water was operated at a constant flow rate of 10 μL·min⁻¹. Reproducible and stable pendant drops of 15 μL were obtained after an injection period of 90 seconds. Image acquisition was always performed after an equilibration time of 10 seconds and further analysis was carried out with the software Mathematica 8.0 (Wolfram research). Drop profiles were obtained by applying a Shen-Castan algorithm to the raw image. All measurements were done by triplicate. Drop shape analysis and interfacial tension determination are detailed in chapter 4.

2.3.9. Phase behaviour of expanded liquids

Determination of the volume expansion coefficient and CO₂ concentration in CO₂-expanded liquid was performed using the high-pressure NMR tube. A volumetric scale was fixed to the reactor to easily measure volume differences. The tube was initially filled with the desired amount of organic solvent, the reactor was then closed and weighted to determine precisely the amount of solvent. The reactor was then successively filled with a moderate pressure of CO₂ (about 5 bar) then decompressed. This step was repeated 5 times in order to purge the reactor from any other gas. The reactor was maintained in a thermostated bath at the desired temperature. The pressure was increased by injecting CO₂ into the reactor and the liquid phase

volume and total reactor mass were recorded at different pressures. Liquid phase density, CO₂ concentration and molar fraction were determined from the total mass of the reactor, subtracting the mass of the upper phase considered as a pure CO₂ phase.

2.3.10. High-pressure electrochemistry

The high-pressure reactor used for electrochemistry is the reactor presented in Figure 2.5. with the three-electrode cap. For the voltammetry of DMFc in scCO₂, only the three-electrodes of the cap were used. The working electrode is a gold disk electrode (geometric area 0.0173 cm²) set in a peek body with a platinum wire as counter electrode and a silver wire as quasi reference electrode. The wire electrodes were bent to position them at the closest possible proximity of the working electrode to decrease uncompensated resistance through the solution. The electrolyte was a room temperature ionic liquid (RTIL), which was synthesized by ion exchange of two precursor salts, lithium tetrakis(pentafluorophenyl)borate (TFPB⁻) and tetradecyl ammonium bromide (TDA⁺). Equimolar solutions of the salts (0.05 mM) in methanol/water 6:1 molar ratio were added together under stirring. The combined solution was stirred for 12 hours to form a highly viscous gel at the bottom of the vessel. The solvent was removed and the gel dissolved in 1,2-dichloroethane. The RTIL was then purified by water extraction to remove the excess of lithium and bromide ions. Ionic chromatography confirms the total elimination of bromide. The solvent was then completely evaporated to leave a viscous clear liquid. For electrochemical measurements, the desired amount of RTIL and acetonitrile used as co-solvent for scCO₂ was introduced in the reactor. The reactor was purged with CO₂ by setting a small flow of CO₂ through the reactor for 10 minutes, during that time the reactor temperature was set as cold as possible to avoid evaporation of the solvent. The reactor was then sealed, temperature set to 313 K and the pressure increased to 100 bars while the reactor was stirred. Electrochemical measurements were performed at variable scan rates under quiescent conditions.

For voltammetry of ruthenium and rhenium catalysts, to obtain a broader potential window the electrode used was a glassy carbon electrode (BASi, USA) equipped with a high-

pressure connection (Swagelok, UK). For calibration of the reference electrode, 1 to 2 mM DMFc was added to the solution. The reactor was initially filled with solvent, electrolyte, catalyst and DMFc used for the calibration of the quasi reference silver wire. The reactor was sealed and purge with CO₂. The pressure was increased with the pump to the desired value and voltammetry was recorded in quiescent conditions. Generally, many voltammograms were recorded in the same solution as the pressure was increased by step of 2 to 5 bar, with voltammogram recorded on each step once the pressure has equalized.

2.4. Bibliography

1. Bosnich, B., M.L. Tobe, and G.A. Webb, *COMPLEXES OF NICKEL(2) WITH A CYCLIC TETRADENTATE SECONDARY AMINE*. Inorganic Chemistry, 1965. **4**(8): p. 1109-1112.
2. Sullivan, B.P., et al., *Hydrido carbonyl complexes of osmium(II) and ruthenium(II) containing polypyridyl ligands*. Organometallics, 1984. **3**(8): p. 1241-1251.
3. Johnson, E.C., et al., *Synthesis and properties of the chloro-bridged dimer $[(bpy)_2RuCl]_2^{2+}$ and its transient $3+$ mixed-valence ion*. Inorganic Chemistry, 1978. **17**(8): p. 2211-2215.
4. Konno, H., et al., *Synthesis and properties of $[Ru(tpy)(4,4'-X_2bpy)H]^+$ ($tpy=2,2':6',2''$ -terpyridine, $bpy=2,2'$ -bipyridine, $X=H$ and MeO), and their reactions with CO_2* . Inorganica Chimica Acta, 2000. **299**(2): p. 155-163.
5. Eggleston, D.S., et al., *Structural variations induced by changes in oxidation state and their role in electron transfer. Crystal and molecular structures of $cis-[Ru(bpy)_2Cl_2].3.5H_2O$ and $cis-[Ru(bpy)_2Cl_2]Cl.2H_2O$* . Inorganic Chemistry, 1985. **24**(26): p. 4573-4580.
6. Staal, L.H., A. Oskam, and K. Vrieze, *The syntheses and coordination properties of $M(CO)_3X(DAB)$ ($M = Mn, Re$; $X = Cl, Br, I$; $DAB = 1,4$ -diazabutadiene)*. Journal of Organometallic Chemistry, 1979. **170**(2): p. 235-245.
7. Paul, A., et al., *Effect of Water during the Quantitation of Formate in Photocatalytic Studies on CO_2 Reduction in Dimethylformamide*. Inorganic Chemistry, 2012. **51**(4): p. 1977-1979.

CHAPTER 3

Reduction by decamethylferrocene in biphasic systems

3.1. Introduction

Due to the very negative potentials required to reduce carbon dioxide and the need for a catalyst to drive multi-electron coupled to multi-proton transfer reactions, the number of compounds capable of reducing CO₂ without external driving force, such as light, is very limited.

The proficiency of hydrogen evolution reaction (HER) at a catalyst has often been taken as an initial indicator of a suitable catalyst for CO₂ reduction. Numerous compounds and metals catalyse the reduction of protons to hydrogen, and have been explored with respect to CO₂ with little success. However, one class of compound, the metallocenes, has recently gained renewed interest with respect to the HER. Hydrogen evolution has been observed using cobaltocene [1] osmocene [2] and decamethylferrocene [3]. This last compound is of particular interest, as it has a relatively high solubility in supercritical CO₂, in the millimolar range.

As with the metallocenes used in the HER research, the intention is to use decamethylferrocene (DMFc) in scCO₂ reduction as a sacrificial electron donor. However, the presence of an electron donor alone is not sufficient for the reduction of CO₂, as electron transfer must be coupled to proton transfer to decrease the reduction potential accordingly. Water is an obvious clean and abundant source of protons, but as discussed in the introduction, it is not miscible with scCO₂. The aqueous protons will therefore need to be transferred from the water phase to the supercritical phase.

3.2. DMFc as electron donor for hydrogen evolution

Metallocenes are known to be capable of generating hydrogen in presence of strong acid in an organic phase [4, 5]. But decamethylferrocene has been demonstrated to produce hydrogen from aqueous protons through biphasic reaction at the interface between two immiscible electrolyte solutions (ITIES) [6]. As DMFc is not soluble in water, it remains in the organic phase, typically 1,2-dichloroethane, while the water phase in contact is the source of protons for hydrogen formation. For the reaction to proceed, the protons need to transfer from the aqueous to the organic phase. This mechanism has been comprehensively studied and understood for decamethylruthenocene [7] and the Nernst equation for the proton transfer is given by:

$$\Delta_o^w \phi = \phi^w - \phi^o = \Delta_o^w \phi_{H^+}^\ominus + \frac{RT}{F} \ln \left(\frac{a_{H^+}^o}{a_{H^+}^w} \right) \quad (3.1)$$

where $\Delta_o^w \phi$ is the Galvani potential difference between the two phases, $a_{H^+}^o$ and $a_{H^+}^w$ the activity of protons in the organic and the water phase respectively and $\Delta_o^w \phi_{H^+}^\ominus$ is the standard transfer potential of the proton from water (w) to organic phase (o) expressing in a voltage scale the standard Gibbs energy of transfer $\Delta G_{tr, H^+}^{\ominus, w \rightarrow o}$:

$$\Delta_o^w \phi = \frac{\Delta G_{tr, H^+}^{\phi, w \rightarrow o}}{F} \quad (3.2)$$

This Nernst equation shows that if the interface is polarised positively at potentials higher than the standard transfer potential of protons, protons will transfer to the organic phase. The Nernst equation can be written in another way to express the ionic partition coefficient P_i of an ion i of charge z_i :

$$P_i = \frac{a_i^o}{a_i^w} = \exp \left[\frac{z_i F}{RT} (\Delta_o^w \phi - \Delta_o^w \phi_i^\phi) \right] = P_i^\phi \exp \left[\frac{z_i F}{RT} \Delta_o^w \phi \right] \quad (3.3)$$

For neutral species, the partition depends only of the properties of the two solvents, while for ionic species the partition depends also on the Galvani potential difference. In presence of a proton acceptor such a DMFc, the proton transferred in the organic phase will quickly react and protonate DMFc, decreasing its concentration in the organic phase. The ion transfer is therefore facilitated by the metallocene in the organic phase due to the subsequent chemical reaction.

The polarisation of the interface can be achieved by two means: with a potentiostat or by the distribution of an electrolyte in the two phases. The partition of the electrolyte between the two phases will result in the polarisation of the interface. The Galvani potential established at the interface is called the distribution potential given by:

$$\Delta_o^w \phi = \frac{\Delta_o^w \phi_{C^+}^\phi + \Delta_o^w \phi_{A^-}^\phi}{2} + \frac{RT}{2F} \ln \left(\frac{\gamma_{C^+}^o \gamma_{A^-}^w}{\gamma_{C^+}^w \gamma_{A^-}^o} \right) \quad (3.4)$$

where γ_i^α is the ionic activity coefficient of the ionic species i in the phase α .

In the case of the distribution of a salt or an acid containing a hydrophobic anion, the interface will be polarised positively as the standard transfer potential of this anion is largely positive. If this standard transfer potential is high enough, protons will transfer spontaneously from water to the organic phase and will therefore be able to react with the DMFc in the

organic phase to produce hydrogen. The different ions investigated for protons transfer are ranging from slightly hydrophilic, BF_4^- , PF_6^- , ClO_4^- , to hydrophobic, tetrphenylborate (TPB). More hydrophobicity can be obtained with the anions of the series of compound called BARF salts, in which a boron centre is covalently bonded to 4 aryl groups, which are in turn fluorinated. Two examples of BARF anions are shown in Figure 3.1.

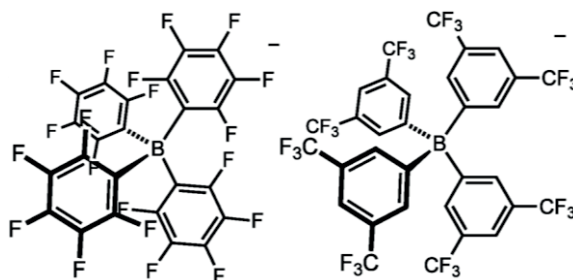


Figure 3.1. Structure of two common BARF anions, tetrakis(pentafluorophenyl)borate (TB^-) and tetrakis(3,5-bis(trifluoromethyl)phenyl)borate (CTB^-).

The standard ionic transfer potential of these different anions are reported in table 3.1. No value for the anion CTB^- are reported in literature but due to the similarities in the structure with the anion TB^- , a standard ionic transfer potential very close to the one of TB^- can be expected.

Table 3.1. Standard Gibbs energy of transfer and standard ionic transfer potential from water to 1,2-DCE for different common hydrophobic anions

Anion	$\Delta G_{tr,i}^{\phi,w \rightarrow DCE}$ [kJ/mol]	$\Delta_{DCE}^w \phi_i^\phi$ [V]
BF_4^-	17.9 ^a	-0.186
PF_6^-	15.9 ^b	-0.165
ClO_4^-	14.9 ^a	-0.154
TPB^-	-33.0 ^c	0.342
TB^-	-68.5 ^c	0.710

For the anion PF_6^- , the solvent is not 1,2-dichloroethane but 1,6-dichlorohexane as no value are reported for this solvent, ^{a,b,c} values respectively taken from [8],[9] and [10].

For protons, the standard ionic transfer potential from water to DCE is estimated to 0.587 V [11]. Therefore, from Equation (3.3), the partition of protons between water and DCE will be positive for polarisation of the interface higher than the standard transfer potential of

proton, causing transfer of protons from water to DCE. The values expressed in Table 3.1. are only valid for the biphasic system water-DCE. When transposed in a water-scCO₂, the exact value of the polarization of interface is unknown, but the difference between the standard ionic transfer potential of the anion and the standard ionic transfer potential of protons should remain comparable. The Gibbs transfer energy is mainly a measure of the interaction between the anion and water, as DCE and scCO₂ are both non-coordinating solvent.

Experimental [12] and theoretical [13] studies have already demonstrated the basic character of DMFc and other ferrocene derivative. Subsequently, DMFc dissolved in DCE can be protonated by the protons transferred to the DCE phase to form a DMFc hydride molecule. Protonation of DMFc is the initial step of hydrogen formation, the following mechanism is not yet fully understood but is presumably happening via a bi-molecular reaction between two DMFc hydride molecules ([DMFc-H]⁺). Considering the intermediate [DMFc-H]⁺ being a hydride complex with two bulky ligands, steric hindrance should largely inhibits the bimolecular elimination pathway. But it is not fully clear that the proton is bonded to the metal centre. If the proton is localized on the ring rather than on the metal centre the steric hindrance should be a smaller barrier to the reaction.

For CO₂ reduction by DMFc, the mechanism of hydrogen evolution is not a key point as CO₂ should interfere in the hydrogen evolution mechanism and use the intermediate [DMFc-H]⁺ as a source of protons and electrons to reduce CO₂.

3.3. CO₂ reduction in water-scCO₂ systems

In a water-scCO₂ systems the same principle of proton transfer from an aqueous to an organic phase explained in the previous section can also be applied, with scCO₂ replacing the organic phase. Assisted transfer of protons to the supercritical phase should lead to a similar formation of [DMFc-H]⁺. The large concentration of CO₂ (15M at 150bar and 40°C) will intensively favour reaction with CO₂ rather than a bimolecular pathway. The high pressure should also limit the production of hydrogen from protons due to *Le Châtelier* principle.

In section 1.2.4, the general mechanism of reduction of CO₂ into formate was discussed. For all catalysts considered, the initial step is the formation on a hydride complex on the catalyst followed by insertion of CO₂ into the hydride bond to generate the formato-complex. This mechanism can be transposed to DMFc, given the reaction chain shown in Figure 3.2. To complete the cycle and release the formate molecule generated, the formato-complex needs to be reduced, the electron is presumably coming from another DMFc molecule. In the overall reaction, two DMFc molecules are oxidized to reduce carbon dioxide into formate.

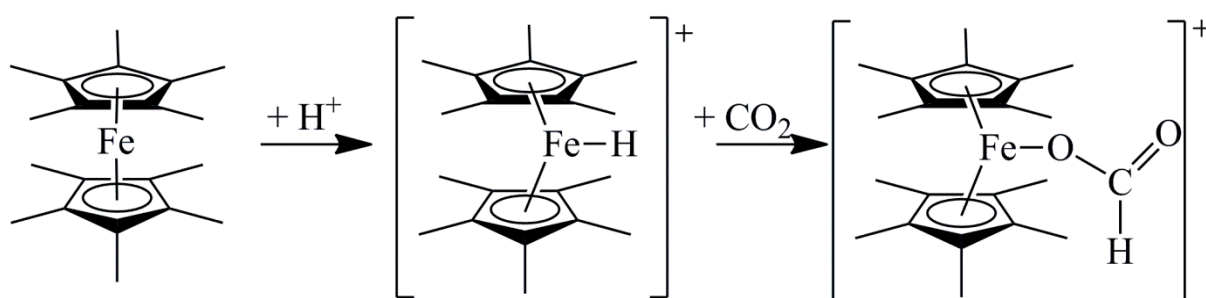
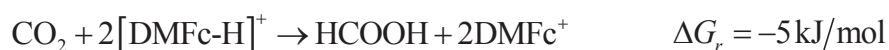


Figure 3.2. Presumed mechanism for formate generation by DMFc.

The overall reaction is thermodynamically feasible from the calculation of the Gibbs energy of the reaction.¹



The activation barrier is, however, estimated to be too important to drive the reaction in standard conditions of pressure. And DFT calculations have so far not been able to resolve the reaction between CO₂ and [DMFc-H]⁺. Performing the reaction under high CO₂ pressure conditions might be highly beneficial for the reaction. The presence of CO₂ as the solvent facilitates the approach of CO₂ to the hydride.

¹ DFT calculations performed by the group of Pr. Clémence Corminboeuf in the Laboratory for Computational Molecular Design

3.3.1. Choice of anion

Different anions have been tested for the reaction, ranging from slightly hydrophilic to very hydrophobic. The procedure used for the experiments is detailed in section 2.3.2 in chapter 2. Quantification of the amount of product generated by the reaction is performed in the following section, the spectral analysis of the solid precipitated on the walls of the reactor can be used to quantify the amount of DMFc oxidized. Visible spectra of pure DMFc and DMFc^+ are shown in Figure 3.3. DMFc shows only one absorption band in the visible region, with its maxima at 430 nm. While DMFc^+ has an absorption band of similar extinction coefficient in the red and near infrared region with its maxima at 776 nm. Additionally, a second absorption band is partially visible in the UV region.

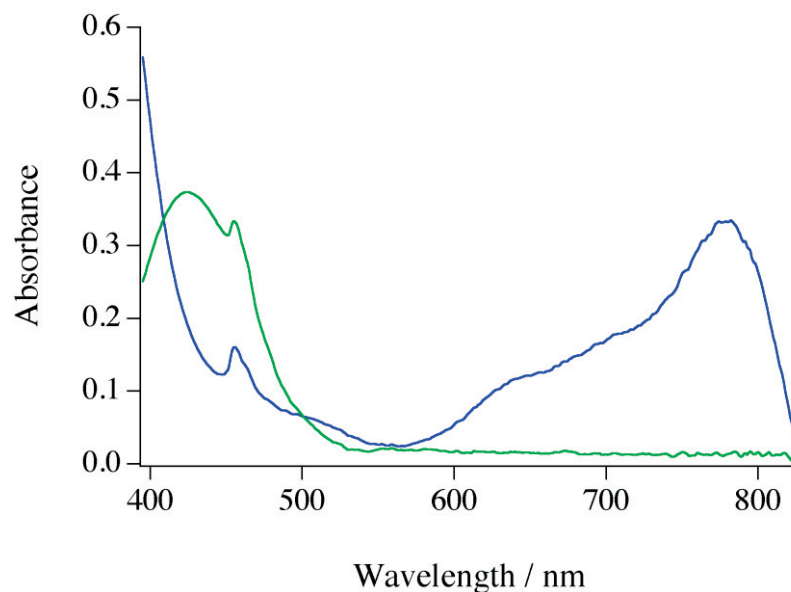


Figure 3.3. Visible spectra of 2.9 mM solution of DMFc (green line) and DMFc^+ (blue line) in acetonitrile. Peak at 450 nm is an artefact caused by the spectrophotometer.

Analysis of the solid recovered after reaction in the reactor is shown in Figure 3.4. As predicted by the standard ion transfer potential of the different anions tested, when using BF_4^- , only 30% of DMFc is oxidized after 4 hours of reaction. This is explained by the fact that the transfer potential of tetraphenylborate is close to that of protons, therefore, the transfer of protons from water to CO_2 is predicted to happen but in a moderate way. In

contrast, for highly hydrophobic anions such as TB^- the oxidation is complete as the transfer potential of these anions is higher than the one of protons.

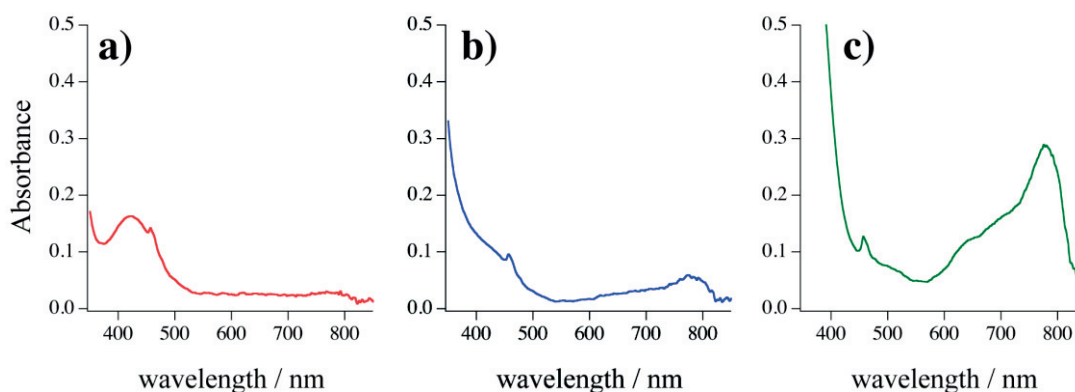


Figure 3.4. Visible spectra of 1 mg of solid recovered after 4 hours of reaction and re-dissolved in 1,2-dichloroethane. Reactions were performed at 150bars 313°K with 30 μ mol DMFc and around 10 ml of water containing 5mM of a) $NaBF_4$, b) $NaTPB$ and c) $LiTB$.

For experiments in presence of highly hydrophobic anion, the DMFc is totally oxidized, therefore amount of product corresponding to the same amount of electrons is expected.

3.3.2. Production yield of reduction products

From the suggested mechanism the major product is presumed to be formate. As a side product hydrogen can also be generated. As carbon monoxide is the most common reduction product of CO_2 it was also quantified. Gas and ionic chromatography were used to detect and quantify those products, following the procedures detailed in section 2.3.1 of chapter 2.

The average amount of formate and hydrogen generated in for different reactions are reported in Table 3.2. For each experiment, the amount of DMFc dissolved in supercritical phase was 30 μ mol. The amount of carbon monoxide detected was slightly above the blank. The carbon dioxide used in the experiment naturally contains around 1 ppm of carbon

monoxide. The amount detected after reaction is around 1.5 ppm. The accuracy of the measure is not sufficient to ensure the generation of carbon monoxide during the reaction.

Table 3.2. Amount of products for different reactions with 30 μmol of DMFc initially in the reactor.

Experiment	Formate [μmol]	Hydrogen [μmol]
DMFc, LiTB	0.4	traces
DMFc, NaCTB	0.8	traces
DMFc, HTB, no water	Less than the blank	5.1

The third experiment reported in Table 3.2 has a different procedure from the other two. In this experiment, no water was used, and the acid salt of the anion TB^- was dissolved with DMFc in acetonitrile prior the addition of CO_2 in the reactor and increasing the pressure to 150 bars. Therefore, proton transfer through the interface was not needed, as the system consists of scCO_2 -acetonitrile single phase. However, for this reaction two problems appeared. First, the two reagents DMFc and HTB had time to react together before the introduction of CO_2 and produced considerable amounts of hydrogen. More than 30% of the DMFc is oxidized to produce hydrogen. The second problem is the contamination of the solvent, in the range of mg/L, with small organic molecules such as formic acid. At the end of the reaction the concentration of formic acid in acetonitrile has decreased compared to the initial solution.

For all experiments the amount of product detected does not account for all the DMFc oxidized in the reactor. This suggests that other compounds than formic acid, carbon monoxide and hydrogen are being produced. As the range of reactant contained in the reactor is very limited, the compounds that could be reacting with the DMFc are the anion, oxygen, or further reduction of formic acid or carbon monoxide.

Fluorinated molecules like TB^- can be reduced by metallocenes [14], and evidences for this reaction have been observed:

- The analysis of the solid precipitated on the walls of the reactor at the end of the reaction by MALDI-TOF shows various decomposition products of TB^- , the two most abundant adducts are presented in Figure 3.5. But the amount of these decomposition products remains very small compared to the amount of TB^- .
- In the ionic chromatography the peak area of the fluoride anion after the reaction has increased compared to the initial solution of $LiTB$, which is caused by the formation of the first adduct.
- The use of the anion CTB^- , the second anion in Figure 3.1., shows a slightly better yield for formate. This anion has no fluoride in the para-position of the phenyl ring, and might therefore be more stable[15]. MALDI-TOF of the precipitate recovered after the reaction with this anion shows less decomposition of the anion.

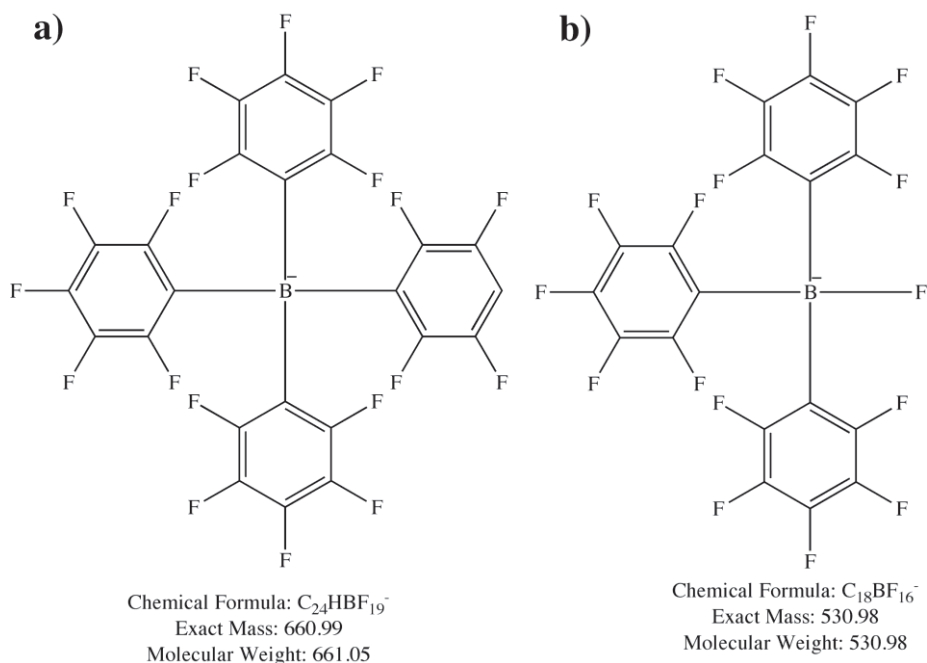


Figure 3.5. Structures of the adducts obtained from TB^- upon a) the loss of fluoride or b) replacement of a ring by fluoride.

The presence of oxygen in the reactor is avoided as much as possible, but it can be the main detrimental factor as if only a small amount of oxygen is present it will quickly be reduced to H_2O_2 and then further reduced to water [3]. A single molecule of oxygen can therefore oxidize four molecules of DMFc and even by purging the system carefully oxygen cannot be completely removed. With water being the final product of reduction of oxygen, the amount of oxygen reduced to water by DMFc cannot be quantified.

Other reduction products of CO_2 were sought by analysis of the water recovered after the reaction, using the headspace gas chromatography method described in section 2.3.1. In experiments with LiTB the headspace analysis of the water recovered at the end shows the presence of an organic volatile compound, which has been identified to be diethylether. This compound is unavoidably present in the LiTB salt. No other products were detected, though it is possible that the method was limited by a relatively high limit of detection.

Although not detected, the presence of other reduction products than formate and carbon monoxide is still possible. The fact that during the third reaction of Table 3.2. the concentration of formic acid in acetonitrile decreases with time corroborates the hypothesis

that formic acid can be reduced further by DMFc. However, to prove the existence of the reaction between formate and DMFc a shake flask experiment has been conducted. The experiment consisted of three vials containing each 5 ml of DCE and 5 ml of water, with different compounds dissolved in the two phases as presented in Figure 3.6. In flask 1) and 2) the DCE solution turned to green in one hour, indicating a complete oxidation of DMFc. Both solutions were evolving hydrogen as bubbles were generated in solution. But in the first vial, the concentration of formic acid in water has also decreased by about 30%. No decrease in formic acid concentration in vial 3) confirms that formic acid has been transformed and not simply transferred to the DCE phase.

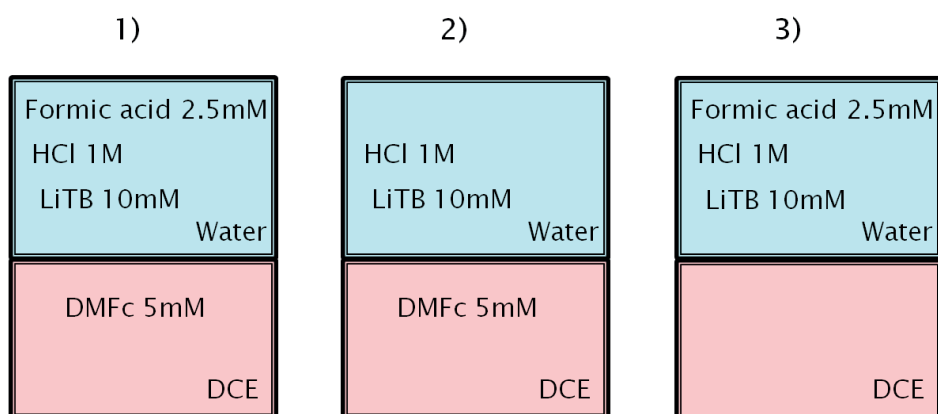


Figure 3.6. Shake flask experiments for the reduction of formate.

3.4. NMR analysis

To validate the hypotheses that CO_2 is reduced by DMFc and to investigate the mechanism of reaction, the reaction between DMFc and HTB in CD_2Cl_2 was followed by NMR under nitrogen and under 50 bars of CO_2 . The procedures of these experiments are detailed in section 2.3.4 of chapter 2.

For the measurement without CO_2 , DMFc and HTB were mixed together in a sealed NMR tube under nitrogen atmosphere. DMFc was quickly oxidized and hydrogen bubbles

evolved from the solution. NMR spectra were recorded every five minutes during the experiment and are presented in Figure 3.7.

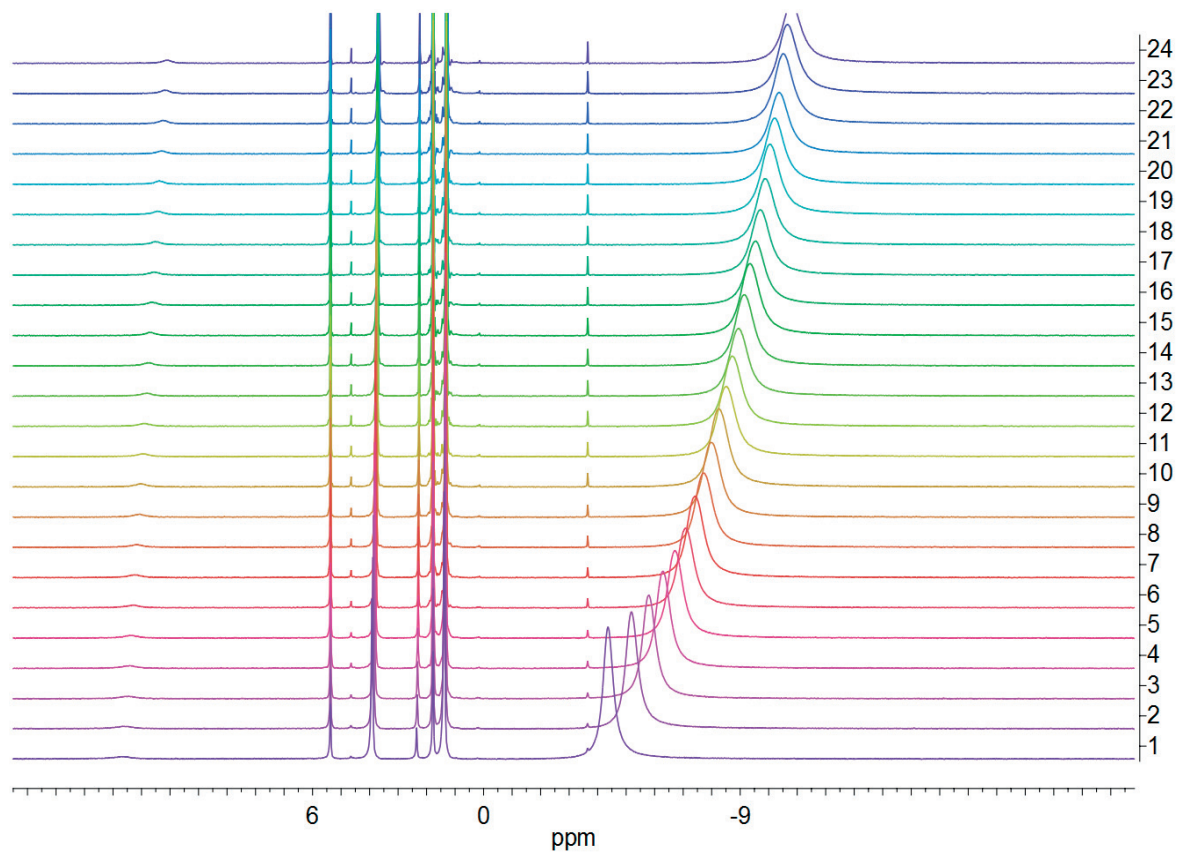


Figure 3.7. NMR of HTB and DMFc in CD_2Cl_2 over 2 hours of reaction, one spectrum taken every five minutes.

All peaks were identified by performing individual NMR spectra of pure compounds and are given from left to right in Table 3.3.

Table 3.3. List of compounds identified

Chemical shift	Compound
12.5	Proton of HTB
5.4	CD ₂ Cl ₂
4.7	H ₂ dissolved
4	-CH ₂ - of diethylether
2.3	Trace of acetone contamination
1.8	Base peak of DMFc
1.4	CH ₃ - of diethylether
-3.6	Hydride [DMFc-H] ⁺
-4 to -10	Coalescent peak of DMFc and DMFc ⁺

Two signals are increasing over the two hours of reaction, the dissolved hydrogen peak and the DMFc hydride peak. This second signal is of greater interest as its increase means that the formation of the hydride is faster than the bimolecular reaction between two hydrides to form hydrogen, and therefore the hydride can accumulate in the solution. The most interesting observation is the peak moving from -4 to -10 ppm, after 24 hours, this signal has stabilized at -38 ppm. This signal is a coalescent peak of two compounds: DMFc and DMFc⁺. When the electron exchange between two compounds is fast compared to the measurement time of the NMR, the two compounds cannot be resolved independently and a single coalescent signal appears. Kinetic of the electron transfer can be estimated from the peaks width and has been reported to be around $2 \times 10^7 \text{ M}^{-1}\text{s}^{-1}$ [16]. However, this value is very dependant of the solvent and the presence of electrolyte [17]. The chemical shift of the coalescent peak is a function of the chemical shift of the two compounds and the molar fraction in the solution, as presented in Equation (3.5):

$$\delta(\text{coalescent}) = x_{\text{DMFc}} \delta(\text{DMFc}) + x_{\text{DMFc}^+} \delta(\text{DMFc}^+) \quad (3.5)$$

Using Equation (3.5), the molar fraction of DMFc and DMFc⁺ can be calculated from the NMR data. The increase of DMFc⁺ concentration is represented in Figure 3.8. As it can be seen, on the first measurement 15% of the DMFc has already been oxidized. Preparing the

solution under inert atmosphere and transferring the tube into the NMR, then calibrating the measure consumes about 10 minutes. By the time of the first measurement the reaction has already had time to progress. This explains the high concentration of DMFc^+ measured initially.

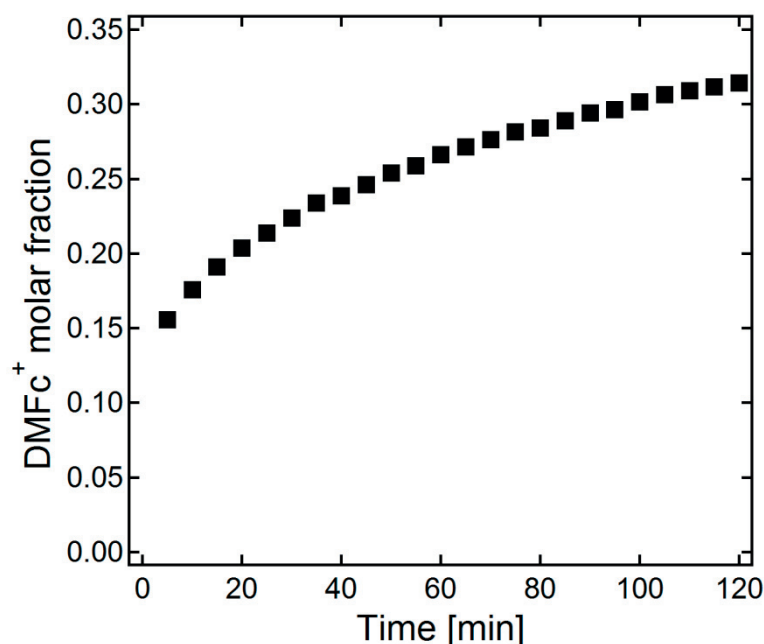


Figure 3.8. DMFc^+ molar fraction evolution over the two hours of NMR experiment.

For a similar experiment but under high pressure of CO_2 , the time between introduction of DMFc and HTB in solution and the begin of recording the NMR spectra is even longer due to the additional preparative step needed to compress with CO_2 . To prevent the compounds from mixing before compression with CO_2 , HTB in CD_2Cl_2 solution was contained in a capillary tube inside the NMR tube as explained in the section 2.3.4. Spectra recorded are displayed in Figure 3.10. The peaks appearing in the spectra are mostly the same as in the previous experiment, but with several important changes. The hydrogen peak is much smaller and does not increase anymore after 30 minutes of reaction. The hydride peak is not present at all, suggesting it is either not formed, or consumed faster than produced. Previous NMR experiments have shown that the hydride peak disappeared when a solution containing DMFc and HTB is compressed with CO_2 . Therefore, the reaction between DMFc hydride and CO_2 is considered to be faster than the bimolecular reaction to produce H_2 , this is supported by the fact that under supercritical conditions no hydrogen is detected in the

reactor. The proposed mechanism in Figure 3.2. seems to be confirmed by these observations. The major difference compared to the previous experiment is the faster shifting of the coalescent signal. After two hours the chemical shift of the signal is much more negative, meaning that around 50% of DMFc has been oxidized. With CO₂, about 60% of the DMFc is oxidized compared to 35% without CO₂. The last signal at -38 ppm is pure DMFc⁺ in solution, this has been confirmed from NMR and X-rays diffraction analysis of crystals recovered in the NMR tube after 24 hours. Figure 3.10. shows the structure of pure DMFc⁺TB⁻ salt obtained by X-rays diffraction analysis. The presence of the signal of DMFc⁺ in addition of the coalescent seems contradictory. But with the capillary containing HTB inside the NMR tube, two different solutions are analyzed simultaneously. Initially, HTB was entirely contained in the capillary while the DMFc was around the capillary. Before installing the tube in the NMR, the solution was shaken vigorously to mix the two solutions. But due to capillarity phenomenon, the HTB solution remains mainly in the capillary. The two solutions, inside and outside of the capillary, are very different in terms of concentration of species. Outside of the capillary, the concentration of DMFc is high and concentration of HTB is low. With opposite situation inside the capillary, an important concentration of acid for a small concentration of DMFc. The speed of reaction in the two solutions might be quite different, with a much faster reaction inside the capillary where the concentration of acid is important compared to the small concentration of DMFc. In Figure 3.9. the NMR spectra of the two solutions are overlapping, with the coalescent signal being a measure of the DMFc outside the capillary, and the steady signal at more negative shift being the DMFc inside the capillary.

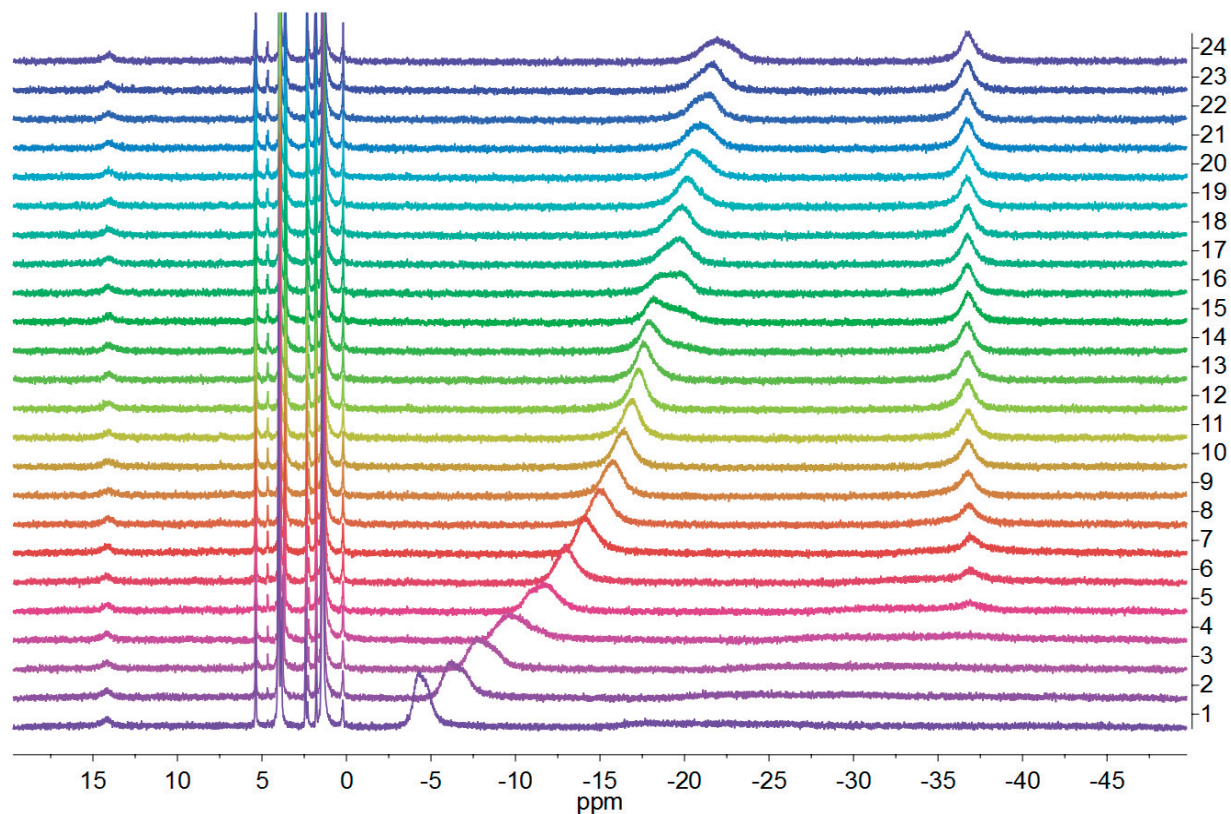


Figure 3.9. High pressure NMR of HTB and DMFc in a mixture CD_2Cl_2 and liquid CO_2 , at 60 bars and 298°K over two hours of reaction, one spectrum taken every five minutes.

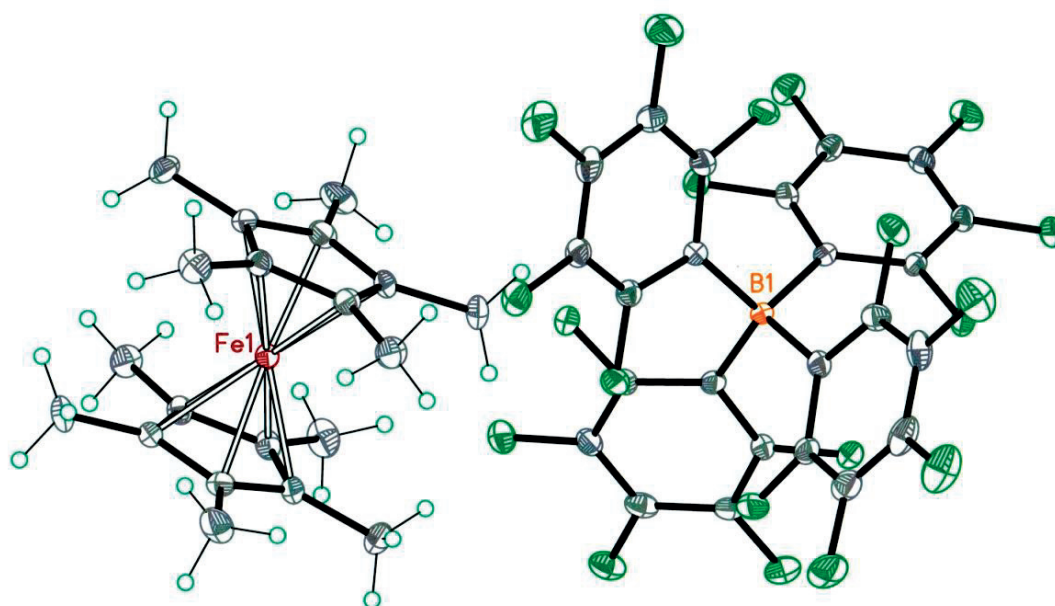


Figure 3.10. Crystal Structure of DMFc-TB at 140°K , orthorhombic lattice system.

These NMR experiments demonstrate the existence of a reaction between the DMFc hydride and CO₂, which is faster than the bimolecular process for hydrogen generation. But no product of CO₂ reduction has been highlighted by this technique. Formate should be easily identified by NMR due to its particular chemical shift of 8.44 ppm. But no peak is detected in this range of the NMR spectra.

3.5. Conclusions

Decamethylferrocene has been demonstrated to be a potential reductive agent for carbon dioxide. Its complete oxidation is observed in the suitable conditions with anions polarizing the interface to transfer protons to the supercritical phase containing the DMFc. The reduction of CO₂ by DMFc highlights the advantages of using supercritical carbon dioxide as solvent and reactant. The large excess of carbon dioxide orientates the reaction selectively toward CO₂ reduction rather than hydrogen evolution. The reduction of CO₂ appears to be conducted at moderate potentials while the most famous CO₂ reduction catalysts operate at very negative potentials.

Efficiency of the reaction suffers however several limitations leading to a maximal effective conversion yield of DMFc into formate of 4%. The major limitation is believed to be the presence of oxygen in the reactor as it is successively reduced by the DMFc hydride to produce hydrogen peroxide and water. Other products are potentially formed as experiments demonstrate a consumption of formate coupled to the oxidation of DMFc. To be detected these products need better detection methods or higher concentrations of products. As DMFc is used as a sacrificial reagent, the amount of product generated is limited by DMFc solubility in scCO₂. The oxidation of DMFc is a simple and reversible reaction, therefore regeneration of the DMFc and making CO₂ reduction catalytic may be a way to enhance the amount of product generated and coupled with better analytic techniques other products could be detected, and therefore new insight on reaction mechanism could be found.

3.6. Bibliography

1. Koelle, U., P.P. Infelta, and M. Graetzel, *Kinetics and mechanism of the reduction of protons to hydrogen by cobaltocene*. Inorganic Chemistry, 1988. **27**(5): p. 879-883.
2. Kunkely, H. and A. Vogler, *Water splitting by light with osmocene as photocatalyst*. Angewandte Chemie International Edition, 2009. **48**(9): p. 1685-1687.
3. Mendez, M.A., et al., *Molecular electrocatalysis at soft interfaces*. Physical Chemistry Chemical Physics, 2010. **12**(46): p. 15163-15171.
4. Karlsson, A., G. Hilmersson, and P. Ahlberg, *Iron diprotonated [1.1] ferrocenophane generated in super-acid and directly observed by NMR spectroscopy*. Journal of physical organic chemistry, 1997. **10**(7): p. 590-592.
5. Mueller-Westerhoff, U.T. and A. Nazzari, *[1.1]Ferrocenophanes as effective catalysts in the photoelectrochemical hydrogen evolution from acidic aqueous media*. Journal of the American Chemical Society, 1984. **106**(18): p. 5381-5382.
6. Hatay, I., et al., *Hydrogen Evolution at Liquid-Liquid Interfaces*. Angewandte Chemie, 2009. **121**(28): p. 5241-5244.
7. Rivier, L., et al., *Decamethylruthenocene Hydride and Hydrogen Formation at Liquid-Liquid Interfaces*. The Journal of Physical Chemistry C, 2015. **119**(46): p. 25761-25769.
8. Hundhammer, B. and T. Solomon, *Determination of standard Gibbs energies of ion partition between water and organic solvents by cyclic voltammetry: Part I*. Journal of Electroanalytical Chemistry and Interfacial Electrochemistry, 1983. **157**(1): p. 19-26.
9. Hundhammer, B., et al., *Ion transfer across the water-o-dichlorobenzene interface*. Journal of Electroanalytical Chemistry and Interfacial Electrochemistry, 1991. **319**(1-2): p. 125-135.
10. Olaya, A.J., et al., *Voltammetric determination of extreme standard Gibbs ion transfer energy*. Journal of Electroanalytical Chemistry, 2010. **644**(1): p. 60-66.
11. Sabela, A., et al., *Standard Gibbs energies of transfer of univalent ions from water to 1,2-dichloroethane*. Electrochimica Acta, 1992. **37**(2): p. 231-235.
12. Bitterwolf, T.E. and A.C. Ling, *Metallocene basicity : II. Reaction of the ferrocenonium cation with O₂ and SO₂*. Journal of Organometallic Chemistry, 1972. **40**(1): p. C29-C32.
13. McKee, M.L., *Computational study of ring- and metal-protonated ferrocene*. Journal of the American Chemical Society, 1993. **115**(7): p. 2818-2824.
14. Bouwkamp, M.W., *The coordination chemistry of decamethylmetallocene cations of trivalent transition metals* 2004: University Library Groningen.
15. Varotto, A., et al., *Self-organization of a new fluorinated porphyrin and C60 films on indium-tin-oxide electrode*. Chemical Communications, 2008(40): p. 4921-4923.
16. Jameson, D.L. and R. Anand, *Examination of Electron Transfer Self-Exchange Rates Using NMR Line-Broadening Techniques: An Advanced Physical Inorganic Laboratory Experiment*. Journal of Chemical Education, 2000. **77**(1): p. 88.
17. Nielson, R.M., et al., *Solvent and electrolyte effects on the kinetics of ferrocenium-ferrocene self-exchange. A reevaluation*. The Journal of Physical Chemistry, 1989. **93**(5): p. 2152-2157.

CHAPTER 4

Photocatalytic reduction by nickel cyclam in biphasic systems

4.1. Introduction

In this chapter, the water-scCO₂ biphasic system previously used in chapter 3 is evaluated for reducing CO₂ using an aqueous catalyst, nickel(II)-1,4,8,11-tetraazacyclotetradecane (Ni(II)cyclam), previously introduced in section 1.2.4. In the previous chapter, CO₂ reduction was conducted on the metallic centre of a complex dissolved in the supercritical phase. This complex was used as a sacrificial reagent, which limits the amount of product that can be obtained. The strategy in this present chapter is to drive the reaction catalytically with a sacrificial electron donor, sodium ascorbate, being consumed. The electrons are transferred to the catalyst *via* a photosensitizing system composed of Ru(bpy)₃.

This catalyst was pioneered by Tinnemans [1] and the mechanism of the catalytic reduction of CO₂ was initially studied electrochemically by Sauvage [2] and photochemically by Calvin [3]. This catalyst has been reported to evolve carbon monoxide and formate with moderate selectivity. The advantages of using supercritical conditions will be evaluated by

determining the improvement in catalytic turnover and selectivity when the reaction is driven in supercritical conditions. It is necessary to mention here that some parts of the present chapter were published as [4].

4.2. Voltammetry of catalyst and photosensitizer

To confirm the activity of the catalyst toward CO₂ reduction, electrochemical characterization of the catalyst under normal conditions of pressure were carried out. With this purpose, cyclic voltammograms were obtained in absence and presence of CO₂. The voltammograms are shown in Figure 4.1. In absence of CO₂, a reduction wave corresponding to the [Ni(II)cyclam]²⁺/[Ni(I)cyclam]⁺ couple is observed. This wave appears to be not fully reversible, but analysis is rather difficult as the wave is at the limit of the potential window in aqueous solutions. In presence of CO₂, a marked increase in the cathodic current in addition of a shift of the signal towards less negative values of potential are observed. This behaviour is in accordance with an electrocatalytic reductive process. The anodic wave observed at 0.85 V vs SHE correspond to the reversible oxidation of [Ni(II)cyclam]²⁺ to [Ni(III)cyclam]³⁺. Comparing voltammograms of the catalyst and the photosensitizer shows that the electron transfer from the photosensitizer to the catalyst is possible as the reduction [Ru(bpy)₃]²⁺ happens at more negative potentials. But, the driving force of the electron transfer is suspected to be quite small as the potential difference between the half-wave potential is only 70 mV, therefore the electron transfer step might limit the rate of the catalytic cycle.

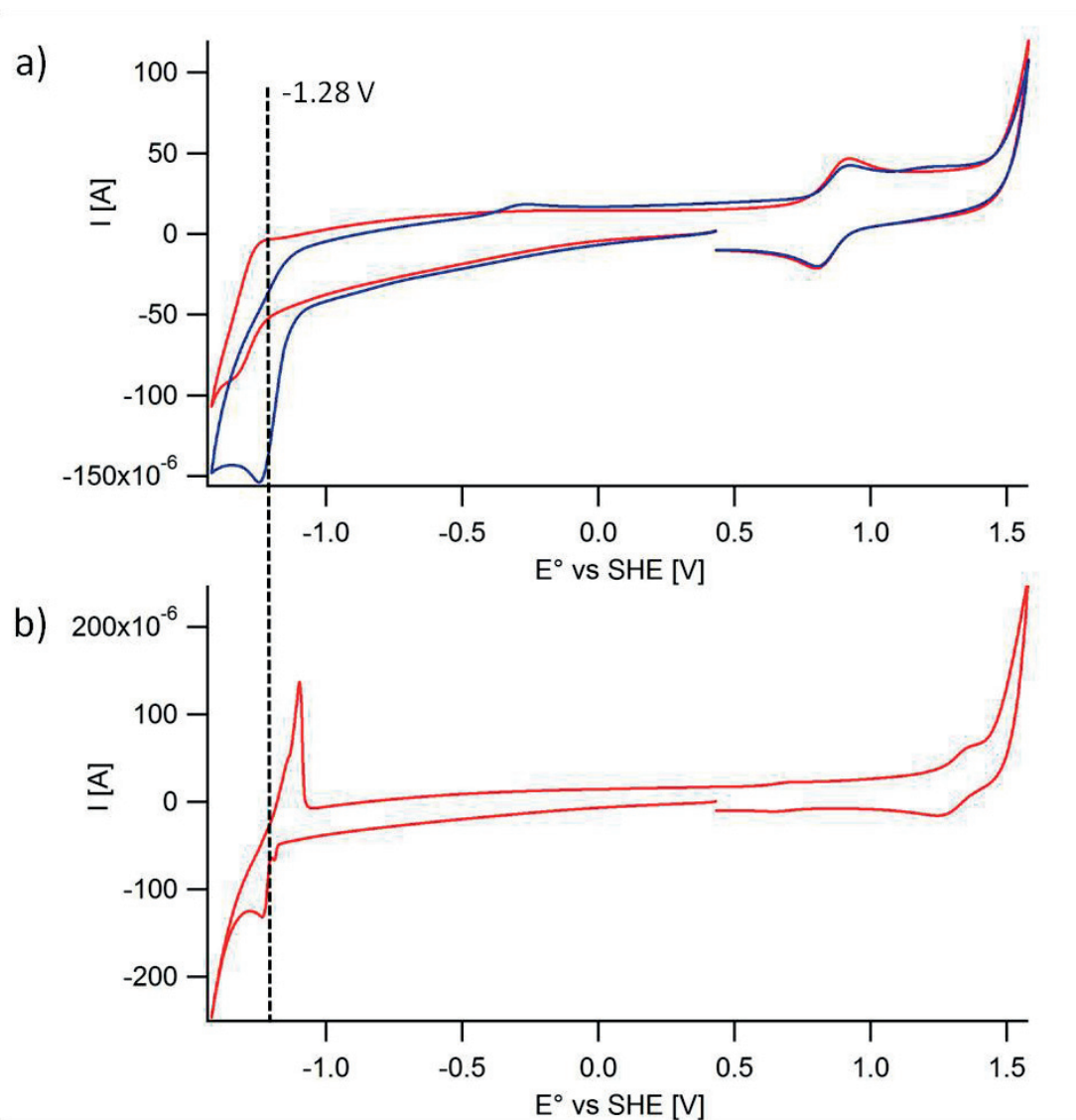


Figure 4.1. Cyclic voltammetry of a) [Ni(II)cyclam]Cl₂ 2mM in absence (red) and in presence (blue) of CO₂ and b) [Ru(bpy)₃]Cl₂ 2mM in KCl 0.1M over a glassy carbon disk electrode (0.13cm²), scan rate = 100mVs⁻¹, CE = Pt, RE = Ag/AgCl (KCl 3M).

4.3. Photocatalytic reduction of CO₂

Photocatalytic reduction experiments were conducted following the procedures described in section 2.3.5 of chapter 2. Results of comparative experiments in which the reaction time

and pressure were varied while keeping constant the concentration of all components are summarized in Figure 4.2. A seven-fold increase in the activity of the catalyst is observed for a pressure increase from 44 to 144 bar for a fixed time of reaction of 4 hours (inset). Only the production of carbon monoxide is determined, as the detection of formate by ionic chromatography was impossible due to the large concentration of ascorbate overlapping with the formate peak.

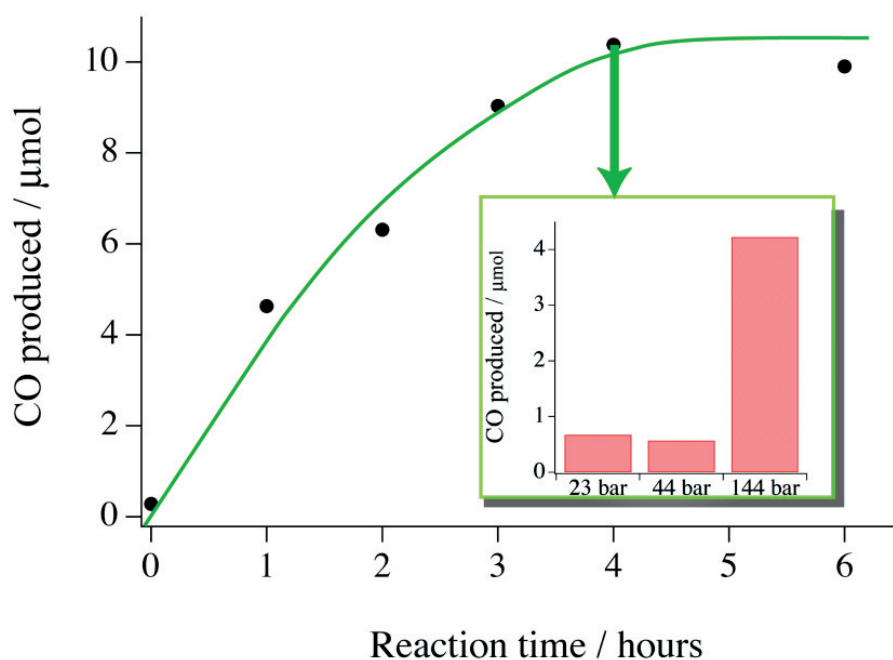


Figure 4.2. CO production as a function of irradiation time. 18 μmol PS, 4.5 μmol Ni(II)cyclam and 3 mmol Asc at 313 °K and 144 bars. Inset presents comparative data after 4 h of reaction at various pressures with 4.5 μmol PS, 18 μmol Ni(II)cyclam and 3 mmol Asc.

The increase in pressure is indeed causing an increase in CO_2 concentration in the water phase, with approximated concentrations of CO_2 in water of 0.5 M at 23 bars, 1 M at 44 bars and 1.4 M at 144 bars [5]. The increase in concentration is highly similar between 23 and 44 bars as it is between 44 and 144 bars. As the increase in concentration from 0.5 to 1 M is not affecting the production of carbon monoxide, it suggests that the productivity at 144 bars is increased by another effect than merely the increase in concentration of CO_2 . The introduction of the water-sc CO_2 in the system could be the main advantage provided by the

high pressures conditions. The nickel complex is rather hydrophobic and is likely to adsorb at the interface, where it is in contact with CO₂ and protons in significant concentrations. Metallic macrocycles are usually surface active in solvent extraction [6] and cobalt porphyrins have been shown to reduce oxygen at water|1,2-dichloroethane interface indicating they are surface-active [7]. Besides, protein adsorption at the water-scCO₂ interface has been reported as a pressure-dependent process [8].

It is clear from Figure 4.2. that the system cannot sustain the reaction indefinitely. Limitations come from either building up concentration of carbon monoxide in the reactor that can poison the catalyst, as reported by Hori for a rhenium catalyst [9, 10], or from the degradation of the catalyst or the photosensitizer, instability of [Ru(bpy)₃]²⁺ in water is well known [11, 12], and was additionally observed in cyclic voltammogram in Figure 4.1. Indeed, two reduction waves were observed with only a single peak-shaped reverse wave. In organic solvents, however, three successive and reversible reduction waves of [Ru(bpy)₃]²⁺ can be observed corresponding to the reduction of the three bipyridyl ligands.

4.4. pH effect on the reactivity

Another key point in the efficiency of the system is the pH of the aqueous solution. From the catalytic mechanism shown in Figure 1.12 of section 1.2.4., one proton is required for the reduction of CO₂ into CO. Therefore the catalytic rate can be improved by lower pH values. But, in the other hand, the catalyst can also evolve hydrogen from aqueous protons, causing the catalytic selectivity for CO₂ reduction to decrease in lower pH conditions. Hence, the determination of the pH as a function of the CO₂ pressure in the reactor was carried out by spectrophotometric determination using bromophenol blue and bromocresol purple as indicators following the procedures described in section 2.3.3. Bromophenol blue was employed in the case where the aqueous phase did not contain any pH buffer. As it can be observed in Figure 4.3, an important decrease, down to 3.5, in the pH is confirmed. The values of pH are determined using the following equation:

$$\text{pH} = \text{Log}_{10} \left(\frac{A(595\text{nm})}{A(438\text{nm})} \right) + pK_a + \text{Log}_{10} \left(\frac{\varepsilon_{A^-}^{595}}{\varepsilon_{HA}^{438}} \right) \quad (4.1)$$

where $A(595\text{nm})$ and $A(438\text{nm})$ are the absorbance of the solution at 595 and 438 nm. These two wavelengths correspond to the absorbance maxima of the non-protonated and protonated indicator respectively, with $\varepsilon_{A^-}^{595}$ and ε_{HA}^{438} being the extinction coefficients of the non-protonated and protonated indicator at their absorbance maxima.

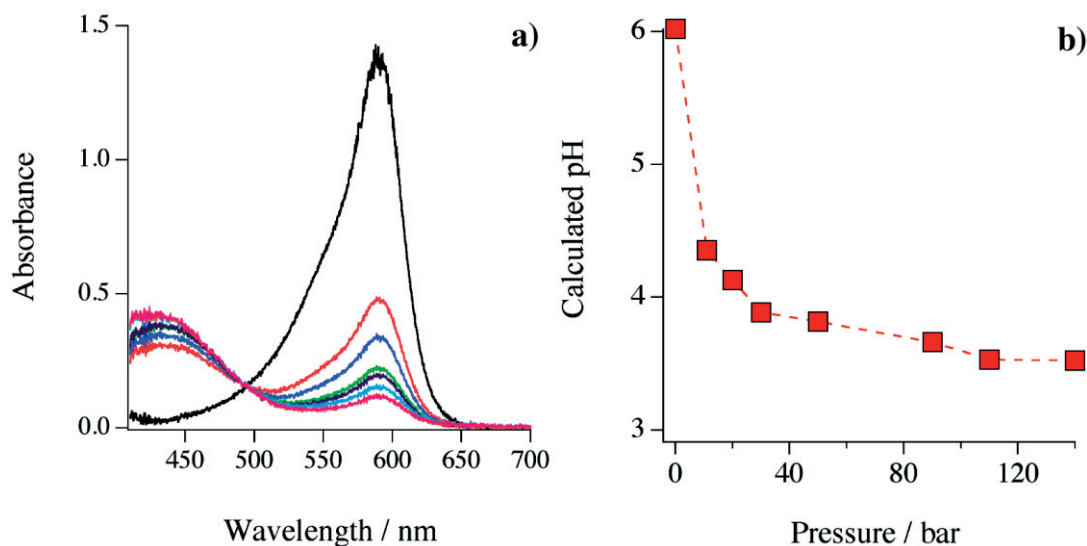


Figure 4.3. a) Visible spectra of an aqueous solution of bromophenol blue 2×10^{-5} M at pressures of 1 (black), 11, 20, 30, 50, 90, 110 and 140 bar (purple). (b) pH as a function of pressure.

In presence of sodium ascorbate 0.5 M, the pH remains slightly above 5 as seen in Figure 4.4, due the buffering capability of sodium ascorbate. Therefore sodium ascorbate has a double-purpose in the reaction: 1) acting as a sacrificial electron donor and 2) acting as pH buffer. The difference in productivity observed in Figure 4.2 is therefore not explained by an increase in proton concentration either.

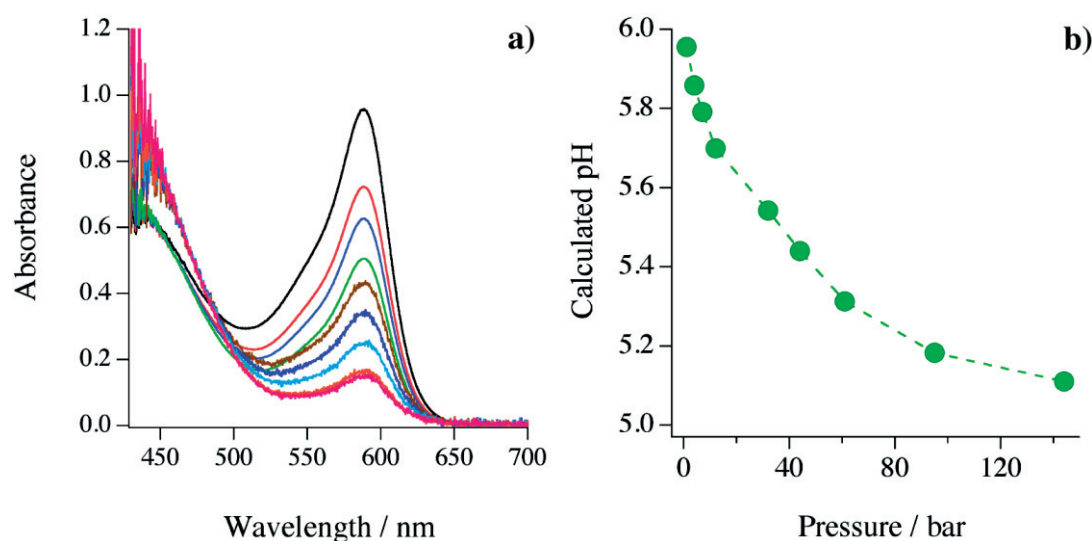


Figure 4.4. (a) Visible spectra of an aqueous solution of ascorbate 0.5 M and bromocresol purple 2×10^{-5} M at pressures of 1, 4, 7, 12, 32, 44, 61, 95 and 144 bar. (b) pH as a function of pressure.

Experiments, in which the pH of the aqueous phase at 144 bars was varied, by controlling the ratio ascorbic acid/ascorbate in the aqueous phase showed that the amount of CO produced is lower for aqueous pH 3 but is similar for pH 4 and 5, as seen in Figure 4.5. At the same time, H₂ production was determined to be maximum at around pH 4, which is in good agreement with the results found by Grant[11]. Although there are some discrepancies in the results published concerning H₂ evolution, most of the reports for this catalytic cycle in water show that H₂ is produced in approximately equal or higher amounts than CO[11, 13, 14]. In the present biphasic system, the comparison of the amounts of H₂ and CO produced clearly indicates that the reaction proceeds more selectively towards CO₂ reduction at all pH values tested, and optimal operation conditions are attained at pH 5. Previous reports at pH 5 estimated the ratio CO/H₂ to be 0.83[11] whereas this ratio is here determined to be 7.1, representing an enhancement in the selectivity of 8.6 times.

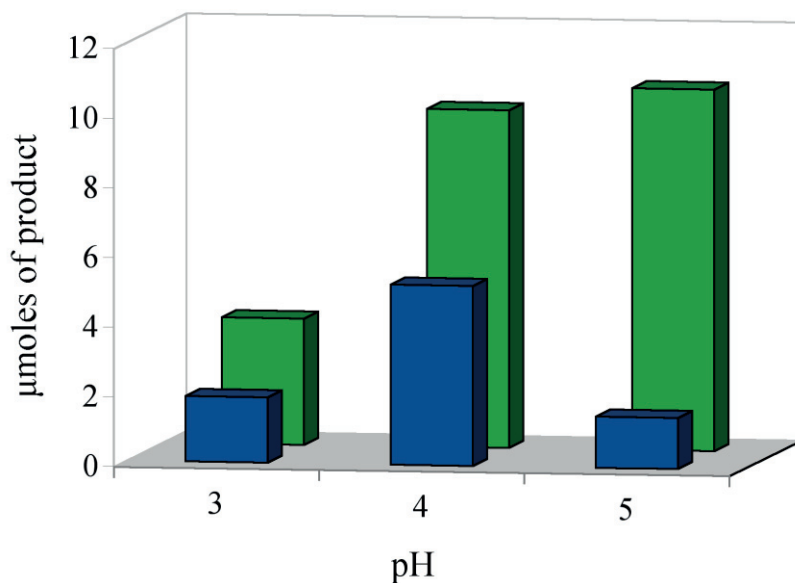


Figure 4.5. CO (green) and H₂ (blue) production as a function of the aqueous pH value at 144 bar and 313 °K. Irradiation time=4 h, 18 μmol PS and 4.5 μmol Ni(II)cyclam.

4.5. Interfacial tension measurement

To confirm the hypothesis of an interfacial reaction, surface tension measurements as a function of the aqueous concentration of Ni(II)cyclam were conducted to attest the adsorption of catalyst at the interface. In a first step, experiments were conducted on the air-water interface with a Wilhelmy plate following the procedures described in section 2.3.7. Surface excess concentration of the catalyst, Γ_{NiCyc} ($\mu\text{mol}\times\text{m}^{-2}$), was determined from the surface tension and the catalyst bulk concentration C_{NiCyc} according to the Gibbs equation:

$$\Gamma_{NiCyc} = -\left(\frac{d\gamma}{d\mu_{NiCyc}}\right)_{T,p,\mu_j} = -\frac{1}{RT}\left(\frac{d\gamma}{d\ln a_{NiCyc}}\right)_{T,p,\mu_j} \approx -\frac{1}{RT}\left(\frac{d\gamma}{d\ln C_{NiCyc}}\right)_{T,p,\mu_j} \quad (4.2)$$

Measurements with the Wilhelmy plate revealed that adsorption of the catalyst does take place and follows a Langmuir-type behaviour as shown in Figure 4.6. A standard Gibbs energy of adsorption for Ni(II)cyclam at the air-water interface and maximum surface

coverage are found to be $-10 \text{ kJ}\cdot\text{mol}^{-1}$ and $1.09 \text{ }\mu\text{mol}\cdot\text{m}^{-2}$ respectively, which is in agreement with the relatively weak adsorption of this complex.

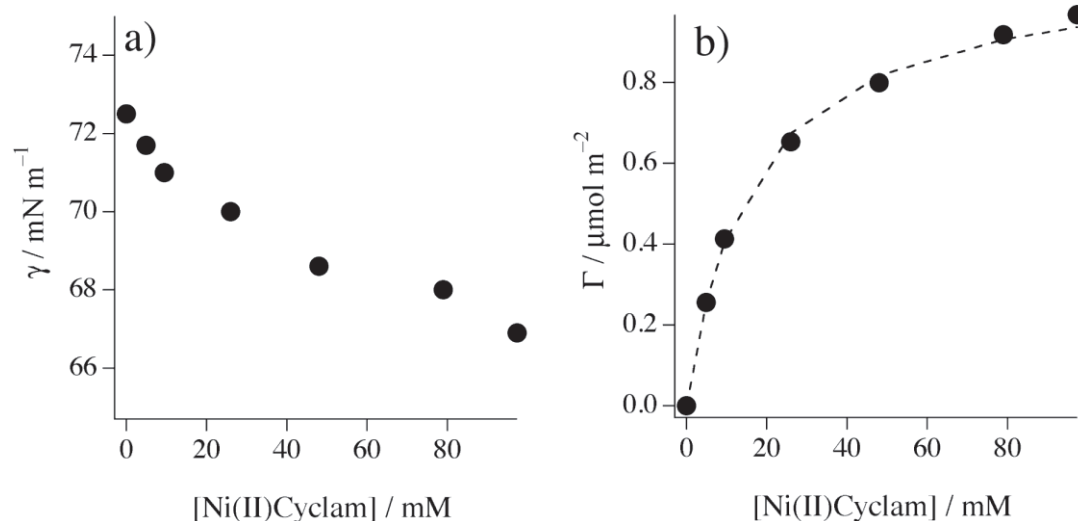


Figure 4.6. (a) Air–water interfacial tension as a function of the Ni(II)cyclam aqueous concentration. (b) Surface excess concentrations calculated from the Gibbs adsorption equation (solid circles). Fitting to a Langmuir isotherm is presented in dashed lines.

The maximum surface coverage can be analogously expressed as the area occupied per molecule at the interface, yielding a value of 152 \AA^2 per molecule of complex adsorbed. The latter indicates that complex molecules adsorbed at the water-air interface assume more likely a planar geometry.

As adsorption of Ni(II)cyclam occurs at the water-air interface, this is also very likely to occur at the water-scCO₂ interface. The custom-built pendant drop setup described in section 2.3.8 was employed to compare drop profile between pure water and a 50mM Ni(II)cyclam aqueous solution.

Illustration of the droplets obtained is presented in Figure 4.7. from which it can be observed a slight elongation of the droplet in presence of Ni(II)cyclam 50mM which is equally observed once the profile is extracted. From these, and using the selected plane method for determining the interfacial tension previously described by Andreas *et al.* [15], the parameter S was determined according to:

$$S = \frac{d_s}{d_E} \quad (4.3)$$

where d_E is diameter at the equator and d_s the diameter of the droplet in a parallel plane located at a distance d_E from the apex defined as the point where the axis of rotation cuts the drop. Thus, in absence of Ni(II)cyclam an average value for S of 0.517 is obtained while in presence of the catalyst this value shifted to 0.537.

According to the theory, the shape of a static pendant drop can be described by the Laplace equation:

$$\frac{d\theta}{dS} = 2 - \beta Y - \frac{\sin(\theta)}{X} \quad (4.4)$$

This equation can be numerically solved by combining it with the following two equations :

$$\frac{dX}{dS} = \cos(\theta) \quad (4.5)$$

$$\frac{dY}{dS} = \sin(\theta) \quad (4.6)$$

where $d\theta/dS$ is the radius of curvature, S the normalized radius of curvature (s/b), $X=x/b$, $Y=y/b$ and the normalization constant, b , is the curvature at the apex of the droplet.

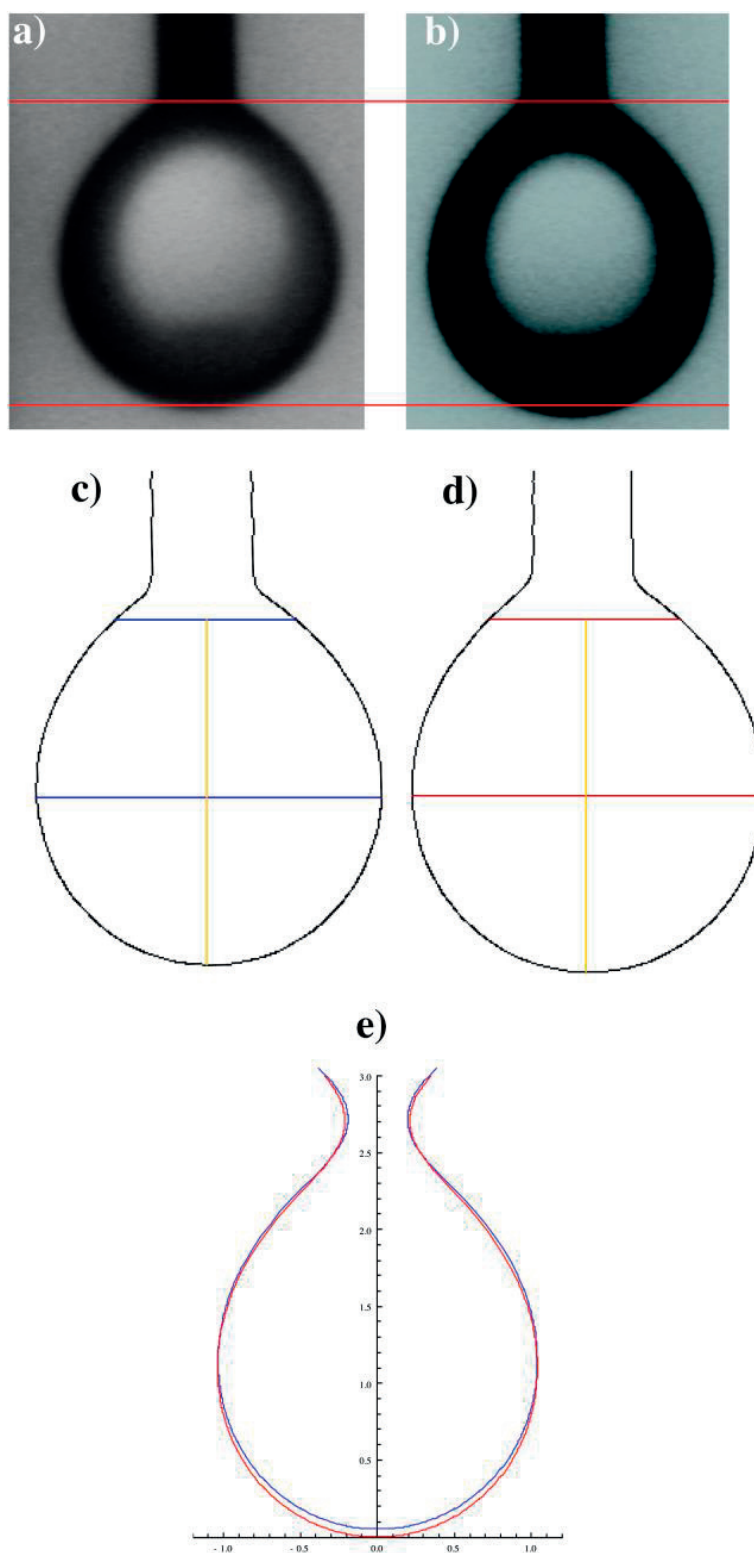


Figure 4.7. Image of the aqueous droplet a) in absence and b) in presence of the Ni(II)cyclam at a concentration of 50mM, c) and d) profiles extracted using Mathematica after applying Shen-Castan algorithm, e) theoretical profiles calculated from the parameter S obtained for c) is presented in blue and for d) in red.

A useful dimensionless parameter, β , is defined as follows:

$$\beta = \frac{\Delta\rho g b^2}{\gamma} \quad (4.7)$$

where γ is the interfacial tension, g the gravitational constant, and $\Delta\rho$ the effective density of the drop, *i.e.* the density difference between water and scCO₂ in this particular case. Herein, the polynomial approximation proposed by Girault *et al.* [16] is used in order to determine the parameter β .

$$\beta = 0.02664 + 0.62945S^2 \quad (4.8)$$

Applying equation (14) to the values of S previously found for the two cases, β is estimated to be equals to 0.195 in the absence and 0.208 in the presence of Ni(II)cyclam. The theoretical profiles presented in Figure 4.7.e) were determined taking into account the values for β aforementioned. Qualitatively comparable elongation of the droplet is observed in the theoretical and experimental drop profiles. Additionally, if one assumes curvature radius at the apex, b , remains approximately constant for both cases, then:

$$\frac{\beta_{H_2O}}{\beta_{NiC}} \approx \frac{\gamma_{NiC}}{\gamma_{H_2O}} = 1.067 \quad (4.9)$$

Meaning that the water-scCO₂ interfacial tension diminishes by approximately 6.7% when Ni(II)cyclam is present at a concentration of 50mM. Analogously a decrease of 5.7% in the air-water interfacial tension is obtained when the surface tensions of pure water and aqueous solution 50 mM of Ni(II)cyclam are compared. These data demonstrate that the catalyst is adsorbing at the interface.

In consequence, it is reasonable to consider that in the present system, Ni(I)cyclam complexes also adsorb at the water-scCO₂ interface, as being even more hydrophobic than the Ni(II)cyclam complex. Both complexes probably assume a planar configuration at the interface, in accordance to the experiments described above. The latter can have a crucial impact on the CO₂ reduction reaction, since binding of CO₂ on Ni(II)cyclam would be largely favoured in a CO₂-rich environment.

The interface is therefore considered to be the key in the explanation of the seven-fold increase in productivity under supercritical conditions, as adsorption of the catalyst at this interface is proven. It is therefore rational to consider that most of the carbon monoxide is produced at the interface. Figure 4.8. presents the reaction mechanism, where the interface is locus of the reduction of CO₂.

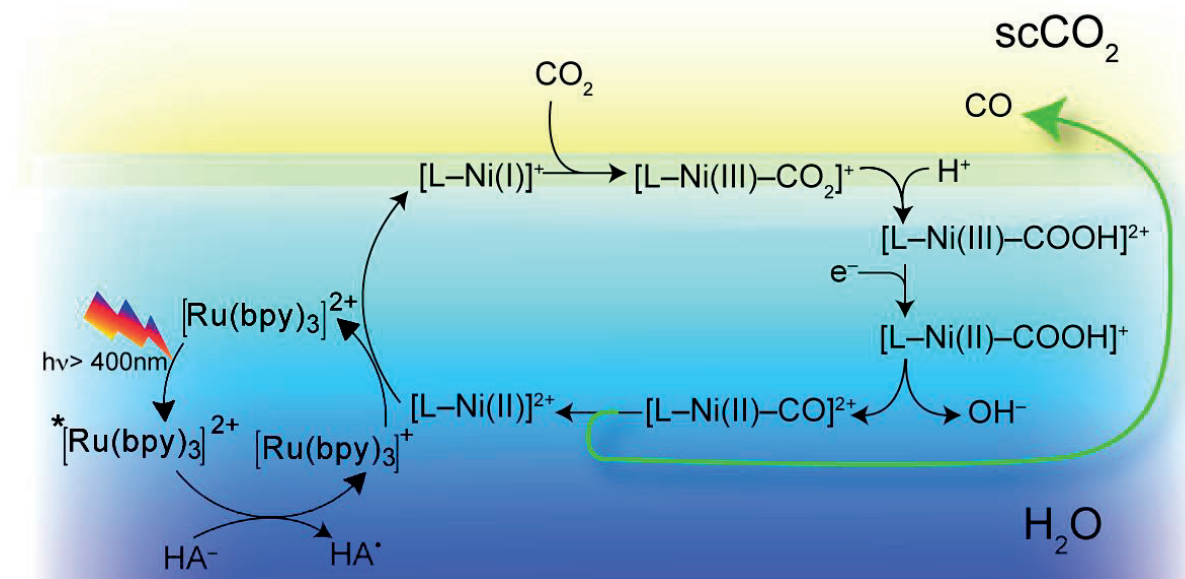


Figure 4.8. Catalytic cycle proposed for the photoreduction of CO₂ using [Ni(II)cyclam] as catalyst in a water–supercritical CO₂ biphasic system.

This mechanism presents two electrochemical cycles, one for the photosensitizer and one for the catalyst, connected together. For the catalytic cycle, only the first involved electron is represented coming from the photosensitizer, but the second one is very likely transferred from a similar cycle.

A common method for comparing the efficiency of the catalyst is by measuring its turnover number, calculated as the molar ratio of CO₂ reduction products to the initial amount of catalyst as explained in section 1.2.2. From the result of Figure 4.2., a *TON* of 1.7 is determined for initial concentrations of catalyst and photosensitizer of 0.5 and 2 mM respectively. As the electron transfer between the photosensitizer and the catalyst appears to be the rate-limiting step, *TON* is increased to 3.5 for a catalyst concentration of 0.1 mM. If we consider that the increase in production yield is caused by the interfacial reaction, the bulk

production of CO for the three different pressure conditions in Figure 4.2. can be considered similar. Therefore in supercritical conditions, the bulk production accounts for only up to 20% of the global carbon monoxide production, therefore 80% is formed at the interface. From the Wilhelmy plate experiment the surface concentration of Ni(II)cyclam in the reactor can be estimated to be around $0.1 \mu\text{mol}\cdot\text{m}^{-2}$ for a bulk concentration of 0.5 mM. For an interface of 10 cm^2 in the reactor, the amount of catalyst adsorbed at the interface is only 0.1 nmol. Considering the same total production of $10.4 \mu\text{mol}$ as for the bulk turnover calculation the turnover number for the adsorbed molecules reached finally 80'000 in four hours of reaction, or 5.5 cycles per second. This number has to be considered carefully, indeed it represents a turnover number per site on the interface rather than a turnover number per molecule, as under vigorous stirring the exchange between bulk catalyst and adsorbed catalyst is presumed to be rather fast.

Some points, such as stirring, interface area, or portion of light shining on the interface can be keys point in the efficiency of the system.

4.6. Conclusions

In summary, this chapter demonstrates that it is possible to reduce super-critical CO₂ using adsorbed Ni(II)cyclam catalysts and that this reduction is more selective to CO production than when carried out simply in water. Under supercritical conditions, the yield and selectivity are increased respectively 7 and 8-folds. The recycling of the catalyst and its reduction by an aqueous sensitizer occurs homogeneously whereas the CO₂ binding process is more likely to occur at the interface. This work clearly shows that the classical Ni(II)cyclam-Ru(bpy)₃-ascorbate photocatalytic cycle becomes much more efficient and selective when carried out at elevated pressures, corroborating the hypothesis that the CO₂ binding step is an interfacial process.

4.7. Bibliography

1. Tinnemans, A.H.A., et al., *Tetraaza-macrocyclic cobalt(II) and nickel(II) complexes as electron-transfer agents in the photo(electro)chemical and electrochemical reduction of carbon dioxide*. Recueil des Travaux Chimiques des Pays-Bas, 1984. **103**(10): p. 288-295.
2. Beley, M., et al., *Nickel (II)-cyclam: an extremely selective electrocatalyst for reduction of CO₂ in water*. Journal of the Chemical Society, Chemical Communications, 1984(19): p. 1315-1316.
3. Grant, J.L., et al., *Photochemical reduction of carbon dioxide to carbon monoxide in water using a nickel (II) tetra-azamacrocyclic complex as catalyst*. Journal of the Chemical Society, Dalton Transactions, 1987(9): p. 2105-2109.
4. Méndez, M.A., P. Voyame, and H.H. Girault, *Interfacial photoreduction of supercritical CO₂ by an aqueous catalyst*. Angewandte Chemie, 2011. **123**(32): p. 7529-7532.
5. Duan, Z. and R. Sun, *An improved model calculating CO₂ solubility in pure water and aqueous NaCl solutions from 273 to 533 K and from 0 to 2000 bar*. Chemical Geology, 2003. **193**(3-4): p. 257-271.
6. Traylor, T.G., et al., *High-yield epoxidations with hydrogen peroxide and tert-butyl hydroperoxide catalyzed by iron(III) porphyrins: heterolytic cleavage of hydroperoxides*. Journal of the American Chemical Society, 1993. **115**(7): p. 2775-2781.
7. Partovi-Nia, R., et al., *Proton Pump for O₂ Reduction Catalyzed by 5,10,15,20-Tetraphenylporphyrinatocobalt(II)*. Chemistry – A European Journal, 2009. **15**(10): p. 2335-2340.
8. Tewes, F. and F. Boury, *Formation and Rheological Properties of the Supercritical CO₂-Water Pure Interface*. The Journal of Physical Chemistry B, 2005. **109**(9): p. 3990-3997.
9. Hori, H., et al., *Rhenium-Mediated Photochemical Carbon Dioxide Reduction in Compressed Carbon Dioxide*. Chemistry Letters, 2000. **29**(5): p. 522-523.
10. Hori, H., et al., *High-pressure photocatalytic reduction of carbon dioxide using [fac-Re(bpy)(CO)₃P(OiPr)₃]⁺ (bpy = 2,2'-bipyridine)*. Journal of Molecular Catalysis A: Chemical, 2002. **179**(1-2): p. 1-9.
11. Grant, J.L., et al., *Photochemical reduction of carbon dioxide to carbon monoxide in water using a nickel(II) tetra-azamacrocyclic complex as catalyst*. Journal of the Chemical Society, Dalton Transactions, 1987(9): p. 2105-2109.
12. Lehn, J.-M. and R. Ziessel, *Photochemical reduction of carbon dioxide to formate catalyzed by 2,2'-bipyridine- or 1,10-phenanthroline-ruthenium(II) complexes*. Journal of Organometallic Chemistry, 1990. **382**(1-2): p. 157-173.
13. Kimura, E., et al., *A new nickel(II) cyclam (cyclam = 1,4,8,11-tetraazacyclotetradecane) complex covalently attached to tris(1,10-phenanthroline)ruthenium(2+). A new candidate for the catalytic photoreduction of carbon dioxide*. Inorganic Chemistry, 1992. **31**(22): p. 4542-4546.

14. Kimura, E., et al., *New Series of Multifunctionalized Nickel(II)-cyclam (cyclam = 1,4,8,11-Tetraazacyclotetradecane) Complexes. Application to the Photoreduction of Carbon Dioxide*. *Inorganic Chemistry*, 1994. **33**(4): p. 770-778.
15. Andreas, J.M., E.A. Hauser, and W.B. Tucker, *BOUNDARY TENSION BY PENDANT DROPS I*. *The Journal of Physical Chemistry*, 1937. **42**(8): p. 1001-1019.
16. Girault, H.H.J., D.J. Schiffrin, and B.D.V. Smith, *The measurement of interfacial tension of pendant drops using a video image profile digitizer*. *Journal of Colloid and Interface Science*, 1984. **101**(1): p. 257-266.

CHAPTER 5

Photocatalytic reduction by $[\text{Ru}(\text{bpy})_2(\text{CO})\text{L}]^{n+}$

5.1. Introduction

In this chapter, in order to build a more stable and efficient photocatalytic system for CO_2 reduction than the one described in the previous chapter, the ruthenium bis-bipyridyl class of catalyst introduced in section 1.2.4 is used. The most referenced complex of this family is $[\text{Ru}(\text{bpy})_2(\text{CO})\text{L}]^{n+}$ where bpy is 2,2'-bipyridine and L is a hydride or a carbonyl ligand. In this chapter only the catalyst $[\text{Ru}(\text{bpy})_2(\text{CO})\text{H}]^+$ will be used in experiments. This catalyst is reported to evolve carbon monoxide and formate through two different catalytic cycles as described in Figure 5.1.

Carbon monoxide is produced following the mechanism proposed by Tanaka *et al.* [1-4], the initial step is the localised reduction of $[\text{Ru}(\text{bpy})_2(\text{CO})_2]^{2+}$ (compound (8) in Figure 5.1.) at the bpy ligand, occurring at -1.20 V vs. saturated calomel electrode (SCE) in aqueous solution. These surplus electrons in the π^* orbital of the bipyridyl redistribute across the metal centre and the σ^* orbital of the Ru-CO bond, thus cleaving the CO molecule from the complex. In the presence of CO_2 , the now neutral penta-coordinated complex (1) is open to

electrophilic attack, resulting in a CO₂ ligand. In aqueous acidic solutions, this complex dehydrates to the starting complex, [Ru(bpy)₂(CO)₂]²⁺, completing the catalytic cycle. In the absence of water, an organic proton carrier, such as triethanolamine, might be able to protonate the bound CO₂ and induce the release of water. Another possibility is through the formation of bicarbonate from the abstraction of hydroxide by CO₂ (between 7 and 8).

Formate evolution follows a different catalytic cycle as proposed by Meyer *et al.* [5, 6] following the earlier work of Hawecker *et al.* [7]. Formate is produced by insertion of CO₂ into the hydride bond of the reduced complex (3). Release of formate follows a second reduction of the complex to generate [Ru(bpy)⁻₂(CO)]⁰ (1) a common intermediate of both cycles. This neutral complex being coordinatively unsaturated, contains an available coordination site for a new ligand. The nature of this ligand would seem to dictate the product to be ultimately formed. Hence, CO will be preferentially produced *via* direct CO₂ coordination, whereas formate predominates when a hydride intermediate is formed instead, followed by CO₂ insertion into the metal-hydride bond.

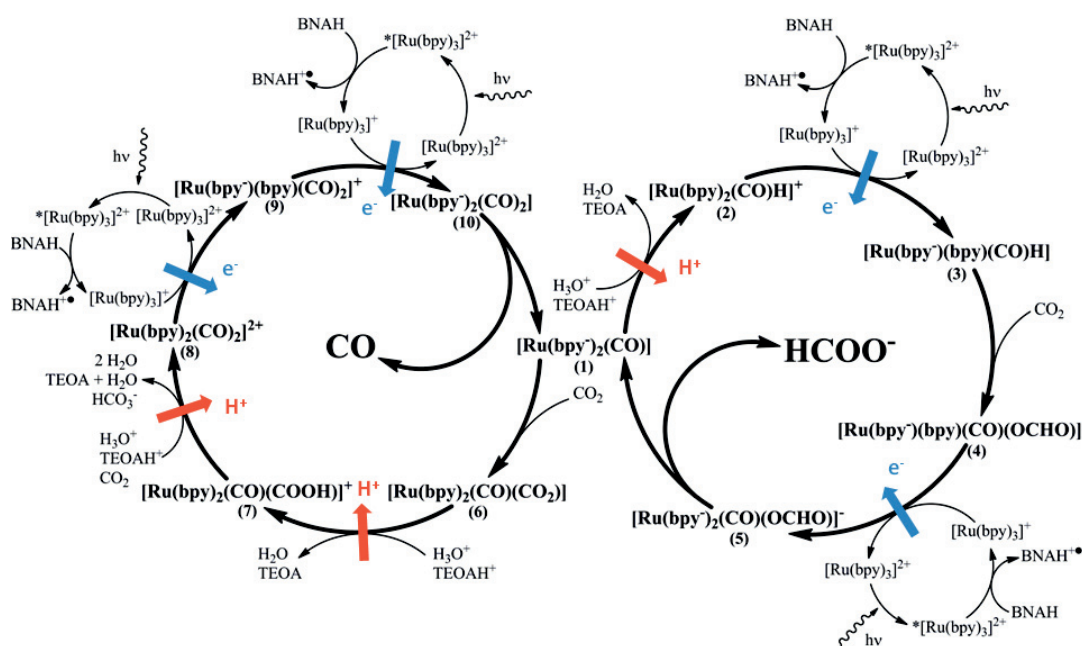


Figure 5.1. The combination of two catalytic cycles for the [Ru(bpy)₂(CO)L]ⁿ⁺ in the reduction of CO₂ to formate or carbon monoxide. The CO cycle was proposed by Tanaka *et al.* [1] and the formate cycle Meyer *et al.* [6].

As this catalyst is highly insoluble in water, a different solvent system from the two previous chapters has been used. Dimethylformamide (DMF) has been chosen as the primary solvent due to the high solubility and stability of the catalyst and the photosensitizer in this solvent. Replacing water by an organic solvent offers also the advantage of using alternative compounds to ascorbate as a sacrificial electron donor, as the most efficient quenchers for $[\text{Ru}(\text{bpy})_3]^{2+}$ are highly insoluble in water. The compound 1-benzyl-1,4-dihydronicotinamide (BNAH) has been chosen as the highest quantum yield for a system composed of the catalyst and sensitizer used in this chapter has been reported for this electron donor [8], with a quantum yield up to 15% for CO evolution and 3% for formate.

Similarly to ascorbate, once oxidized BNAH becomes a strong proton donor, which can supply the CO_2 reduction reaction in protons. But a reversible proton acceptor is required in solution to transport the proton from BNAH to the catalytic unit. In this chapter, to serve this purpose two compounds will be tested: water and the organic base triethanolamine (TEOA). When pressurized with scCO_2 , the systems DMF-water- scCO_2 and DMF-TEOA- scCO_2 have different phase equilibria. As described in section 1.3. a pure organic phase of DMF and TEOA are completely miscible with scCO_2 , while systems containing water can have one or two phases depending on the proportion of water. Single-phase systems have the advantage of an important concentration of CO_2 , while biphasic systems enable the possibility of product extraction in the upper scCO_2 phase. This can be particularly interesting for production of important amount of carbon monoxide as this compound is known to coordinate strongly to metal complexes and thus could inhibit catalytic reaction.

High-pressure photocatalytic reductions on carbon dioxide have been explored by Hori *et al.* [9, 10] but for a rhenium polypyridyl catalyst, $[\text{fac-ReCl}(\text{bpy})(\text{CO})_3]^+$. They demonstrated enhanced catalysis by a factor 5.1 at 25 atm compared to 1 atm, with enhancements in part attributed to the increased stability of the catalyst.

In this chapter, a comprehensive study on the influence of CO_2 pressure and concentration on the efficiency and productivity of the catalyst $[\text{Ru}(\text{bpy})_2(\text{CO})(\text{L})]^{n+}$ in different solvent conditions is conducted. Particular attention will be given to understand the limitations of the system on the turnover number (TON) and turnover frequency (TOF) of the

catalyst. It is important to mention here that some parts of the present chapter were published in [11].

5.2. Optimal solvent conditions

High-pressure experiments and product analyses were carried out following the procedures described in section 2.3.5 and 2.3.1. Before starting to evaluate the effect of pressure on the photocatalytic system composed of $[\text{Ru}(\text{bpy})_2(\text{CO})\text{H}]^+$ as catalyst, $[\text{Ru}(\text{bpy})_3]^{2+}$ as photosensitizer and BNAH as electron donor, attention was given to find the optimal solvent conditions, more specifically the water content of the liquid phase DMF-water. The molar fraction of water in DMF was varied from 0 to 0.85 molar ratio and the photocatalytic reaction carried out at 150 bars and 313 K for 2 hours. Quantification of carbon monoxide, formate and hydrogen were performed and results are shown in Figure 5.2. Hydrogen is not reported on the figure, as the amount detected was too low to be quantified.

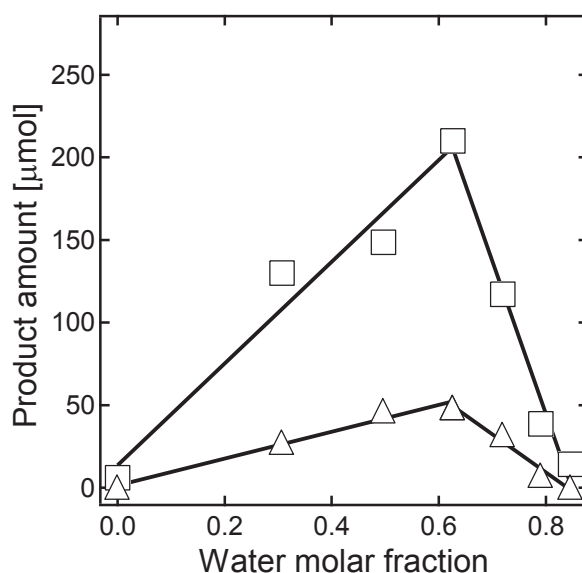


Figure 5.2. The production of CO (white square) and HCOO^- (white triangle) over 2 hours as a function of the water molar fraction in DMF. Reaction medium comprises 2 μmol catalyst ($[\text{Ru}(\text{bpy})_2(\text{CO})\text{H}][\text{PF}_6]$), 8 μmol of photosensitizer ($[\text{Ru}(\text{bpy})_3]\text{Cl}_2$), and 1 mmol BNAH. The pressure was 150 bars and temperature 313 K.

The composition of the biphasic water-DMF / scCO_2 system was monitored through the sapphire window of the reactor. Under supercritical conditions, seemingly small changes in the relative composition of the liquid phase strongly affected the reaction conditions and final composition. Without water or with only a small amount, up to 1 mL in a DMF volume of 17 mL, the liquid phase and CO_2 were completely miscible and a single phase was formed. Increasing the amount of water, but keeping the total volume of the water-DMF phase constant, changes the equilibrium. This led to a biphasic system in which the top phase is mainly scCO_2 and the bottom phase a mixture of DMF and water.

Production of both carbon monoxide and formate follows the same trend, both reaching a maximum at a water molar fraction of 0.6 (30 % water in volume). Without water, no products are formed presumably due to the absence of a proton carrier. In the presence of an excess of water, the catalyst and/or the photosensitizer are less stable, resulting in a sharp decline in productivity. Indeed, the post reaction solutions in the presence of too much or too little water were considerably darker red/orange colour than the optimum conditions. Other authors have also reported the instability of the catalyst in high water content conditions [6, 12]. Achieving a balance between CO_2 concentration and water concentration, explains the product trends in Figure 5.2. A phase separation is observed to be more favourable to CO production.

When the water is replaced by the same volume of TEOA, a single phase is observed. Figure 5.3 shows comparative results of the two different solvent systems. A similar total production is achieved for both systems, indicating similar stability of the catalyst and photosensitizer. The difference comes from the ratio of the two products, CO and HCOO^- . This difference can be explained by the different nature of the proton carrier in the solution. Referring back to Figure 5.1., at the point of the common intermediate (1), proton or CO_2 addition on the metal centre dictates the path to be followed. If proton addition is slow, addition of CO_2 into the reduced catalyst will be favoured and the main product will then be carbon monoxide.

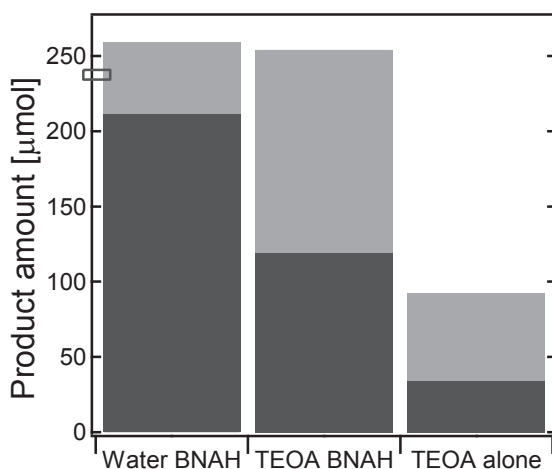


Figure 5.3. A comparison of the total product formed over 2 hours for three systems with different proton carrier (water or TEOA) and electron donor (BNAH). In dark grey is the total CO formed, and in lighter grey, the total formate. All are in the presence of DMF with 2 μmol catalyst, 8 μmol of photosensitizer, and where applicable, 1 mmol BNAH. The pressure was 150 bars and temperature 313 K.

As TEOA can also be used as sacrificial electron donor with the photosensitizer, a control experiment was performed to ensure that BNAH was acting as the electron donor. It appears that TEOA can indeed be used as quencher for the photosensitizer but the efficiency is 60% less than when BNAH is used. This indicates that in presence of BNAH and TEOA, BNAH is the dominant electron donor.

5.3. Effect of pressure

The main objective of this thesis is to investigate the effect of CO_2 pressure on the production of catalytic systems. The reactions used the optimum water volume conditions determined previously, 30% water in volume. The pressure inside the reactor was varied from 10 to 150 bars solely through the addition of pure CO_2 . The effect of CO_2 pressure is shown in Figure 5.4. The plot overlays the amount of formate, carbon monoxide and total product formed ($\text{CO} + \text{HCOO}^-$), against pressure. For carbon monoxide, production increased linearly over the pressure range. Overall, carbon monoxide production increased 120% between 10 bars and

150 bars. The formate yield remained unaffected by CO_2 pressure yielding between 50 and 60 μmol over the pressure range studied. The independence of formate production on pressure has been noted previously over the 1-10 bars range [12].

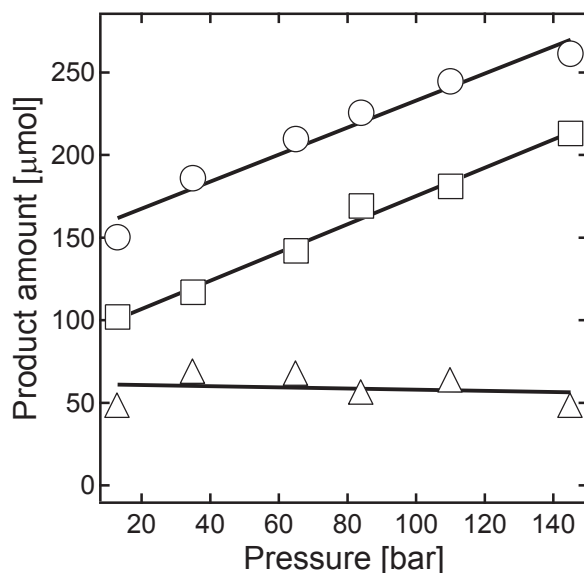


Figure 5.4. The production of CO (white square), HCOO^- (white triangle), and the total amount (white circle) over 2 hours in the water-DMF system, as a function of pressure. The molar fraction of water in DMF was 0.6 and the reaction medium consisted of 2 μmol catalyst, 8 μmol of photosensitizer, and 1 mmol BNAH. The temperature was 313 K.

These results may be explained by referring to the catalytic cycles in Figure 5.1. The most important step dictating whether formate or carbon monoxide will form occurs at the common intermediate (1), the penta-coordinated catalyst awaiting the addition of either H^+ or CO_2 . As the CO_2 pressure and concentration increase, the carbon monoxide cycle is favoured, as CO_2 is more abundant and forced into the vacant coordination site. This does not account for the steady rate of production of formate that is independent of the CO_2 pressure. Formate synthesis evidently does not compete with CO, as the CO increase is greater than the formate production, and the latter does not decrease with pressure. In the catalytic scheme, the formate cycle undergoes CO_2 insertion after the first reduction. For the formate cycle, the rate limiting step is probably the electron transfer step (2)-(3) due to the very negative redox potential required to reduce the hydride complex. For the CO cycle, the CO_2 concentration is involved

in the rate limiting step, which can be the oxidative addition of CO_2 (1)-(6) or hydroxide abstraction by proton attack or bicarbonate formation with CO_2 .

As shown in Figure 5.5., when performing the reaction in TEOA-DMF rather than in water-DMF, the overall productivity across the whole pressure range was also 250 μmol . Yet, a significant change in product distribution is depicted, as we observe formate at its highest at 10 bars and 180 μmol , declining to 130 μmol as the pressure is increased. For carbon monoxide however, the initial yield is just 20 μmol at 10 bars, but this increases linearly with pressure until 120 μmol is obtained at 150 bars.

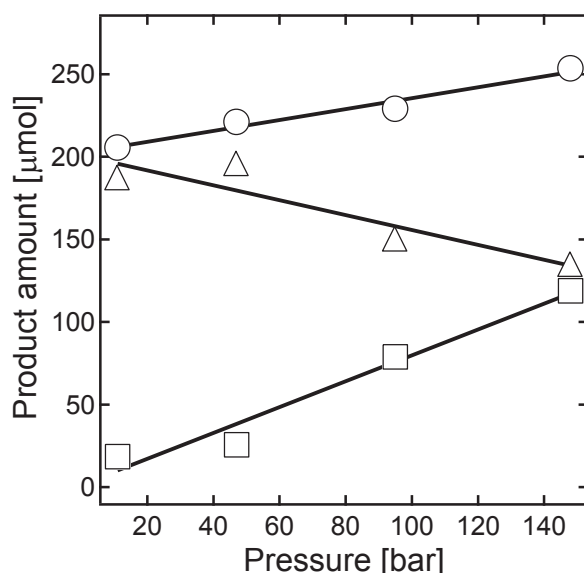


Figure 5.5. The production of CO (white square), HCOO^- (white triangle), and the total amount (white circle) over 2 hours in the TEOA-DMF system, as a function of pressure. The TEOA volume fraction was 0.3 and the reaction medium consisted of 2 μmol catalyst, 8 μmol of photosensitizer, and 1 mmol BNAH with a temperature of 313 K.

Unlike the water-DMF system, these results show that using TEOA as the proton carrier favours the formate catalytic cycle, and that increasing CO_2 concentration results in competitive catalysis as the initial step of the catalytic cycle consists of addition of CO_2 instead of H^+ . The competitive step might therefore be rate-determining for both cycles. Carbon monoxide production is especially favoured by the supercritical conditions, as the transition from high pressure to supercritical is met with a 300% increase in CO. Formate concentration decreases somewhat with increasing pressure, suggesting the competition in the

catalytic cycles, but may also be due to a detrimental change in the reaction medium as the reaction components are diluted by the formation of a single phase.

Selectivity in product formation has been suggested in previous publications, with Tanaka *et al.* [1] observing a clear pH dependence on the CO_2 reduction products, with alkaline systems especially favouring the formation of formic acid. More recently, a publication by Tamaki *et al.* [13] noted that the absence of TEOA decreased formate production *ca.* 5 fold and also decreased selectivity towards this product.

5.4. Turnover number and frequency

The photocatalytic activity and efficiency of the system under supercritical conditions was determined by calculating the turnover number (*TON*) over a 2-hour period and the initial turnover frequency (*TOF_{ini}*) over 15 minutes of reaction. For the two solvent systems considered in the previous section, the same total amount of product is reached at high pressures, *ca.* 250 μmol . This corresponds to a *TON* for the catalyst of 120 in 2 hours, and to a *TOF_{ini}* of 113 h^{-1} (reaction 1 in Table 5.1.). The quantum yield of the reaction over two hours, using a monochromatic blue LED, was 9.8%. Compared to the catalytic system investigated in the precedent chapter, these values correspond to a 70-folds increase for similar concentration of catalyst and photosensitizer.

These results are difficult to compare to those by Tanaka [2, 14, 15], Lehn [7] and others [13, 16] owing to the wide variation in reaction conditions. In the original, and most comparable study, due to the use of the same catalyst, photosensitizer and electron donor, by Ishida *et al.* in 1988 [14], under atmospheric pressure the total product after 10 hours was 85 μmol , with no more than 30 μmol in the first 2 hours. Yet, in using just 0.5 μmol of catalyst (unlike the 2 μmol used herein), this corresponded to a quantum yield of 14.8 % for CO and 2.7 % for formate. But owing to the wide variation in reactor volumes, reaction time, surface of windows and light intensity, a comparison with published results is not really meaningful.

It is therefore more interesting to identify and estimate the different limiting factors in the reaction system used herein.

5.5. Limiting factors

Because both the water-DMF and TEOA-DMF reactions reach a very similar total productivity, a common limitation is likely to occur in both systems. The following sections describe a series of experiments varying catalyst concentration, irradiation time, light intensity, electron donor concentration, and product saturation. For each experiment, unless otherwise stated, the optimized water-DMF system was used for 2 hours at a pressure of 150 bars. The BNAH electron donor concentration was in a large excess at $0.03 \text{ mol}\cdot\text{L}^{-1}$ (1 mmol), the catalyst, $[\text{Ru}(\text{bpy})_2(\text{CO})\text{H}][\text{PF}_6]$, was used at a concentration of $62 \text{ }\mu\text{mol}\cdot\text{L}^{-1}$ (2 μmol) and the photosensitizer, $[\text{Ru}(\text{bpy})_3]\text{Cl}_2$, at a concentration of $250 \text{ }\mu\text{mol}\cdot\text{L}^{-1}$ (8 μmol). The results corresponding to the subsequent variations in parameters are summarized in Table 5.1, and discussed in the following sections.

Table 5.1. Product amount, turnover number and initial turnover frequency TOF_{ini} (h^{-1}) for different reaction conditions. Product amount (μmol) and TON were calculated after 2 hour reactions except for experiment 5, which was a 16 hour reaction.

	Catalyst [μmol]	PS [μmol]	BNAH [mmol]	Pressure [bar]	Light [mW]	CO [μmol]	TON	TOF_{ini}	HCOOH [μmol]	TON	TOF_{ini}
1.	2	8	1	150	200	210	105	78	48	24	35
2.	2	8	1	10	200	103	52	56	48	24	29
3.	0.1	8	1	150	200	102	1020	1120	10	100	480
4.	0.1	8	1	10	200	54	540	280	18	180	360
5.	2	8	1	150	40	80	40	17	59	29.	9
6.	2	8	2	150	200	193	97	73	91	45	45
7.	2	8	3	150	200	220	110	78	143	72	60
8.	2	0	1	150	200	20	10	ND	10	5	ND
9.	0	8	1	150	200	18	2*	ND	3	0.4 *	ND

* calculated using the photosensitizer amount; ND = not determined

5.5.1. Catalyst and photosensitizer concentration

From experiments in which the amount of catalyst was varied, as shown in Figure 5.6., the amount of catalyst in the reactor can be decreased by a factor of 4 (2 to 0.5 μmol) without any significant modification of the TON . Reducing this amount further, however, causes a significant decrease in productivity.

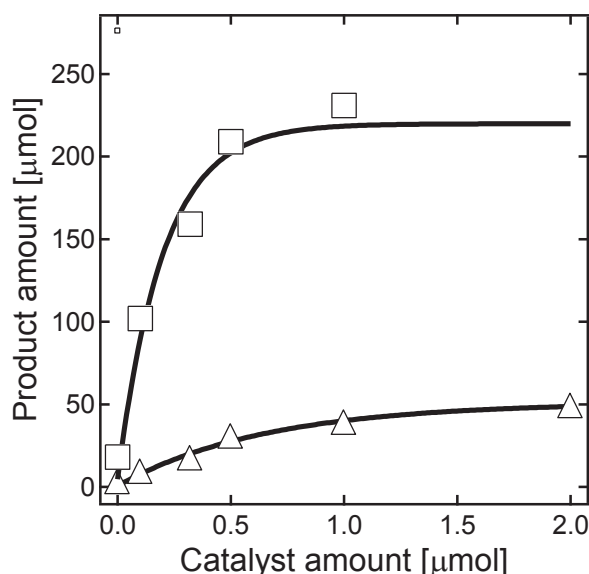


Figure 5.6. The effect of catalyst ($[(\text{Ru}(\text{bpy})_2(\text{CO})\text{H}][\text{PF}_6])$) concentration on the photocatalytic production of CO (white squares) and HCOO^- (white triangles) over 2 hours. The water-DMF system with 1 mmol BNAH and 8 μmol of photosensitizer was used at a pressure of 150 bars and temperature of 313 K.

Using the values determined from the smallest added amount of catalyst (result 3 in Table 5.1.), a limiting TON and TOF_{ini} can be estimated. With 0.1 μmol of catalyst ($3 \mu\text{mol}\cdot\text{L}^{-1}$), the total amount of product formed is 112 μmol in 2 hours (102 μmol CO and 10 μmol HCOO^-). The total TON is therefore 1120 the TOF_{ini} is 1600 h^{-1} (calculated from the production of 28 μmol CO and 12 μmol HCOO^- in 15 minutes), values that are considerably larger than the previously mentioned numbers for the optimised volume ratio system. It shows that in the concentration conditions used before, the catalytic turnover is not a limiting factor and degradation of the catalyst is not responsible for the limit in total production.

Without catalyst (result 9 in Table 5.1.), a small amount of product is still detected, 18 and 3 μmol for CO and HCOOH respectively. This is produced by the conversion of the photosensitizer, $[\text{Ru}(\text{bpy})_3]^{2+}$, into a catalytic unit by the loss of one bipyridyl ligand. The yield is very small compared to that of just 0.1 μmol of catalyst however, indicating that photosensitizer degradation is negligible during the 2 hour reaction. Reactions conducted without a photosensitizer (result 8 in Table 5.1.) show that the catalyst alone is photoactive. This has been observed for other metal carbonyl complexes, which operate catalytically as a single species in the CO_2 reduction cycle [17, 18]. Indeed, the catalyst used herein is

absorbing light, and its excited state can be quenched by BNAH to reduce and activate the catalyst. However, the reaction efficiency is limited, as carbon monoxide production decreased 90% from 200 μmol to 20 μmol , and formate production decreased 80% to 10 μmol . Studies by Tanaka *et al.* [19, 20] found that the catalytic intermediates (2) and (4) in Figure 5.1., can be photo-excited at the bpy ligand and accept an electron from the BNAH directly, whereas the double carbonyl ligand intermediates (complexes (8) and (9), Scheme 1) of the carbon monoxide catalytic cycle are not activated by visible light. UV-vis spectroscopy of the catalyst intermediates indicates that the colourless compound, $[\text{Ru}(\text{bpy})_2(\text{CO})_2]^{2+}$ is indeed inactive in light above 300 nm wavelength, whereas compounds (2) and (4) of the formate catalytic cycle are bright yellow solids with typical Ru-bpy MLCT absorbance peaks in the blue light region (*ca.* 450 nm). Control reactions without light did not produce anything.

Performing the experiments at 10 bars with 0.1 μmol catalyst (reaction 4 in Table 5.1.) led to a 2-fold decrease in CO yield (54 μmol) compared to the experiment at high pressures with the same amount of catalyst (reaction 3.). This is a comparable decrease to the high and low pressure experiments with 2 μmol catalyst thus maintaining the observation that increasing the pressure to 150 bars doubles the CO production. Formate production however is favoured at low pressures and the yield doubled to 18 μmol , indicating no dependence on CO_2 concentration or pressure but a possible competition with CO formation. The total TOF_{ini} at low pressures decreased to 640 h^{-1} (calculated from the production of 7 μmol CO and 9 μmol HCOO^- in 15 minutes), which corresponds to a 4-fold decrease in CO production rate, and an unchanging rate for HCOO^- production when compared to the high-pressure system.

The results shown in Figure 5.7. indicate that the reaction is complete after 2 hours. Formate production reaches 80% completion in just 30 minutes compared to 40% for CO. Reducing the light power from 200 to 40 mW reduced the TOF_{ini} proportionally (*ca.* 5 fold) from 78 to 17 for CO and 36 to 9 for HCOO^- . For a lower light intensity experiment, the reaction was slower, with the plateau in CO productivity observed after 16 h. The lower intensity was quite detrimental to the final yield for CO, as a TON of 40 was observed compared to 105 in the 200 mW experiment. For HCOO^- the final TON was independent of light intensity and remains *ca.* 27.

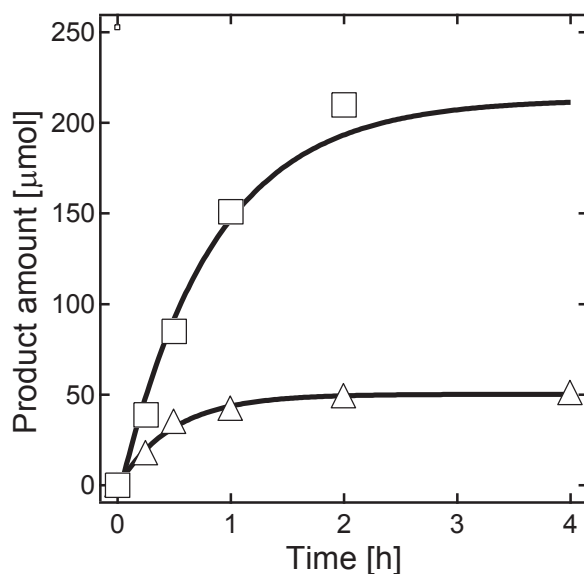


Figure 5.7. The effect of varying irradiation time on the production of CO (white squares) and HCOO⁻ (white triangles). The water-DMF system with 1 mmol BNAH, 2 μmol catalyst and 8 μmol of photosensitizer was used at a pressure of 150 bars and temperature of 313 K, light intensity 200 mW.

For a 15-minute reaction at 200 mW, the total product yield reaches 57 μmol, corresponding to a TOF_{ini} of 113 h⁻¹. This initial turnover frequency is much lower than the previously mentioned limiting turnover frequency for a small amount of catalyst, therefore one limitation may come from the photosensitisation cycle. The irradiation time of 2 hours was optimum for the 200 mW reaction, as the total productivity reaches a plateau at this time. Considering the shortest irradiation time of 15 min however, the quantum yield is at its highest, with 17.4% of monochromatic light converted to products. A comparable quantum yield of 19.3 % was obtained at 40 mW.

5.5.2. Electron donor

Two electrons are necessary for the production of one molecule of carbon monoxide or formate, therefore two molecules of BNAH are required per molecule of product. The electron donor, BNAH, is present in the catalytic system in significant excess to the catalyst and photosensitizer concentrations. Considering that *ca.* 250 μmol of product is produced in 2

hours of reaction with 2 μmol of catalyst under 150 bars, *ca.* 500 μmol of BNAH is consumed, which is 50% of the initial amount. The decrease in BNAH concentration over time might decrease the rate of the photosensitizing cycle, but this does not explain the appearance of a plateau at 50% consumption.

A series of experiments in which the amount of BNAH in the reactor was 1, 2 and 3 mmol was conducted is shown in Figure 5.8 and summarized in Table 5.1 (reactions 1, 6 and 7). At 1 mmol, *ca.* 250 μmol of total product is obtained. In the reactions with more BNAH however, we observe a trend in which the total CO produced remains at approximately 200 μmol , yet the formate concentration increases 50 μmol (*i.e.* 100 %) per mmol of BNAH. This indicates that the two catalytic cycles undergo two distinct limiting factors that lead to a plateau in the production rate. Carbon monoxide production seems more limited by its own saturation concentration and the formate by the electron donor concentration. Indeed, the TOF_{ini} for CO production is not influenced at all by the electron donor concentration, but for HCOO^- production the TOF_{ini} increases consistently with the electron donor concentration. This confirms that the limiting step for CO production involves CO_2 concentration only, presumably the oxidative addition of CO_2 on complex (1) or hydroxide abstraction from CO_2 on complex (7) to form bicarbonate. For HCOO^- the limiting step involves the electron donor concentration indicating a limitation in the photosensitizing cycle or in the electron transfer from photosensitizer to the hydride catalyst (2). Indeed, the reduction potential of $[\text{Ru}(\text{bpy})_2(\text{CO})\text{H}]^+$ is 140 mV more negative than $[\text{Ru}(\text{bpy})_3]^{2+}$ (-1.450 V and -1.310 V *vs* SCE respectively) [21], indicating an unfavourable electron transfer. This electron transfer will be highly influenced by the concentration of reduced photosensitizer, therefore influenced by the concentration of the electron donor.

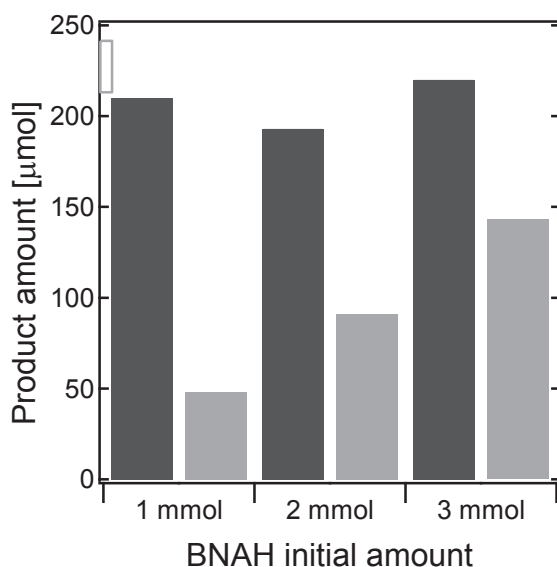


Figure 5.8. The effect of increasing electron donor concentration on the production of CO (dark grey) and HCOO⁻ (grey) over 2 hours. The water-DMF system with 2 μmol catalyst and 8 μmol photosensitizer was used at a pressure of 150 bar and temperature of 310 K.

5.5.3. Interferences

For carbon monoxide production, even with a large amount of electron donor (3 mmol) the final concentration does not exceed 220 μmol in the 32 mL reactor used throughout the experiments. It was considered that CO was reaching a saturation concentration, which may have been limiting the reaction by poisoning the catalytic or photosensitization cycles. This was previously reported by Hori *et al.* [9] for a rhenium complex in a high-pressure mixed solvent single phase. To ascertain if the CO was reaching a maximum limit after 2 hours and was poisoning the catalyst, the reaction was decompressed at 2-hour intervals, the products analysed, and an additional 1 mmol of BNAH was added to the reactor before recompressing with CO₂. The results from three consecutive decompressions are shown in Figure 5.9.

Carbon monoxide ceased to be produced to the same levels (*i.e.* 200 μmol) after the first 2 hour compression, yet the formate was consistently produced at the rate of 50 μmol (± 10 μmol) per compression. This supports that there are two independent cycles occurring to produce the respective products, and they are each limited in different ways.

For carbon monoxide, the theory that a saturating product concentration is poisoning the catalytic cycle is corroborated by this experiment, as production of CO resumes after removing the carbon monoxide produced in the first run. However, production decreased in the two subsequent runs to 135 and 104 μmol for the 2nd and 3rd respectively. A second experiment was then performed in which the gas phase was removed and replenished with pure CO_2 in the three subsequent reactions, but further BNAH was not added to the liquid phase. The results strongly indicate the detrimental effect of not replacing the BNAH on CO formation, as productivity decreased to 43 and 2 μmol by the 2nd and 3rd runs respectively. Formate production was also affected in similar proportions when the electron donor was not replenished.

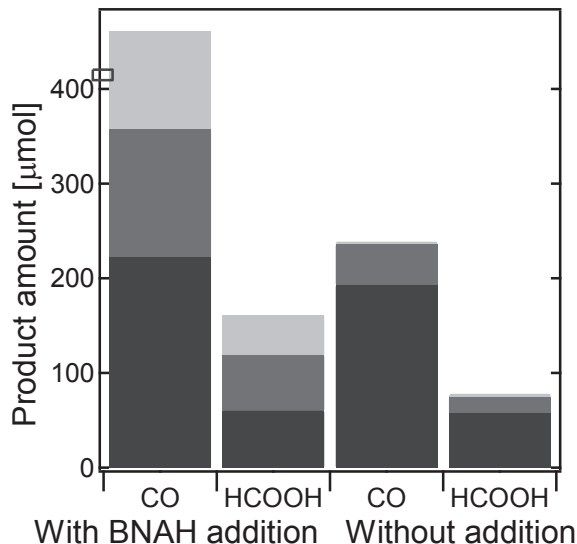
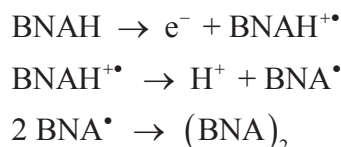
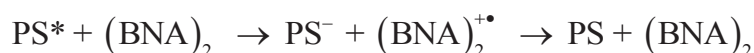


Figure 5.9. Products formed following periodic 2-hour reactions and decompression of the reactor (1st run in dark grey, 2nd in intermediate grey, and 3rd in light grey), with and without addition of 1 mmol of BNAH between runs. The water-DMF system with an initial amount of 1 mmol BNAH, 2 μmol catalyst and 8 photosensitizer was used at a pressure of 150 bars and temperature of 313 K.

It appears that another product that is detrimental for the catalytic reaction is generated in solution. This product is believed to be the BNA₂ dimer, which is the product of the oxidation of BNAH formed by the three successive following reactions:



This dimer is in itself a very strong reductant, stronger than BNAH ($E_{\text{ox}} = 0.26 \text{ V vs SCE}$ [22], $E_{\text{ox}} = 0.57 \text{ V vs SCE}$ [23] respectively). With respect to the quenching rate constant published by Tamaki *et al.* [24], the dimer quenches the excited state of $[\text{Ru}(\text{bpy})_3]^{2+}$ twenty times faster than BNAH. However, unlike for BNAH, the BNA₂ quenching is highly inefficient due to back electron transfer from the photosensitizer to BNA₂. Finally, the BNA₂ is unchanged but the photosensitizer is no longer excited, as presented in the following reactions:



With BNAH as quencher, the back electron transfer is certainly hindered by the chemical modification of BNAH⁺ induced by the loss of one proton. As the reaction proceeds, BNAH is converted into BNA₂ and the quenching becomes more and more governed by BNA₂ leading to an inefficient light adsorption process. A mathematic model of the photosensitizing system, developed in the following section, demonstrates the importance of BNA₂ on the efficiency of the photosensitizing cycle.

An increase in the initial amount of BNAH in the reactor might reduce the negative effect of the presence of BNA₂ in the reactor. But as shown in Figure 5.8., the amount of carbon monoxide produced did not change even with 3-fold the initial amount of BNAH in the reactor. The main limitation for carbon monoxide therefore comes from a limiting concentration of products. As pressure increases the concentration of CO₂ in the reactor, the dilution of CO product in the supercritical fluid might explain the improved efficiency of the system at higher pressures.

5.6. Mathematic model

The chain of reactions considered for making a mathematic model of the photosensitisation cycle is presented in Figure 5.10. To simplify the model only the photosensitizer cycle is considered, as the catalytic cycle is apparently not rate limiting in the overall process, which was discussed in Section 5.5.1.

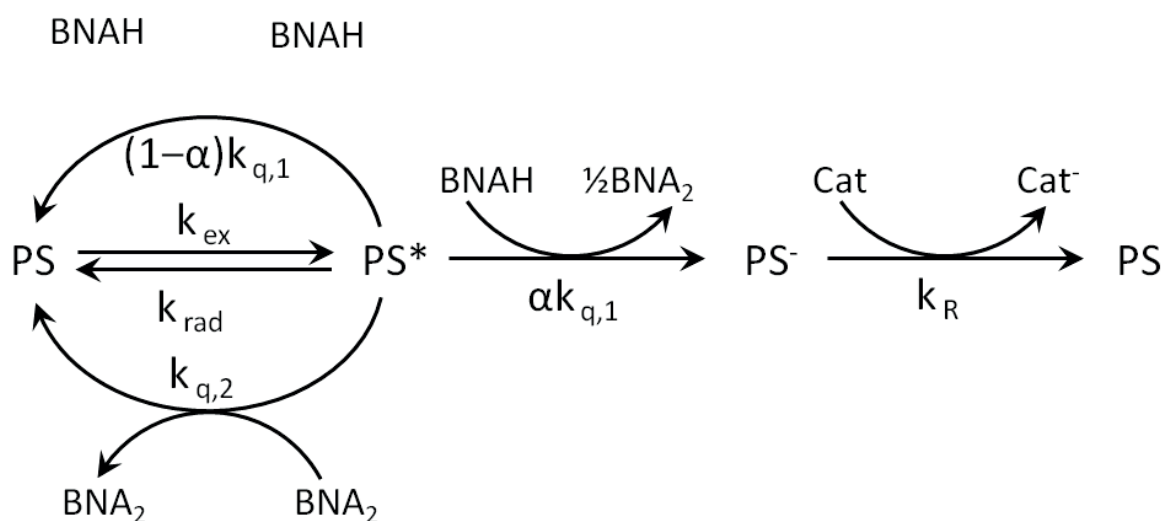


Figure 5.10. Chain of reactions inducing reduction of the catalyst, PS : $[\text{Ru}(\text{bpy})_3]^{2+}$, PS* the excited state : $*[\text{Ru}(\text{bpy})_3]^{2+}$, and PS⁻ : $[\text{Ru}(\text{bpy})_3]^+$.

Initial step is the excitation of the photosensitizer, with k_{ex} the rate constant of this process. This rate constant is function of light intensity, but is unknown and will be tuned to match the present model with experimental results. The excited state PS* can deactivate without quenching by fluorescence, phosphorescence and non-radiative pathways outside of quenching. The rate constant of all these process together is obtained from the lifetime of the excited state in absence of quencher. Lifetime reported in pure DMF is about 600 ns [25], giving a rate constant k_{rad} of $1.66 \cdot 10^6$ $[\text{s}^{-1}]$. In presence of BNAH, two quenching mechanisms are possible; efficient quenching leading to the formation of the reduced photosensitizer PS⁻ and inefficient quenching leading back to the initial state of the photosensitizer PS. The cage escape coefficient α represents the probability of efficient quenching. As this factor is

presumed to be the main limitation for the quantum yield in optimal conditions, the maximal quantum obtained experimentally ($\Phi_{\max} = 0.2$) is used as a first-order approximation. In presence of the dimer BNA_2 , quenching by this compound is possible, but this quenching is purely inefficient leading back to PS. Quenching rate constant for BNAH and BNA_2 have been obtained by the lifetime of the excited state in presence of the quencher and reported by Tamaki [13]: $k_{q,1} = 1.64 \cdot 10^7 M^{-1} s^{-1}$ and $k_{q,2} = 3.09 \cdot 10^8 M^{-1} s^{-1}$. Once reduced, the photosensitizer transfers one electron to the catalyst, the rate constant of this reaction is unknown but as this reaction is not in competition with any other, this rate constant is of moderate importance. The amount of product generated by the whole system is determined from the amount of BNA_2 generated.

The differential equations dictating evolution of the system are the following:

$$\frac{d[PS]}{dt} = -k_{ex}[PS] + k_{rad}[PS^*] + (1-\alpha)k_{q,1}[BNAH][PS^*] + k_{q,2}[BNA_2][PS^*] + k_R'[PS^-] \quad (5.1)$$

$$\frac{d[PS^*]}{dt} = k_{ex}[PS] - k_{rad}[PS^*] - k_{q,1}[BNAH][PS^*] - k_{q,2}[BNA_2][PS^*] \quad (5.2)$$

$$\frac{d[BNAH]}{dt} = -\alpha k_{q,1}[BNAH][PS^*] \quad (5.3)$$

$$[PS]_{initial} = [PS] + [PS^*] + [PS^-] \quad (5.4)$$

$$[BNAH]_{initial} = [BNAH] + 1/2[BNA_2] \quad (5.5)$$

with $0 \leq \alpha \leq 1$ and $k_R' = k_R[Cat]$

Two different equilibrations exist on two different timescales for this system; the two first equations reach a steady-state in a very short time ($\ll 1$ second) due to the very short lifetime of the excited state of the photosensitizer. Equation (5.3) represents the long-term consumption of electron donor and generation of CO_2 reduction product with variations over hours of reaction.

The concentration of the different states of the photosensitizer can be solved for the steady state conditions, from equations (5.1), (5.2) and (5.4):

$$[\text{PS}^*] = \frac{k_{\text{ex}} k_{\text{R}}'}{k_{\text{ex}} k_{\text{R}}' + \alpha k_{\text{ex}} k_{q,1} [\text{BNAH}] + k_{\text{R}}' k_{q,1} [\text{BNAH}] + k_{\text{R}}' k_{q,2} [\text{BNA}_2] + k_{\text{rad}} k_{\text{R}}'} [\text{PS}]_{\text{initial}} \quad (5.6)$$

$$[\text{PS}^-] = \frac{\alpha k_{\text{ex}} k_{q,1} [\text{BNAH}]}{k_{\text{ex}} k_{\text{R}}' + \alpha k_{\text{ex}} k_{q,1} [\text{BNAH}] + k_{\text{R}}' k_{q,1} [\text{BNAH}] + k_{\text{R}}' k_{q,2} [\text{BNA}_2] + k_{\text{rad}} k_{\text{R}}'} [\text{PS}]_{\text{initial}} \quad (5.7)$$

Equation (5.3) is then integrated to obtain the concentration of BNAH at a function of time, with the excited state of the photosensitizer being a function of BNAH concentration as given by equation (5.6):

$$[\text{BNAH}]_t = [\text{BNAH}]_{\text{initial}} e^{(-\alpha k_{q,1} [\text{PS}^*] t)} \quad (5.8)$$

The set of values for the rate constants and initial conditions used for numerical simulations are shown in Table 5.2.

Table 5.2. Values for the different rate constant and initial concentration used for numerical simulations

k_{ex}	0.4 s^{-1}
k_{rad}	$1.66 \cdot 10^6 \text{ s}^{-1}$
$k_{q,1}$	$1.64 \cdot 10^7 \text{ s}^{-1} \text{ M}^{-1}$
$k_{q,2}$	$3.05 \cdot 10^8 \text{ s}^{-1} \text{ M}^{-1}$
k_{R}'	10^9 s^{-1}
α	0.2
$[\text{PS}]_{\text{initial}}$	$5 \cdot 10^{-4} \text{ M}$
$[\text{BNAH}]_{\text{initial}}$	0.0625 M

The consumption of BNAH over time can therefore be plotted as shown in Figure 5.11. Two decays of BNAH concentration are represented: in light grey, a theoretical exponential decrease that would be obtained if absence of quenching by BNA_2 , and in dark grey a decrease obtained from the equations aforementioned with quenching by BNA_2 slowing down considerably the overall process.

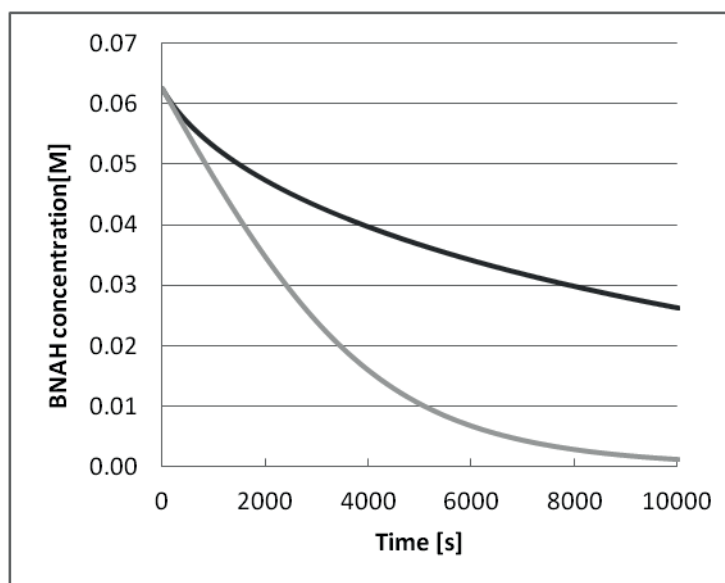


Figure 5.11. Decay of BNAH concentration in the reactor, in grey considering only the quenching from BNAH, in dark grey with the inefficient quenching from BNA₂ considered.

The production of BNA₂ calculated by the model can be compared with the amount of reduction product experimentally determined as shown in Figure 5.12.

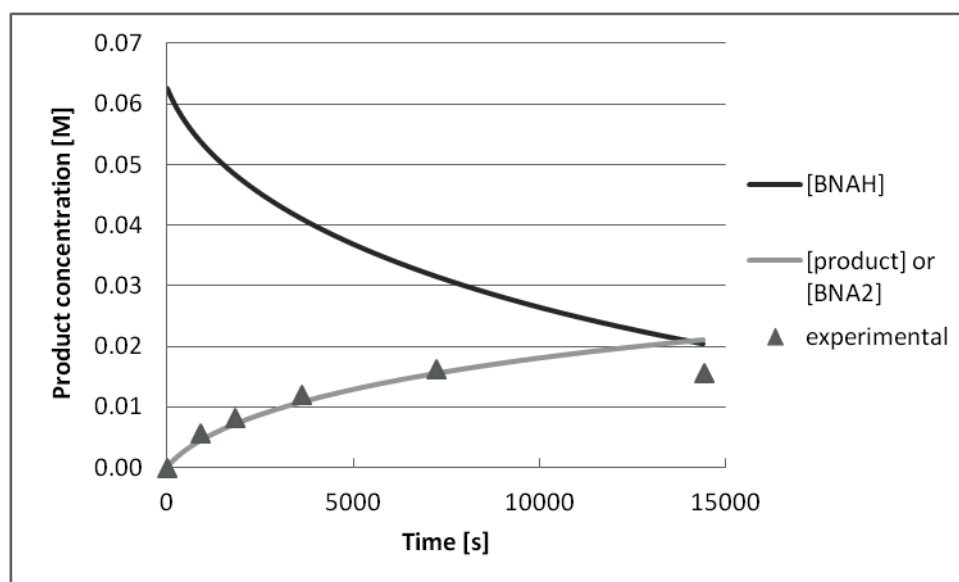


Figure 5.12. Comparison of the model with experimental production rate, for conventional high-pressure conditions (150 bars, optimized water/DMF ratio, 1 mmol BNAH, 2 μ mol catalyst, 8 μ mol photosensitizer).

The mathematic model is validated by the experimental data, except for the 4 hour experiment where saturation of CO is believed to hinder the catalytic cycle. The model presented here is considering bulk concentration and production rate, but the concentration of the excited photosensitizer is not equally distributed in the solution. Due to the high light absorption of the solution, almost all the light is absorbed within the first 4 millimetres of solution after the sapphire window. Concentration of PS* is therefore considerably higher in this reduced volume. Diffusion of different species, such as BNAH, BNA₂, CO₂ between the bulk and the window may therefore also limit the reaction rate.

The mathematic model used in here is not totally representing the real situation. One spatial dimension can be included to have a better representation of the reality. The activity of the photosensitizing cycle is depending on the light intensity ($I(x)$), which is not a bulk value, but depends on the distance from the windows (x), as predicted by the following equation:

$$I(x) = I_0 \cdot 10^{-\varepsilon[\text{PS}]_{ini}x} \quad (5.9)$$

where, ε is the molar extinction coefficient of the photosensitizer and $[\text{PS}]_{ini}$ its initial concentration and I_0 the light intensity at the window. With the concentration of photosensitizer used and its high extinction coefficient ($14600 \text{ M}^{-1} \cdot \text{cm}^{-1}$), 99.98% of light intensity is absorbed in the first 5 mm of solution. From the very short lifetime of the excited state of the photosensitizer, diffusion of the excited state is excluded and the reduction of the catalyst is mainly happening in the reduced volume in the first 5 mm behind the window. A better mathematic model can be constructed considering that the excitation rate constant k_{ex} , is function of light intensity. The concentrations of the three states of the photosensitizer are consequently function of distance and time. Concentration of BNAH and BNA₂, however are always considered as bulk values. Changes in concentration for these two compounds happen over long time, diffusion of these compounds will therefore equilibrate the concentration over the entire volume.

The software MATLAB has been used to solve a mathematic model with inclusion of the distance, while matching the previous results for BNAH and BNA₂ evolution. Concentrations of ground and excited state of the photosensitizer are presented in Figure 5.13 for long and short time span.

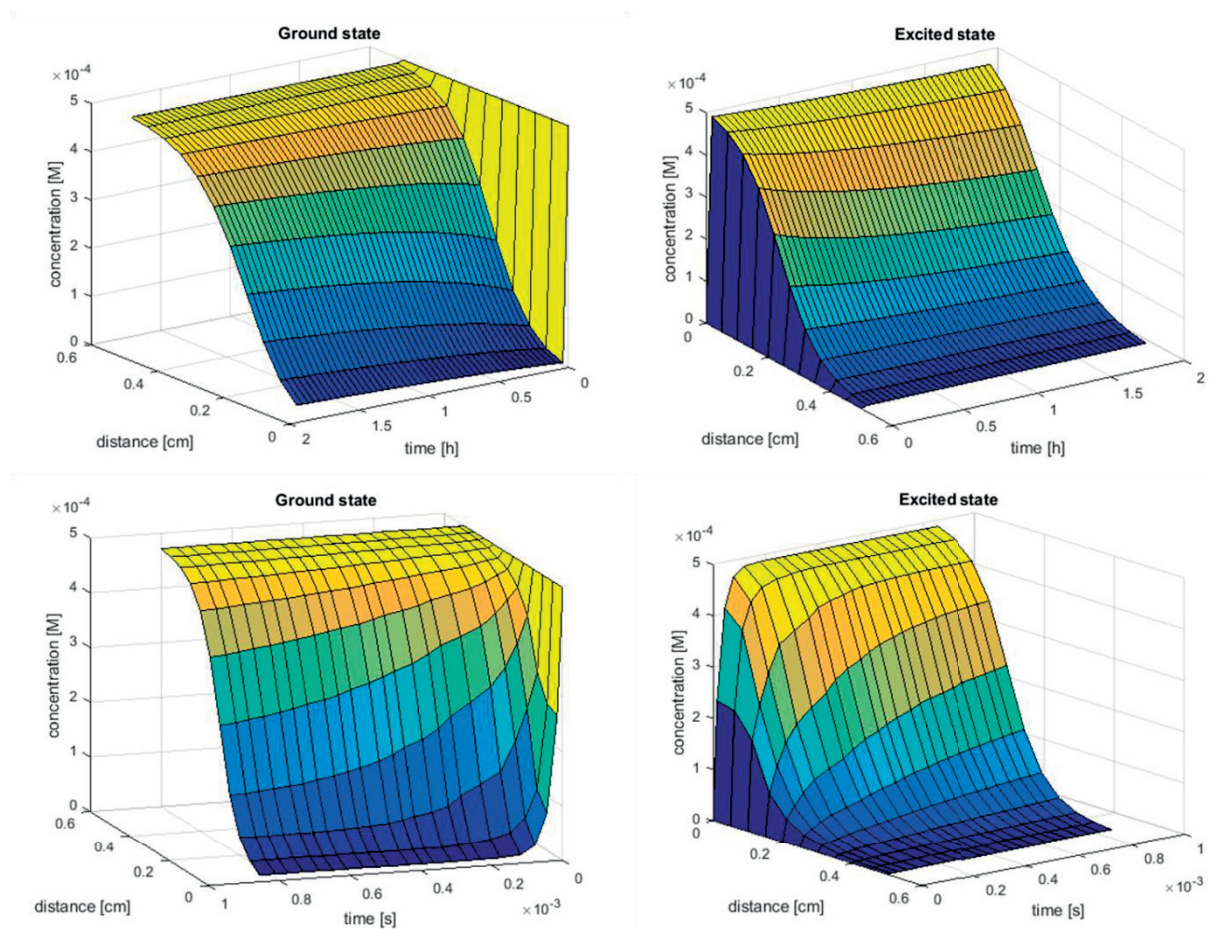


Figure 5.13. Simulation of the evolution of concentration of the ground and excited state of the photosensitizer over time and distance from the window. On the top, long term evolution over 2 hours of reaction. On the bottom, short term equilibration over the first microsecond. Time and distance axis are reverted on excited state graphic for better visibility.

Over the 5 mm considered, the concentrations of the two species change totally. The photosensitizer is almost totally in its excited state at the windows while at 5 mm from the windows the ground state is highly dominating. Due to the important value taken for the rate of electron transfer from photosensitizer to catalyst, the lifetime of the reduced form of the photosensitizer is very small. Its concentration is therefore small compared to the concentration of the two other states. This explains that the graphics for ground and excited state appears to be the reciprocal of each other. Variations of concentrations over the two hours of reaction are limited, only a slight decrease of the concentration of the excited is observed. This decrease is caused by a faster deactivation of the excited when the concentration of BNA_2 is increasing. The initial sharp change in concentration is more

detailed on the two graphs on the bottom of Figure 5.13. Equilibration of the concentrations happens in approximately one microsecond after the light has been turned on.

From the concentration of the excited state determined, and considering a bulk evolution of the concentration of BNAH and BNA_2 , the production of CO over the surface of the window as a function of time and distance can be determined. As shown in Figure 5.14., most of the production of carbon monoxide happens in the first 2 mm and in the first hour of reaction.

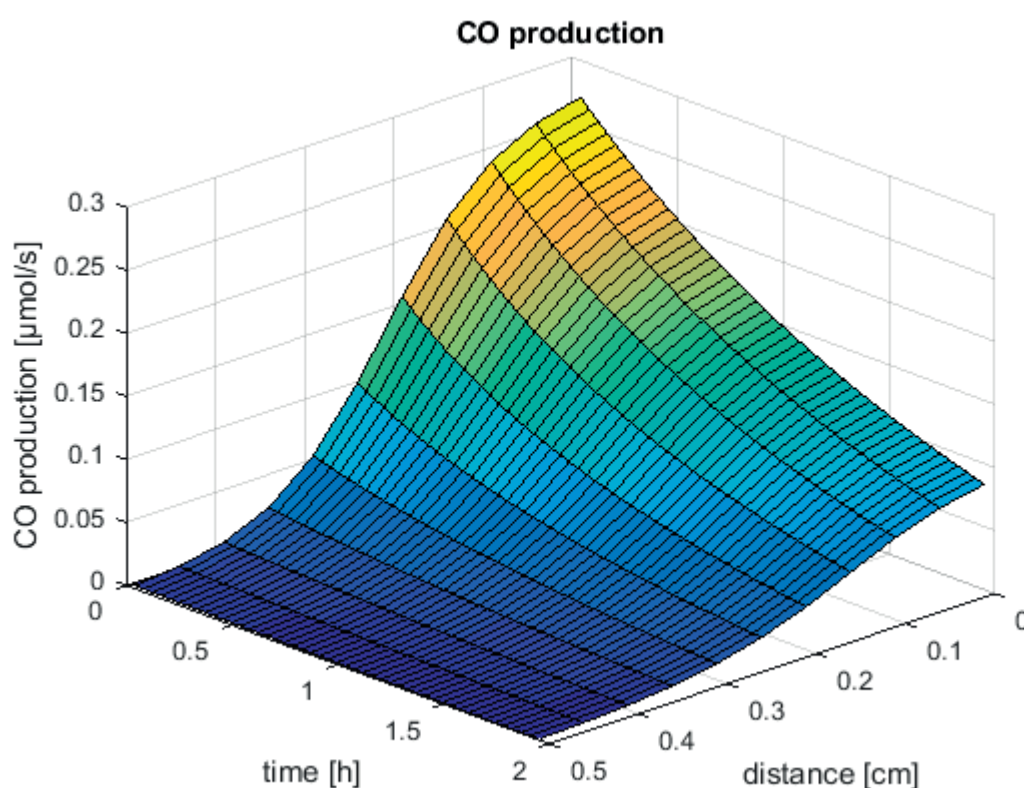


Figure 5.14. Production rate of carbon monoxide over time and distance over the surface of the windows of the reactor (2.83 cm^2).

Volume integration of the surface gives the overall production of carbon monoxide in the reactor. For the data presented in Figure 5.14. the amount of product generated is determined to be $234 \mu\text{mol}$ in 2 hours. From these values, a more accurate determination of the turnover number and initial turnover frequency is possible as the amount of catalyst and photosensitizer reacting can be estimated. For $2 \mu\text{mol}$ of catalyst in the reactor only 0.125

μmol is present in the first 4 mm behind the window of the reactor and participating in the generation of all the products of reduction of CO_2 . Therefore at 150 bars with 2 μmol of catalyst (reaction 1. of table 5.1.) TON is determined to be 2064 cycle over two hours of reaction with a TOF_{ini} of 1808 h^{-1} . With catalyst concentration decreased to 0.1 μmol (reaction 3. of table 5.1.) these values are increased to 17'778 for TON and 25'397 for TOF_{ini} . But these values must be taken with caution as diffusion of the catalyst is possible, increasing the amount of catalyst molecules that are participating in the formation of the products.

5.7. Conclusions

The effects of increased CO_2 pressure and imparting supercritical conditions on the catalytic reaction of the well characterized CO_2 reduction catalyst $[\text{Ru}(\text{bpy})_2(\text{CO})(\text{H})]^+$, have been presented. CO_2 reduction was comprehensively optimized with respect to proton carrier, co-solvent and CO_2 concentration/pressure, providing further insight into the catalytic cycles, the relationship between catalyst, photosensitizer and electron donor, and demonstrating the advantages of vastly increasing CO_2 concentration on the catalytic system.

The two products identified in the analysis were carbon monoxide and formate. The former was found to have a linear relationship with pressure over a 10-150 bars range, such that production was consistently doubled. Formate however, was independent of CO_2 concentration in water-DMF solutions, and decreased 25% in a TEOA/DMF medium between 10 and 150 bars. Increasing the CO_2 concentration therefore favours the CO catalytic cycle and is rate limiting for the reaction, whereas formate is independent of CO_2 concentration due to insertion later in the catalytic cycle. It was found that the greatest CO yields were obtained from a biphasic water-DMF / supercritical CO_2 system rather than a single phase of all components. This was suggested to be due to the extraction of CO from the liquid phase where the catalyst was present to the upper supercritical CO_2 phase, thus preventing the catalytic cycle from being poisoned. Nonetheless, a saturation concentration of *ca.* 200 μmol was identified in subsequent experiments to be a limiting value.

Turnover numbers and frequencies for the optimized systems were considerably greater than previously reported in the literature [2, 12-15]. For a system irradiated for 2 hours with 2 μmol of catalyst, the *TON* was 120 with a *TOF_{ini}* of 174 h^{-1} but this reached 1120 h^{-1} and 1600 h^{-1} when the catalyst was used at its limit of 0.1 μmol . The rapid turnover and overall productivity of the systems compared to the literature demonstrates the enhancement offered by operating the reaction at high-pressure over the range of 10-150 bars, and the potential for obtaining much more product in a short time frame.

The role of the dimer BNA_2 in the inhibition of the photosensitizing cycle was demonstrated by mathematic simulation, which also demonstrates that the reaction is taking place in a reduced volume in the first millimetre of solution behind the windows irradiated. Taking into account this reduced volume of reaction for the determination of the *TON* and *TOF_{ini}*, gives higher values of 17'778 and 25'397 respectively. But these values do not take into consideration diffusion of the catalyst, which could increase greatly the amount of catalyst molecule participating in the reaction.

5.8. Bibliography

1. Ishida, H., K. Tanaka, and T. Tanaka, *Electrochemical CO₂ reduction catalyzed by ruthenium complexes [Ru(bpy)₂(CO)₂]²⁺ and [Ru(bpy)₂(CO)Cl]⁺. Effect of pH on the formation of CO and HCOO*. *Organometallics*, 1987. **6**(1): p. 181-186.
2. Ishida, H., K. Tanaka, and T. Tanaka, *Photoreduction of carbon dioxide in the [Ru(bpy)₂(CO)₂]²⁺ (bpy = 2,2'-bipyridine)/[Ru(bpy)₃]²⁺ or [Ru(phen)₃]²⁺ (phen = phenanthroline)/triethanolamine/N,N-dimethylformamide system*. *Chem. Lett.*, 1987(6): p. 1035-8.
3. Ishida, H., et al., *Selective formation of formate in the electrochemical carbon dioxide reduction catalyzed by [Ru(bpy)₂(CO)₂]²⁺ (bpy = 2,2'-bipyridine)*. *J. Chem. Soc., Chem. Commun.*, 1987(2): p. 131-2.
4. Tanaka, K., *Metal-catalyzed reversible conversion between chemical and electrical energy designed towards a sustainable society*. *Chem. Rec.*, 2009. **9**(3): p. 169-186.
5. Bruce, M.R.M., et al., *Electrocatalytic reduction of carbon dioxide based on 2,2'-bipyridyl complexes of osmium*. *Inorg. Chem.*, 1992. **31**(23): p. 4864-73.
6. Pugh, J.R., et al., *Formation of a metal-hydride bond and the insertion of carbon dioxide. Key steps in the electrocatalytic reduction of carbon dioxide to formate anion*. *Inorg. Chem.*, 1991. **30**(1): p. 86-91.
7. Hawecker, J., J.-M. Lehn, and R. Ziessel, *Photochemical reduction of carbon dioxide to formate mediated by ruthenium bipyridine complexes as homogeneous catalysts*. *J. Chem. Soc., Chem. Commun.*, 1985(2): p. 56-58.
8. Fujita, E., *Photochemical carbon dioxide reduction with metal complexes*. *Coordination Chemistry Reviews*, 1999. **185–186**: p. 373-384.
9. Hori, H., et al., *High-pressure photocatalytic reduction of carbon dioxide using [fac-Re(bpy)(CO)₃P(OiPr)₃]⁺ (bpy = 2,2'-bipyridine)*. *Journal of Molecular Catalysis A: Chemical*, 2002. **179**(1–2): p. 1-9.
10. Hori, H., et al., *Efficient rhenium-catalyzed photochemical carbon dioxide reduction under high pressure*. *Inorganic Chemistry Communications*, 2003. **6**(3): p. 300-303.
11. Voyame, P., et al., *Photoreduction of CO₂ using [Ru(bpy)₂(CO)L]ⁿ⁺ catalysts in biphasic solution/supercritical CO₂ systems*. *Inorganic chemistry*, 2013. **52**(19): p. 10949-10957.
12. Lehn, J.M. and R. Ziessel, *Photochemical reduction of carbon dioxide to formate catalyzed by 2,2'-bipyridine- or 1,10-phenanthroline-ruthenium(II) complexes*. *J. Organomet. Chem.*, 1990. **382**(1-2): p. 157-173.
13. Tamaki, Y., et al., *Photocatalytic CO₂ reduction with high turnover frequency and selectivity of formic acid formation using Ru(II) multinuclear complexes*. *Proc. Natl. Acad. Sci. U. S. A.*, 2012. **109**: p. 15673-15678, S15673/1-S15673/7.
14. Ishida, H., K. Tanaka, and T. Tanaka, *Photochemical carbon dioxide reduction by an NADH model compound in the presence of ruthenium complexes [Ru(bpy)₃]²⁺ and [Ru(bpy)₂(CO)₂]²⁺ (bpy = 2,2'-bipyridine) in water/DMF*. *Chem. Lett.*, 1988(2): p. 339-42.
15. Ishida, H., et al., *Photochemical carbon dioxide reduction catalyzed by bis(2,2'-bipyridine)dicarbonylruthenium(2+) using triethanolamine and 1-benzyl-1,4-dihydronicotinamide as an electron donor*. *Inorg. Chem.*, 1990. **29**(5): p. 905-11.

16. Tamaki, Y., et al., *Development of highly efficient supramolecular CO₂ reduction photocatalysts with high turnover frequency and durability*. Faraday Discuss., 2012. **155**: p. 115-127.
17. Hawecker, J., J.M. Lehn, and R. Ziessel, *Photochemical and electrochemical reduction of carbon dioxide to carbon monoxide mediated by (2,2'-bipyridine)tricarbonylchlororhenium(I) and related complexes as homogeneous catalysts*. Helv. Chim. Acta, 1986. **69**(8): p. 1990-2012.
18. Chauvin, J., et al., *Towards New Molecular Photocatalysts for CO₂ Reduction: Photo-Induced Electron Transfer versus CO Dissociation within [Os(NN)(CO)₂Cl₂] Complexes*. Chem.--Eur. J., 2011. **17**(15): p. 4313-4322.
19. Ooyama, D., et al., *Structural and spectroscopic characterization of ruthenium(II) complexes with methyl, formyl, and acetyl groups as model species in multi-step CO₂ reduction*. J. Organomet. Chem., 2001. **619**(2): p. 299-304.
20. Tanaka, K. and D. Ooyama, *Multi-electron reduction of CO₂ via Ru-CO₂, -C(O)OH, -CO, -CHO, and -CH₂OH species*. Coord. Chem. Rev., 2002. **226**(1-2): p. 211-218.
21. Juris, A., et al., *Ru(II) polypyridine complexes: photophysics, photochemistry, eletrochemistry, and chemiluminescence*. Coord. Chem. Rev., 1988. **84**(0): p. 85-277.
22. Patz, M., et al., *Oxidation mechanism of NAD dimer model compounds*. Chem. Lett., 1997(6): p. 567-568.
23. Fukuzumi, S., et al., *Energetic comparison between photoinduced electron-transfer reactions from NADH model compounds to organic and inorganic oxidants and hydride-transfer reactions from NADH model compounds to p-benzoquinone derivatives*. J. Am. Chem. Soc., 1987. **109**(2): p. 305-316.
24. Tamaki, Y., et al., *Photocatalytic CO₂ reduction with high turnover frequency and selectivity of formic acid formation using Ru (II) multinuclear complexes*. Proceedings of the National Academy of Sciences, 2012. **109**(39): p. 15673-15678.
25. Juris, A., et al., *Ru (II) polypyridine complexes: photophysics, photochemistry, eletrochemistry, and chemiluminescence*. Coordination Chemistry Reviews, 1988. **84**: p. 85-277.

CHAPTER 6

Electrochemistry in expanded liquid and supercritical fluids

6.1. Introduction

In the two preceding chapters, photocatalytic reduction of carbon dioxide has been demonstrated to be feasible, but the process requires the consumption of a sacrificial electron donor. Inhibition of photocatalysis in presence of the dimer BNA₂ demonstrated the importance of irreversibility in the oxidation reaction of the electron donor. The consumption of an organic electron donor renders the photocatalytic process economically inexploitable. It is therefore interesting to investigate if the photosensitizing system can be replaced by a pure electrochemical system in which the catalyst is supplied in electron at an electrode surface.

The objectives of this chapter are to describe the high-pressure electrochemical conditions that will be used in the next chapter to study the electrocatalytic reduction of CO₂ with ruthenium and rhenium polypyridyl catalysts. In a first part, voltammetry in expanded liquids will be described for systems with a moderate pressure up to 50 bars. In the second part, voltammetry in supercritical conditions will be addressed with the determination of the volume of co-solvent required to render the supercritical phase conductive thus enabling

voltammetry on a macroscale electrode. Analysis of the voltammetric behavior of the reversible oxidation of decamethylferrocene (DMFc) will give insight on the nature of the supercritical phase close to the electrode. It is necessary to mention here that some parts of the present chapter were published in [1, 2].

6.2. Electrochemistry in expanded liquids

Voltammetry of CO₂-expanded liquids have only been scarcely studied, to date, only the work of Chanfreau *et al.* have been reported. They have studied the voltammetric behaviour of ferrocene in CO₂-expanded DMF to determine its diffusion coefficient as a function of pressure [3]. They have then investigated the electrocarboxylation reaction of benzyl chloride to synthesize phenylacetic acid in pressurized mixtures of CO₂ and DMF [4]. Their objective was to use an electrochemical process to replace the Grignard reaction commonly used in these processes. In the electrocarboxylation process, an organic halide is reduced on the electrode to a carbanion, which can further react with CO₂ to form the desired carboxylate. The carbanion formed at the electrode is indeed highly reactive. Therefore, increasing vastly the concentration of CO₂ by using CO₂-expanded DMF has the advantage of increasing the selectivity of the reaction. A pressure of 60 bars was found to be the optimal operating pressure.

As presented in section 1.2.3 of chapter 1, the current measured for a catalyst operating the electrocatalytic reduction of CO₂ depends on few parameters that are highly influenced by the composition of the gas-expanded liquid phase. The concentration of the catalyst is influenced by the volume of the phase. Thus, increasing the pressure cause the dilution of the catalyst. The diffusion coefficient of the catalyst in the media is also impacting the current measured. With an increase of pressure, this coefficient is supposed to decrease as the viscosity of the liquid is decreasing. Finally, the concentration of CO₂ has also an impact on the catalytic rate.

6.2.1. Phase composition

Determination of the expanded liquid phase volume and the CO_2 concentration were performed using the high-pressure NMR tube using the procedure described in section 2.3.9. The tube was initially filled with 3 mL of a solution of 0.2 M tetrabutylammonium hexafluorophosphate (TBAPF_6) in DMF. It has been observed that even a moderate concentration of electrolyte is decreasing the solubility of CO_2 in the liquid phase. At 50 bars the concentration of CO_2 decrease from 14 M to 10 M in presence of 0.2 M TBAPF_6 . In Figure 6.1., results for liquid phase volume, CO_2 concentration and molar fraction at a temperature of 20°C are shown.

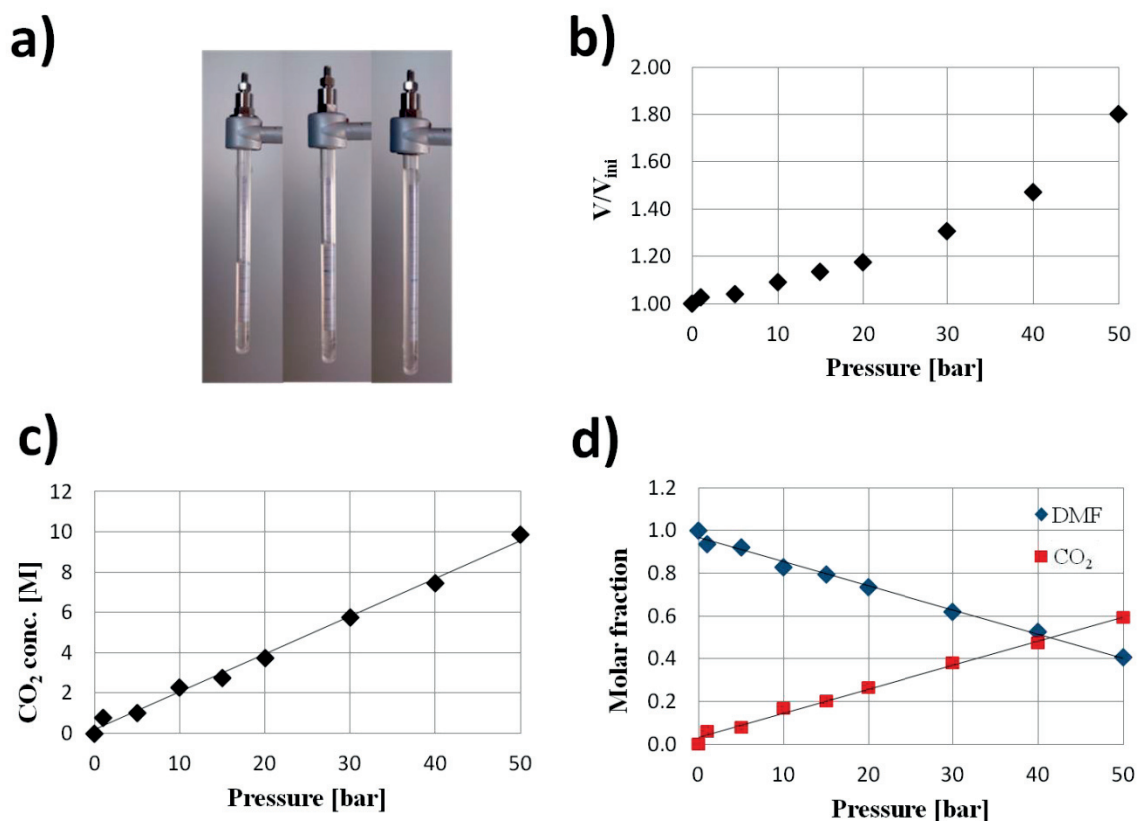


Figure 6.1 a) Photography of the reactor filled with 3 mL of 0.1 M TBAPF_6 in DMF at 1, 10 and 50 bars of CO_2 . b) Normalised volume of the solution as a function of CO_2 pressure. c) Concentration of CO_2 as a function of CO_2 pressure. d) Molar fraction of DMF and CO_2 in the liquid phase.

As it appears from these data, the volume of the liquid is increasing rather linearly between 1 and 20 bars, with a more steep increase above 20 bars. As at 20°C, the pressure of condensation of CO₂ is 57.3 bar, the volume of the liquid phase above this pressure is limited by the volume of the reactor. Concentration and molar fraction are following a linear increase over the complete pressure range considered. The experimental protocol was validated by comparison of results obtained in absence of electrolyte in pure DMF with results obtained by Duran-Valencia *et al.* [5] using gas chromatography analysis. Their method however, has the advantage of determining the composition of the gas phase in addition to the expanded liquid phase, with the gas phase being composed at 99.94% of CO₂ at 5.6 bar. This result supports the approximation used in the calculations, consisting of considering that the DMF was exclusively in the liquid phase.

Phase composition for different systems can therefore be determined by the method developed here such as the water-DMF liquid phase used in chapter 5. The concentration of CO₂ determined experimentally for different volume fractions of water is decreasing considerably in presence of water as shown in Figure 6.2. But the concentration of CO₂ determined by this method is the sum of the concentration of the different species that are in equilibrium in water : CO₂, H₂CO₃, HCO₃⁻ and CO₃²⁻.

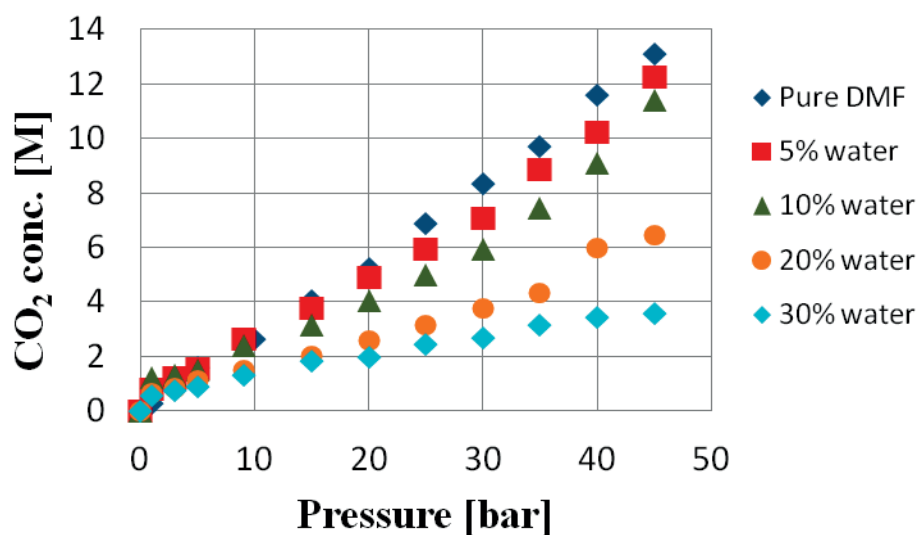


Figure 6.2. Concentration of CO₂ determined experimentally in DMF-water mixture as a function of pressure at 20°C.

6.2.2. Diffusion coefficient as function of pressure

In addition to the phase volume and composition, the diffusion coefficient of the CO₂ reduction catalyst studied by voltammetry is of great importance to evaluate its activity. Diffusion coefficients are commonly determined by rotating disk electrodes, but this method is unsuitable for high-pressure electrochemical analyses. Diffusion coefficients were determined from measurement of cyclic voltammetry of a reversible reduction with different scan rate (from 0.025 V/s to 0.5 V/s) at different pressures. The peak currents are function of the electrode surface, catalyst concentration, scan rate and diffusion coefficient as described by the Randles-Sevcik equation (Equation (1.9)). Knowing the catalyst concentration from the previous section, the diffusion coefficient at each pressure was determined from the linear relationship observed between the peak current and the square root of the scan rate.

To enable the determination of the diffusion coefficient of a catalyst, this latter must have a totally reversible reduction wave. The catalyst [ReCl(bpy)(CO)₃] was chosen, as it displays two successive reduction waves on voltammetry, with only the second wave being catalytic for CO₂ reduction. The first reduction wave of the complex is totally reversible and Randles-Sevcik equation is applicable. Similar analysis with the catalyst [Ru(bpy)₂(CO)H]⁺ is impossible as this catalyst reacts with CO₂ after the first reduction of the complex. But due to high similarities in term of size and nature of the ligands, the diffusion coefficients of these two catalysts should be comparable.

In Figure 6.3 a), the Randles-Sevcik analysis of the reversible wave of the catalyst under 20 bars of pressure is displayed. From similar analysis conducted in the same solution at different pressures, the diffusion coefficients are determined (Figure 6.3. b)). The diffusion coefficient is increasing linearly in the initial pressure increase up to 15 bars, with a 30% increase observed over this pressure range. This increase in diffusion coefficient is well explained by the Stokes-Einstein equation :

$$D_i = \frac{k_B T}{6\pi\eta r} \quad (6.1)$$

where k_B is the Boltzmann's constant, η the dynamic viscosity of the solvent and r the radius of the spherical particle considered. Viscosity of CO₂-expanded liquid is known to be highly influenced by CO₂ molar fraction. Foster *et al.* have experimentally determined the viscosity of CO₂-expanded methanol solution by falling-weight viscometry [6]. For them, the apparent correlation factor appeared to be the composition of the liquid phase and the degree of its volume expansion rather than the phase density or the pressure. They observed a linear relationship between the viscosity and the CO₂ molar fraction, which corroborates well the linear dependence observed herein between pressure and diffusion coefficient, as has a linear relationship is also observed between pressure and CO₂ molar fraction.

Above 20 bars of pressure, the diffusion coefficient remains more or less constant. This result is a bit surprising as CO₂ molar fraction is keeping increasing linearly until the liquid phase fills the entire reactor, which only happens at a pressure of 40. Therefore above this pressure, change in solution composition and liquid viscosity are suspected to be very limited with pressure. But the reactor volume constraint cannot explain the steady value of the diffusion coefficient observed between 20 and 40 bars. Conventional methods used with gas-expanded liquids for measuring fluids viscosity, such as falling-weight viscometry or electromagnetic viscometry are macroscale methods. While with voltammetry the diffusion coefficient are measured through a microscale layer on the electrode surface. The results obtained herein can be explained by heterogeneities in the solution, with the existence of a microscale film on the surface of the electrode and the wall of the reactor having a slightly different composition than the bulk solution.

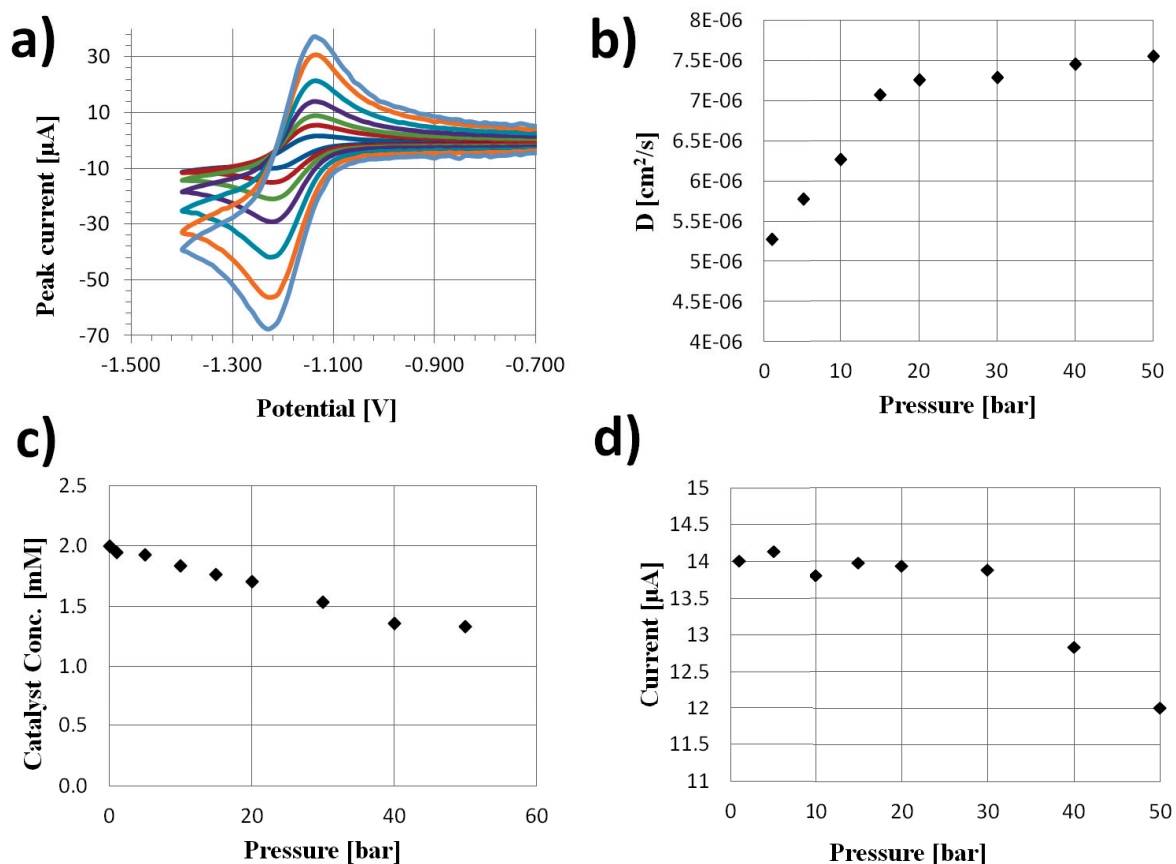


Figure 6.3. a) Cyclic voltammetry at 10, 25, 50, 100, 200, 350 and 500 mV/s of the reversible wave of $[\text{ReCl}(\text{bpy})(\text{CO})_3]$ in DMF with 0.2 M TBAPF₆ on a glassy carbon electrode at 20°C and 20 bars CO_2 . b) Diffusion coefficient obtained from Randles-Sevcik equation for $[\text{ReCl}(\text{bpy})(\text{CO})_3]$ in DMF as a function of CO_2 pressure at 20°C. c) Catalyst concentration in the high-pressure reactor as a function of pressure for an initial concentration of 2 mM $[\text{ReCl}(\text{bpy})(\text{CO})_3]$. d) Peak current of the reversible reduction wave of the catalyst as a function of pressure.

The behavior of the reversible peak current of the catalyst while the pressure is raising (Figure 6.3. d)) is well explained by the changes in diffusion coefficient and concentration up to 20 bars. Indeed both counter-balance each other at moderate pressures thus maintaining a constant reversible peak current. At higher pressures, the continuous dilution of the catalyst leads to a decrease in peak current as the diffusion constant remains stable. At 50 bars however, a continuous decrease in the current is not expected as the catalyst as already reached the concentration limit caused by the limited volume of the reactor. The decrease in peak current observed at this pressure is therefore not fully explained. At this pressure, the

important concentration of CO_2 in the liquid phase, approaching 10 M, is disturbing the voltammetry owing to the resistive character of liquid or supercritical CO_2 . As it seen in Figure 6.4. the potential is shifted to more negative values and the peak separation is increased from 90 mV to 120 mV indicating an ohmic drop in the solution between the electrodes. Appearance of an additional reduction wave before the reversible wave analyzed is very detrimental for accurate measures of the current peak height. This wave is attributed to the direct reduction of CO_2 on the connection of the glassy carbon electrode. Indeed, this wave is observed even in absence of catalyst. The glassy carbon electrode is not designed to support high-pressure, and after some series of experiments, the electrode appeared recessed by about 1 mm into the plastic body. The solution can therefore diffuse behind the working electrode and reaches the contact made of copper or brass on which the reduction of CO_2 is catalyzed. As it appears here, voltammetric analysis for comparison of catalyst activities is particularly difficult at pressure above 40 bars, where the molar fraction of CO_2 is above 50%.

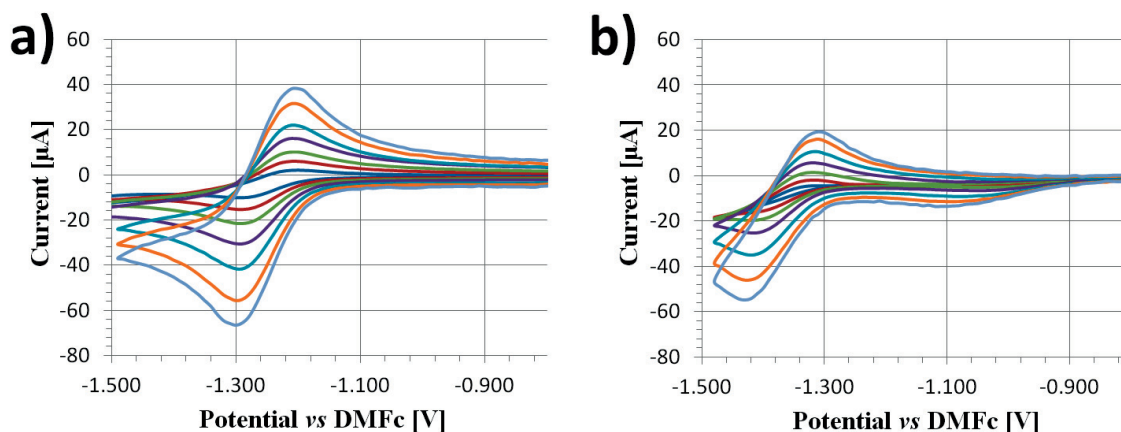


Figure 6.4. Cyclic voltammetry at 10, 25, 50, 100, 200, 350 and 500 mV/s of the reversible wave of $[\text{ReCl}(\text{bpy})(\text{CO})_3]$ in DMF with 0.2 M TBAPF_6 on a glassy carbon electrode at 20°C a) under 10 bars CO_2 b) under 50 bars CO_2 .

6.3. Electrochemistry in scCO₂

As it appeared in the precedent section, the high resistivity of the phase with molar fraction of CO₂ above 0.5 is causing important distortions on voltammetry. Therefore conducting voltammetry at higher pressures in supercritical conditions is challenging. As previously mentioned in chapter 1, scCO₂ is not a suitable solvent for electrochemistry owing to a very low dielectric constant ($\epsilon < 1.8$). Solubility of compounds is highly limited, especially for ionic species. With conventional organic solvent electrolytes proving insoluble in the supercritical phase [7, 8]. Consequently scCO₂ electrochemical research has predominantly focused on overcoming the low dielectric constant of the solvent. The first studies exclusively using scCO₂ as solvent were in the late 1980s by Wightman *et al.* [9-11]. Using water as a co-solvent and a microelectrode arrangement the group found that water aided the solvation of electrolyte [NHex₄ⁿ⁺][PF₆]⁻ and allowed for a defined ferrocene (Fc/Fc⁺) redox wave to be observed. Water was necessary to obtain an electrochemical signal with 0.64 M without electrolyte giving rise to an uncharacteristic reverse peak [9]. This was postulated to be due to the deposition of insoluble Fc⁺ ions on the electrode surface. Addition of electrolyte reduced the intensity of this reverse wave and conventional, reversible redox voltammetry for Fc was observed with 0.13 M water. Wightman and Michael later studied the direct modification of the microelectrode surface with a conductive ionic polymer membrane (Nafion), providing a conductive interface with which the dissolved Fc could interact (Figure 6.5. a)) [12]. Further developments lead to the appearance of surface modified electrodes that even allowed for studies of metallocenes without a polar co-solvent [13].

In the 1990s Abbott *et al* showed that very hydrophobic electrolytes, especially the class of the tetraalkylammonium tetraarylborate salts, could be dissolved in scCO₂ to a limited extent to give conductive media without a polar modifier [7, 8]. Voltammetry could be obtained, but analysis of data was difficult due to complications arising from strong adsorption processes at the electrode surface [14]. The latter publication was also the first attempt to achieve macroscale voltammetry in this resistive medium (Figure 6.5 b)). Abbott and Harper's comprehensive study highlighted the importance of solvent density on the

solubility of the electrolyte with conductivity increasing from 10^{-8} to 10^{-7} S·cm $^{-1}$ over the 313 – 343 K temperature range at 100 bars. At 300 bars, it was an order of magnitude higher. The authors attributed the better conductivity to improved solvation properties at pressures and temperatures where greater fluid densities are obtained. Bulky, hydrophobic electrolytes have since been commonplace in scCO $_2$ electrochemistry, with recent advances focusing on the halogenation of the ions. An extensive study by Bartlett *et al.* evaluated the conductivity of a series of electrolytes and determined that cation fluorination has little effect but for the anion it was crucial [15]. Specifically fluorinated derivatives of [BAR $_4$] $^{-}$, the BARF anions previously seen in chapter 3, were the most soluble and conductive in a mixed scCO $_2$ /acetonitrile fluid [15].

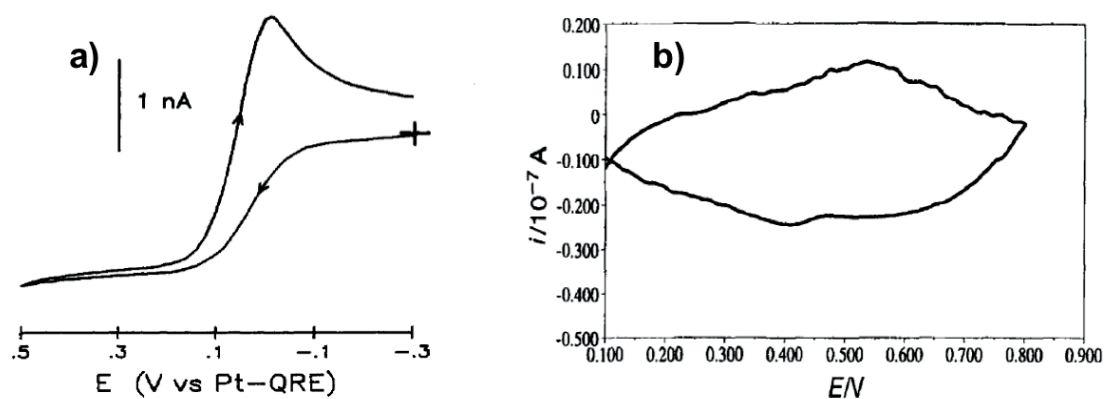


Figure 6.5. Examples of voltammetry in scCO $_2$, a) Fc (200 μ M) in scCO $_2$ containing 0.13 M water at 80°C and 89 bars. Scan rate 100mVs $^{-1}$ using a Nafion-coated Pt microelectrode (50 μ m) [11] b) TDDA $_2$ Ni(mnt) $_2$ (5 mM) in scCO $_2$ at 300 bars and 70°C containing 0.1 M n DecN $_4^+$ B(C $_6$ H $_5$) $_4^-$ electrolyte. Scan rate 1mV·s $^{-1}$ and 1 mm Pt electrode [14].

An alternative strategy proposed to enhance the ionic conductivity of the scCO $_2$ is to add a highly polar and miscible co-solvent. To-date methanol [15, 16], dimethylformamide [3] or acetonitrile [2, 15] have been employed. Organic co-solvents form a single phase with the CO $_2$ on reaching the critical point, and considerably improve the solubility of supporting electrolyte. This mixed solvent phase has been largely documented in the field electrodeposition [15, 17, 18], with Bartlett *et al.* recently reviving interest in SCFs as media for the electrodeposition of metals. Their research efforts have demonstrated that the unique

mass transport properties and lack of surface tension in supercritical media permits the formation of well-defined nano-structured electrodeposits [17].

6.3.1. Conductivity in scCO₂

Ferrocene and ferrocene derivative are frequently used as reference for the calibration of voltammetry in organic solvents. Due to its high solubility in scCO₂ decamethylferrocene (DMFc) has been chosen as redox couple for the analysis of voltammetry in scCO₂. This complex is used in the high-pressure three-electrode setup described in section 2.3.10, using the gold-disk electrode as working electrode and acetonitrile as polar co-solvent. The better electrolytes for scCO₂ electrochemistry are highly fluorinated salts and consist of bulky ions. Recent publications by Bartlett *et al* [19-21] explored a variety of lipophilic electrolytes for use in the supercritical medium, and specifically applied tetrabutylammonium hexafluorophosphate (TBAPF₆), tetrabutylammonium tetrafluoroborate (TBABF₄) and tetrabutylammonium tetrakis(3,5-trifluoromethyl phenyl) borate (TBATFMPB) as electrolytes for metal electrodeposition in scCO₂ fluid, the latter exhibiting the best conductivity. Studies by Abbott *et al.* [22-24] during the late 1990's found that increasing the cation size also gave favourable results with respect to the lipophilicity of the salt and solubility in supercritical CO₂ and non-polar solvents. Consequently, the electrolyte used in the present investigation used the large tetra(decyl)ammonium cation (TDA⁺) and tetrakis(pentafluorophenyl)boron anion (TB⁻). The anion was previously used in chapter 3 and proven to be capable to transfer protons from a water phase to a scCO₂ phase. The synthesis of the salt is reported in section 2.3.10. The bulky electrolyte formed was found to be a room temperature ionic liquid (RTIL), with a melting point of approximately 25°C, an unusual property given the symmetry of both ions. Similar RTILs have been used by Samec *et al.* in the study of charge-transfer process at the interface between water and ionic liquids [25].

In the presence of no other solvent, the molten electrolyte was found to swell slightly as the CO₂ pressure increased. But its solubility in scCO₂ remains negligible, leading to the formation of a biphasic system under supercritical conditions. The TDATB/scCO₂ fluid did

not give a significant current response over a 4 V potential window, and was therefore considered to be non-conducting.

A polar co-solvent was consequently introduced in the reactor to enable solubilization of the electrolyte in the supercritical phase. The TDATB and DMFc were therefore dissolved in varying amounts of acetonitrile to give a transparent yellow liquid. The liquid readily dissolved in the scCO_2 , preceded by extensive expansion of the solvent phase during the CO_2 saturation stage and formation of a single phase above critical pressure (*ca.* 73 at 313K). Electrochemical experiments were undertaken at 100 bar and 313K to ensure supercritical conditions.

In the scCO_2 - CH_3CN solution a current response was observed on the μA scale. The electrolyte concentration was 10 mM and the DMFc concentration 0.5 mM in the final volume of the reactor (18mL). The volume of acetonitrile added to the reactor was varied between 0.5 and 8 mL corresponding to a mole ratio $\text{CH}_3\text{CN}/\text{CO}_2$ of 0.04 to 0.60 respectively at 100 bar and 313K. The mole ratio was determined similarly as in expanded liquids. The CH_3CN -TDATB mixture did not dissolve in the scCO_2 until a ratio of at least 0.07 was achieved, and as shown in Figure 6.6 appreciable solution conductivity was not observed until a mole ratio of 0.13 (2 mL) was used, corresponding well to literature values [19, 26, 27].

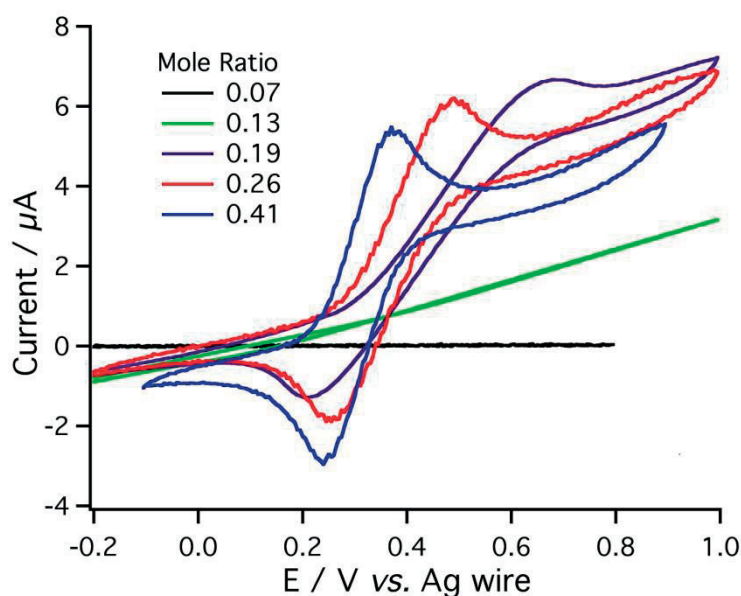


Figure 6.6. Overlay of cyclic voltammograms for increasing mole ratios of $\text{CH}_3\text{CN}/\text{CO}_2$. The solution in each experiment contained 10 mM TDATB electrolyte and 0.5 mM DMFc. The scan rate is $200 \text{ mV}\cdot\text{s}^{-1}$.

Above a ratio of 0.19 the DMFc redox couple became discernable, however, after a mole ratio of 0.3 any improvement in the DMFc voltammetry was not significant. In the absence of any electrolyte, a redox couple for DMFc was not observed, even at ratios as high as 0.8 (*i.e.* 10 mL).

Despite some degree of uncompensated resistance, the redox couple for DMFc was evident at ca. 0.3 V (*vs* Ag quasi reference electrode). The voltammetric behaviour shown in Figure 6.6. is similar to the response of a rotating disc electrode in a fully supported acetonitrile solution. The measured current is the sum of a steady-state component indicative of a fixed diffusion layer thickness, and of a peak shape response attributed to semi-infinite linear diffusion. As the mole ratio CH₃CN/CO₂ was increased, the steady state component decreased indicating a thicker diffusion layer. Indeed, extrapolation of the limiting current i_{lim} gave a diffusion layer thickness δ of 39, 54 and 59 μm for 0.19, 0.26 and 0.41, mole ratio respectively, at 200 $\text{mV}\cdot\text{s}^{-1}$ from the equation:

$$\delta = (FDC_{DMFc}A)/i_{lim} \quad (6.2)$$

where D is the diffusion coefficient of DMFc, C_{DMFc} its concentration and A the electrode area.

Conductivity studies of the TDATB electrolyte in acetonitrile at 40°C show an increase from 100 $\mu\text{S}\cdot\text{cm}^{-1}$ to 10 $\text{mS}\cdot\text{cm}^{-1}$. It would appear that this intrinsic conductivity increase is sufficient to raise the conductivity of the supercritical fluid and acetonitrile to eliminate a migrational flux component, and therefore observe near reversible voltammetry at 0.3 mole ratio and above. As the most peak-shaped voltammetry was achieved after a mole ratio of 0.41, scan rate dependence experiments were performed in this composition.

6.3.2. Scan rate dependence of DMFc in CH₃CN and scCO₂/CH₃CN

The scan rate dependence experiments, shown in Figure 6.7. indicate a semi-infinite linear diffusion process. Using the Randles-Sevcik equation (Equation (1.9)), a linear plot was obtained with a $R^2 = 0.9995$. However, extrapolation to zero scan rate yielded a steady-state component of 2 μA (Figure 3b). The near steady-state voltammetry observed at 25 $\text{mV}\cdot\text{s}^{-1}$, illustrated in the in-set of Figure 3a, gave a comparable limiting current of 2.4 μA . A steady-state response was also readily achieved at considerably higher scan rates (1 $\text{V}\cdot\text{s}^{-1}$), when the system was placed under moderate stirring using a magnetic stirrer.

The electrochemical response of the same three-electrode set-up was also observed under atmospheric pressure in only acetonitrile and electrolyte. In similar conditions of concentration: 0.5 mM and 10 mM, for DMFc and electrolyte respectively, at a temperature of 313 K. As expected, typical peak-shaped voltammograms attributed to semi-infinite linear diffusion were observed at a macro electrode in quiescent conditions at 25 $\text{mV}\cdot\text{s}^{-1}$ and above. Furthermore, extrapolation of the scan rate dependence plot yielded zero current at zero scan rate, confirming the absence of any steady-state component (Figure 6.8.). The comparison of CH₃CN to scCO₂/CH₃CN voltammetry clearly indicates an intrinsic difference in mass transport regimes, especially as the magnitude of Faradaic current in both conditions is the same.

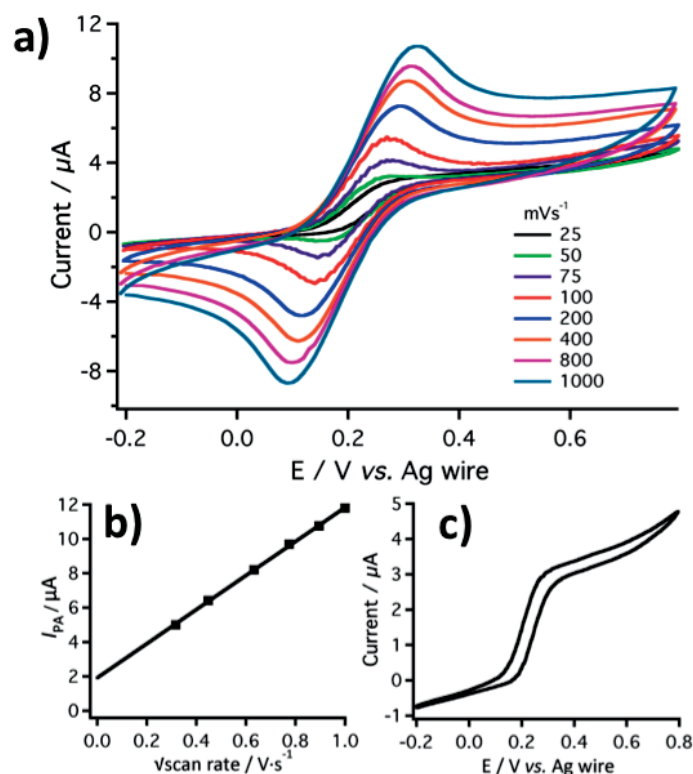


Figure 6.7. Overlay of cyclic voltammograms obtained for DMFc at increasing scan rate (25 - 1000 mV·s⁻¹). Medium consists of DMFc (0.5 mM), TDATB (10 mM), CH₃CN (mole ratio 0.41) and CO₂ at 100 bars (10 MPa) and 313 K. b) Plot of anodic peak current vs. the square root of the scan rate. c) The steady-state CV observed at 25 mV·s⁻¹.

Randles-Sevcik analysis of the results shown in Figures 6.7 and 6.8 also allowed for the estimation of the DMFc diffusion coefficient, D . The calculated value of $1.86 \cdot 10^{-5} \text{ cm}^2 \cdot \text{s}^{-1}$ in supercritical conditions was almost the same as in pure acetonitrile ($1.85 \cdot 10^{-5} \text{ cm}^2 \cdot \text{s}^{-1}$) at the same temperature and concentration of electrolyte. This second value is in good agreement with the previously reported constant for DMFc measured in acetonitrile [28], when the higher temperature of 313 K and different electrolytes used are taken into consideration. This result appears highly surprising as a marked increase in diffusion coefficient for a rhenium complex was observed in CO₂-expanded DMF. Acetonitrile is less viscous than DMF, therefore a smaller change in diffusion coefficient can be expected, but not similar values. Chanfreau reported a decrease in diffusion coefficient of ferrocene at pressure above 60 bars in DMF-scCO₂ phase [3]. Similarly, binary diffusion coefficients of ferrocene and 1,1'-dimethylferrocene in scCO₂ measured by the Taylor dispersion method

and chromatographic impulse response were reported to decrease while the pressure was raising [29].

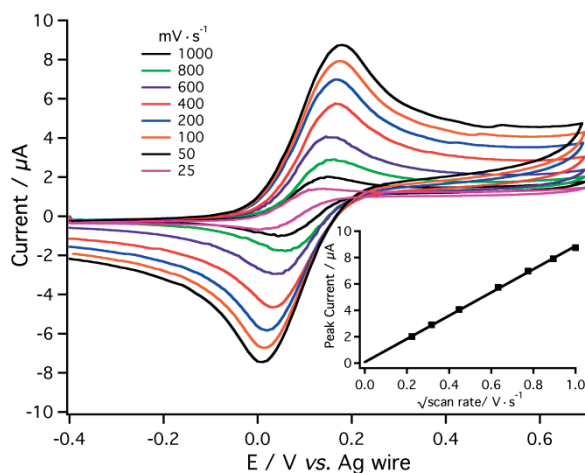


Figure 6.8. Overlay of cyclic voltammograms obtained in atmospheric conditions of pressure for DMFc (0.5 mM) at increasing scan rates (25 – 1000 mV s⁻¹) in CH₃CN fully supported by TDATB (10 mM), at 313 K. Inset) The plot of anodic peak current vs. square root of scan rate.

6.3.3. Diffusion in the scCO₂/CH₃CN single phase

The fact that the diffusion coefficients calculated for DMFc in supercritical conditions and in pure acetonitrile are near identical is either a huge coincidence or suggests that a liquid-like acetonitrile phase is forming at the electrode surface. Determination of the diffusion coefficient as a function of pressure expanded liquid and supercritical conditions would help to confirm the second hypothesis. The thickness of the suspected layer of acetonitrile is restricted in the supercritical conditions, giving rise to a steady-state response at moderate scan rates, below 50 mV·s⁻¹. From the near steady-state voltammogram observed at 25 mV·s⁻¹ in the scCO₂/CH₃CN solution, a diffusion layer thickness of 60 µm was determined from the limiting current. Given the strict limits of the diffusion layer in the scCO₂ fluid, it may be inferred that beyond the liquid-like phase is a more turbulent, supercritical-like phase. This bulk phase exhibits high natural convection, owing to the low viscosity of the supercritical fluid, and inevitable density differences throughout. Compton *et al.* [30, 31] observed a

comparable steady-state response at macro electrodes in a series of studies exploring sonoelectrochemistry. The exhibited restriction in diffusion layer thickness was much more pronounced in their studies however, ranging between 1 and 6 μm [31].

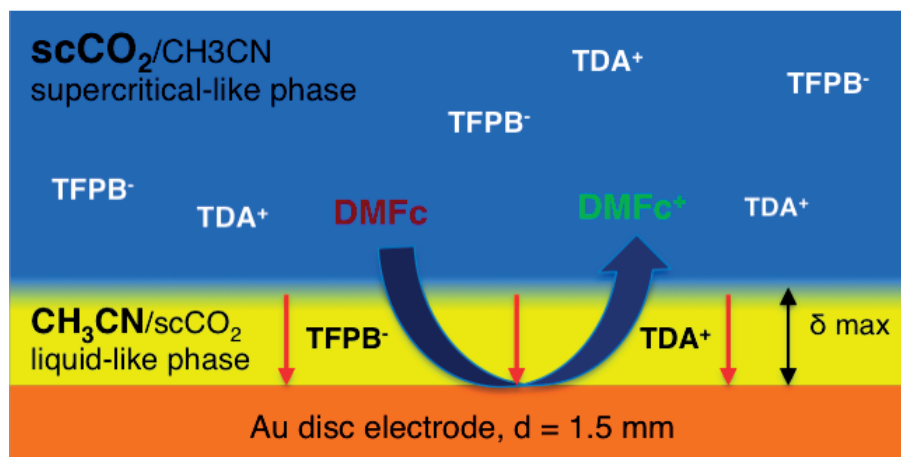


Figure 6.9. A schematic representation of the proposed thin-layer of CH_3CN (yellow) compressed and restricted by the more turbulent bulk $\text{scCO}_2/\text{CH}_3\text{CN}$ phase (blue). The electrolyte and DMFc concentrations are considered uniform throughout the two liquids, and the diffusion layer thickness is assumed not to propagate beyond the thin layer of CH_3CN .

The electrochemical system may therefore be considered in terms of both thin-layer and convective-diffusion voltammetry. The proposed system is depicted in Figure 6.9. with a thin layer of mostly acetonitrile at the electrode surface restricted in thickness by the $\text{scCO}_2/\text{CH}_3\text{CN}$ phase in the bulk solution, both of which are fully supported by the electrolyte. The DMFc concentration is uniform throughout the reactor, and supplements the liquid CH_3CN thin layer on depletion of the diffusion layer. Consequently, the diffusion coefficient calculated is that of DMFc in pure acetonitrile and electrolyte, rather than in a more mixed and diffuse solution with scCO_2 , which would have different viscosity and density.

When electrochemical reactions are performed at a macro interface (*i.e.* at an electrode over a mm in diameter), in a liquid medium the key limitation on the current magnitude is the rate of mass-transport. Typically, when voltammetry is carried out in a large volume of stagnant liquid a depletion of redox species concentration occurs near the electrode surface limiting the measured currents and imposing a concentration gradient towards the electrode. The rate of mass transport is considered entirely dependent on this gradient and the rate at which the redox species can diffuse to the electrode from the bulk concentration. At high scan

rates, diffusion limited mass transport effects are particularly pronounced. On the contrary, in well-stirred or convective media the rate of redox species consumption at the electrode is comparable to the fast mass transfer rate to the electrode, thus providing a constant, steady flux of material for oxidation or reduction (*i.e.* steady-state). The intermediate case with a thin layer of stagnant liquid phase, between an electrode and highly convective solution, should exhibit transitional behavior. Voltammograms simulated by the finite elements methods at $50 \text{ mV}\cdot\text{s}^{-1}$ with thin layer thickness varied does reflect the transitional voltammetry observed experimentally at thickness between 60 and 70 μm .

6.4. Conclusions

Voltammetry in high CO_2 content solutions was achieved through two different approaches. In the first one, the concentration of CO_2 was progressively increased by the expansion of the liquid phase as CO_2 was compressed in the solution. Liquid phase volume, CO_2 concentration and diffusion coefficient of $[\text{ReCl}(\text{bpy})(\text{CO})_3]$ were determined over a pressure range of 1 to 50 bars. The diffusion coefficient is increasing with pressure up to 20 bars, and remains stable above this pressure.

In the second approach, voltammetry was performed in supercritical conditions, starting from pure scCO_2 with a RTIL used as electrolyte. Acetonitrile was added as co-solvent to the supercritical phase to increase the conductivity of the phase to enable voltammetric measurements without the aid of a modified electrode surface or microelectrode dimensions. The low viscosity supercritical carbon dioxide fluid evidently enhances diffusion to the electrode, as steady-state voltammetry is observed at high scan rates of up to $50 \text{ mV}\cdot\text{s}^{-1}$. Moderate stirring of the solution also gave near steady-state voltammetry at scan rates as high as $1000 \text{ mV}\cdot\text{s}^{-1}$. Experimental and simulation results suggest that a quiescent liquid-like film of mostly CH_3CN and electrolyte is formed at the electrode surface, which is limited in thickness but supplemented by a more convective, supercritical-like phase in the bulk

solution. The presence of this film enables electrochemical studies of species dissolved in the supercritical phase.

6.5. Bibliography

1. Toghil, K.E., M.A. Méndez, and P. Voyame, *Electrochemistry in supercritical fluids: A mini review*. Electrochemistry Communications, 2014. **44**: p. 27-30.
2. Toghil, K.E., et al., *Steady-state macroscale voltammetry in a supercritical carbon dioxide medium*. Physical Chemistry Chemical Physics, 2013. **15**(3): p. 972-978.
3. Chanfreau, S., et al., *Electrochemical determination of ferrocene diffusion coefficient in liquid media under high CO₂ pressure: Application to DMF–CO₂ mixtures*. Journal of Electroanalytical Chemistry, 2007. **604**(1): p. 33-40.
4. Chanfreau, S., et al., *Electrocarboxylation in supercritical CO₂ and CO₂-expanded liquids*. The Journal of Supercritical Fluids, 2008. **46**(2): p. 156-162.
5. Duran-Valencia, C., et al., *Isothermal Vapor–Liquid Equilibria of the Carbon Dioxide (CO₂)–N,N-Dimethylformamide (DMF) System at Temperatures from 293.95 K to 338.05 K and Pressures up to 12 MPa*. Journal of Chemical & Engineering Data, 2001. **46**(6): p. 1589-1592.
6. Sih, R., F. Dehghani, and N.R. Foster, *Viscosity measurements on gas expanded liquid systems—Methanol and carbon dioxide*. The Journal of Supercritical Fluids, 2007. **41**(1): p. 148-157.
7. Abbott, A.P., et al., *Tetrakis(decyl)ammonium tetraphenylborate: a novel electrolyte for non-polar media*. Journal of the Chemical Society, Faraday Transactions, 1996. **92**(10): p. 1747-1749.
8. Abbott, A.P. and J.C. Harper, *Double layer capacitance and conductivity studies of long chain quaternary ammonium electrolytes in supercritical carbon dioxide*. Physical Chemistry Chemical Physics, 1999. **1**(5): p. 839-841.
9. Philips, M.E., et al., *Effect of added water on voltammetry in near-critical carbon dioxide*. The Journal of Physical Chemistry, 1987. **91**(15): p. 3934-3936.
10. Niehaus, D., et al., *Voltammetry of ferrocene in supercritical carbon dioxide containing water and tetrahexylammonium hexafluorophosphate*. The Journal of Physical Chemistry, 1989. **93**(16): p. 6232-6236.
11. Michael, A.C. and R.M. Wightman, *Microelectrodes coated with ionically conducting polymer membranes for voltammetric detection in flowing supercritical carbon dioxide*. Analytical Chemistry, 1989. **61**(3): p. 270-272.
12. Michael, A.C. and R.M. Wightman, *Voltammetry in supercritical carbon dioxide at platinum microdisk electrodes coated with perfluorinated ion-exchange membranes*. Analytical Chemistry, 1989. **61**(19): p. 2193-2200.
13. Sullenberger, E.F. and A.C. Michael, *Voltammetry with poly(ethylene oxide)-coated microelectrodes in carbon dioxide*. Analytical Chemistry, 1993. **65**(17): p. 2304-2310.
14. Abbott, A.P. and J.C. Harper, *Electrochemical investigations in supercritical carbon dioxide*. Journal of the Chemical Society, Faraday Transactions, 1996. **92**(20): p. 3895-3898.
15. Bartlett, P.N., et al., *Phase behaviour and conductivity study on multi-component mixtures for electrodeposition in supercritical fluids*. Physical Chemistry Chemical Physics, 2010. **12**(2): p. 492-501.

16. Jun, J. and P.S. Fedkiw, *Ionic conductivity of alkali-metal salts in sub- and supercritical carbon dioxide+methanol mixtures*. Journal of Electroanalytical Chemistry, 2001. **515**(1–2): p. 113-122.
17. Bartlett, P.N., et al., *Electrodeposition from supercritical fluids*. Physical Chemistry Chemical Physics, 2014.
18. Ke, J., et al., *Electrodeposition of metals from supercritical fluids*. Proceedings of the National Academy of Sciences of the United States of America, 2009. **106**(35): p. 14768-14772.
19. Bartlett, P.N., et al., *Phase behaviour and conductivity study on multi-component mixtures for electrodeposition in supercritical fluids*. Phys. Chem. Chem. Phys., 2010. **12**(2): p. 492-501.
20. Cook, D., et al., *The electrodeposition of copper from supercritical CO₂/acetonitrile mixtures and from supercritical trifluoromethane*. Phys. Chem. Chem. Phys., 2010. **12**(37): p. 11744-11752.
21. Ke, J., et al., *Electrodeposition of metals from supercritical fluids*. Proc. Natl. Acad. Sci. U. S. A., 2009. **106**(35): p. 14768-14772, S14768/1-S14768/5.
22. Abbott, A.P., et al., *Tetrakis(decyl)ammonium tetrphenylborate. A novel electrolyte for non-polar media*. J. Chem. Soc., Faraday Trans., 1996. **92**(10): p. 1747-1749.
23. Abbott, A.P. and J.C. Harper, *Electrochemical investigations in supercritical carbon dioxide*. J. Chem. Soc., Faraday Trans., 1996. **92**(20): p. 3895-3898.
24. Abbott, A.P. and J.C. Harper, *Double layer capacitance and conductivity of long chain quaternary ammonium electrolytes in supercritical carbon dioxide*. Phys. Chem. Chem. Phys., 1999. **1**(5): p. 839-841.
25. Samec, Z., J. Langmaier, and T. Kakiuchi, *Charge-transfer processes at the interface between hydrophobic ionic liquid and water*. Pure Appl. Chem., 2009. **81**(8): p. 1473-1488.
26. Wu, W., et al., *Effect of Organic Cosolvents on the Solubility of Ionic Liquids in Supercritical CO₂*. J. Chem. Eng. Data, 2004. **49**(6): p. 1597-1601.
27. Wu, W., et al., *Solubility of room-temperature ionic liquid in supercritical CO₂ with and without organic compounds*. Chem. Commun. (Cambridge, U. K.), 2003(12): p. 1412-1413.
28. Matsumoto, M. and T.W. Swaddle, *The Decamethylferrocene(+/0) Electrode Reaction in Organic Solvents at Variable Pressure and Temperature*. Inorg. Chem., 2004. **43**(8): p. 2724-2735.
29. Kong, C.Y., et al., *Measurements of Binary Diffusion Coefficients for Ferrocene and 1,1'-Dimethylferrocene in Supercritical Carbon Dioxide*. Journal of Chemical & Engineering Data, 2010. **55**(9): p. 3095-3100.
30. Holt, K.B., et al., *Sonoelectrochemistry at platinum and boron-doped diamond electrodes: achieving 'fast mass transport' for 'slow diffusers'*. J. Electroanal. Chem., 2001. **513**(2): p. 94-99.
31. Compton, R.G., F. Marken, and T.O. Rebbitt, *Sonovoltammetric measurement of the rates of electrode processes with fast coupled homogeneous kinetics: making macroelectrodes behave like microelectrodes*. Chemical Communications, 1996(9): p. 1017-1018.

CHAPITRE 7

Electrocatalytic reduction by ruthenium and rhenium catalysts

7.1. Introduction

In chapter 6, the conditions for operating electrochemical measurements at elevated pressures have been well described. The objectives of this chapter will be to apply the electrochemistry in expanded liquids and in supercritical CO₂ to the study of two catalysts of the polypyridyl family. The principal objective of this chapter is to investigate the effect of CO₂ pressure on the catalytic mechanisms for CO₂ reduction. The first catalyst will be the ruthenium catalyst previously used in chapter 5, [Ru(bpy)₂(CO)H]⁺. As it was already demonstrated in chapter 5, this catalyst has an overall complex mechanism owing to the existence of two different catalytic cycles producing two different products: carbon monoxide and formate. Analysis of the voltammetry is therefore complicated as different reactions are happening simultaneously. The catalytic cycles are shown again in Figure 7.1. The photosensitization cycles that were supplying the catalyst in electrons in chapter 5 are now replaced with electron transfers happening at the electrode. The potentials of these electron transfers are reported *versus* SHE

and were determined experimentally by Tanaka and Meyer for the carbon monoxide and formate cycle respectively [1, 2].

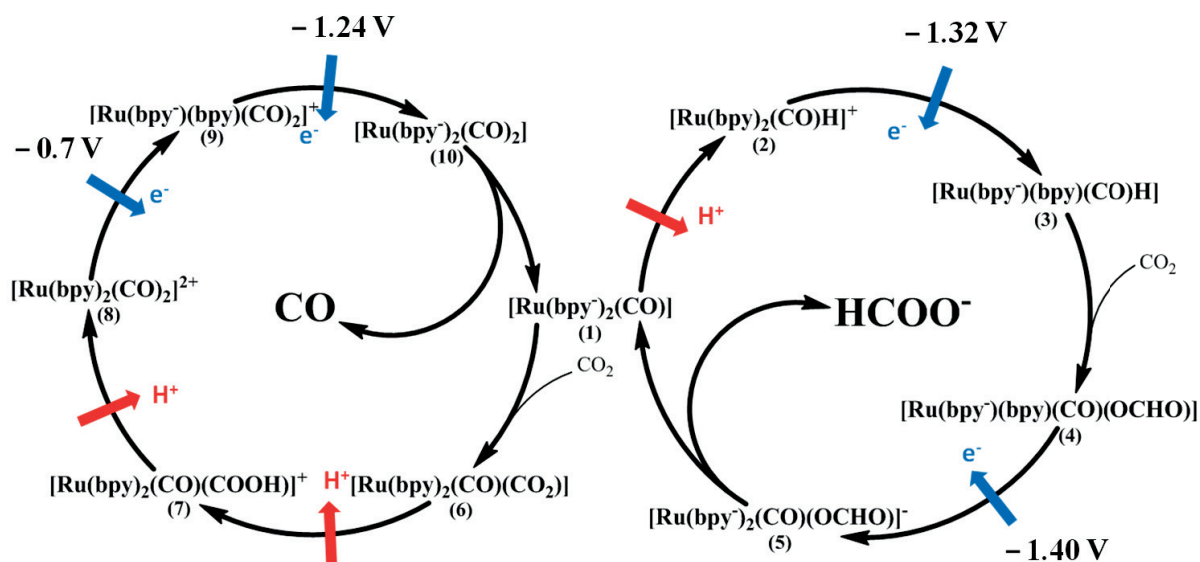


Figure 7.1. The combination of two catalytic cycles for the $[\text{Ru}(\text{bpy})_2(\text{CO})\text{L}]^{n+}$ in the catalytic reduction of CO₂ to formate or carbon monoxide.

In addition, an alternative catalyst will be investigated: $[\text{ReCl}(\text{bpy})(\text{CO})_3]$. This catalyst has the advantage of being totally selective toward CO evolution. Additionally, the mechanism of CO evolution has been investigated recently by Kubiak *et al.* by density functional theory [3]. The computed mechanism obtained is shown in Figure 7.2., and will serve as a good base for the understanding of the voltammetric behavior of this catalyst. With a unique mechanism for CO₂ reduction, determination of the apparent rate constant of the catalytic process is possible. And therefore quantification of the advantage provided by high CO₂ pressure can be done.

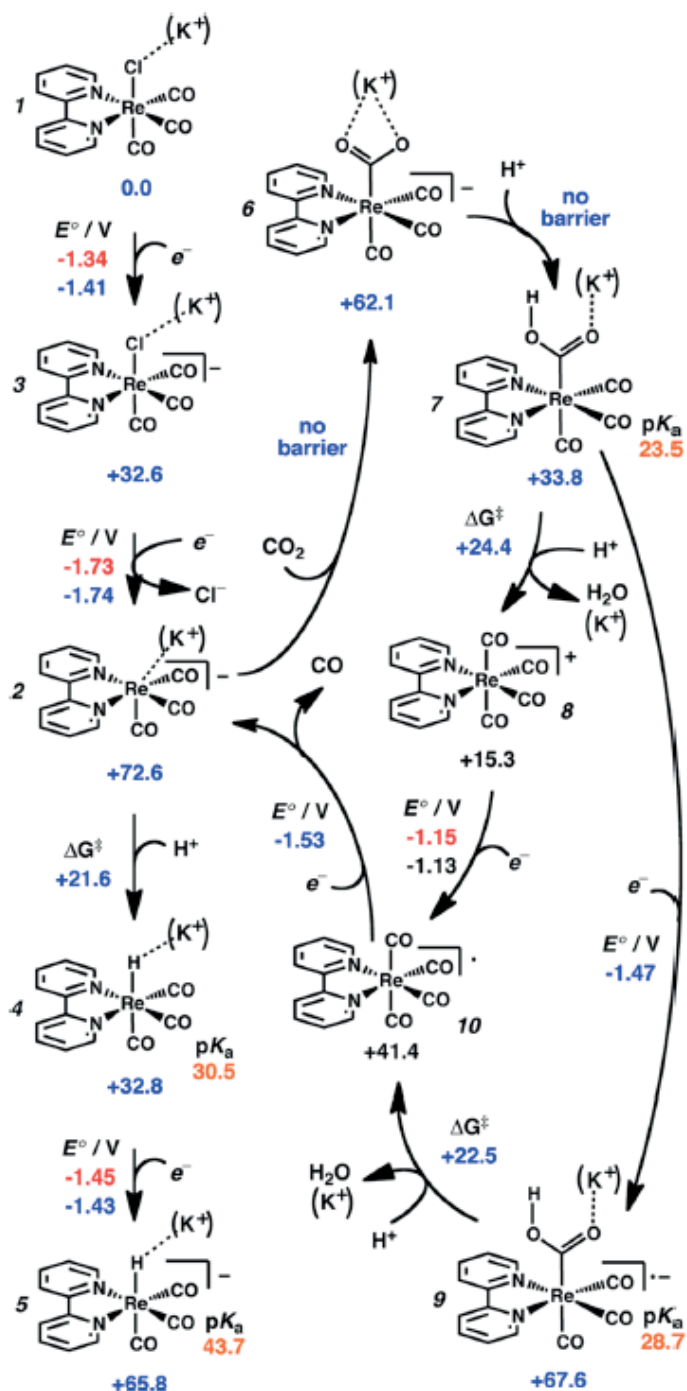


Figure 7.2. Complete mechanism of CO₂ reduction by [Re(bpy)(CO)₃Cl] proposed by Kubiak, in red experimentally obtained reduction potentials and in blue calculated data [4].

The first objective of this chapter is to investigate the electrochemical behaviour of two chosen catalysts and determine how the catalytic mechanism is affected by different factors

such as proton donor concentrations or CO₂ pressures. In the preceding chapter, the difficulties of conducting electrochemistry under high pressures have already been discussed. As it was shown, the solution become highly resistive, which is causing important distortion in the voltammetry due to ohmic drop. Additionally under high pressures, perfect sealing of the reactor becomes difficult, and connections of the electrodes can be exposed in the solution. These connections are made of copper, which can catalyze the direct reduction of CO₂, thus causing the appearance of new voltammetric signal at high pressures. For these reasons, catalytic activity of the two selected catalysts will be investigated in a limited range of pressure, up to 50 bars in expanded organic solvent.

In the field of electrochemical reduction of CO₂, the effect of CO₂ pressure have been mainly limited to the study of product distribution as a function of pressure in electrolysis experiments. While catalytic mechanism investigation by voltammetry has only been scarcely performed and exclusively restricted to heterogeneous catalysis. Abbott reported a decrease in the reduction potential in supercritical state for the reduction of CO₂ on Pt and Pb electrode surfaces [5]. Sakara *et al.* reported a change in reduction product selectivity on copper electrodes while the pressure was increased. Hydrogen being the major product at low pressures, CO at high pressures, and at intermediate pressures different hydrocarbons were observed such as methane, ethylene and ethanol [6]. For homogeneous catalysis of CO₂ reduction, high-pressure voltammetry is a field that has not been explored yet for the investigation of catalytic mechanisms.

7.2. Ruthenium catalyst

7.2.1. Voltammetric behaviour

For cyclic voltammograms (CV) reported in this chapter, the setup and procedure used was described in sections 2.2.2 and 2.3.10. Initially, the gold disk electrode was used, and was thereafter replaced by a glassy carbon electrode to improve the voltammetry. Calibration of the

potential window was achieved by introduction of decamethylferrocene (DMFc) in the solution to have a reference reversible oxidation wave in the cyclic voltammograms. The electrode potential is therefore always given *versus* the half-wave potential of DMFc.

Voltammetric behaviour of the catalyst $[\text{Ru}(\text{bpy})_2(\text{CO})\text{H}](\text{PF}_6)$ in acetonitrile and atmospheric conditions of pressure is presented in Figure 7.3. On the right of the CV, the reversible oxidation of DMFc is shown. In the negative potential region, in absence of CO_2 two successive reversible reduction waves are observed. These two reduction waves are attributed to the reduction of the two bipyridyl ligands in the catalyst. The first reduction wave corresponds to the step (2-3) in Figure 7.1., while the second reduction is only observed in absence of CO_2 . Under atmospheric CO_2 pressure, the first wave becomes irreversible even at a scan rate of 1000mV/s. Two additional waves are appearing with CO_2 , the wave at 1.4 V corresponds to the reduction of the formato complex formed upon CO_2 addition on the reduced hydride complex, which is corresponding to the step (4-5) in Figure 7.1. The second reduction wave was unexpected from the mechanism previously discussed. As this wave appears at potentials more negative, the catalytic complexes that are responsible of this reduction current have already undergo one complete catalytic cycle. Therefore, the determination of the mechanism involved here is impossible at the present stage. The reduction potential is more negative than any step shown in Figure 7.1. and slightly more negative than the second reduction of the hydride complex. Variation in the conditions of pressure and proton concentration will be used in the following section to obtain more insight in the mechanisms involved.

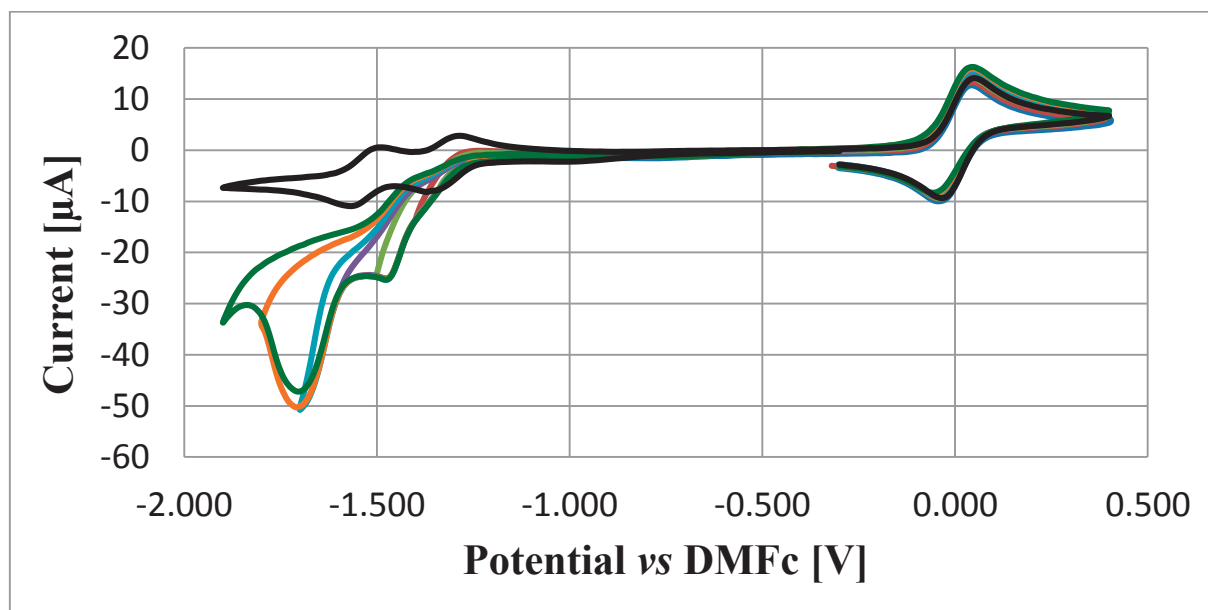


Figure 7.3. CV in AcN 0.1 M TBAPF₆ of 1mM [Ru(bpy)₂(CO)H](PF₆), gold working electrode, potential calibrated versus DMFc⁺/DMFc, scan rate 100mV/s, in black under argon in colour under atmospheric pressure of CO₂ with different vertex potentials.

7.2.2. Variation in protons and CO₂ concentrations

The acetonitrile used as solvent in the preceding section is not completely dry, the water present as contaminant (0.1%) can be the source of protons required for CO₂ reduction. This corresponds to a concentration of 55mM. For the next experiments, 50µL of water was added to the reactor to increase its concentration to 275mM. With this higher water concentration, the shapes of the different CVs are highly modified as shown in Figure 7.4. Voltammograms from the left hand side are taken with addition of water. In addition to the change in proton donor concentration, CO₂ pressure was also varied between 1 and 6 bars. The scan rate was increased to 500mV/s as the difference in voltammograms shape is more pronounced at higher scan rate.

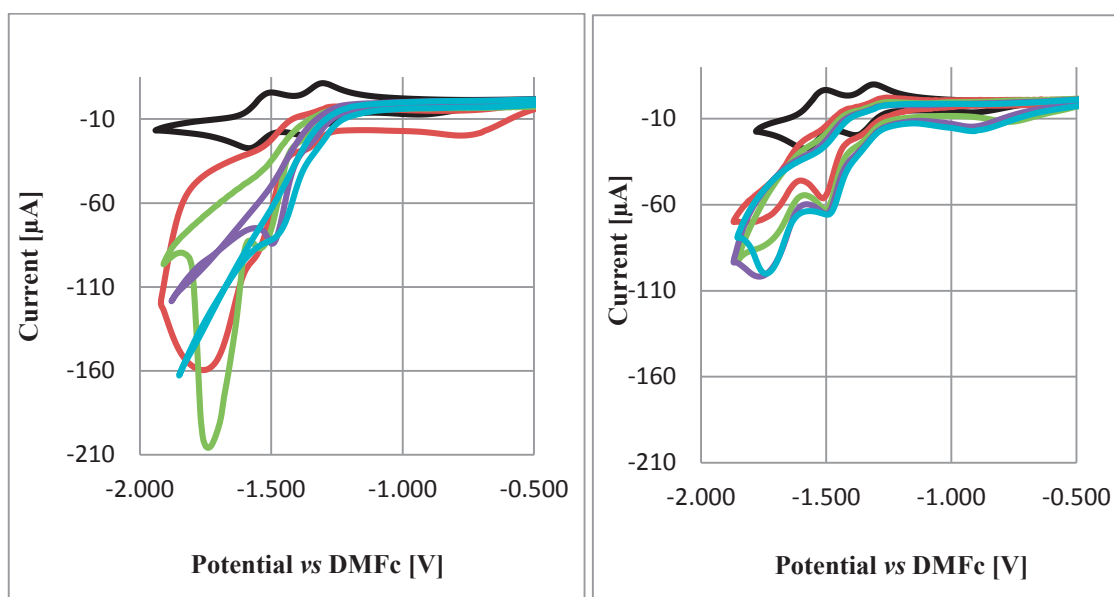


Figure 7.4. CV in AcN 0.1 M TBAPF₆ of 1mM [Ru(bpy)₂(CO)H](PF₆) with 275mM water (left) and without water (right), gold working electrode, potential calibrated versus DMFc⁺/DMFc, scan rate 500mV/s, under argon in black and in colour for different pressure of CO₂ (1 bar in red, 2 bars in green, 4 bars in purple and 6 bars in blue).

The first catalytic wave, corresponding to the reduction of the formato complex, appears almost not affected by the concentration of water and CO₂ pressure. While the second unidentified wave, is highly increased in presence of water. The effect of pressure on this catalytic wave is surprising. In presence of water the current measured for this wave is maximal for a CO₂ pressure of 2 bars, but above this pressure this wave is not observed in presence of water.

The use of a gold working electrode limits severely the range of pressure that can be studied, especially with addition of water. Above a pressure of 3 bars, the current measured comes almost exclusively from the direct reduction of CO₂ on the gold electrode surface. Hori and Ikeda have demonstrated that the reduction of carbon dioxide is efficiently catalyzed by gold electrode in aqueous solution [7]. In Figure 7.5. comparison with a solution without catalyst demonstrate that the catalyst is not participating in the reduction current measured.

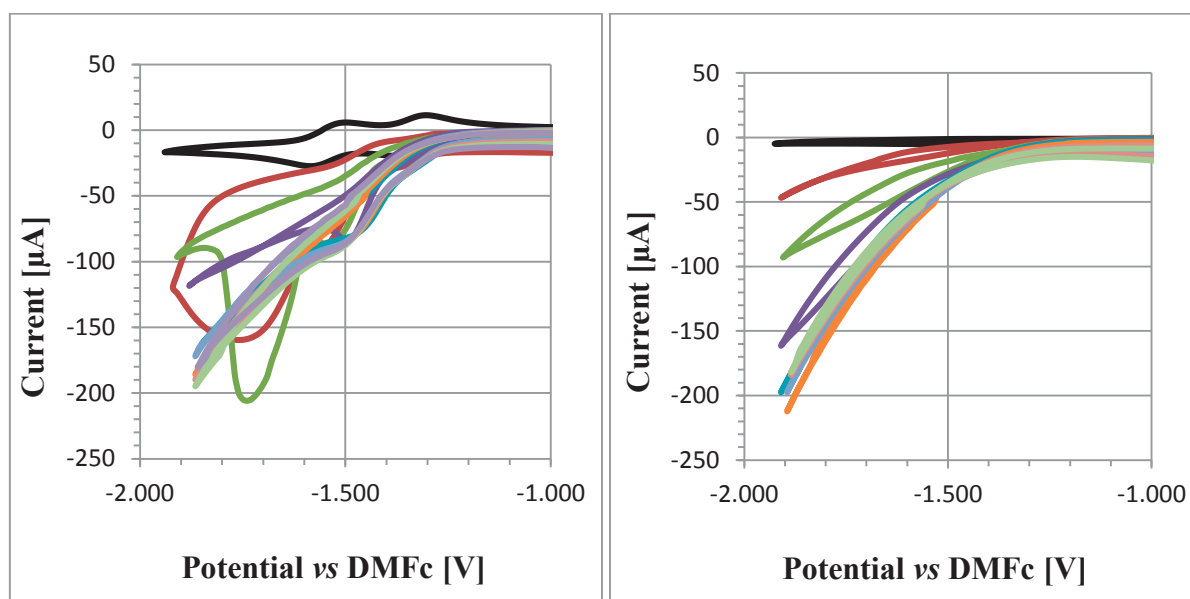


Figure 7.5. CV in AcN 0.1 M TBAPF₆ with 275mM water of 1mM [Ru(bpy)₂(CO)H](PF₆) (left) and no catalyst (right), gold working electrode, potential calibrated versus DMFc⁺/DMFc, scan rate 500mV/s, in black under argon and in colour for different pressure of CO₂ (1, 2, 4, 6, 8, 10, 12, 14 and 16 bars).

As can be seen, the reduction current measured at 3 bars and above is totally similar with and without catalyst. To observe the activity of the catalyst toward CO₂ reduction, a limited range of pressure will be investigated. To compare more easily the activity of the catalyst in different conditions, subtraction of the current measured in absence of catalyst will be performed for the following voltammograms. Additionally, to improve the readability of the figures, only the forward scan are displayed. In the following four figures, the effect of water addition is shown at four different CO₂ pressure and with scan rate ranging from 50 to 1000mV/s. With higher scan rate implying larger current. On the left hand side the voltammograms are measured with addition of water, while on the other side, no water has been added.

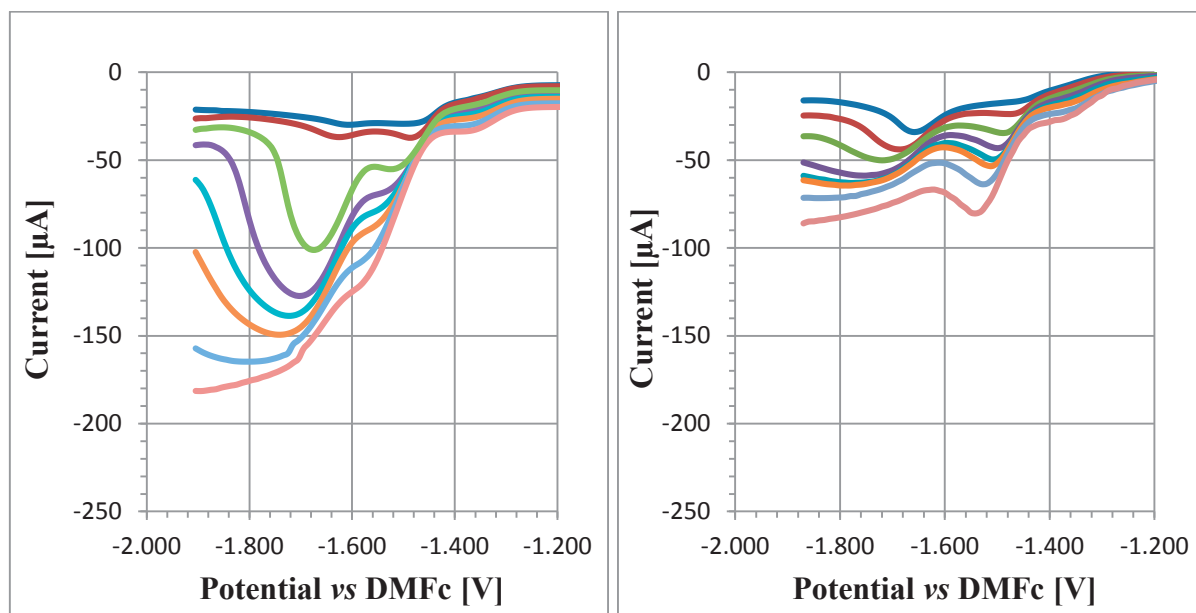


Figure 7.8. Blank subtracted linear scan in AcN 0.1 M TBAPF₆ with 275 mM of water added (left) and dry acetonitrile (right) of 1mM [Ru(bpy)₂(CO)H](PF₆), gold working electrode, potential calibrated versus DMFc⁺/DMFc, under CO₂ at atmospheric pressure at different scan rate (50 , 100, 200, 300, 400, 500, 750 and 1000 mV/s).

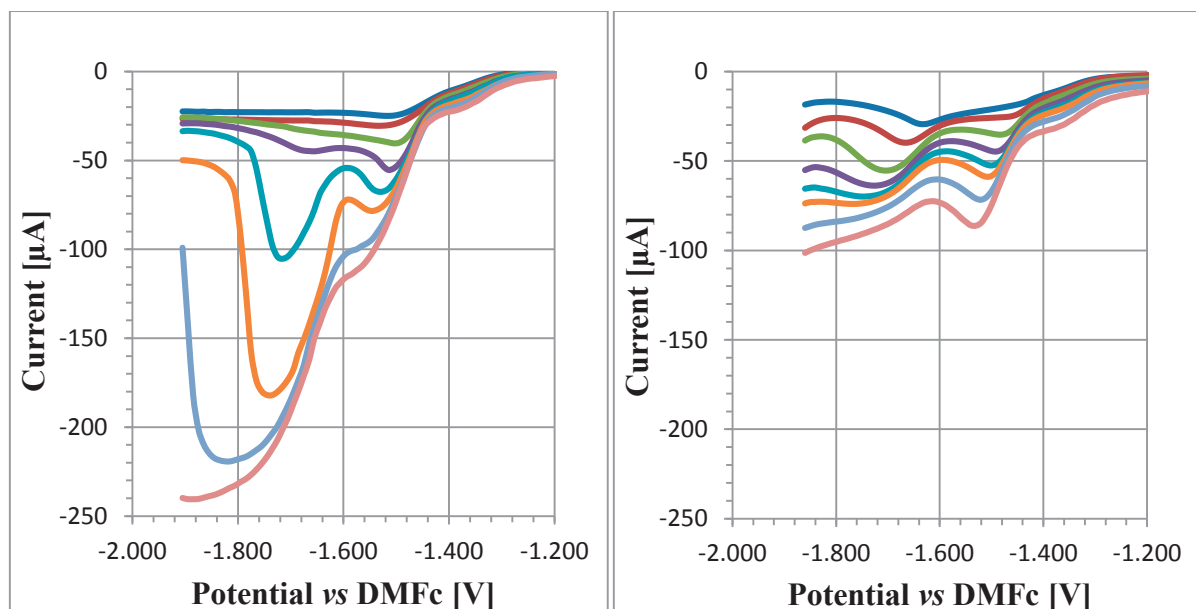


Figure 7.9. Blank subtracted linear scan in AcN 0.1 M TBAPF₆ with 275 mM of water added (left) and dry acetonitrile (right) of 1mM [Ru(bpy)₂(CO)H](PF₆), gold working electrode, potential calibrated versus DMFc⁺/DMFc, under 2 bars of CO₂ pressure at different scan rate (50 , 100, 200, 300, 400, 500, 750 and 1000 mV/s).

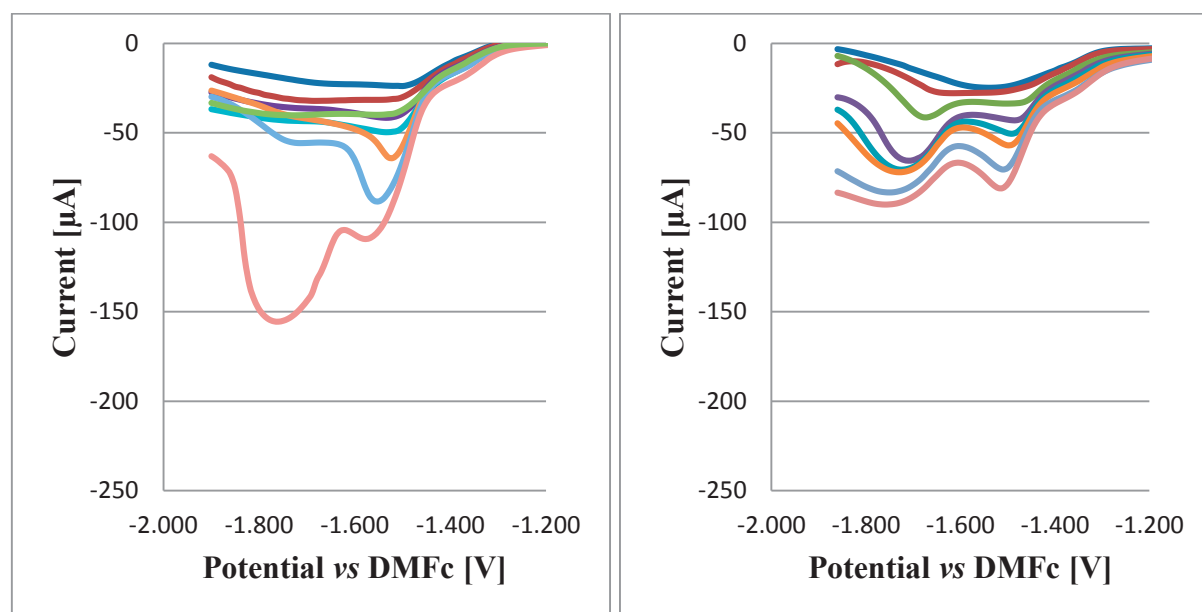


Figure 7.10. Blank subtracted linear scan in AcN 0.1 M TBAPF₆ with 275 mM of water added (left) and dry acetonitrile (right) of 1mM [Ru(bpy)₂(CO)H](PF₆), gold working electrode, potential calibrated versus DMFc⁺/DMFc, under 4 bars of CO₂ pressure at different scan rate (50 , 100, 200, 300, 400, 500, 750 and 1000 mV/s).

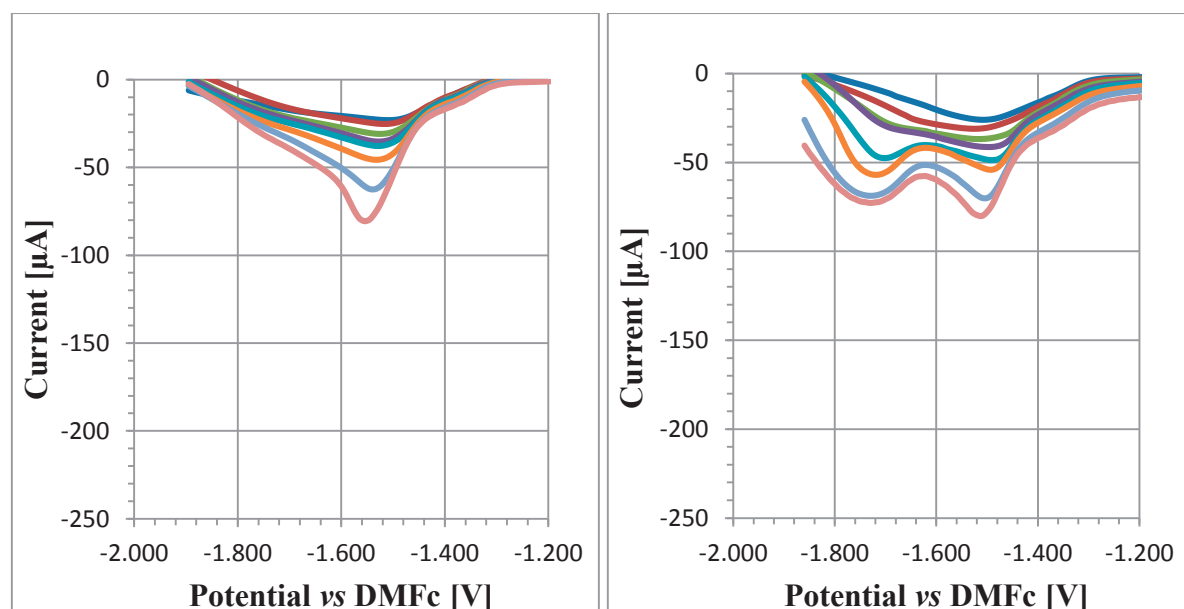


Figure 7.11. Blank subtracted linear scan in AcN 0.1 M TBAPF₆ with 275 mM of water added (left) and dry acetonitrile (right) of 1mM [Ru(bpy)₂(CO)H](PF₆), gold working electrode, potential calibrated versus DMFc⁺/DMFc, under 6 bars of CO₂ pressure at different scan rate (50 , 100, 200, 300, 400, 500, 750 and 1000 mV/s).

Without addition of water, at the four different pressures considered, the activity of the catalyst is very similar. The current wave corresponding to the reduction of the formate complex remains constant over the pressure range considered. This result is in good agreement with the results of chapter 5, in which it has been observed that the production of formate was not affected by a pressure increase.

In presence of water the behaviour of this current wave is very similar, and no noteworthy increase is observed. But for the second reduction wave at more negative potentials, major differences are observed with pressure and scan rate. This reduction wave is not present under all conditions of pressure and scan rate. A fast scan rate favours this catalytic wave, but increasing the pressure above 2 bars tends to decrease this catalytic wave. Depending on the pressure, the wave is not visible at all scan rates; the minimal scan rate required increases with pressure. The disappearance of this wave at higher pressures implies that the carbon monoxide evolution mechanism is not involved in the current measured, as a steady increase with pressure would be expected. But CO₂ addition on the reduced penta-coordinated complex after completion of a first catalytic cycle might be the cause of the disappearance of the wave at higher pressures. As the catalyst in solution is the hydride form, the mechanism of the first cycle is inevitably the formate mechanism. But after a complete cycle, the catalyst will follow one of the two cycles depending on the concentration of protons and CO₂. At low pressures, the carbon monoxide cycle seems not to participate in the catalytic current observed.

Scan rate is also an important factor influencing the mechanism; at low scan rates this reduction wave is not visible at all. The minimal scan rate required to observe this wave is also increasing with pressure. This is apparently indicating the existence of a competition between an electron transfer reaction with a reaction implying CO₂. The reduction potential of this catalytic wave is very similar with the second reduction potential of the hydride complex. A possible mechanism explaining the observed behaviour includes two successive reductions of the hydride complex, followed by reaction with CO₂. The mechanism of the reaction with CO₂ however, is unknown. But this reaction is apparently much faster than the other mechanisms proposed in Figure 7.1. The mechanism proposed here is not the only possibility. Fast scan rate and low CO₂ concentration can also favour the polymerization reaction of the complexes. Deronzier *et al.* have observed the formation of a film of [Ru⁰(bpy)(CO)₂]_n on platinum

electrode surface while using $[\text{Ru}^{\text{II}}(\text{bpy})_2(\text{CO})_2]^{2+}$ as catalyst. In their voltammetry, a sharp reductive current peak was observed and attributed to the formation of the film. In the reverse scan, a sharp reverse peak attributed to the desorption of the film was observed [8]. In the present case, nor a sharp reduction peak nor an oxidation peak in the reverse scan are observed. As both should be observed in presence of a polymerization process, the formation of a catalytic film of $[\text{Ru}^0(\text{bpy})(\text{CO})_2]_n$ is apparently not happening in the conditions used here. Therefore, the most probable explanation of the important catalytic wave observed under low CO_2 pressure with fast scan rate is a faster catalytic reaction between the reduced hydride complex $[\text{Ru}(\text{bpy}^-)_2(\text{CO})\text{H}]$ and CO_2 . But no further investigations on this mechanism have been performed.

7.2.3. Pressure effect on glassy carbon electrode

The use of a gold electrode was demonstrated in Figure 7.5. to highly hinder the possibility of conducting electrochemical experiments at high pressures due to the large current measured for the direct reduction of CO_2 on the gold surface. Replacing the gold electrode by a glassy carbon electrode was performed to study the effect of CO_2 pressure over a 50 bars range. Dimethylformamide (DMF) was used as solvent to replace acetonitrile as volume expansion and diffusion coefficient determination were performed in this solvent in chapter 6.

In this alternative solvent and on glassy carbon electrode, the voltammetric behaviour of the catalyst is comparable. At fast scan rates and low pressures, the second wave is also observed. The effect of pressure appears to be very limited as shown in Figure 7.12., the catalytic current is increasing between 1 and 15 bars but above this value the current reach a maximal value and even decrease at high pressure due to the dilution of the solution. The increase observed here is rather limited compared to the steady increase in photocatalytic production of carbon monoxide over a 10-150 bars pressure range observed in chapter 5.

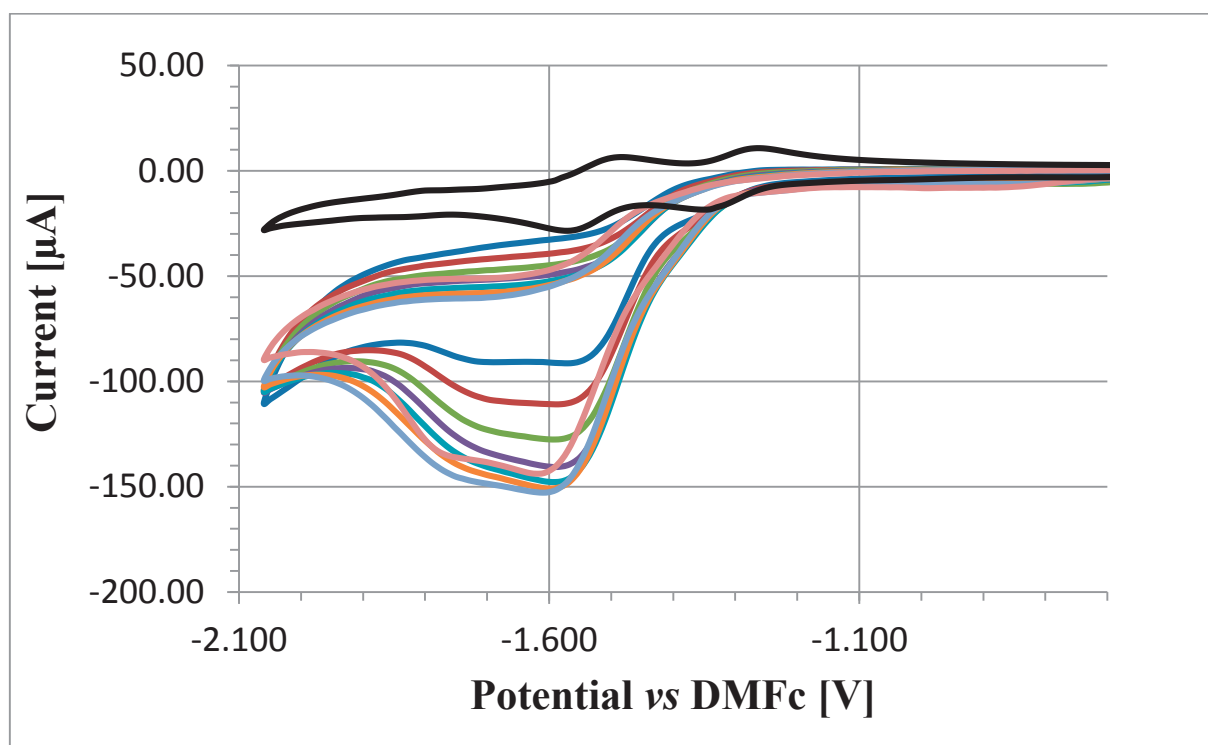


Figure 7.12. CV in dimethylformamide 0.1 M TBAPF₆ with 300mM water of 1mM [Ru(bpy)₂(CO)H](PF₆), glassy carbon working electrode, potential calibrated versus DMFc⁺/DMFc, scan rate 100mV/s, under argon in black and different pressure of CO₂ (1, 3, 5, 10, 15, 20, 30 and 50 bars) in colour.

7.3. Rhenium catalyst

7.3.1. Voltammetric behaviour

The voltammetric behaviour of the catalyst [ReCl(bpy)(CO)₃] is presented in Figure 7.13. In absence of CO₂, the catalyst presents also two reduction waves, but only the first one is reversible. On the second reduction, the loss of a chloride, as shown in Figure 7.2., renders the reduction step irreversible. This step being the activation of the catalyst, after which CO₂ addition on the catalyst happens and a two-electron reduction cycle can proceed. Under atmospheric pressure of CO₂, a catalytic current is observed at the second reduction with two successive reduction waves. With the first one at the same potential of the irreversible reduction of [ReCl(bpy⁻)(CO)₃]⁻, and the second about 200 mV more negative. The first wave

corresponds to the mechanism shown in Figure 7.2., but the second wave is unidentified. From Figure 7.2., two mechanisms appear possible depending if the second proton is transferred to the catalyst before or after the first electron of the catalytic cycle. On the voltammetry, these two mechanisms are not discernible as the potential required to complete the cycle is the same. With addition of a weak organic acid as proton source, trifluoroethanol (TFE), the catalytic current is increased for the first wave and decreased for the second. The second waves appears to be attributed to a reaction mechanism in absence of protons, such as the reduction of $[\text{Re}(\text{bpy})(\text{CO})_3(\text{CO}_2)]^-$, the complex resulting of the addition of CO_2 on the activated catalyst.

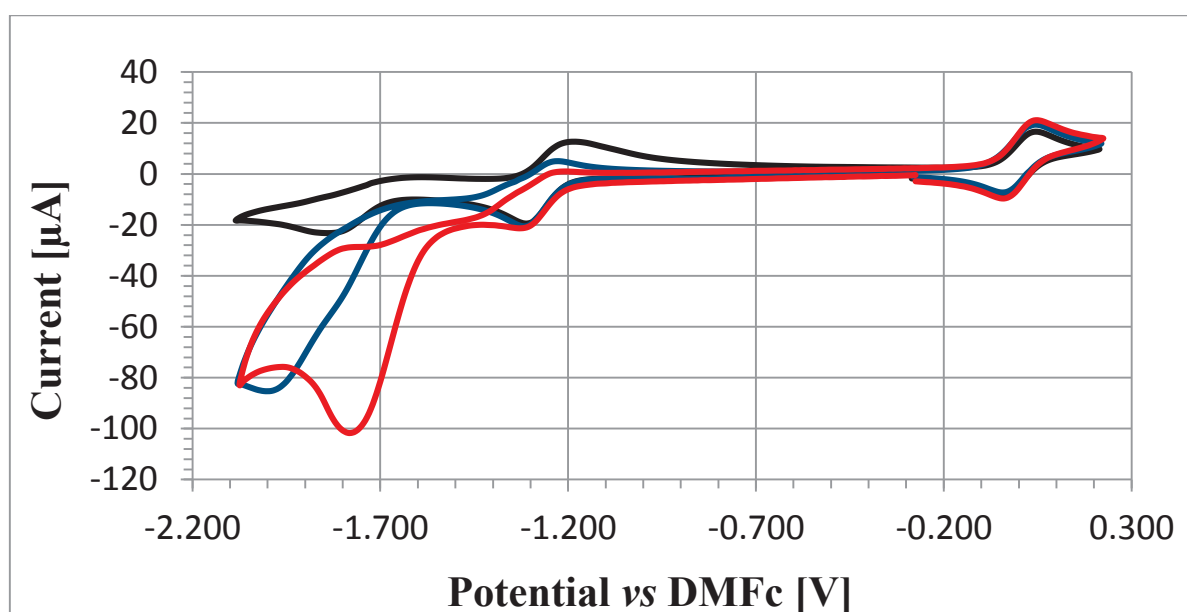


Figure 7.13. CV in DMF 0.1 M TBAPF₆ of 1mM $[\text{ReCl}(\text{bpy})(\text{CO})_3]$, glassy carbon working electrode, potential calibrated versus DMFc⁺/DMFc, scan rate 100mV/s, in black under argon, in blue under atmospheric pressure of CO₂ and in red with CO₂ and addition of 1M trifluoroethanol.

The potential required for the activation of the catalyst is about 200 mV more negative than the potential required for the catalytic cycle. Therefore crossing of the forward and the reverse scan happens often. For this reason, in the following figures only the forward scans are displayed. In the following sections, variation in reaction mechanism will be investigated in presence of increasing the proton donor concentration or the CO₂ pressure.

7.3.2. Proton donor concentration

As seen in the previous figure, increasing the proton donor concentration is increasing the first catalytic wave. The mechanism involved here appears to be that expected from Figure 7.2. The catalytic current is increasing with proton concentration as the second proton addition appears to be the rate-determining step due to the high activation energy barrier of this step.

But as seen in Figure 7.14., a second effect is observed between the activation wave and the first catalytic wave. This indicates that a large concentration of trifluoroethanol (TFE) is promoting the release of chloride anion by the complex after the first reduction of the complex. TFE is a coordinating solvent, solubilising the released anion and stabilizing the complex after the loss of chloride. This effect has been observed by different authors. Spectroelectrochemical investigations by Johnson have shown that in weakly coordinating solvents such as TFE, the release of chloride was happening after the first reduction event [9]. By voltammetry, this effect was also observed by Schreier with a similar catalyst in presence of large concentrations of methanol used as proton donor [10].

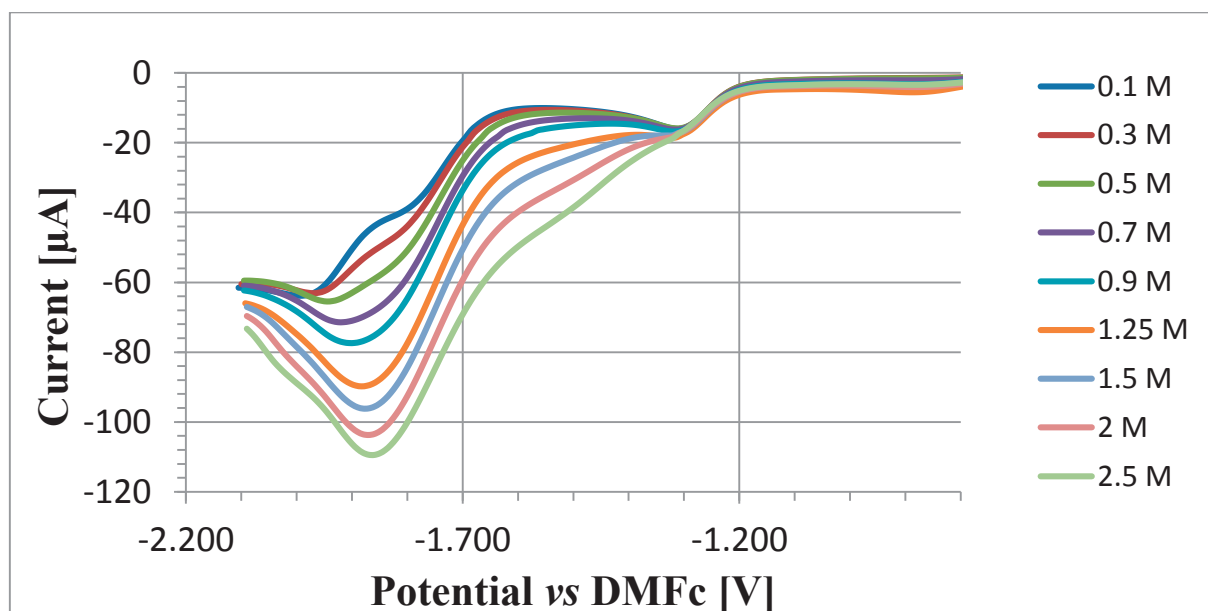


Figure 7.14. Linear scan voltammetry in DMF 0.1 M TBAPF₆ of 1mM [ReCl(bpy)(CO)₃], glassy carbon working electrode, potential calibrated versus DMFc⁺/DMFc, scan rate 100mV/s, with different concentration of TFE.

Increase of the catalytic rate with proton donor concentration has been observed by Wong for different acids, such as trifluoroethanol, phenol, water or methanol [11]. With TFE being the most effective in enhancing the rate of catalysis owing to its higher acidity. Extracting the catalytic rate using Equation (1.15) from chapter 1 is impossible as the voltammogram is peak shaped rather than tending to a plateau current, even for small scan rates. But the ratio of the peak current to the reversible wave current is a good indication on the increase in catalytic activity. In Figure 7.15., a linear increase for the peak current observed up to a TFE concentration of 1.25 M. This result is in good agreement with the mechanism shown in Figure 7.3. With the second proton addition being the rate-limiting step. At higher proton concentrations, the peak current should tend to a limiting value as a different rate-limiting step appears. But due to the change in the activation mechanism with high acid concentration, the catalytic current keeps increasing but with a different slope.

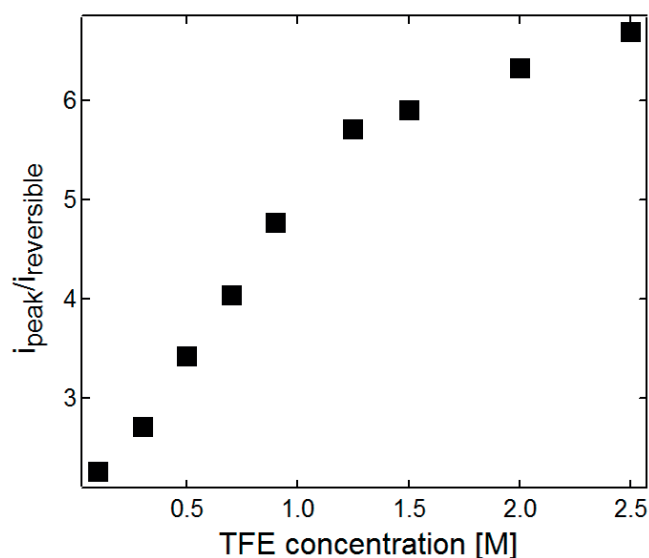


Figure 7.15. Normalised catalytic peak current as a function of acid concentration.

7.3.3. Pressure effect

From the mechanism described in Figure 7.2., CO_2 addition on the complex is a barrierless process. Therefore, the catalytic current should not be much influenced by the CO_2

pressure. But experimentally, in absence of a proton source in solution, the increase of pressure has a tremendous impact on the catalytic current measured. With 2.5 M TFE the catalytic current peak was increasing from 40 to 110 μA in atmospheric conditions. While increasing CO_2 pressure increases the catalytic current peak up to 550 μA . With the highest catalytic current measured for a pressure of 30 bars. Further increase in pressure leads to important dilution due to volume expansion, and shift of the potential due to ohmic drop caused by the increasing resistivity of the solution. Catalytic waves measured at 40 and 50 bars have a reduced slope due to ohmic drop. A sharp current peak is observed between 15 and 40 bars, corresponding to an adsorption process on the electrode, possibly caused by the polymerization of the catalyst on the electrode. But this process remains limited, and do not interfere much in the voltammetry.

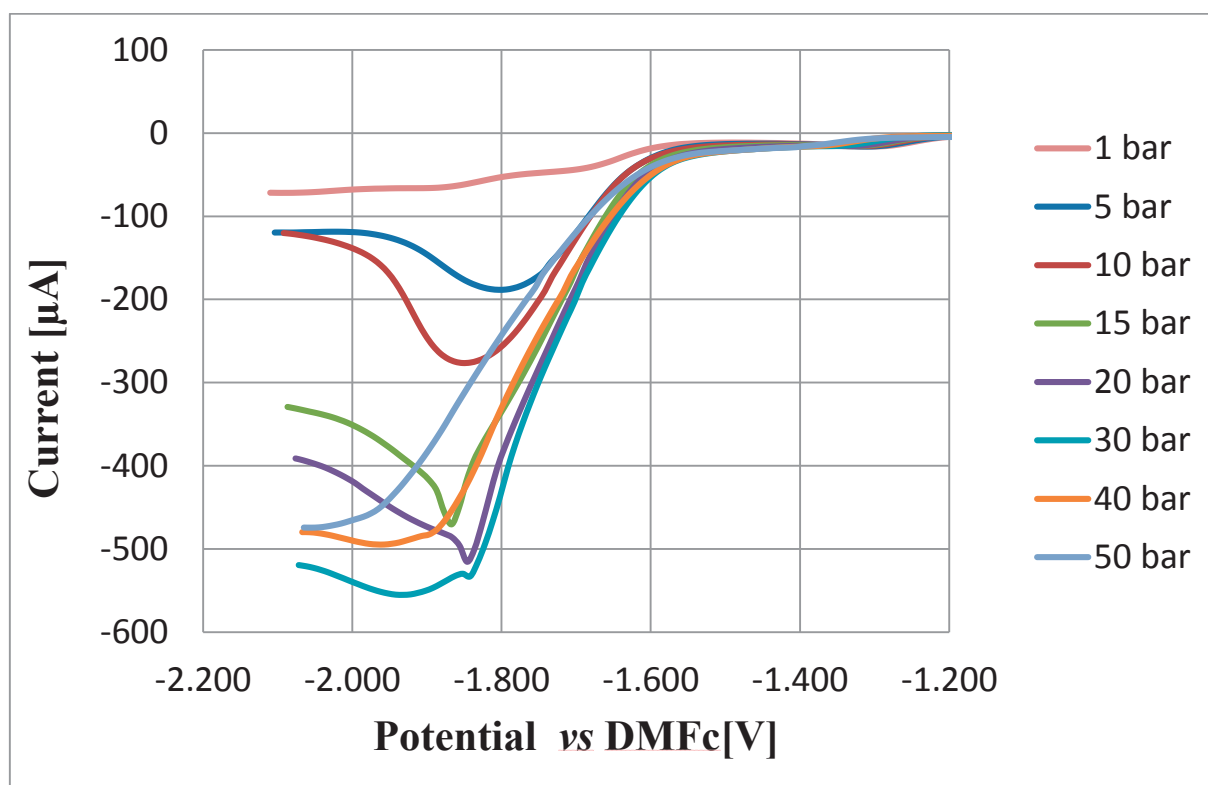


Figure 7.17. Linear scan voltammetry in DMF 0.1 M TBAPF_6 of 2mM $[\text{ReCl}(\text{bpy})(\text{CO})_3]$, glassy carbon working electrode, potential calibrated versus $\text{DMFc}^+/\text{DMFc}$, scan rate 25mV/s, with increasing CO_2 pressure.

In the presence of a S-shaped voltammetry exhibiting a stable plateau current, the rate constant of the catalytic process can be determined from the plateau current as presented in

section 1.2.3. But, as the voltammograms are peak shaped, even at a scan rate of 25 mV/s, Equation (1.15) cannot apply. The method used to determine the rate constant is the *foot-of-the-wave analysis* developed by Savéant *et al.* [12]. The peak-shape of the voltammetry is caused by the consumption of the substrate and limitation in the diffusion. But at the foot of the wave, these factors play a smaller role and the current measured is given by the rate of the catalytic reaction.

In this method, the current at the base of the wave is compared to the peak current of the non catalytic process. The wave that is analyzed with this method is the second reduction of the catalyst, corresponding to the activation and release of chloride. The peak current in absence of catalysis is therefore given by the modified Randles-Sevcik equation for irreversible process:

$$i_p = 0.496nFAC \left(\frac{nFvD}{RT} \right)^{1/2} \quad (1.12)$$

where F is the Faraday constant, A the electrode surface, C the concentration of the catalyst, v the scan rate (in V/s) and D the diffusion coefficient of the catalyst. The catalyst concentration and diffusion coefficient have been determined in chapter 6 for the different conditions of pressure used herein.

The current of a catalytic S-shaped wave was also given in chapter 1, for a multi-step catalytic reaction, with second electron transfer easier than the first:

$$i = \frac{nFAC \sqrt{Dk_{obs}}}{1 + \exp \left[\frac{nF}{RT} (E - E_{cat}^{\circ}) \right]} \quad (1.16)$$

where k_{obs} is the apparent rate constant of the catalytic cycle and supposed to be first order to CO_2 concentration. As the voltammograms obtained are peak-shaped, this equation is valid only at the foot of wave.

The apparent rate constant is obtained by plotting i/i_p as a function of $1/\left(\exp\left[\frac{2F}{RT}(E - E_{cat}^{\circ})\right]\right)$ and determined by the linear relationship at the foot of the wave. The

non-catalytic peak current cannot be determined experimentally at high pressures and was then calculated from Equation (1.12) using the values of concentration and diffusion determined in section 6.2.2. The current ratio is given by the two previous equations:

$$\frac{i}{i_p} = \frac{2\sqrt{k_{obs}}}{0.496} \sqrt{\frac{RT}{vF}} \cdot \frac{1}{1 + \exp\left[\frac{2F}{RT}(E - E_{cat}^{\circ})\right]} \quad (7.1)$$

The apparent rate constant can then be directly obtained from the slope, as done in Figure 7.18. a). In Figure 7.18. b), the apparent rate constant as a function of CO₂, obtained with a similar analysis at different pressures are plotted.

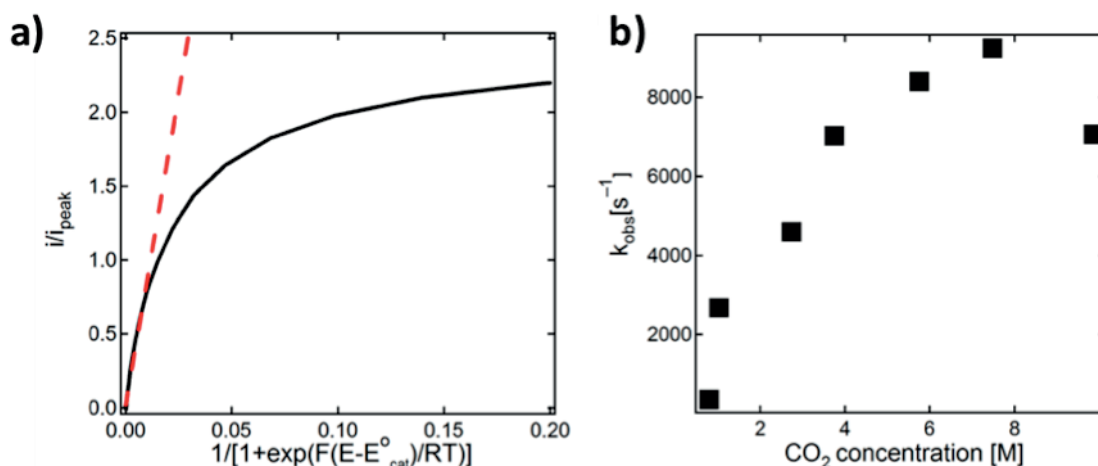


Figure 7.18. a) Foot-of-the-wave analysis at 10 bars, in black experimental data and in red linear fitting near the foot of the wave. b) Apparent rate constant as a function of CO₂ concentration for 1-50 bars pressure range.

The rate constant obtained appears to vary linearly *versus* the CO₂ concentration up to a concentration of 4 M, corresponding to a pressure of 20 bars. Above this pressure, the concentration of CO₂ is important enough to cause a significant ohmic drop in the solution. Therefore, the observed decrease in rate constant at high pressures, might be due to the uncompensated resistance of the solution rather than a modification of the mechanism changing the rate determining step of the catalytic cycle. Compensation of the ohmic drop is therefore necessary for mechanism analysis at high pressures, but with the experimental setup and potentiostat used herein, this was impossible to achieve.

In the previous section, proton addition appeared to be the rate-limiting step of the catalytic cycle. It appears contradictory that from the results with increasing pressures, the rate-determining step involves CO_2 . To determine if the same catalytic mechanism is involved in both cases, in the next section, comparison of voltammograms at high pressures with and without proton donor is performed.

7.3.4. Proton donor concentration at high pressures

In Figure 7.19, voltammograms obtained at 4 different pressures are compared. In red the voltammograms are measured with a TFE concentration of 1 M, while the voltammograms in blue are the same as in the previous section, in absence of proton donor.

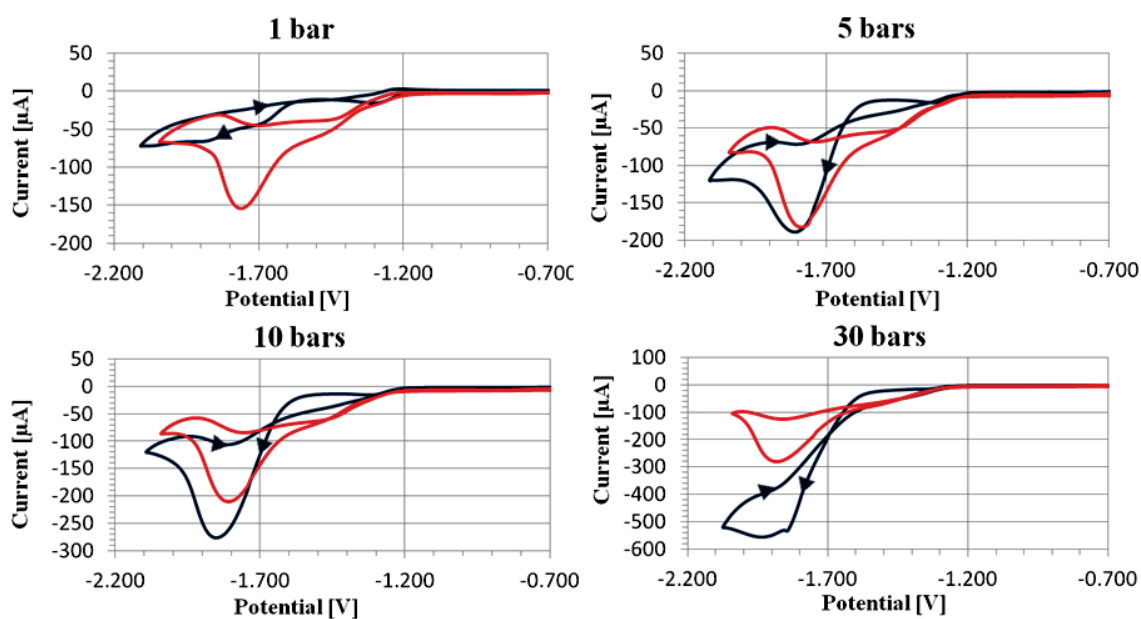


Figure 7.19. CV in DMF 0.1 M TBAPF₆ of 2mM [ReCl(bpy)(CO)₃], glassy carbon working electrode, potential calibrated versus DMFc⁺/DMFc, scan rate 25mV/s, for different CO₂ pressures, in blue without addition of acid, in red with 1M TFE.

With an important concentration of acid, the pressure has a very limited effect on the catalytic current measured. The increase in peak current is very limited and the shape of the voltammogram is not changing at all. In absence of TFE, the peak current is much smaller at

atmospheric pressure but become much higher under high-pressure conditions. Surprisingly, the catalytic current is larger at elevated pressures in absence of proton donor. Indicating that at in absence of proton donors, a different mechanism appears, and this mechanism is highly influenced by CO₂ concentration.

As an increase in proton donor concentration at high pressures is causing a decrease in the catalytic activity, the change in mechanism is happening at the first proton transfer step. In high acid concentration conditions, as this step is barrierless, this protonation is presumed to be fast and the catalytic cycle follows the mechanism of Figure 7.2. But at high pressures in absence of protons, a new catalytic cycle appears, replacing the first protonation step. With this catalyst, evolution of carbonate during the reduction of CO₂ to carbon monoxide has been reported previously [13]. Therefore, an additional mechanism is suspected, in which a second molecule of CO₂ replaces the two protons in the abstraction of the oxygen atom from the CO₂ molecule bound to the complex. Gibson, Kubiak *et al.* [14] have shown that a bimolecular reaction was possible with this type of catalyst. Formation of a supramolecular complex made of two hydrogen-bonded catalytic unit was highly favourable for the catalytic reductive disproportionation of CO₂ into CO and CO₃²⁻. The proposed mechanism for this catalytic cycle is shown in Figure 7.20.

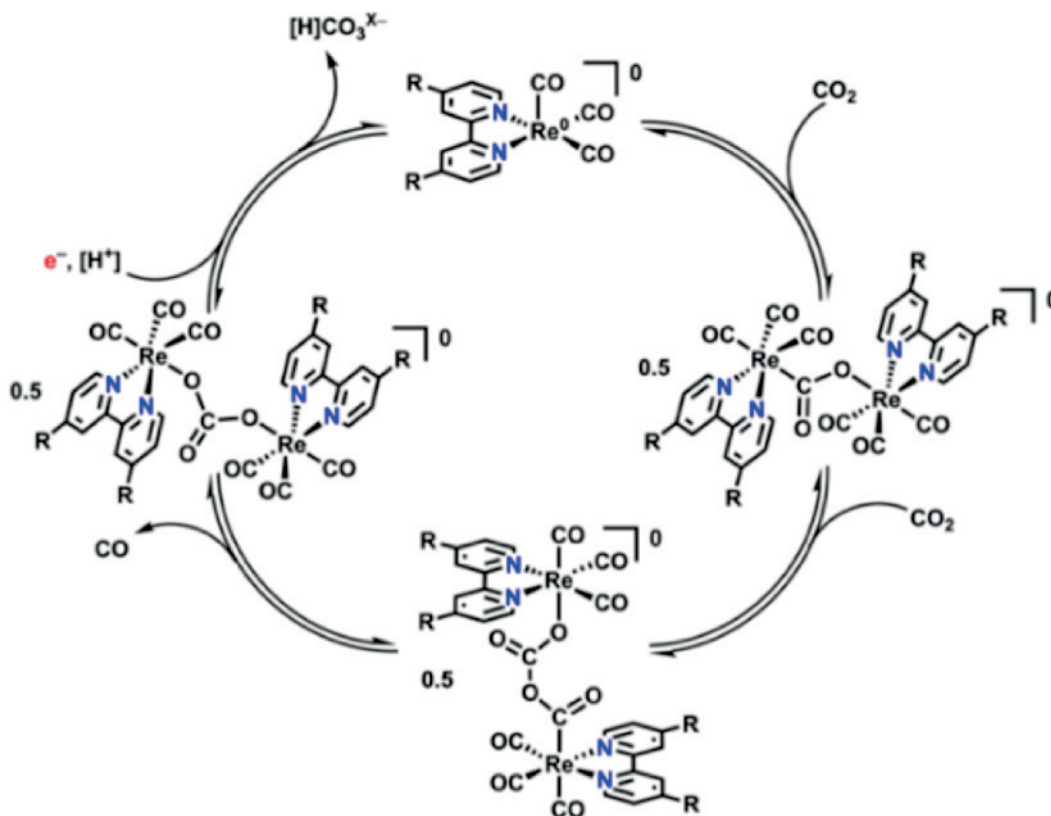


Figure 7.20. Proposed bimolecular mechanism for electrocatalytic reduction of CO₂ in absence of proton donor [14].

In absence of a proton donor, this mechanism can explain the observed dependence between the apparent rate constant and CO₂ concentration. Confirmation of the existence of this mechanism could be done by recording voltammetry with different concentrations of catalyst, as this mechanism is supposed to be second order in catalyst.

7.4. Conclusions

Voltammetry in CO₂-expanded liquids has been conducted for two catalysts, [Ru(bpy)₂(CO)H]⁺ and [ReCl(bpy)(CO)₃]. The suspected catalytic mechanisms were confirmed by voltammetry for both complexes under atmospheric pressure and at low proton donor concentrations.

In initial experiments with the former catalyst, a gold working electrode was used. But this electrode limits severely the range of pressures that can be studied as the direct reduction of CO₂ on the electrode surface is generating an important catalytic current in presence of weak proton donors and above a pressure of 2 bars. In presence of water, at low pressures, an additional catalytic wave is observed at fast scan rates. This catalytic wave is attributed to the second reduction of the hydride form, which is then reacting with CO₂ through a faster catalytic mechanism.

Replacing the gold working electrode by glassy carbon enables voltammetry at higher pressures. But for this ruthenium catalyst, CO₂ concentration seems to have limited impact on the catalytic rate. Indeed, increase in current was only observed up to a pressure of 15 bars.

For the rhenium catalyst, additional mechanisms were observed when increasing the proton donor concentration or CO₂ pressure. Above a TFE concentration of 1 M, 1-electron activation of the complex was observed, reducing the required potential for the activation of the catalyst. In absence of proton donor under higher pressures of CO₂, an alternative mechanism is also observed. This mechanism has the highest catalytic rate observed for CO₂ reduction and can be attributed to a bimolecular pathway catalyzing the disproportionation of CO₂ into CO and CO₃²⁻

7.5. Bibliography

1. Ishida, H., K. Tanaka, and T. Tanaka, *Electrochemical CO₂ reduction catalyzed by ruthenium complexes [Ru(bpy)₂(CO)₂]²⁺ and [Ru(bpy)₂(CO)Cl]⁺. Effect of pH on the formation of CO and HCOO*. *Organometallics*, 1987. **6**(1): p. 181-186.
2. Pugh, J.R., et al., *Formation of a metal-hydride bond and the insertion of carbon dioxide. Key steps in the electrocatalytic reduction of carbon dioxide to formate anion*. *Inorganic Chemistry*, 1991. **30**(1): p. 86-91.
3. Keith, J.A., et al., *Elucidation of the selectivity of proton-dependent electrocatalytic CO₂ reduction by fac-Re(bpy)(CO)₃Cl*. *Journal of the American Chemical Society*, 2013. **135**(42): p. 15823-15829.
4. Keith, J.A., et al., *Elucidation of the Selectivity of Proton-Dependent Electrocatalytic CO₂ Reduction by fac-Re(bpy)(CO)₃Cl*. *Journal of the American Chemical Society*, 2013. **135**(42): p. 15823-15829.
5. Abbott, A.P. and C.A. Eardley, *Electrochemical Reduction of CO₂ in a Mixed Supercritical Fluid*. *The Journal of Physical Chemistry B*, 2000. **104**(4): p. 775-779.
6. Hara, K., et al., *Electrochemical Reduction of CO₂ on a Cu Electrode under High Pressure Factors that Determine the Product Selectivity*. *Journal of the Electrochemical Society*, 1994. **141**(8): p. 2097-2103.
7. Noda, H., et al., *Kinetics of Electrochemical Reduction of Carbon Dioxide on a Gold Electrode in Phosphate Buffer Solutions*. *Bulletin of the Chemical Society of Japan*, 1995. **68**(7): p. 1889-1895.
8. Chardon-Noblat, S., et al., *Formation of Polymeric [Ru(bpy)(CO)₂]_n Films by Electrochemical Reduction of [Ru(bpy)₂(CO)₂](PF₆)₂: Its Implication in CO₂ Electrocatalytic Reduction*. *Inorganic Chemistry*, 1994. **33**(19): p. 4410-4412.
9. Johnson, F.P.A., et al., *Electrocatalytic Reduction of CO₂ Using the Complexes [Re(bpy)(CO)₃L]_n (n = +1, L = P(OEt)₃, CH₃CN; n = 0, L = Cl⁻, Otf⁻; bpy = 2,2'-Bipyridine; Otf⁻ = CF₃SO₃) as Catalyst Precursors: Infrared Spectroelectrochemical Investigation*. *Organometallics*, 1996. **15**(15): p. 3374-3387.
10. Schreier, M., et al., *Efficient and selective carbon dioxide reduction on low cost protected Cu₂O photocathodes using a molecular catalyst*. *Energy & Environmental Science*, 2015. **8**(3): p. 855-861.
11. Wong, K.-Y., W.-H. Chung, and C.-P. Lau, *The effect of weak Brønsted acids on the electrocatalytic reduction of carbon dioxide by a rhenium tricarbonyl bipyridyl complex*. *Journal of Electroanalytical Chemistry*, 1998. **453**(1): p. 161-169.
12. Costentin, C., et al., *Turnover numbers, turnover frequencies, and overpotential in molecular catalysis of electrochemical reactions. Cyclic voltammetry and preparative-scale electrolysis*. *Journal of the American Chemical Society*, 2012. **134**(27): p. 11235-11242.
13. Sullivan, B.P., et al., *One-and two-electron pathways in the electrocatalytic reduction of CO₂ by fac-Re(bpy)(CO)₃Cl (bpy= 2, 2'-bipyridine)*. *Journal of the Chemical Society, Chemical Communications*, 1985(20): p. 1414-1416.
14. Machan, C.W., et al., *Supramolecular Assembly Promotes the Electrocatalytic Reduction of Carbon Dioxide by Re(I) Bipyridine Catalysts at a Lower Overpotential*. *Journal of the American Chemical Society*, 2014. **136**(41): p. 14598-14607.

CHAPTER 8

General conclusions and perspectives

The results presented in this thesis describe the catalytic reduction of CO₂ in different pressurized systems, such as biphasic solvent systems, supercritical CO₂ with co-solvent addition or expanded liquids. With each system demonstrating the advantage of using high-pressure conditions.

Reduction of carbon dioxide was initially conducted in biphasic systems composed of supercritical CO₂ and water. In this biphasic system decamethylferrocene was used as an electron donor and reaction centre to conduct the reduction of CO₂ in the dark. The beneficial effect of high pressure was to generate the biphasic system in which protons were transferred from the aqueous to the supercritical phase. Phase in which the important concentration of CO₂ orientated the reaction selectively toward CO₂ reduction rather than H₂ evolution. But very low yield for product were obtained. The main limitations were believed to be caused by side reactions, such as oxygen reduction or degradation of the anion transferring protons through the interface.

With DMFc, the reduction of CO₂ is conducted at very moderate potential. Additionally recycling of the DMFc is a simple one-electron process, and can be integrated to

catalytically reduce CO₂ in an effort to generate higher reaction yield. But integration of an electrochemical recycling of DMFc gives rise to additional problems. To recycle the DMFc on an electrode, an oxidation process must happen on the counter electrode. But oxidation of the products of CO₂ reduction at the counter electrode or generation of oxygen that will further oxidize DMFc must be avoided. In conventional electrolysis system, to avoid this kind of inconveniences, membranes are used to separate the products of each electrode reaction. But the high-pressure conditions necessary for the reduction of CO₂ by DMFc appears incompatible with the use of usual membranes.

In the same biphasic system, photocatalytic reduction of CO₂ was explored and demonstrated to be more efficient and selective towards CO production when driven in supercritical conditions. The main advantage of this biphasic system appeared to be the existence of the interface at which the aqueous catalyst, Ni(II)Cyclam could adsorb. Adsorption of the catalyst was demonstrated at the air-water and the scCO₂-water interfaces. The recycling of the catalyst was believed to occurs homogeneously in the aqueous phase whereas the CO₂ binding process was occurring at the interface. Integration of microelectrodes in the reactor is part of the ongoing work. With these types of electrodes, recording approach curves of the interface in the aqueous phase could be a valuable tool to demonstrates the interfacial activity of this catalyst.

Activity and stability of the Ni(II)Cyclam and the photosensitizing cycle were an important limitation in chapter 4. To improve the photocatalytic system, a different catalyst was used, a ruthenium polypyridyl catalyst, the aqueous phase was also replaced by an organic solvent dimethylformamide, as this catalyst is not soluble in water. The photocatalytic reduction of CO₂ at high pressure was conducted in two different solvent conditions. Addition of water as proton carrier lead to the formation of a biphasic system, while with triethanolamine a single phase was formed. The total production of the two systems were similar but the product distribution was slightly different, with formate being favour with TEOA. CO production was found to have a linear relationship with pressure while formate evolution was independent of pressure.

Two major limitations were identified, the saturation concentration of CO in solution and the formation of the BNA₂ dimer, from the oxidation of the sacrificial electron donor. The biphasic system was favourable to CO production due to the extraction of the product in the supercritical phase, preventing the catalyst from being poisoned. The limitation caused by the BNA₂ dimer highlights the importance of the irreversibility of the oxidation of the electron donor in photocatalytic systems. It has been demonstrated with a mathematic model that in presence of a reversible electron donor, the back electron transfer occurring between the photosensitizer and the quencher inhibits totally the production. With this limitation, it appears highly difficult to improve further the photocatalytic system or to couple the reduction of CO₂ to the oxidation of water to mimic natural photosynthesis.

Due to the limitations inherent to the photocatalytic reduction of CO₂, the last part of the thesis moved away from mimicking natural photosynthesis and was focused on the electrocatalytic reduction of CO₂. Due to the forecasted development and expansion of photovoltaic energy, electrocatalytic reduction of CO₂ appear as a more attractive process. In this part, the research was focused on the mechanism of CO₂ reduction by two molecular catalysts. Pressure was used to determine the effect of CO₂ concentration of the catalytic mechanism in expanded liquids.

Voltammetry at elevated CO₂ pressure could not be achieved in pure scCO₂ phase due to the very low dielectric constant of the media. Two different solvent systems were used to conduct voltammetry in pressurized CO₂ systems : CO₂-expanded liquids and scCO₂ with addition of an organic co-solvent to solubilise a room temperature ionic liquid as electrolyte. In the expanded liquids, volume expansion, phase composition and diffusion coefficient of a rhenium catalyst were determined over a range of pressure of 1 to 50 bars. Change in viscosity of the expanded liquid was explaining well the increase in diffusion coefficient up to a pressure of 20 bars. But above this pressure, the increase in diffusion coefficient was limited. This modification in behaviour was attributed to heterogeneities in the solution with the formation of a film on the electrode of different composition than the bulk solution. In supercritical conditions with addition of an organic co-solvent a similar film formation was suspected on the electrode surface. Experimental and simulation results suggest that a liquid-like film was formed at the electrode surface.

Mechanistic analysis of ruthenium and rhenium polypyridyl catalysts were performed in expanded liquids with moderate pressure. At pressures higher than 40 bars, voltammetry appeared highly distorted due to ohmic drop in the solution and by incomplete sealing of electrode connections. Improving the electrochemical setup and the reactor connection is under way to enable better voltammetric measurements at higher pressure especially in supercritical conditions.

For the ruthenium catalyst the effect of CO₂ concentration on the catalytic activity was found to be very moderate. A surprising catalytic activity was appearing at fast scan rates and between 1 and 2 bars of pressure. The catalytic mechanism involved in these conditions was not fully understood. A possible explanation was the formation of a highly reduced hydride intermediate reacting with CO₂ via a faster catalytic mechanism.

The rhenium catalyst was suspected to have a unique catalytic mechanism, which appeared simpler for voltammetric analysis. Variations in proton donor concentration confirmed that the rate limiting step was a protonation reaction. But at higher pressure in absence of proton donor, a large increase in catalytic current was observed. This results demonstrated that the reaction could happen in absence of proton to form CO and CO₃²⁻.

In this last chapter, the research was focused only on the reduction of CO₂ and do not consider the oxidation process necessary on the counter electrode. But for developing a complete process for the reduction of CO₂, an oxidation process must be coupled. Ideally, this process would be oxidation of water as in natural photosynthesis, generating oxygen and protons which are consumed in the reduction of CO₂. A new electrochemical reactor is in development to conduct electrolysis experiments. Ruthenium and rhenium catalyst are expensive material, in future researches different catalytic material will be tested as cheaper alternative. Heterogeneous catalysis on the electrode surface is also a possibility to investigate. Gold electrode showed an important catalytic activity toward CO₂ reduction, but cheaper metals such as copper appear promising.

Patrick Voyame
Ch. du Banc-vert 27
1110 Morges
021 801 63 11
079 720 01 61
patrick.voyame@epfl.ch

29 ans
Célibataire
Suisse

Défense de Thèse : Photocatalytic and Electrocatalytic Reduction of Carbon Dioxide in Pressurized Systems

Formation

- Fin de doctorat à l'EPFL, au Laboratoire d'Electrochimie Physique et analytique Février 2016
- Master en chimie moléculaire et biochimie à l'EPFL Février 2011
- Bachelor en chimie à l'EPFL Juillet 2008
- Maturité gymnasiale avec option spécifique biologie et chimie et option complémentaire sport Juillet 2004
- Certificat école secondaire à Beausobre à Morges en section scientifique Juillet 2001

Activités parallèles à mes études

- Travail au musée L'Alimentarium dans le cadre de l'exposition recherche en alimentation Mars 2010 à Septembre 2010
- Service Militaire 2009-2010
- Cours de soutien privé en mathématiques et sciences Entre 2007 et 2010
- Cours de moniteur jeunesse + sport I Octobre 2004
- Moniteur de gymnastique à la FSG Morges Depuis 2003

Langues

- Français : langue maternelle
- Anglais : bon niveau (lu, écrit, parlé)
- Allemand : notions scolaires et gymnasiales

Publications

1. Schaming, Delphine, Imren Hatay, Fernando Cortez, Astrid Olaya, Manuel A. Méndez, Pei Yu Ge, Haiqiang Deng, Patrick Voyame, Zahra Nazemi, and Hubert Girault. "Artificial photosynthesis at soft interfaces." *CHIMIA International Journal for Chemistry* 65.5 (2011): 356-359.
2. Méndez, Manuel A., Patrick Voyame, and Hubert H. Girault. "Interfacial photoreduction of supercritical CO₂ by an aqueous catalyst." *Angewandte Chemie* 123.32 (2011): 7529-7532.
3. Toghil, Kathryn E., Patrick Voyame, Dmitry Momotenko, Astrid J. Olaya, and Hubert H. Girault. "Steady-state macroscale voltammetry in a supercritical carbon dioxide medium." *Physical Chemistry Chemical Physics* 15.3 (2013): 972-978.
4. Voyame, Patrick, Kathryn E. Toghil, Manuel A. Méndez, and Hubert H. Girault. "Photoreduction of CO₂ using [Ru (bpy)₂ (CO) L] n⁺ catalysts in biphasic solution/supercritical CO₂ systems." *Inorganic chemistry* 52.19 (2013): 10949-10957.
5. Toghil, Kathryn E., Manuel A. Méndez, and Patrick Voyame. "Electrochemistry in supercritical fluids: A mini review." *Electrochemistry Communications* 44 (2014): 27-30.

